Semiconductors, Vol. 37, No. 3, 2003, pp. 239–248. Translated from Fizika i Tekhnika Poluprovodnikov, Vol. 37, No. 3, 2003, pp. 257–265.

ELECTRONIC AND OPTICAL PROPERTIES OF SEMICONDUCTORS

Temperature Dependence of the Band Structure of 3*C*, 2*H*, 4*H*, and 6*H* SiC Polytypes

S. M. Zubkova*, L. N. Rusina*, and E. V. Smelyanskaya**

** Frantsevich Institute of Materials Science Problems, National Academy of Sciences of Ukraine, ul. Krzhizhanovskogo 3, Kiev-142, 03680 Ukraine*

e-mail: svzubkova@yahoo.com

*** National Technical University of Ukraine "Kiev Polytechnical Institute," pr. Peremogi 37, Kiev, 03056 Ukraine*

Submitted October 22, 2001; accepted for publication April 2, 2002

Abstract—The temperature dependences of significant energy extrema at the high-symmetry points Γ, *X*, *L*, *K*, *M*, *A*, and *H* of the Brillouin zone in the cubic and hexagonal modifications of SiC, as well as the energies of the main interband transitions at these points, were calculated for the first time by the empirical-pseudopotential method. The effect of the temperature dependence of the electron–phonon interaction on the crystal band structure was taken into account via the Debye–Waller factors, and the contribution of the linear expansion of the lattice was accounted for via the temperature dependence of the linear-expansion coefficient. The special features of the temperature dependences of the energy levels and of energies of the interband and intraband transitions are analyzed in detail. The results of the calculations are in good agreement with the known experimental data on the characteristics of SiC-based *p–n* structures operating in the breakdown mode. For example, the temperature coefficient of the energy of the X_{1c}–X_{3c} transition, which is responsible for the narrow violet band in the breakdown-electroluminescence spectra of reverse-biased *p–n* junctions, was found to be significantly smaller than the temperature coefficients for the interband transitions (from the conduction to valence band). This fact is quite consistent with the experimental curve of the temperature coefficient of the emission spectrum, which has a minimum in the same wavelength range. *© 2003 MAIK "Nauka/Interperiodica".*

1. INTRODUCTION

Numerous investigations performed in Russia, the United States, Germany, and Japan since the 1930s have shown that single-crystal SiC is one of the most promising and valuable materials for solid-state electronics [1]. Due to the high hardness, chemical inertness, and radiation resistance, this material has no competitors in the design of devices aimed at operating under extreme conditions. Because of the low diffusivity of impurities and defects in SiC, the parameters of SiC-based devices degrade very slowly. Silicon-carbide devices satisfy the strictest performance requirements; specifically, they can operate at temperatures above 800 K; their resistance to neutron fluxes exceeds that of Si, GaAs, and GaP devices by 1.5–2 orders of magnitude; and they can operate in corrosive media and strong magnetic fields.

The intense electroluminescence and photoluminescence of SiC makes it possible to design a wide range of optoelectronic devices based on various SiC polytypes; these devices include photodetectors and injection and breakdown multicolor light-emitting diodes, whose emission covers the entire visible wavelength range.

Since the field of application of SiC in solid-state electronics is steadily expanding, more and more detailed knowledge of the electronic structure of SiC and of the effect of external factors on the electronic structure of SiC is required. Although the effect of pressure on the SiC band structure has already been calculated [2], there is virtually no available experimental and theoretical data on the effect of temperature on the band structure of different SiC polytypes.

The aim of this study is to theoretically investigate the temperature dependence of the band structure of cubic (3*C*) and hexagonal (2*H*, 4*H*, and 6*H*) SiC polytypes.

2. BRIEF REVIEW OF THE CURRENT STATE OF THE THEORY OF TEMPERATURE DEPENDENCE OF THE BAND STRUCTURE OF SEMICONDUCTORS

The temperature dependence of one-electron energy levels $E(T)$ is caused by two effects. These are the thermal expansion of the lattice, which manifests itself in the dependence of the energy levels on the unit-cell volume, and the electron–phonon interaction (see review [3]). According to the Brooks–Yu theory [4], the main contribution to the dependence $E(T)$ of the one-electron band structure can be expressed in terms of the temperature dependence of the pseudopotential form factors.

It is well known that the empirical-pseudopotential method reduces to solving the Schrödinger equation

$$[-\nabla^2 + V(r)]\psi_k(r) = E(k)\psi_k(r), \quad (1)$$

where $V(r)$ is the crystal pseudopotential. The Fourier components of $V(r)$ completely govern the band structure of the crystal. Regarding the crystal pseudopotential as a superposition of the pseudopotentials of the atoms forming the crystal, we obtain

$$V(G) = \sum_j S_j(G)V_j(G), \quad (2)$$

where $S_j(G) = e^{iG, r_j}$ is the structure factor, G is the reciprocal-lattice vector, r_j is the radius vector of the jth atom, and $V_j(G)$ is the Fourier component of the jth atomic pseudopotential. In accordance with the Brooks–Yu theory, at finite temperatures, $S_j(G)$ transforms into

$$S_j(G) = e^{iG, r_j}e^{-W_j(G, T)}, \quad (3)$$

where $W_j(G, T)$ is the Debye–Waller factor for the jth atom. A large number of approximate, including semiempirical, formulas are used in practice [3]. For example, for crystals with diamond or sphalerite structures,

$$W_j(G, T) = \frac{1}{6}|G|^2\langle u_j^2\rangle. \quad (4)$$

Here, $\langle u_j^2\rangle$ is the total mean-square displacement of the jth atom. In fact, the use of the Debye–Waller factor in the form given by (4) is equivalent to the replacement of the potential $V_j(G)$ by the temperature-dependent potential

$$V_j(G, T) = V_j(G)\exp\left(-\frac{1}{6}|G|^2\langle U_j^2\rangle\right). \quad (5)$$

Thus, allowance is made for the effect of the temperature dependence of the electron–phonon interaction on the crystal band structure.

The thermal expansion of the lattice is taken into account by the simple replacement of the form-factor scale [5], i.e., by multiplying the Fourier components of the pseudopotential by $a^3(0)/a^3(T)$ (a is the lattice constant).

Generally speaking, the complete theory takes into consideration one more type of contribution to the temperature dependence of the band structure, the so-called self-energy considered by Fan [6]. The calculations of the temperature dependence of the interband gaps for the crystals with a zinc-blende structure showed [7] that, at high temperatures, the Debye–Waller factors contribute most significantly to this dependence because the contributions of the other two types, which are of opposite signs, substantially compensate each other. The self-energy terms are specific to each electronic state and to each phonon state; therefore, the calculation of these terms is rather time-consuming. It was shown in [8] that the errors in determining the Debye–Waller factors often exceed the corrections for the self-energy introduced by Fan. Accordingly, we disregarded the self-energy contribution in this study.

The Debye–Waller factor governs the measured temperature dependence of the intensity of X-rays scattered by a particle in the crystal

$$I = I_0 e^{-W_j(G, T)} \quad (6)$$

and is determined experimentally.

For calculating the temperature dependence of the crystal band structure, both measured and calculated values of the Debye–Waller factor are used. Thus, the temperature dependence of the band gap $E_g(T)$ was calculated in [9, 10] for crystals of the III–V and II–VI compounds. The model of rigid ions considered in the lattice dynamics was used to calculate the Debye–Waller factors. The theory of the temperature dependence $E_g(T)$ was developed in [11] for cubic crystals of the IV, III–V, and II–VI types. The temperature dependences of the direct and indirect band gaps, E_{gd} and E_{gi}, of Si and Ge crystals were studied in detail in [12–14]. The coefficient of the variance of E_{gi} with temperature calculated for Ge exceeds the relevant value for Si by a factor of 2, which is due to the fact that $E(T)$ dependences for these crystals have different minima at the points L and X of the lower conduction bands of these crystals.

As far as we know, similar calculations have not been performed for SiC. The effect of polytypism on the thermal properties of SiC was studied in [15]. Along with the free energy and Debye temperature, the temperature dependences of the mean-square displacements of Si and C atoms in cubic SiC in the temperature range of 0–400 K were calculated in terms of the charged-bond model, as well as from first principles in the density-functional approximation. At room temperature, the averaged displacement of the C (Si) atom from the equilibrium position was found to be equal to 0.057 Å (0.051 Å). With an increase in the temperature, the displacement–temperature curves approach each other. For the hexagonal polytypes 2*H*-, 4*H*-, and 6*H*-SiC, the deviations of the mean-square displacements of C and Si atoms from the relevant values for 3*C*-SiC were calculated.

3. COMPARATIVE STUDY OF THE BAND STRUCTURE OF THE 3*C*-, 2*H*-, 4*H*-, AND 6*H*-SiC POLYTYPES VIA THE EMPIRICAL-PSEUDOPOTENTIAL METHOD

In this study, the band structures of the cubic (3*C*) and hexagonal (2*H*, 4*H*, and 6*H*) modifications of SiC were calculated by the empirical-pseudopotential method with the use of 116, 197, 385, and 477 plane waves, which corresponds to the choice of $|G_{max}|^2 \leq$

Table 1. Temperature dependence of the pseudopotential form factors of C and Si atoms in SiC

C atom	Pseudopotential form factors, Ry					
T, K	*V*(3)	*V*(4)	*V*(8)	*V*(11)	*V*(12)	*V*(16)
0	−0.4521	−0.4142	−0.1109	0.1294	0.1840	0.1319
50	−0.4521	−0.4142	−0.1109	0.1293	0.1840	0.1318
100	−0.452	−0.4141	−0.1109	0.1292	0.1839	0.1317
150	−0.4517	−0.4139	−0.1107	0.1290	0.1836	0.1314
200	−0.4513	−0.4134	−0.1105	0.1288	0.1832	0.1310
250	−0.4508	−0.4128	−0.1103	0.1284	0.1827	0.1306
300	−0.45	−0.412	−0.11	0.128	0.182	0.13
350	−0.4492	−0.4111	−0.1096	0.1275	0.1813	0.1293
400	−0.4483	−0.4103	−0.1093	0.1270	0.1806	0.1287
Si atom	Pseudopotential form factors, Ry					
T, K	*V*(3)	*V*(4)	*V*(8)	*V*(11)	*V*(12)	*V*(16)
0	−0.1669	−0.0201	0.1313	0.0020	0	0
50	−0.1668	−0.0201	0.1312	0.0020	0	0
100	−0.1668	−0.0201	0.1311	0.0020	0	0
150	−0.1667	−0.0201	0.131	0.0020	0	0
200	−0.1665	−0.0201	0.1306	0.0020	0	0
250	−0.1663	−0.0200	0.1304	0.0020	0	0
300	−0.166	−0.02	0.13	0.002	0	0
350	−0.1657	−0.0199	0.1296	0.0020	0	0
400	−0.1653	−0.01991	0.1291	0.0020	0	0

18.75. Calculations were carried out at the high-symmetry points and along the high-symmetry directions in the Brillouin zones of the fcc and the hexagonal lattices. The Brillouin zones of these lattices are shown below in the figures illustrating the relevant band structures. In order to obtain fairly reliable temperature dependences, the band structure was calculated for nine sets of form factors for each polytype (Table 1), which were determined from (5) in the temperature range of 0–400 K with an interval of 50 K.

We have estimated how the temperature dependence

$$G^2(T)/4\pi^2 = \{3, 4, 8, 11, 12, 16\}/\{a_{\mathrm{SiC}}^2(T)/a_0^2\}$$

affects the accuracy of calculating the form factors for SiC via the form factors of Si and C atoms by the method reported in [16]. It was found that the quantity $G^2(T)$ varies by no more than 0.3% in the range of 0–400 K. Therefore, we can disregard the temperature dependence in $V\{G_i^2[a_{\mathrm{SiC}}(T)]\}$.

In order to take into account the change in the form-factor scale caused by the thermal expansion of the crystal lattice, we used the temperature dependences of the lattice constants $a(T)$ and $c(T)$, which were obtained from the data on the temperature dependence of the linear-expansion coefficient of the lattice. The temperature-dependent mean-square deviations of the Si and C atoms from the equilibrium sites were taken from [17], where they were calculated as functions of the eigenfrequencies and eigenvectors of the phonon states obtained in terms of the modified rigid-ion model.

We will briefly dwell on the major features of the band structures of the polytypes under consideration and compare them with each other and with the results of calculations performed in other studies. The band structure of the cubic SiC polytype at 300 K was calculated by three methods: (i) the conventional calculation for the cubic 3*C*-cell (Fig. 1); (ii) the unconventional calculation for the hexagonal 3*H*-cell (for convenience of comparison with the hexagonal polytypes); and (iii) the calculation in the coordinate system for 6*H*-SiC with the alternation of layers *abcabc* (for direct comparison of the band structures calculated in the same coordinate system). As should be expected, all three calculation methods yield the same width of the indirect band gap, which is equal to 2.31 eV. The comparison shows that the triple degeneracy of the valence-band maximum (disregarding the spin–orbit interaction) is, evidently, retained in all three calculation meth-

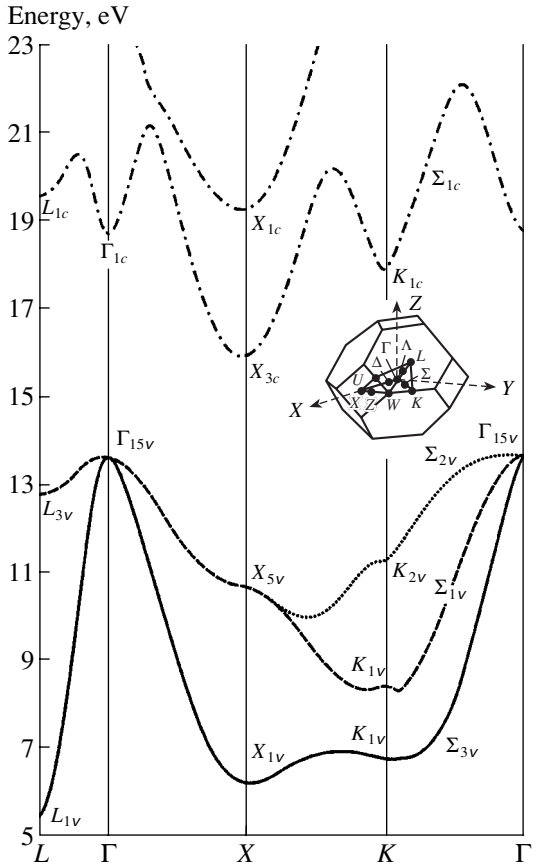

Fig. 1. Band structure of 3*C*-SiC.

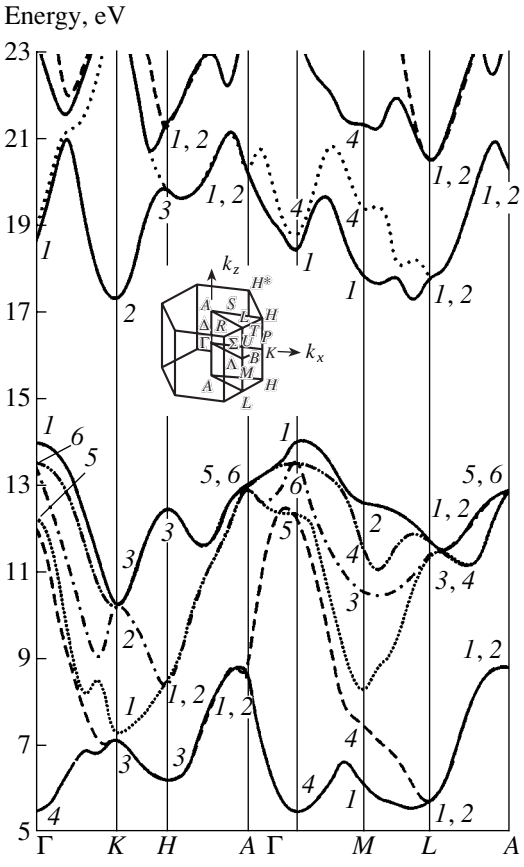

Fig. 2. Band structure of 2*H*-SiC.

ods. Notably, the level $\Gamma_{15v}(3\times)$ in 3*C*-SiC transforms into $\Gamma_1(1\times)$ and $\Gamma_6(2\times)$ in 3*H*-SiC; a similar transformation occurs in 6*H*-SiC (*abcabc*).

Figures 2, 3, and 4 show the band structures of the hexagonal polytypes 2*H*-, 4*H*-, and 6*H*-SiC at 300 K. The use of symmetrized combinations of plane waves for the high-symmetry points allowed us to determine the irreducible representations, according to which the relevant electronic states are transformed. As can be seen from these figures, the maximum of the valence band becomes split and the splitting $\Delta(\Gamma_1 - \Gamma_6)$ increases with an increase in the degree of hexagonality.

For example, $\Delta(\Gamma_1 - \Gamma_6) = 0.285$, 0.407, and 0.466 eV for the 6*H*-, 4*H*-, and 2*H*-SiC polytypes with degrees of hexagonality of 33, 50, and 100%, respectively. These data are qualitatively consistent with the results of [18], although the latter are rather underestimated in comparison with the results of this study and the experimental data.

The lower conduction bands and the upper valence bands of the three SiC polytypes, calculated in the same coordinate system that was used for 6*H*-SiC, are shown in Fig. 5 in a form convenient for comparison. The alternation of layers *abcabc* corresponds to cubic SiC with a degree of hexagonality of 0%, the alternation of layers *abcbac* corresponds to 6*H*-SiC with a degree of hexagonality of 33.3%, and the alternation of layers *ababab* corresponds to 2*H*-SiC with a degree of hexagonality of 100%. Figure 5 shows high similarity of the band structures of these polytypes. It can be seen fairly well how the energy levels vary with an increase in the degree of hexagonality from 3*H*- to 2*H*-SiC. For example, the minimum of the lower conduction band is located at the point $M[2\pi/a](0.82, 0, 0)$ in the Brillouin zone of 3*H*-SiC, at the point $[2\pi/a](0.82, 0, 0.05)$ along the *M*–*L* direction in the Brillouin zone of 6*H*-SiC, and at the point $K[2\pi/a](0.94, 0, 0)$ in the Brillouin zone of 2*H*-SiC. In the chosen system of reference, these minima have energies of 15.898, 16.526, and 17.397 eV, respectively. The latter value differs by 0.01 eV from the energy of the next minimum in the conduction band of 2*H*-SiC, which is located at the same point as the lower minimum in the conduction band of 6*H*-SiC. The maxima of the upper valence bands of these polytypes are located at the point Γ and have energies of 13.684, 13.919, and 14.039 eV for 3*H*-, 6*H*-, and 2*H*-SiC, respectively.

In order to make the data more illustrative, the inset in Fig. 5 shows the dependences of the valence-band maximum and the conduction-band minimum calculated in the same coordinate system on the degree of

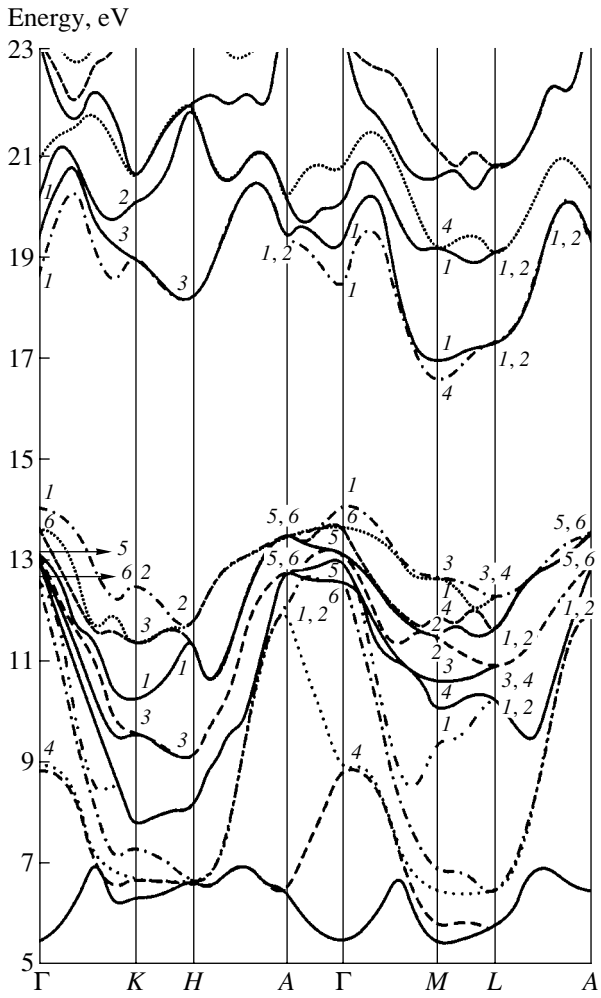

Fig. 3. Band structure of 4*H*-SiC.

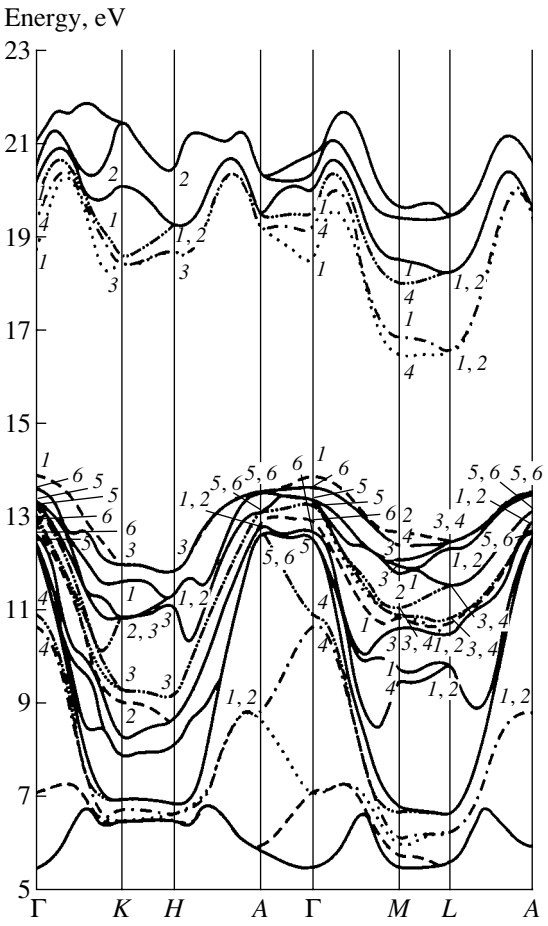

Fig. 4. Band structure of 6*H*-SiC.

hexagonality of the polytypes. The conduction-band minimum depends more heavily on the degree of hexagonality. Indeed, when changing from 6*H* to 2*H*, the energy of the conduction-band minimum grows seven times faster than that of the valence-band maximum. We should note that, in order to include the 4*H*-SiC polytype in the unified coordinate system, we had to perform the calculation for 12*H*-SiC with the appropriate alternation of layers.

The energies of the fundamental interband transitions, along with the published results of calculations and experimental data, are listed in Table 2. Comparison shows good agreement with the results of calculations performed using the pseudopotential method in other studies and with the experimental data. The calculations in the local-density approximation in terms of the generalized density-functional theory yield underestimated results, especially for the indirect band gap. The results we obtained are very sensitive to the choice of the atomic form factors and to the lattice parameters.

4. ANALYSIS OF THE TEMPERATURE COEFFICIENTS OF THE ENERGIES OF THE FUNDAMENTAL INTERBAND TRANSITIONS AND ELECTRONIC LEVELS

On the basis of the data on the band structure obtained in the previous section, we have calculated the temperature dependences of the energies of the fundamental interband transitions and electronic levels for the 3*C*-, 2*H*-, 4*H*-, and 6*H*-SiC polytypes. The basic features and characteristics of these dependences have also been studied.

4.1. Cubic 3*C*-SiC

The analysis of the temperature dependence of significant energy levels in the conduction and valence bands at the high-symmetry points of the Brillouin zone, Γ, *X*, *L*, and *K* (zinc-blende lattice), showed that the temperature coefficient of variation in the energies of the lower levels in the conduction band is negative; the magnitude of this coefficient exceeds the relevant

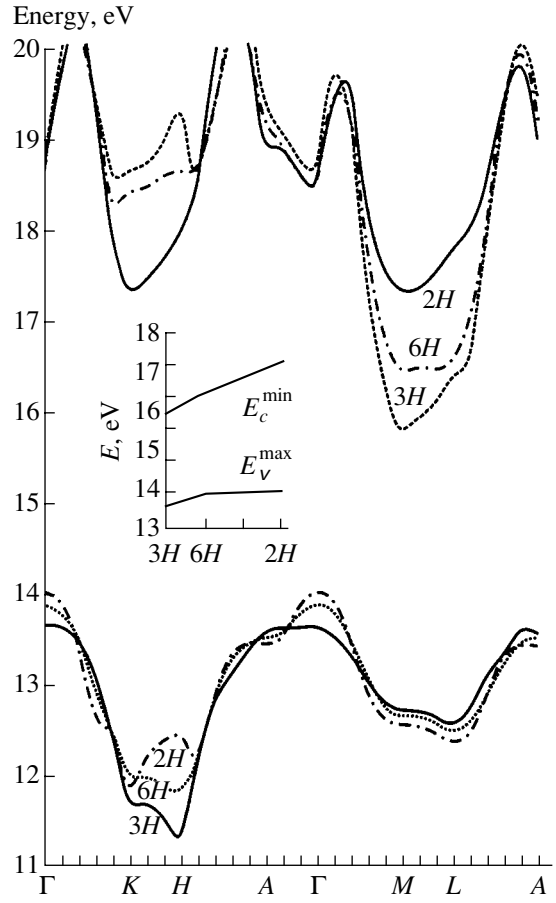

Fig. 5. Lower conduction bands and upper valence bands in 3*H*-, 6*H*-, and 2*H*-SiC calculated in the unified coordinate system for 6*H*-SiC (the alternations of layers *abcabc*, *abcbac*, and *abababab* correspond to cubic SiC with a degree of hexagonality of 0%, to 6*H*-SiC with a degree of hexagonality of 33.3%, and to 2*H*-SiC with a degree of hexagonality of 100%, respectively). The inset shows the dependences of the valence-band maximum E_v^{max} and the conduction-band minimum E_c^{min} on the degree of hexagonality in the 3*H*-, 6*H*-, and 2*H*-SiC polytypes.

temperature coefficient for the levels in the upper valence band (which is positive), on average, by 30% in the temperature range of 0–400 K. Thus, with an increase in temperature, the levels of the conduction and valence bands approach one other, and the widths of the direct and indirect band gaps vary in the temperature range of 0–400 K at an average rate of $dE_{gd}(\Gamma_{1c} - \Gamma_{15v})/dT = -3.6 \times 10^{-4}$ eV/K and $dE_{gi}(X_{3c} - \Gamma_{15v})/dT = -2.8 \times 10^{-4}$ eV/K, respectively. In the range of $T = 300$–400 K, the temperature coefficient of the width of the indirect band gap is equal to $dE_{gi}(X_{1c} - \Gamma_{15c})/dT = -3.1 \times 10^{-4}$ eV/K, which is consistent with the experimental value of about -4×10^{-4} eV/K [3].

Table 3 presents, as a typical example of all polytypes considered, the temperature dependences of the energies of six basic interband transitions and the energies of the one-electron levels at the high-symmetry points of the Brillouin zone of 3*C*-SiC. It can be seen that the conduction-band levels smoothly descend, while the valence-band levels smoothly ascend as temperature increases. In accordance with the decrease in the rate of variation, the calculated levels can be lined up as follows: Γ_{1c}, L_{1c}, Γ_{15v}, L_{3v}, L_{3c}, X_{1c}, X_{3c}, X_{3v}, and Γ_{15c}.

Analysis showed that the rates of the temperature-caused variation in the energies of the band levels and interband transitions (temperature coefficients α_T) increase with temperature. For example, in the temperature range of 200–400 K, the average value of α_T for the valence-band levels exceeds the average value of α_T in the range of 0–200 K by a factor of 1.5. The average value of α_T for the conduction-band levels in the range of 200–400 K exceeds that in the range of 0–200 K by a factor of 6.2.

4.2. Hexagonal 2*H*-SiC

On the basis of the calculations of the band structure for 2*H*-Si*C* at different temperatures, the temperature dependences of the energies of the electronic levels and interband transitions at the high-symmetry points of the Brillouin zone, Γ, *K*, *H*, *A*, *M*, and *L* (wurtzite lattice), were analyzed. As in the case of cubic SiC, the energy levels in the conduction and valence bands smoothly approach each other with an increase in temperature and the interband-transition energies decrease. Thus, for the widths of the direct and indirect band gaps, we have $dE_{gd}(\Gamma_{1c} - \Gamma_{1v})/dT = -3.2 \times 10^{-4}$ eV/K and $dE_{gi}(K_{2c} - \Gamma_{1v})/dT = -2.4 \times 10^{-4}$ eV/K, respectively, in the range of 0–200 K. In the range of 200–400 K, the widths of the direct and indirect band gaps are equal to -4.7×10^{-4} and -3.7×10^{-4} eV/K, respectively.

For the interband transitions M_{1c}–Γ_{1v}, L_{1c}–Γ_{1v}, K_{2c}–Γ_{6v}, and M_{1c}–Γ_{6v}, the temperature coefficients α_T at temperatures from 0 to 400 K are equal to -3.0×10^{-4}, -2.8×10^{-4}, -3.0×10^{-4}, and -3.4×10^{-4} eV/K, respectively. The temperature coefficient averaged over these transitions is equal to $\alpha_T = -1.3 \times 10^{-4}$ eV/K at T = 0–200 K and $\alpha_T = -3.2 \times 10^{-4}$ eV/K at T = 200–400 K.

4.3. Hexagonal 4*H*-SiC

As in the previous cases, the energies of the electronic levels and the interband transitions smoothly vary with temperature. The widths of the direct ($\Gamma_{1c} - \Gamma_{1v}$) and indirect ($M_{4c}$–$\Gamma_{1v}$) band gaps decrease with an increase in temperature at the rates of -1.4×10^{-4} and -1.8×10^{-4} eV/K, respectively, in the range of 0–200 K and at the rates of -3.3×10^{-4} and -4.3×10^{-4} eV/K, respectively, in the range of 200–400 K. For the other transitions between the valence and conduction bands, α_T ranges from -1.1×10^{-4} to -1.4×10^{-4} eV/K at T = 0–200 K and from -3.6×10^{-4} to -4.2×10^{-4} eV/K at T = 200–400 K.

Table 2. Comparison of the main interband spacings of the 3*C*-, 2*H*-, 4*H*-, and 6*H*-SiC polytypes

Polytype	Interband spacings					
3*C*	X_{3c}–Γ_{15v}	X_{3c}–L_{3v}	Γ_{1c}–Γ_{15v}	X_{3c}–X_{5v}	X_{1c}–Γ_{15v}	L_{1c}–Γ_{15v}
	2.31*	3.19*	5.03*	5.23*	5.59*	5.83*
	2.40 [16]	3.26 [16]	5.14 [16]	5.27 [16]	5.64 [16]	5.93 [16]
	2.39 [19]	3.57 [19]	6.00 [19]	6.00 [19]	5.66 [19]	6.54 [19]
	2.35 [20]	3.55 [20]	7.42 [20]	5.99 [20]	5.5, 4.7 [20]	4.20 [20]
	2.646 [21]					
	1.24 [22]		6.30 [22]			5.37 [22]
	1.21 [23]		6.27 [23]			5.32 [23]
	1.27 [18]		5.99 [18]			
2*H*	K_{2c}–Γ_{1v}	M_{1c}–Γ_{1v}	L_{1c}–Γ_{1v}	K_{2c}–Γ_{6v}	M_{1c}–Γ_{6v}	Γ_{1c}–Γ_{1v}
	3.37*	3.72*	3.81*	33.87*	4.22*	4.47*
	3.35 [16]	3.75 [16]	3.82 [16]	4.02 [16]	4.42 [16]	4.46 [16]
	3.33 [19]					4.86 [23]
	2.05 [22]	2.72 [22]				
	2.10 [18]	2.72 [18]	3.31 [18]			5.07 [18]
	2.76 [24]					
4*H*	M_{4c}–Γ_{1v}	M_{1c}–Γ_{1v}	M_{4c}–Γ_{6v}	L_{1c}–Γ_{1v}	M_{1c}–Γ_{6v}	M_{4c}–Γ_{5v}
	2.62*	2.98*	3.02*	3.32*	3.38*	3.48*
	2.80 [16]	3.15 [16]	3.22 [16]	3.57 [16]	3.58 [16]	3.70 [16]
	3.27 [19]	K_{2c}–Γ_{1v}	$\boxed{\Gamma_{1c}–\Gamma_{1v}}$			
	2.14 [22]	5.14*	4.48*			
	2.18 [18]	3.81 [22]	5.18 [22]		2.59 [18]	
	2.89 [24]	3.88 [18]	5.40 [18]			
6*H*	M_{4c}–Γ_{1v}	L_{1c}–Γ_{1v}	M_{4c}–Γ_{6v}	L_{1c}–Γ_{6v}	M_{1c}–Γ_{1v}	M_{4c}–Γ_{5v}
	2.66*	2.73*	2.95*	3.012*	3.014*	3.27*
	2.45 [16]	2.51 [16]	2.67 [16]	2.73 [16]	2.90 [16]	2.91 [16]
	3.02 [19]	K_{3c}–Γ_{1v}	$\boxed{\Gamma_{1c}–\Gamma_{1v}}$			
	1.98 [22]	4.87*	4.66*			
	1.96 [18]	3.41 [22]	5.18 [22]			
	2.92 [24]		5.49 [18]			

Note: Astericks indicate the data obtained in this study. The experimental data are from [19]. The other theoretical results were obtained using the empirical-pseudopotential method [16], the approximation of the Green function and screened Coulomb potential [20], the local-density approximation in the generalized density-functional theory (GDFT/LDA) [21], the *ab initio* method of self-consistent pseudopotential [22], the method of local pseudopotentials [23], the DFT/LDA method [18], and the LMTO method [24].

4.4. Hexagonal 6*H*-SiC

As in the case of the above-considered polytypes, the energies of the electronic levels and interband transitions calculated for 6*H*-SiC smoothly vary with temperature. The widths of the direct ($\Gamma_{1c} - \Gamma_{1v}$) and indirect ($M_{4c}$–$\Gamma_{1v}$) band gaps decrease with an increase in temperature in the range of 0–200 K at rates of -1.8×10^{-4} and -2.5×10^{-4} eV/K, respectively, and at rates of -4.6×10^{-4} and -3.2×10^{-4} eV/K, respectively, in the range of 200–400 K.

The latter result is in good agreement with the experimental value of -3.3×10^{-4} eV/K [25]. For the other transitions between the valence and conduction bands, α_T ranges from -1.2×10^{-4} to -1.4×10^{-4} eV/K at T = 0–200 K and from -3.7×10^{-4} to -4.1×10^{-4} eV/K at T = 200–400 K.

Table 3. Temperature dependence of the interband spacings and one-electron energy levels of 3*C*-SiC

T, K	X_{3c}–Γ_{15v}	X_{3c}–L_{3v}	Γ_{1c}–Γ_{15v}	X_{3c}–X_{5v}	X_{1c}–Γ_{15v}	L_{1c}–Γ_{15v}	X_{1c}–X_{3c}
0	2.37546	3.24896	5.11829	5.28421	5.65828	5.90467	3.28282
50	2.37483	3.2484	5.11539	5.28367	5.65643	5.90266	3.2816
100	2.37177	3.24534	5.11052	5.2807	5.65441	5.89954	3.28264
150	2.35989	3.23419	5.09734	5.27151	5.64512	5.88891	3.28523
200	2.34661	3.22165	5.07866	5.26045	5.63042	5.87274	3.28381
250	2.33187	3.20767	5.06052	5.24823	5.61512	5.85614	3.28325
300	2.30977	3.18643	5.03323	5.22905	5.59303	5.83197	3.28326
350	2.2876	3.16528	5.00508	5.21015	5.56912	5.80601	3.28152
400	2.26139	3.14002	4.97325	5.18748	5.54438	5.77894	3.28299

T, K	Γ_{15v}	Γ_{1c}	X_{3v}	X_{3c}	X_{1c}	L_{3v}	L_{1c}	L_{3c}
0	13.45972	18.57800	10.55097	15.83518	19.11800	12.58621	19.36438	23.17272
50	13.46054	18.57593	10.55170	15.83537	19.11697	12.58697	19.3632	23.17266
100	13.46132	18.57184	10.55238	15.83309	19.11572	12.58775	19.36085	23.17127
150	13.47087	18.56820	10.55925	15.83076	19.11598	12.59656	19.35977	23.17010
200	13.48022	18.55888	10.56638	15.82683	19.11064	12.60518	19.35296	23.16747
250	13.48813	18.54866	10.57177	15.82000	19.10325	12.61233	19.34427	23.15854
300	13.49790	18.53113	10.57862	15.80767	19.09093	12.62124	19.32987	23.14488
350	13.50826	18.51334	10.58571	15.79586	19.07738	12.63058	19.31427	23.13012
400	13.52124	18.49449	10.59515	15.78262	19.06561	12.64261	19.30017	23.11738

Note: The energies are given in eV.

5. SPECIAL FEATURES OF THE TEMPERATURE COEFFICIENTS OF THE ENERGIES OF SOME INTRABAND TRANSITIONS

We will briefly dwell on the features of the temperature dependence of the energy of the X_{1c}–X_{3c} transition between the subbands of the conduction band of 3*C*-SiC. This dependence is shown in Fig. 6. For comparison, the typical temperature dependence of the energy of the interband transition $E_{gd}(2H) = f(T)$ is also shown. We assume that the X_{1c}–X_{3c} transition is responsible for the narrow violet band in the breakdown-electroluminescence spectrum of *p*–*n* structures based on 3*C*-SiC [26]. In contrast to the interband transitions, $E(X_{1c}$–$X_{3c})$ changes abruptly (by steps) with an increase in temperature and the sign of the temperature coefficient α_T periodically changes. Notably, the averaged magnitude of α_T turned out to be significantly smaller than the magnitude of the temperature coefficient of the interband-transition energy. For example, at T = 300–400 K, $\alpha_T(X_{1c}$–$X_{3c}) = -0.8 \times 10^{-4}$ eV/K; whereas, for the interband transitions, α_T ranges from -2.6×10^{-4} to -4×10^{-4} eV/K.

The temperature coefficient of the shift of the emission bands at 300 and 400 K was evaluated in [27] by measuring the breakdown-electroluminescence spectra of *p*–*n* structures based on 3*C*-SiC. Within the narrow violet band in the range of 3.2–3.3 eV, the minimum of α_T, approximately equal to $-(0.9$–$1.0) \times 10^{-4}$ eV/K, was observed in [27]. This value is in agreement with the value of -0.8×10^{-4} eV/K obtained in this study for the X_{1c}–X_{3c} transition with the energy of ~3.28 eV.

The energies of the transitions between the sublevels of the conduction band of 2*H*-SiC increase with temperature. Thus, the temperature coefficient averaged over the M_{4c}–M_{1c}, Γ_{4c}–Γ_{1c}, and K_{1c}–K_{2c} transitions is smaller than the value of α_T for the interband transitions by a factor of 3–6 and is equal to 0.36×10^{-4} and 0.56×10^{-4} eV/K in the temperature ranges of 0–200 and 200–400 K, respectively. Concerning the 4*H*-SiC and 6*H*-SiC polytypes, the energies of the transitions between the subbands of the conduction band at the points Γ, *M*, *K*, and *L* vary as the temperature increases by an order of magnitude slower than the interband-transition energies. In this case, $\alpha_T > 0$ at the point Γ, and $\alpha_T < 0$ at the points *M*, *K*, and *L*.

We have also calculated the temperature dependences of the energies of the direct transitions Σ_1–Σ_3 and Σ_2–Σ_3 between the valence band split-off owing to the spin–orbit coupling and the valence band doubly degenerate at the point Γ, as well as the temperature dependences of the energies of the indirect transitions of high-energy electrons in the lower conduction band

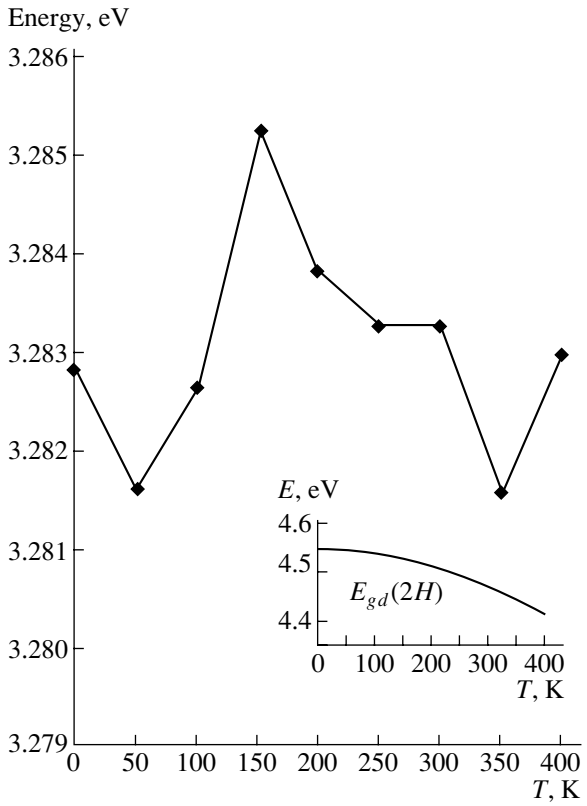

Fig. 6. Temperature dependence of the energy of the X_{1c}–X_{3c} transition in 3*C*-SiC. The inset shows the temperature dependence of the direct band gap in 2*H*-SiC.

along the *X*–*L*, *X*–Γ, and *X*–*K* directions in cubic SiC (Fig. 1). The broad band in the spectrum of the breakdown electroluminescence from reverse-biased *p*–*n* structures based on SiC is generally attributed to these transitions.

For the Σ_1–Σ_3 and Σ_2–Σ_3 transitions, the positive temperature coefficient α_T, averaged over the results of the calculations at five points in the *k* space, turned out to be equal to 0.36×10^{-4} and 0.28×10^{-4} eV/K, respectively, in the range of 0–200 K and to 0.7×10^{-4} and 3.5×10^{-4} eV/K, respectively, in the range of 200–400 K.

The positive temperature coefficients of the energies of the indirect transitions in the conduction band along the directions *X*–*L*, *X*–Γ, and *X*–*K* are equal to 0.8×10^{-4}, 0.6×10^{-4}, and 0.07×10^{-4} eV/K, respectively.

5. CONCLUSIONS

The investigation of the temperature dependences $E(T)$ of the energies of the electronic levels and main interband spacings for the 3*C*-, 2*H*-, 4*H*-, and 6*H*-SiC polytypes, which are of interest both from theoretical and applied points of view, showed that the temperature coefficients of the energies of the transitions between the valence and conduction bands are always negative and that they smoothly decrease with an increase in temperature.[1]

At the same time, the temperature dependences of the energies of the transitions between the subbands of the valence and conduction bands, which are believed to play an important role in breakdown electroluminescence [26, 27], are of a substantially different nature. Thus, as a rule, the energies of these transitions change by steps with an increase in temperature. These changes are accompanied by a change in the temperature-coefficient sign, which is illustrated by the example of the X_{1c}–X_{3c} transition (Fig. 6).

As follows from the calculations, the values of the temperature coefficients of the intraband-transition energies are smaller by a factor of 4–10 in comparison with the values of α_T of the transitions between the valence and conduction bands.

The obtained results can be used to explain the very high temperature stability of electroluminescence accompanying the controlled electric breakdown in SiC *p*–*n* structures, which was observed in [26]. It is highly probable that this stability may be due to the very small values of the temperature coefficients of the shift of the fundamental emission bands, i.e., the narrow violet band against the background of the main broad band. Therefore, the heating of a *p*–*n* structure caused by the supply current virtually does not affect the emission quantum yield. As a result, the devices based on SiC *p*–*n* structures fed by reverse current and operating in the breakdown mode, such as reference emitters, breakdown LEDs, and nanosecond and subnanosecond pulsed lasers, are characterized by high thermal stability.[2]

REFERENCES

1. P. A. Ivanov and V. E. Chelnokov, Fiz. Tekh. Poluprovodn. (St. Petersburg) **29**, 1921 (1995) [Semiconductors **29**, 1003 (1995)].
2. F. Engelbrecht, J. Zeman, G. Wellenhofer, *et al.*, Phys. Rev. B **56**, 7348 (1997).
3. V. V. Sobolev and V. V. Nemoshkalenko, *Electronic Structure of Solids in the Region of Fundamental Absorption* (Naukova Dumka, Kiev, 1992), Chap. 2, p. 403.

[1] The solution of the system of equations obtained by the empirical-pseudopotential method for all polytypes at different temperatures yields two groups of levels separated by the band gap. Notably, the levels of the valence bands rise and the levels of the conduction bands descend with an increase in temperature.

[2] With the aim of analyzing the temperature dependence of the breakdown-emission spectra as completely as possible, we should calculate the temperature dependences of the matrix elements of the relevant interband transitions caused by an applied electric field. These matrix elements are constructed using the actual pseudowave Bloch functions that represent the eigenvectors of the system of equations used in the empirical-pseudopotential method. This system of equations needs to be solved for each specific temperature (Section 3). Preliminary evaluations have shown that the contribution of the transition matrix elements to the temperature dependence is negligibly small.

4. Ch. Keffer, T. M. Hayes, and A. Bienenstock, Phys. Rev. Lett. **21**, 1676 (1968).
5. Y. W. Tsang and M. L. Cohen, Phys. Rev. B **3**, 1254 (1971).
6. H. Y. Fan, Phys. Rev. **82**, 900 (1951).
7. C. K. Kim, P. Lautenschlager, and M. Cardona, Solid State Commun. **59**, 797 (1986).
8. K. Baumann, Phys. Status Solidi B **63**, K71 (1974).
9. Y. F. Tsay, B. Gong, S. S. Mitra, and J. F. Vetelino, Phys. Rev. B **6**, 2330 (1972).
10. Y. F. Tsay, S. S. Mitra, and J. F. Vetelino, J. Phys. Chem. Solids **34**, 2167 (1973).
11. D. Auvergne, J. Camassel, H. Mathieu, and M. Cardona, Phys. Rev. B **9**, 5168 (1974).
12. P. B. Allen and M. Cardona, Phys. Rev. B **23**, 1495 (1981).
13. P. B. Allen and M. Cardona, Phys. Rev. B **27**, 4760 (1983).
14. P. Lautenschlager, P. B. Allen, and M. Cardona, Phys. Rev. B **31**, 2163 (1985).
15. A. Zywietz, K. Karch, and F. Bechstedt, Phys. Rev. B **54**, 1791 (1996).
16. H.-G. Junginger and W. Haeringen, Phys. Status Solidi **37**, 709 (1970).
17. J. F. Vetelino, S. P. Gour, and S. S. Mitra, Phys. Rev. B **5**, 2360 (1972).
18. P. Kackell, B. Wenzien, and F. Bechstedt, Phys. Rev. B **50**, 10761 (1994).
19. *Physics of Group IV Elements and III–V Compounds of Landolt-Bornstein Numerical Data and Functional Relationships in Science and Technology*, Ed. by O. Modelung, M. Schultz, and H. Weiss (Springer, New York, 1982), New Series, Group III, Vol. 17a.
20. M. Rohlung, P. Kruger, and J. Pollmann, Phys. Rev. B **48**, 17791 (1993).
21. I. N. Remediakis and E. Kaxiras, Phys. Rev. B **59**, 5536 (1999).
22. C. H. Park, B.-Ho Cheong, K.-Ho Lee, and K. J. Chang, Phys. Rev. B **49**, 4485 (1994).
23. Y. Fujino, H. Sato, and N. Otsuka, in *Materials Problem Solving with Transmission Electron Microscope*, Ed. by L. W. Hobbs, K. W. Westmacott, and D. B. Williams (Materials Research Society, Pittsburgh, 1986); Mater. Res. Soc. Symp. Proc. **62**, 349 (1986).
24. V. I. Gavrilenko, A. V. Postnikov, N. I. Klyui, and V. G. Litovchenko, Phys. Status Solidi B **162**, 477 (1990).
25. W. J. Choyke and L. Patrick, Phys. Rev. **105**, 1721 (1957).
26. A. M. Genkin and V. N. Rodionov, Fiz. Tekh. Poluprovodn. (Leningrad) **13**, 789 (1979) [Sov. Phys. Semicond. **13**, 463 (1979)].
27. M. V. Belous, A. M. Genkin, and V. K. Genkina, Fiz. Tekh. Poluprovodn. (St. Petersburg) **33**, 727 (1999) [Semiconductors **33**, 672 (1999)].

Translated by Yu. Sin'kov

Semiconductors, Vol. 37, No. 3, 2003, pp. 249–255. Translated from Fizika i Tekhnika Poluprovodnikov, Vol. 37, No. 3, 2003, pp. 266–271.

ELECTRONIC AND OPTICAL PROPERTIES OF SEMICONDUCTORS

Fine Structure of the Long-Wavelength Edge of Exciton–Phonon Absorption and Hyperbolic Excitons in Silicon Carbide of 6*H* Polytype

A. P. Krokhmal'

Shevchenko National University, Vladimirskaya ul. 64, Kiev, 01033 Ukraine

e-mail: krokhmal@mail.univ.kiev.ua

Submitted May 7, 2002; accepted for publication June 17, 2002

Abstract—The fine structure of the long-wavelength edge of the polarization spectra of exciton–phonon absorption in moderate-purity *n*-type 6*H*-SiC crystals with a concentration of uncompensated donors $N_D - N_A = (1.7–2.0) \times 10^{16}$ cm^{-3} at $T = 1.7$ K was studied. The analysis of new special features found at the absorption edge and the reliable detection of the onset of exciton–phonon steps related to the emission of phonons from acoustical and optical branches allowed highly accurate determination of a number of important parameters such as the band gap, the exciton band gap, the exciton binding energy, and the energies of spin–orbit and crystal–field splitting of an exciton. For the first time, transitions with the emission of LA phonons to the 1*S* exciton state with an M_1-type dispersion law were detected in $\mathbf{E} \parallel Z(C)$ polarization (the electric-field vector is parallel to the optical axis of the crystal). This observation supports the previously predicted "two-well" structure of the conduction band minimum in 6*H*-SiC. *© 2003 MAIK "Nauka/Interperiodica".*

INTRODUCTION

The possible existence of points with a zero angle of slope of energy bands in the Brillouin zone in crystals with a wurtzite structure (crystallographic class 6*mm* (C_{6v})) was predicted and analyzed in [1, 2]. In particular, it was shown that zero slope is always realized at the points Γ and *M*; furthermore, accounting for spin–orbit interaction, the point *M* ceases to be analytic and the extremum becomes displaced from this point. In addition, two pairs of stationary points appear in each of the lines Σ and *T*'. Two of the points correspond to extrema, and the other two are of the saddle type [2].

Silicon carbide 6*H*-SiC is an indirect-gap semiconductor with a wurtzite-type structure. The maximum of its *p* valence band is at the center of the Brillouin zone [3–5] and is split by the intrinsic field of a crystal in combination with a spin–orbit interaction that is weaker by $\Delta_{cf} = 48.7$ meV and $\Delta_{so} = 7.8$ meV [6], respectively. The main body of currently available data indicates that the absolute minimum of the conduction band in 6*H*-SiC lies either at the point *M* or in the line *M*–*L* of the Brillouin zone [3–5, 7–10]. The majority of recent theoretical studies suggest that, due to the interaction between the lower closely located "folded" conduction zones with the same symmetry, the absolute minimum of the conduction band shifts to the point *U* in the line *M*–*L*, a "camel's back" structure is formed, and a van Hove singularity of the type M_1 appears at the point *M* [5, 11–13]. According to estimations [5, 11–13], the height of the barrier between the two symmetrical valleys at *U* points and the "saddle" at point *M* ranges from 3.8 to 5.7 meV and the minimum itself is spaced from the point *M* by ~$0.4\pi/c$. However, in our opinion, there is still no direct spectroscopic evidence for the existence of a saddle singularity in the dispersion relation of a combined density of states in a lower conduction band in 6*H*-SiC. It is known that, in indirect-gap semiconductors, M_1-type singularities in the dispersion relation of the density of states in the absolute extrema of the bands affect the dispersion relation of the exciton states and clearly manifest themselves in some perfect crystals by the characteristic shape of the exciton–phonon steps in the fine structure of the long-wavelength edge of fundamental absorption [14, 15].

In 6*H*-SiC, the long-wavelength edge of fundamental absorption is governed by indirect transitions to exciton states with both optical and acoustical phonons involved; the structure of this edge was studied at low temperatures for two polarizations $\mathbf{E} \perp C$ and $\mathbf{E} \parallel C$ (**E** is the electric-field vector, *C* is the optical axis, $C \parallel C_6 \parallel Z$) [16]. The edge absorption at different temperatures was thoroughly studied in [17] for the polarization $\mathbf{E} \perp C$ only, since the edge structure in the case $\mathbf{E} \parallel C$ was found in [16] to be poorly resolvable. It should also be noted that the structure of the edge absorption as observed in differential spectra has still not been completely identified [18, 19].

In this study, we performed special experiments in order to investigate the fine structure of the long-wavelength edge of exciton–phonon absorption in 6*H*-SiC crystals and to ascertain the special features predicted in [2, 11].

1063-7826/03/3703-0249$24.00

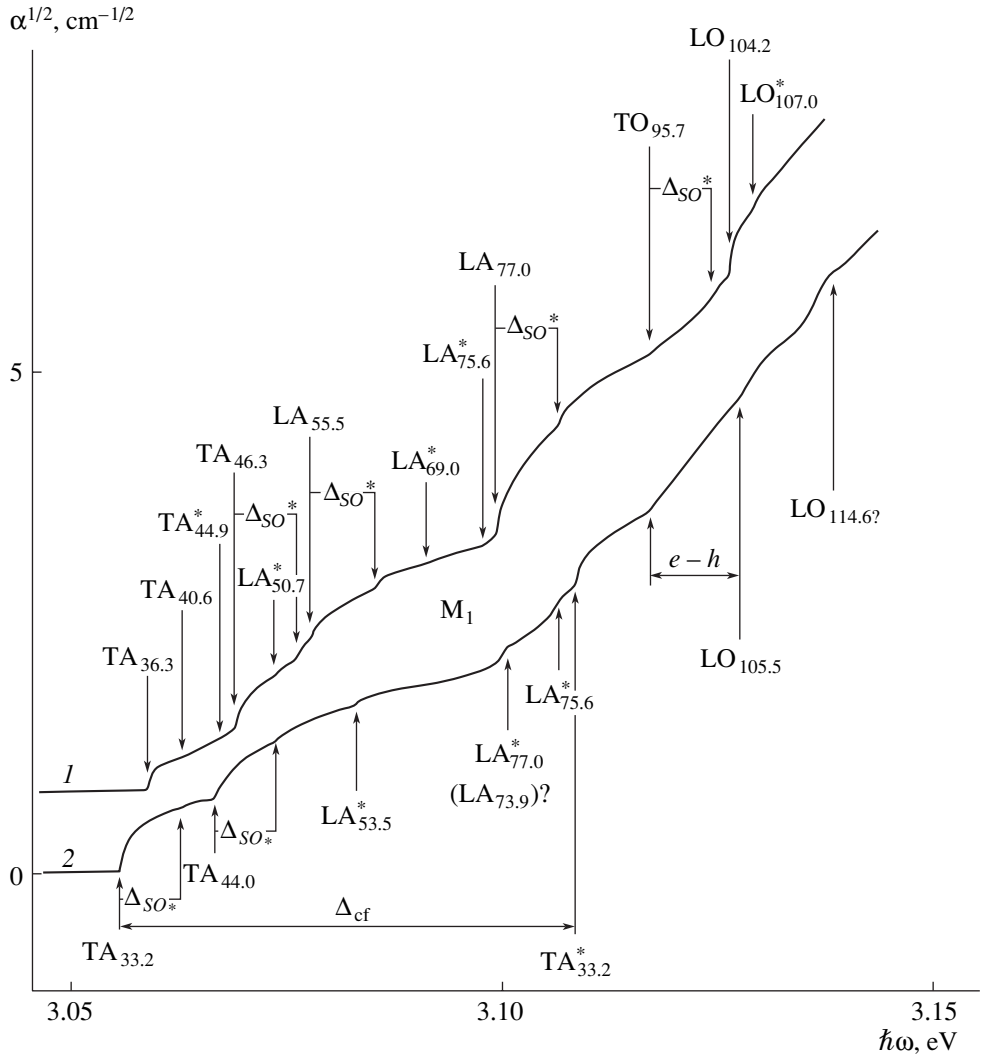

Polarization spectra of the edge absorption in *n*-6*H*-SiC single crystals at $T = 1.7$ K in $\mathbf{s} \parallel \langle 2\bar{1}\bar{1}0 \rangle \parallel X$ configuration for (*1*) $\mathbf{E} \parallel Y$ and (*2*) $\mathbf{E} \parallel Z(C)$. Sample thickness $d = 1.057$ mm. Arrows indicate the onset of the steps in exciton–phonon absorption, the numbers stand for the energies (in meV) of the corresponding phonons retaining their quasi-momentum during the optical transitions. The special features observed for the first time are marked with asterisks. Because of the presence of the near-edge absorption band at 2.98 eV, which is due to the photoionization of nitrogen with the transition of electrons to the upper conduction band [31], the curve for $\mathbf{E} \parallel Y$ starts from a nonzero value.

EXPERIMENTAL RESULTS

Because of the small spin–orbit splitting of the valence band and the low barrier predicted for the "two-valley" conduction band minimum, the sought-for peculiarities in the dispersion relation for the density of states of indirect excitons should be poorly pronounced. For the experiment, we chose nominally undoped 6*H*-SiC single crystals with a low content of impurities, since the perturbations of the exciton states by the electric field of charged defects and by screening are minimal in such crystals. In indirect-gap semiconductors, these effects are known [20] to appreciably decrease the intensity of exciton–phonon steps and to smudge their edges. The absorption spectra were derived from the edge absorption measured at low temperatures with high resolution by a modernized DFS-8-2 grating spectrometer with a reciprocal linear dispersion of 0.3 nm/mm.

A number of low-resistivity *n*-type 6*H*-SiC single crystals grown from the vapor phase by the Lely resublimation method were selected. As expected, growth-related nitrogen appeared to be the main donor impurity. This fact was indicated by the low-temperature spectra of edge photoluminescence (PL) with a characteristic discrete *PRS* structure associated with the recombination of excitons bound at neutral nitrogen atoms [16, 21]. Other evidence for the low concentration of neutral nitrogen was provided by the near-IR absorption spectra measured for two samples in the case of $\mathbf{E} \parallel C$. These spectra display a fairly weak (the absorption coefficient $\alpha \leq 5$ cm^{-1}) doublet band peaked

at $\hbar\omega = 1.33$ and 1.39 eV, which is well known and typical of nitrogen-doped 6*H*-SiC crystals [22–24]. Knowing the absorption coefficient in this band, we estimated [24] the concentration of uncompensated donors $n = N_D - N_A$ as $n \approx (1.7–2.0) \times 10^{16}$ cm^{-3} at the compensation level $K \leq 0.12$. The latter estimate was obtained, taking [23, 24] into account, from the ratio between the intensities of components with peaks at $\hbar\omega = 1.33$ and 1.39 eV within the absorption band.

For all five samples selected, the edge-absorption spectra measured at $T = 1.7$ K in $\mathbf{E} \perp C$ polarization show a more distinct and complex structure of the exciton–phonon steps than that observed in [16, 17] (see figure). New additional steps were discovered in the absorption spectra in the case of $\mathbf{E} \perp C$. Some of these newly detected steps are shifted to higher energies by (7.3 ± 0.1) meV with respect to the starting point of steps related to 1*S* excitons stemming from the upper valence band $\Gamma_9(A)$ with the emission of TA, LA, and TO phonons, which retain their quasi-momentum during optical transitions. These additional steps should be attributed to the 1*S* exciton arising from the lower *so*-split-off valence band $\Gamma_8(B)$.[1] The value obtained for the spin–orbit splitting of the exciton $\Delta_{so}^{ex} = (7.3 \pm 0.1)$ meV slightly exceeds that previously determined from the modulation spectra in [18, 19] and is close to the values of the spin–orbit splitting of the valence band, $\Delta_{so} = 7.8$ meV [6] and 7.7 meV [13], obtained by piezospectroscopy of excitons bound at neutral nitrogen atoms. Furthermore, we observed, for the first time, kinks near the intense steps related to the transition of an exciton from the upper valence band $\Gamma_9(A)$ to the 1*S* state with the emission of TA and LA phonons with the highest energies (46.3 and 77.0 meV, respectively). An especially pronounced "splitting" of 1.4 ± 0.1 meV is exhibited by the most intense step with the emission of a 77.0-meV LA phonon. The distinct onset of an exciton–phonon absorption threshold (at the photon energies corresponding to the wavelengths in free space) for acoustic phonons with given energies of 46.3 and 77.0 meV enabled highly accurate determination of the exciton band gap in 6*H*-SiC at $T = 1.7$ K as $E_{g\,ex} = (3.0224 \pm 0.0001)$ eV. The obtained value of $E_{g\,ex}$ practically coincides with $E_{g\,ex} = 3.0223$ eV, which was previously determined [26] from an analysis of the edge absorption and the intrinsic PL spectrum of excitons. New, poorly pronounced exciton–photon steps observed at $\hbar\omega = 3.0732$ and 3.0912 eV can be attributed to the formation of 1*S* excitons from the upper valence band $\Gamma_9(A)$ with the emission of 50.8- and 68.8-meV LA phonons, which were related in [16] to the wave vectors from the extended zone $k_c = 2\pi/c$ and $4\pi/c$, respectively. We observed also for the first time a step at 3.1293 eV arising from the emission of 107.0-meV LO phonons and a step of higher intensity at 3.0852 eV, whose origination should be considered in more detail. If we ascribe the appearance of this step to the transitions from the valence band $\Gamma_9(A)$ to the 1*S* exciton state with the emission of an LA phonon, the energy of the latter will be equal to 62.8 meV. However, none of the available exciton–phonon PL spectra of either free or bound excitons in 6*H*-SiC [16, 26–28] indicates the presence of a transition involving LA phonons of such energy. Nevertheless, two poorly pronounced 62.5- and 63.0-meV phonon features of A_1 symmetry with their wave vectors within the extended zone $k_c = 4\pi/c$ were observed in the Raman spectra [29]. At the same time, this step may correspond to transitions from the *so*-split-off $\Gamma_8(B)$ band with the emission of a 55.5-meV LA phonon. Similar steps with the emission of 55.5-meV phonons were previously observed in the spectrum of wavelength-modulated edge absorption [19]. However, the spectra of the intrinsic exciton luminescence [27, 29] and the PL of excitons bound at a neutral donor (nitrogen) [16] indicate the presence of LA phonons with lower energies of 53 and 53.5 meV, respectively. In what follows, we will show that this discrepancy in the phonon energies determined from the absorption spectra and PL may be due to the two-valley structure of the conduction-band minimum. It should be noted that an increase in the concentration of uncompensated donors or acceptors to $\sim(5–8) \times 10^{16}$ cm^{-3} results in a noticeable smearing of the fine "splitting" structure and lowers the sharpness of the exciton–phonon absorption thresholds.

For the case of $\mathbf{E} \parallel C$, the absorption edge starts at the energy $\hbar\omega = 3.0556$ eV with an intense step corresponding to an exciton transition from the upper valence band $\Gamma_9(A)$ to the 1*S* state with the emission of 33.2-meV TA phonons. The next intense step at $\hbar\omega = 3.0664$ eV stems from the emission of a 44.0-meV TA phonon. Such phonons efficiently interact with excitons in $\mathbf{E} \parallel C$ polarization [16]. In addition, low-height steps are observed at $\hbar\omega = 3.0630$, 3.0738, and 3.0832 eV and can be attributed to the origination of the 1*S* exciton from the *so*-split-off $\Gamma_8(B)$ band with the emission of 33.2- and 44.0-meV TA phonons and a 53.3-meV LA phonon, respectively. It is important to note that a comparatively weak feature clearly observed at 3.1010 eV is typical of hyperbolic exciton–phonon transitions to an M_1-type saddle point [14, 15]. Similar features are also observed at $\hbar\omega = 3.107$ and 3.1386 eV; however, they are less pronounced. If the origination of an indirect 1*S* exciton to energies of about 3.10 eV in either polarization involves an LA phonon with the same energy of 77.0 eV, then the distance between the starting points of the exciton–phonon steps corresponding to hyperbolic and parabolic dispersion relations yields a barrier height between M_0 and M_1 singularities in the dispersion relation for the density of states of an indirect 1*S* exciton $\delta = (1.6 \pm 0.1)$ meV. In this case, differ-

[1] Here, a more adequate classification of irreducible spinor representations is used for the bands at the Γ point of the C_{6v}' wavevector group [25].

ent intensities of the respective exciton–phonon steps may be explained by the different densities of exciton states: in the "plane" valleys of the M_0 type [5], this density is appreciably higher than that in the M_1-type singularities. According to [16], LA phonon lines of four types are encountered in the vicinity of 0.77 eV in the exciton–phonon PL spectrum of excitons bound at neutral donors. According to [16, 28], 77.0-meV LA phonons have the highest density of states at the edge of the extended zone ($6\pi/c$) and efficiently interact with excitons in $\mathbf{E} \perp C$ polarization. In $\mathbf{E} \parallel C$ polarization, only the 73.9-meV phonons are active; however, their density of states is about one order of magnitude lower than that of the 77.0-meV phonons [16]. If the excitons of the saddle point originate with the emission of 73.9-meV LA phonons, then the height of the barrier between M_0 and M_1 singularities in the dispersion relation for indirect 1*S* excitons (with allowance made for the 3.1-meV difference between the corresponding phonon energies) will be equal to $\delta = 4.7$ meV. This value falls within the range from 3.8 to 5.7 meV calculated for the minimum of the conduction band in [5, 11–13]. A singularity of the M_1 type is clearly displayed in $\mathbf{E} \parallel C$ polarization only at 3.1010 eV; this value is close to the excitation energy of 1*S* excitons with the emission of 77.0-meV LA phonons that have the highest density of states at the edge of the extended zone [16, 17, 28]. This circumstance led us to believe that the height of the barrier between M_0 and M_1 singularities in the dispersion relation for the density of exciton states should be $\delta = 1.6$ meV. The successive special feature at $\hbar\omega = 3.107$ eV has a lower intensity, is not so well pronounced as the previous one, and, presumably, also stems from the transitions of an exciton to the saddle point M_1, but which start from the lower valence band $\Gamma_8(C)$ with the emission of a 75.6-meV LA phonon [16, 28]. For the first time, we clearly observed the onset of an intense step at 3.1088 eV, which can be associated with the origination of a 1*S* exciton from the lower crystal-field-split-off valence band $\Gamma_8(C)$ with the emission of a 33.2-meV TA phonon. In this case, the level of the 1*S* exciton that originated from the valence band $\Gamma_8(C)$ lies deeper than that of the 1*S* exciton that originated from the upper valence band $\Gamma_9(A)$ by $\Delta_{cf}^{\text{ex}} = (53.2 \pm 0.1)$ meV. This difference coincides with the value of splitting $\Delta_{cf}^{\text{ex}} = (53 \pm 1)$ meV obtained from an analysis of exciton electroabsorption [18]. It should be noted here that the unidentified line *D* observed at 3.11 eV in the spectrum of electroabsorption for $\mathbf{E} \parallel C$ polarization [18] is also evidently due to exciton origination from the lower valence band $\Gamma_8(C)$ (split off by crystal field) with the emission of 33.2-meV TA phonons.

An important feature of the dependence of the square root of the absorption coefficient on photon energy at $\mathbf{E} \parallel C$ is the linear portion ranging from 3.1173 to 3.1277 eV (see figure). This section of the curve may be attributed to indirect band-to-band transitions with the emission of the lowest energy 33.2-meV TA phonons. In this case, the bandgap width in 6*H*-SiC at $T = 1.7$ K turns out to be equal to $E_g = (3.0841 \pm 0.0002)$ eV, from whence the exciton binding energy follows as $E_{\text{ex}} = (61.7 \pm 0.2)$ meV. The resulting value of the binding energy (evidently, of the *A* exciton) is appreciably smaller than the exciton Rydberg Ry = 78 meV previously determined from the spectrum of exciton electroabsorption [18].

DISCUSSION

In indirect-gap semiconductors, exciton wave functions are transformed in terms of irreducible representations of a $G_{\mathbf{k}_{\text{ex}}}$ group, which is the intersection of the groups of wave vectors for holes and electrons: $G_{\mathbf{k}_e} \cap G_{\mathbf{k}_h} \longrightarrow G_{\mathbf{k}_{\text{ex}}}$. If the conduction-band minimum in 6*H*-SiC is localized at the point *U* of the Brillouin zone, then the group $G_{\mathbf{k}_{\text{ex}}} \longleftrightarrow U$ is isomorphic to the point group C_{2v} and coincides with this group at the point *M*. Therefore, at the center of the Brillouin zone, the two-valued representations for holes Γ_9 and Γ_8 of the group $G_{\mathbf{k}_h} \longleftrightarrow C_{6v}$ transform into the two-valued representations U_5 or M_5 of the $G_{\mathbf{k}_{\text{ex}}}$ group. Then, each of the valence subbands, $\Gamma_9(A)$, $\Gamma_8(B)$, and $\Gamma_8(C)$, gives rise to fourfold degenerate 1*S* excitons, each containing four ordinary states of symmetry:

$$D_{\text{ex}} = D_c \times D_v^* \times D_{env} = U_5(M_5) \times U_5^*(M_5) \times U_1(M_1) = U_1(M_1) + U_2(M_2) + U_3(M_3) + U_4(M_4). \quad (1)$$

Here, the *S*-type envelope wave functions of the relative motion of electrons and holes are transformed according to the completely symmetric irreducible representation $U_1(M_1)$. These exciton states are split due to an exchange interaction into paraexcitons and orthoexcitons. Since this splitting contains no common representations, the spin–orbit mixing of states is absent in the first approximation. Therefore, one of them is purely singlet and the other three are triplet and are randomly degenerate in the absence of an external magnetic field. Optical transitions to triplet exciton states are forbidden in the electric dipole approximation, because they require the spin flip of a bound electron, but the operator of the electric dipole transition does not act on the spin operator. Nevertheless, such transitions may be observed due to the mixing of two upper valence bands [30].

Let us consider the symmetry of a singlet exciton. Disregarding spin–orbit interaction, at first, one can represent the *S*-exciton wave function only in terms of the Bloch functions of the valence and conduction bands; after that, the two-particle spin function may be included. The spin function of a singlet *S* exciton is antisymmetric and is transformed according to the complete

rotation-group representation D_0^-, which appears in the $G_{\mathbf{k}_{ex}}$ group as M_2; the wave function of a triplet S exciton is symmetric and transforms as $D_1^+ \longrightarrow M_2 + M_3 + M_4$ (for simplicity, we write only the representations at M point). If the conduction band minimum has $U_4(M_4)$ symmetry [5, 31], then the symmetry of a singlet exciton originating from the twofold-degenerate upper valence band Γ_6 ($\Gamma_9 + \Gamma_8$) and from the Γ_1 (Γ_8) band split off by the crystal field has the form

$$\begin{aligned} {}^1D_{\text{ex}} &= M_4^c \times \Gamma_6^v \times M_1^{env} \times D_0^{-(s)} \\ &\longrightarrow M_4 \times (M_3 + M_4) \times M_1 M_2 \\ &= {}^1M_1(z) + {}^1M_2(xy) \end{aligned} \tag{2}$$

and

$$\begin{aligned} {}^1D_{\text{ex}} &= M_4^c \times \Gamma_1^v \times M_1^{env} \times D_0^{-(s)} \\ &\longrightarrow (M_4 \times M_1 \times M_1 \times M_2) = {}^1M_3(x), \end{aligned} \tag{3}$$

respectively.[2]

Thus, the twofold-degenerate exciton state that originated from the upper valence band Γ_6 separates into the crossed group into two states $M_1 + M_2$ even without regard for spin–orbit interaction. However, because of the spin–orbit mixing of two upper valence bands A and B in the $G_{\mathbf{k}_h}$ group [6, 16], the reliable experimental determination of the symmetry of holes in the upper valence band seems, as yet, impossible. Therefore, the singlet exciton from the upper valence band $\Gamma_9(A)$ may be either of the $M_1(z)$ type, with its wave functions transforming in terms of the z coordinate, or of the $M_2(xy)$ type, with the wave functions transforming in terms of the xy product.

Let us consider the relevant selection rules in the dipole approximation. Assume that a singlet 1S exciton that originated from the upper valence band $\Gamma_9(A)$ has $M_1(z)$ symmetry. A completely symmetric initial state of unexcited crystal provides for nonzero probability of the following exciton–phonon transitions: $M_1^{\text{ex}} M_4^{E1}(y) M_4^{\text{ph}} \neq 0$ for $\mathbf{E} \parallel Y$ polarization, $M_1^{\text{ex}} M_3^{E1}(x) M_3^{\text{ph}} \neq 0$ for $\mathbf{E} \parallel X$ polarization, and $M_1^{\text{ex}} M_1^{E1}(z) M_1^{\text{ph}} \neq 0$ for $\mathbf{E} \parallel Z(C)$ polarization.[3] For the excitation from the lower valence band $\Gamma_8(B)$ split off due to spin–orbit coupling, we then have $M_2^{\text{ex}} M_4^{E1}(y) M_3^{\text{ph}} \neq 0$ for $\mathbf{E} \parallel Y$ polarization, $M_2^{\text{ex}} M_3^{E1}(x) M_4^{\text{ph}} \neq 0$ for $\mathbf{E} \parallel X$ polarization, and $M_2^{\text{ex}} M_1^{E1}(z) M_2^{\text{ph}} \neq 0$ for $\mathbf{E} \parallel Z(C)$ polarization. The following dipole exciton–phonon transitions from the valence band $\Gamma_8(C)$ split off by the crystal field are allowed: $M_3^{\text{ex}} M_1^{E1}(z) M_3^{\text{ph}} \neq 0$ for $\mathbf{E} \parallel Z(C)$, $M_3^{\text{ex}} M_4^{E1}(y) M_2^{\text{ph}} \neq 0$ for $\mathbf{E} \parallel Y$, and $M_3^{\text{ex}} M_3^{E1}(x) M_1^{\text{ph}} \neq 0$ for $\mathbf{E} \parallel X$.

Note that the figure shows the edge of exciton–phonon absorption in the $\mathbf{s} = (\mathbf{k}/k) \parallel \langle 2\bar{1}\bar{1}0 \rangle \parallel X$ arrangement for $\mathbf{E} \parallel Y$ and $\mathbf{E} \parallel Z(C)$ polarizations (the case of $\mathbf{E} \parallel X$ is not realized). When $\mathbf{E} \parallel Y$, the exciton–phonon transitions from $\Gamma_9(A)$ and $\Gamma_8(B)$ bands involve acoustical and optical phonons of $M_4(U_4)$ and M_3 symmetries, respectively. Hence, it follows that the observed energy spacing between the corresponding steps cannot be exactly identified with the value $\Delta_{so}^{\text{ex}} = (7.3 \pm 0.2)$ meV, since the different symmetry of the phonons involved in the transitions entails a slight difference in their energy. In the $\mathbf{E} \parallel Z(C)$ polarization, the exciton transitions from the $\Gamma_9(A)$ band can involve both acoustical and optical phonons of M_1 symmetry, while the transitions from the $\Gamma_8(B)$ band involve only optical phonons of M_2 symmetry (since there are no acoustical phonons of such symmetry). This circumstance can explain the low intensity of the exciton–phonon steps in $\mathbf{E} \parallel C$ polarization, which are related to the transitions from the $\Gamma_8(B)$ band with the emission of acoustical phonons. Apparently, such transitions are only possible due to the spin–orbit mixing of the two upper valence bands A and B.

At the same time, the nonanalyticity of the point M owing to spin–orbit interaction and the shift of the extremum along the lines Σ and T' [2] reduce the exciton state symmetry to C_s. This gives rise to the state $D_{\text{ex}} = 2\Sigma_1 + 2\Sigma_2$ in the line Σ and the state $D_{\text{ex}} = 2T_1' + 2T_2'$ in the line T'. In the groups of wave vectors Σ and T', with the corresponding planes of symmetry $(\sigma_v|0)$ and $(\sigma_v'|c/2)$ oriented to match the elements of the symmetry group C_{2v} for the point M, the excitons $M_2(xy)$ and $M_3(x)$ in the Σ line pass to $\Sigma_2(x)$, whereas $M_1(z)$ and $M_4(y)$ converts to $\Sigma_1(y, z)$; in the line T', the excitons $M_3(x)$ and $M_1(z)$ turn into $T_1'(x, z)$, whereas $M_2(xy)$ and $M_4(y)$ transforms into $T_2'(y)$. Thus, in the Σ line, the singlet and triplet A excitons have $\Sigma_1(y, z)$ and $\Sigma_1(y, z) + 2\Sigma_2(x)$ symmetry, respectively, whereas the singlet and triplet B excitons have $\Sigma_2(x)$ and $2\Sigma_1(y, z) + \Sigma_2(x)$ symmetries in the respective order or vice versa. The singlet and triplet C excitons show $\Sigma_1(y, z)$ and $\Sigma_1(y, z) + 2\Sigma_2(x)$ symmetry, respectively. In line T', the singlet and

[2] When the symmetry elements σ_v' of group C_{2v} are related to the elements σ_v' of group C_{6v}, which is important to avoid confusion with the notation of representations, the x and y coordinates are transformed according to irreducible representations M_3 and M_4, respectively.

[3] Superscripts of the irreducible representations indicate the symmetry of the corresponding exciton states, the electric dipole operator of transition, and the phonons.

triplet A excitons are of $T_1'(x, z)$ and $T_1'(x, z) + 2T_2'(y)$ symmetry, respectively; at the same time, the singlet and triplet B excitons are of $T_2'(y)$ and $T_1'(x, z) + 2T_2'(y)$ symmetries in the respective order or vice versa. The singlet and triplet C excitons have $T_1'(x, z)$ and $2T_1'(x, z) + T_2'(y)$ symmetry, respectively. Here, it is important to note that the exciton states considered are no longer purely singlet or triplet, since the singlet and triplet states of the same symmetry are mixed in the first approximation due to spin–orbit coupling. Because of the lack of a sufficiently thick crystal to cut off the required sample, we failed to obtain the absorption spectrum in the $\mathbf{s} \parallel Y \parallel \langle 01\bar{1}0 \rangle$ arrangement for $\mathbf{E} \parallel X$ and $\mathbf{E} \parallel Z$ polarizations; therefore, we will not discuss the corresponding selection rules, compare the results of calculations with experimental data, or make any conclusions concerning the localization point of the conduction band minimum. Even if such spectra were available, this point could hardly be identified by considering the selection rules and comparing them to the experiment because of the mixing of both the two upper bands and the singlet and triple exciton states.

In what follows, we will discuss a number of new special features in the spectrum of exciton–phonon absorption. In my opinion, the kink near the highest intensity step with the emission of a 77.0-meV LA phonon in $\mathbf{E} \parallel Y$ (or $\mathbf{E} \perp C$) cannot be attributed to exciton-state splitting. If the kink were caused by splitting of the exciton state due to the exchange coupling, it would also be present at least near the other intense steps. Therefore, the observed kink should be associated with the transition of a singlet exciton to the 1S state with the emission of a 75.6-meV LA phonon, for which the density of states is by an order of magnitude lower than that for 77.0-meV LA phonons [16, 27]. The kink observed near the step with the emission of 46.3-meV TA phonons also seems to be due to the emission of a lower energy phonon. Transitions that were accompanied with the emission of lower energy phonons were observed in recent experiments with resonant excitation in "hot" exciton luminescence [28]. It is important to note that the presence of such kinks in the exciton–phonon absorption spectra, especially near the 77.0-meV step, indicates high purity of 6H-SiC crystals.

Another topic for separate discussion is the value obtained for the exciton binding energy in 6H-SiC crystals. The linear spectral dependence of the square root of the absorption coefficient in the region of photon energies higher than $\hbar\omega = 3.1173$ eV in $\mathbf{E} \parallel Z(C)$ polarization may be explained as follows. For a 1S exciton that originated from the two mixed upper valence bands $\Gamma_9(A)$ and $\Gamma_8(B)$, transitions to the minimum of the M_0-type exciton band with the emission of the highest energy 77.0-meV LA phonons are symmetry-forbidden. Transitions to the M_1-type saddle point are allowed, but the density of states in the 1S exciton band at this critical point is considerably lower than that in the "flattened" M_0-type valleys [5]. This entails a lower intensity of the corresponding exciton–phonon step, which is superimposed on the exciton absorption from the split-off (by the crystal field) $\Gamma_8(C)$ band with the emission of 33.2-meV TA phonons. Exciton transitions from the valence $\Gamma_8(C)$ band with the emission of the higher energy 44.0-meV TA phonons are apparently forbidden. The successive gap in the phonon spectrum [29] implies that no exciton–phonon transitions occur until the starting energy of the LO mode is attained. Instead, indirect band-to-band transitions to the conduction band minimum with the emission of 33.2-meV TA phonons are realized since the mixing between $\Gamma_8(C)$ and $\Gamma_8(B)$ bands is negligibly small. Thus, the determined value of the exciton binding energy in 6H-SiC $E_{g\,\mathrm{ex}} = 61.7$ meV seems to be more realistic than that previously derived from the analysis of exciton electroabsorption [18].

In conclusion, the polarization study of the long-wavelength edge of exciton–phonon absorption in moderately pure 6H-SiC crystals allowed a highly accurate determination of a number of important parameters at the liquid-helium temperature, in particular, the band-gap width, the exciton-gap width, the exciton binding energy, and the magnitudes of spin–orbit and crystal–field splitting of an exciton. Furthermore, the transitions to the M_1-type saddle point in the dispersion relation of a 1S exciton band were discovered, thus supporting the existing theoretical prediction of a two-valley structure of the conduction band minimum in 6H-SiC. The small height of the barrier between M_0 and M_1 singularities and the lower density of exciton states at the critical point M_1 enabled the distinct observation of hyperbolic excitons with the emission of 77.0-meV LA phonons, which have the highest density of states at the Brillouin zone edge. It can be inferred that the edge-absorption spectra for a higher purity crystal of a larger thickness that would be sufficient for cutting off an appropriate sample might reveal the presence of hyperbolic excitons with some other phonons involved, in both $\mathbf{E} \parallel C$ and $\mathbf{E} \perp C$ polarizations. In the latter case, transitions with the emission of 55.5-meV LA phonons are plausible candidates.

ACKNOWLEDGMENTS

I thank G.N. Mishinova for providing me with the experimental crystals and for measuring their low-temperature PL spectra.

REFERENCES

1. É. I. Rashba, Fiz. Tverd. Tela (Leningrad) **1**, 407 (1959) [Sov. Phys. Solid State **1**, 368 (1959)].

2. É. I. Rashba and V. I. Sheka, *Solid State Physics*, Ed. by A. F. Ioffe (Akad. Nauk SSSR, Leningrad, 1959), No. 2, p. 162.
3. H. G. Junginger and W. van Haeringen, Phys. Status Solidi **37**, 719 (1970).
4. V. I. Gavrilenko, A. V. Postnikov, N. I. Klyui, and V. G. Litivchenko, Phys. Status Solidi B **162**, 477 (1990).
5. C. Persson and U. Lindefelt, J. Appl. Phys. **82**, 5496 (1997).
6. I. S. Gorban', A. P. Krokhmal', and I. A. Rozhko, Fiz. Tverd. Tela (Leningrad) **31** (12), 126 (1989) [Sov. Phys. Solid State **31**, 2095 (1989)].
7. P. J. Collwell and M. V. Klein, Phys. Rev. B **6**, 498 (1972).
8. B. W. Wessels and H. C. Gatos, J. Phys. Chem. Solids **38**, 345 (1977).
9. I. S. Groban', V. A. Gubanov, V. D. Kulakovskiĭ, *et al.*, Fiz. Tverd. Tela (Leningrad) **30**, 1605 (1988) [Sov. Phys. Solid State **30**, 928 (1988)].
10. W. R. L. Lambrecht and B. Segal, Phys. Rev. B **52**, 2249 (1995).
11. W. R. L. Lambrecht, S. Limpijumnong, S. N. Rashkeev, and B. Segal, Phys. Status Solidi B **202**, 5 (1997).
12. C. Persson and U. Lindefelt, J. Appl. Phys. **86**, 5036 (1999).
13. F. Engelbrecht, J. Zeman, G. Wellenhofer, *et al.*, Phys. Rev. B **56**, 7348 (1997).
14. P. J. Dean and D. G. Thomas, Phys. Rev. **150**, 690 (1966); G. F. Glinskiĭ, A. A. Kopylov, and A. N. Pikhtin, Fiz. Tekh. Poluprovodn. (Leningrad) **12**, 1327 (1978) [Sov. Phys. Semicond. **12**, 785 (1978)].
15. I. S. Gorban', V. A. Gubanov, and Z. Z. Yanchuk, Ukr. Fiz. Zh. **29**, 146 (1984); I. S. Gorban', V. I. Gubanov, M. V. Chukichev, and Z. Z. Yanchuk, Fiz. Tekh. Poluprovodn. (Leningrad) **19**, 1312 (1985) [Sov. Phys. Semicond. **19**, 803 (1985)].
16. W. J. Choyke and L. Patrick, Phys. Rev. **127**, 1868 (1962).
17. A. N. Pikhtin and D. A. Yas'kov, Fiz. Tverd. Tela (Leningrad) **12**, 1597 (1970) [Sov. Phys. Solid State **12**, 1267 (1970)].
18. V. I. Sankin, Fiz. Tverd. Tela (Leningrad) **17**, 1820 (1975) [Sov. Phys. Solid State **17**, 1191 (1975)].
19. R. G. Humphreys, D. Bimberg, and W. J. Choyke, Solid State Commun. **39**, 163 (1981).
20. V. I. Safarov, A. N. Titkov, and I. S. Shlimak, Fiz. Tekh. Poluprovodn. (Leningrad) **5**, 771 (1971) [Sov. Phys. Semicond. **5**, 680 (1971)].
21. A. P. Krokhmal', Ukr. Fiz. Zh. **26**, 418 (1981).
22. O. V. Vakulenko and O. A. Govorova, Fiz. Tverd. Tela (Leningrad) **12**, 1857 (1970) [Sov. Phys. Solid State **12**, 1478 (1970)].
23. M. P. Lisitsa, O. V. Vakulenko, Yu. S. Krasnov, and V. N. Solodov, Fiz. Tekh. Poluprovodn. (Leningrad) **5**, 2047 (1971) [Sov. Phys. Semicond. **5**, 1785 (1971)].
24. G. B. Dubrovskii, A. A. Lepneva, and E. I. Radovanova, Phys. Status Solidi B **57**, 423 (1973).
25. S. V. Bogdanov and V. A. Gubanov, Fiz. Tekh. Poluprovodn. (Leningrad) **22**, 728 (1988) [Sov. Phys. Semicond. **22**, 453 (1988)].
26. M. Ikeda and H. Matsunami, Phys. Status Solidi A **58**, 657 (1980).
27. R. P. Devaty and W. J. Choyke, Phys. Status Solidi A **162**, 5 (1997).
28. I. G. Ivanov, T. Egilsson, A. Henry, *et al.*, Phys. Rev. B **64**, 85203 (2001).
29. D. W. Feldman, J. H. Parker, W. J. Choyke, and L. Patric, Phys. Rev. **170**, 698 (1968).
30. E. Mooser and M. Schlüter, Nuovo Cimento B **18**, 164 (1973).
31. I. S. Gorban' and A. P. Krokhmal', Fiz. Tekh. Poluprovodn. (St. Petersburg) **35**, 1299 (2001) [Semiconductors **35**, 1242 (2001)].

Translated by A. Sidorova

Semiconductors, Vol. 37, No. 3, 2003, pp. 256–258. Translated from Fizika i Tekhnika Poluprovodnikov, Vol. 37, No. 3, 2003, pp. 272–274.

ELECTRONIC AND OPTICAL PROPERTIES OF SEMICONDUCTORS

Effect of Gadolinium Impurity on Transmittance and Reflectance of $Hg_3In_2Te_6$ Crystals

P. M. Gorleĭ, O. G. Grushka, and Z. M. Grushka

Fed'kovich National University, Chernovtsy, 58012 Ukraine

Submitted June 4, 2002; accepted for publication June 17, 2002

Abstract—The results of measuring the optical transmission and reflection spectra in the transparency region of $Hg_3In_2Te_6$:Gd semiconducting crystals are reported. It is shown that, in the entire wavelength range under investigation (2–25 μm), doping with Gd results in an increase in the continuous structureless absorption by impurities and defects, which introduce a quasi-continuous spectrum of localized states within the band gap. A decrease in transmittivity is accompanied by a decrease in the wavelength-independent reflectivity. Variation in the refractive index is attributed to changes in the bonding and electronic polarization of $Hg_3In_2Te_6$:Gd crystals. It is ascertained that polarization constants depend linearly on the strength of internal electric fields which exist in the vicinity of impurity defects. © *2003 MAIK "Nauka/Interperiodica".*

Unordered materials (mainly amorphous and imperfect semiconductors) are finding ever-increasing application in electronic and optoelectronic devices operating under extreme conditions [1, 2]. Materials similar to the $Hg_3In_2Te_6$ compound [3] belong to the aforementioned unordered (imperfect) semiconductors; in this compound, the crystalline structure of the sphalerite type (a cationic sublattice) has a high concentration ($\gtrsim 10^{21}$ cm^{-3}) of stoichiometric vacancies. The properties common to these semiconductors are a high resistance to ionizing radiation, a weak dependence of electrical parameters on introduced impurities, and pinning of the Fermi level near the midgap due to the self-compensation effect. It is of interest to investigate the role of structural disordering in impurity compensation without intensionally introducing centers with an opposite charge state.

In our studies, we used $Hg_3In_2Te_6$ crystals which were grown by the Bridgman–Stockbarger method and had various concentrations of gadolinium impurity. The gadolinium concentration N_{Gd} in the samples (see Table 1) was estimated from the results of measuring static magnetic susceptibility [4].

The X-ray diffraction studies showed that doping with gadolinium does not affect the structure type (the T_d symmetry); however, the lattice parameter a determined from the (642) reflection in the X-ray diffraction pattern (the CuK_α radiation) noticeably increases as the gadolinium concentration increases (see Table 1). An increase in the lattice parameter is related to a decrease in the material density, whereas an observed certain broadening of reflection spots occurs owing to an increase in stresses in the lattice and to the appearance of random fields.

We used the results of measurements of the electrical conductivity, the Hall coefficient, and the thermopower in $Hg_3In_2Te_6$:Gd crystals, which had bipolar conductivity (as in intrinsic semiconductors), to calculate the effective electron masses m^*/m_0 (see Table 2) in the situation where the isoenergy surfaces are spherical and the charge carriers are scattered by acoustical lattice vibrations. Electrical measurements have shown that impurity states are not involved in dc conduction and the Fermi level located near and slightly above the midgap descends slightly as the impurity concentration increases.

Studies of the absorption-coefficient α spectrum in the region of the fundamental-absorption edge have shown that the dependence of α on the photon energy $h\nu$ for all samples follows the Urbach rule $\alpha \propto \exp(h\nu/E_0)$. The slope of the linear portion of the dependence $\ln\alpha = f(h\nu)$ decreases and the parameter E_0 increases as the impurity concentration in the samples increases. The most probable reason for such a frequency dependence of the absorption coefficient can be related to potential fluctuations caused by structural disorder, which results in an increase in E_0 [2]. Fluctuations give rise to tails of the density of localized states near the conduction- and valence-band edges; these tails penetrate deep into the band gap.

In order to obtain information about states in the band gap, we measured the spectra of optical transmission T and reflection R in the transparency region in the wavelength range λ = 2.0–25 μm, i.e., in the photon-energy region $h\nu < E_g$ (E_g = 0.74 eV is the direct band gap of $Hg_3In_2Te_6$ at 300 K). As can be seen from the figure, in the wavelength range of 2.0 μm < λ < 25 μm, the shape of the spectra for doped samples 2–5 is the same as for undoped sample 1; i.e., the transmission coefficient T increases slightly as the wavelength λ increases from 2.0 to 20 μm, whereas the reflection coefficient R remains constant. The difference between the doped and undoped samples consists only in the magnitudes

Table 1. Technology-related parameters of $Hg_3In_2Te_6$ samples and their optical characteristics in the wavelength range $\lambda = 2$–20 μm in relation to gadolinium concentration

Sample no.	N_{Gd}, 10^{19} cm^{-3}	a, Å	d, cm	T	R	α, cm^{-1}	k
1	0	6.2846	0.20	0.56–0.57	0.27	0.11–0.04	1.8×10^{-6}–5.8×10^{-6}
2	0.5	6.2857	0.19	0.50–0.52	0.24	0.97–0.78	1.6×10^{-5}–1.3×10^{-4}
3	1.3	6.2879	0.18	0.40–0.43	0.20	2.70–2.30	4.3×10^{-5}–3.7×10^{-4}
4	1.6	6.2900	0.20	0.24–0.28	0.17	5.29–4.53	8.4×10^{-5}–7.2×10^{-4}
5	2.3	6.2915	0.19	0.15–0.20	0.15	8.28–6.77	1.3×10^{-4}–1.1×10^{-3}

Note: a is the lattice constant, d is the sample thickness, T is transmittance, R is reflectance, α is the absorption coefficient, and k is the extinction coefficient.

Table 2. The parameters characterizing the electronic polarizability in $Hg_3In_2Te_6$ samples

Sample no.	m^*/m_0	n	ε	a_B, Å	E_B, eV	E_i, kV/cm	a_p	Δa_p	$\Delta a_p/E_i$, 10^{-4} cm/kV
1	0.80	3.17	10.0	6.62	0.11	–	0.10	–	–
2	0.86	2.92	8.5	5.26	0.16	39.8	0.12	0.02	5.0
3	1.06	2.62	6.8	3.39	0.31	96.3	0.15	0.05	5.1
4	1.18	2.40	5.8	2.60	0.48	136.7	0.17	0.07	5.1
5	1.39	2.26	5.1	1.94	0.73	204.4	0.20	0.10	4.9

Note: m^*/m_0 is the effective electron mass; ε is the permittivity; n is the refractive index; a_B is the Bohr radius; E_B is the Bohr energy; E_i is internal electric field; and a_p and Δa_p are the polarization constant and its variation, respectively.

of measured parameters, which decrease as the dopant concentration increases; specifically, when measured immediately beyond the fundamental-absorption edge, the transmittance and reflectance are smaller in doped material than in the undoped sample.

The additional absorption, which correlates with the impurity concentration N_{Gd} in the samples that have an electrical conductivity of ~10^{-4} Ω^{-1} cm^{-1} and a charge-carrier concentration of ~10^{13} cm^{-3} at 300 K, is not related to absorption by free carriers. The cause of a decrease in transmittance is the absorption by impurities and defects. The absorption coefficient α and the extinction coefficient k were calculated using the following formulas [5]:

$$T = \frac{(1-R)^2 e^{-\alpha d}}{1-R^2 e^{-2\alpha d}}, \quad k = \frac{\alpha\lambda}{4\pi}.$$

Here, d is the sample thickness listed in Table 1.

As can be seen from Table 1, the extinction coefficient remains very small compared to the refractive index n in the formula [5] $R = [(n-1)^2 + k^2]/[(n+1)^2 + k^2]$ even for the highest impurity concentrations. This circumstance makes it possible to ignore the quantity k and calculate the refractive index for the samples under investigation using the expression $n = (1 + \sqrt{R})/(1 - \sqrt{R})$; correspondingly, the permittivity $\varepsilon = n^2$ can be determined.

The obtained values of ε (see Table 2) correspond to the permittivities ε_{opt}, which depend on electronic polarization caused by displacement of electron clouds. These values are much smaller than those of static permittivity ($\varepsilon_{st} \approx 18.5$), which differs from ε by an additional component that is controlled by relative displacement of ions in a ternary semiconducting compound (by ionic polarization) in an external electric field. We observe a correlation between a decrease in the permittivity and a decrease in the density of material; however, the behavior of ε cannot be explained by mere variation in the density on the basis of the Clausius–Mossotti equation [6].

As is customary [6], we expressed variations in refractive indices in terms of polarization constants; for an isotropic medium having only electronic polarization, these constants are expressed as $a_p = 1/n^2 = 1/\varepsilon$. For crystals (including those with the T_d symmetry) without a center of inversion, it is known that the polarization constants increase under the effect of an external electric field (the so-called electrooptical effect). In the case under consideration, an external field is absent; most probably, the observed increment Δa_p (see Table 2) is related to the formation of an internal electric field caused by additional defects and local stresses of extrinsic origin. In order to estimate the strength of a characteristic internal field, we used the expression [7] $E_i = (n_t a_B^3)^{3/5} E_B/e a_B$, where $a_B = \varepsilon\hbar^2/m^*e^2$ is the Bohr

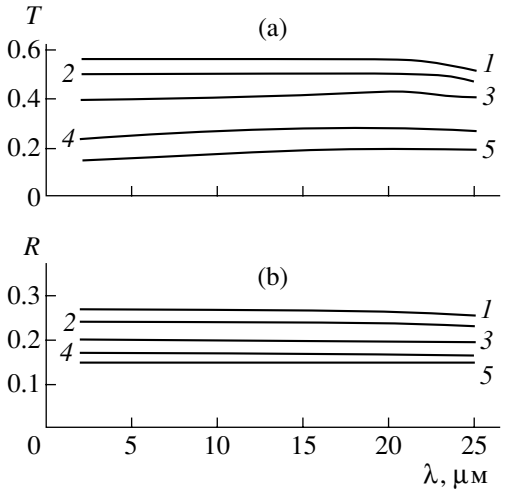

The (a) transmittance and (b) reflectance spectra for $Hg_3In_2Te_6$ samples either (*1*) undoped or (*2–5*) doped with Gd. Numbers at the curves correspond to the sample numbers. The values of N_{Gd} are listed in Table 1.

radius and $E_B = m^*e^4/2\varepsilon^2\hbar^2$ is the Bohr energy. It can be seen from Table 2 that the energy E_i increases as the impurity concentration in the samples increases. With allowance made for experimental error, the dependence $\Delta a_p = f(E_i)$ can be described by the linear electrical-effect relation $\Delta a_p = rE_i$, where, according to Table 2, $r = \Delta a_p/E_i \approx 5 \times 10^{-4}$ cm/kV. Thus, strong fields existing in the vicinity of impurity defects affect the refractive index n and the permittivity ε of $Hg_3In_2Te_6$ crystals.

Dependences of a_B and E_B on the impurity concentration (see Table 2) indicate that, as the Bohr radius decreases, electrons are localized more strongly, their Bohr energy E_B increases as the energy of binding to impurity atoms increases, and, correspondingly, the ionization potential increases. This potential affects the electronic polarizability. The lower the ionization potential, the smaller the polarizability [6]. This observation is consistent with a specific feature of unordered systems in which, due to a distortion of the initial matrix, the tendency towards pairing of electrons in bonding configurations becomes favorable [1]. Notably, fluctuations of the bond lengths and angles result in a spread of the band edges and give rise to localized states, which are distributed quasi-continuously over the band gap. These states, which are formed near both allowed bands, are related to donor and acceptor levels. The overlap of these levels ensures self-compensation of introduced impurities and pins the Fermi level near the midgap.

REFERENCES

1. A. Madan and M. Shaw, *The Physics and Applications of Amorphous Semiconductors* (Academic, Boston, 1988; Mir, Moscow, 1991).
2. *Amorphous Silicon and Related Materials*, Ed. by H. Fritzsche (World Sci., Singapore, 1989; Mir, Moscow, 1991).
3. G. G. Grushka, A. P. Bakhtinov, and Z. M. Grushka, J. Adv. Mater. **4** (1), 36 (1997).
4. O. G. Grushka, P. M. Gorleĭ, A. V. Bestsennyĭ, and Z. M. Grushka, Fiz. Tekh. Poluprovodn. (St. Petersburg) **34**, 1197 (2000) [Semiconductors **34**, 1147 (2000)].
5. Yu. I. Ukhanov, *Optical Properties of Semiconductors* (Nauka, Moscow, 1977).
6. I. S. Zheludev, *Physics of Crystalline Dielectrics* (Nauka, Moscow, 1968; Plenum, New York, 1971), Vols. 1 and 2.
7. V. L. Bonch-Bruevich, I. P. Zvyagin, R. Kaĭper, A. G. Mironov, R. Énderlaĭn, and B. Ésser, *Electron Theory of Unordered Semiconductors* (Nauka, Moscow, 1981).

Translated by A. Spitsyn

Semiconductors, Vol. 37, No. 3, 2003, pp. 259–262. Translated from Fizika i Tekhnika Poluprovodnikov, Vol. 37, No. 3, 2003, pp. 275–278.

ELECTRONIC AND OPTICAL PROPERTIES OF SEMICONDUCTORS

Photoelectric Properties of ZnO Films Doped with Cu and Ag Acceptor Impurities

A. N. Gruzintsev*, V. T. Volkov, and E. E. Yakimov

Institute of Microelectronic Technology and Ultrahigh-Purity Materials, Russian Academy of Sciences, Chernogolovka, Moscow oblast, 142432 Russia

**e-mail: gran@ipmt-hpm.ac.ru*

Submitted June 4, 2002; accepted for publication June 17, 2002

Abstract—The influence exerted by doping with Cu and Ag acceptor impurities at a content of 1, 3, and 5 at. % on the luminescence and photoconductivity of zinc oxide films has been studied. Electron-beam evaporation in optimal modes has been used to obtain films with predominant luminescence in the UV spectral range. It has been shown that the incorporation of copper yields three types of point defects in ZnO: Cu_{Zn} ($3d^{10}$), Cu_{Zn} ($3d^9$), and Cu_i; and in silver, a single type: Ag_{Zn} ($3d^{10}$). Precipitation of a silver oxide phase at the highest impurity concentration has been observed. Impurity incorporation leads to a pronounced increase in the resistance and photosensitivity of films. © *2003 MAIK "Nauka/Interperiodica".*

1. INTRODUCTION

Owing to its piezoelectric properties, high electronic conductivity, and optical transparency, zinc oxide has found wide application in various optoelectronic devices. The *p*-type impurity conduction (with a hole concentration of more than 10^{19} cm^{-3}) [1–4], successfully obtained recently by means of doping with Group-V acceptors (N, P, and As), makes it possible to consider ZnO as the most promising member of the family of wide-bandgap semiconductors (ZnSe, SiC, GaN, etc.). When zinc oxide is doped with aluminum and gallium donor impurities, it is conventionally used as a low-resistivity transparent contact with high radiation, chemical, and thermal resistance. Thus, the high electron or hole conduction, combined with a wide direct band gap (3.37 eV), makes zinc oxide a promising material for the development of semiconductor emitters of visible and UV light.

First attempts have been made to develop light-emitting diodes based on zinc oxide doped with donor and acceptor impurities [5]. However, the diodes described exhibited no luminescence at all, despite the fact that undoped ZnO films commonly show pronounced UV photoluminescence (PL) in the bound-exciton range (370 nm) [6]. Therefore, it is necessary to select the dopant in such a way that it would not only ensure the required type and magnitude of conductivity, but would also leave the emission spectrum and transparency of zinc oxide intact.

It should be noted that the preceding study [7] by the authors of the present communication was concerned with the influence of copper, silver, and gold impurities on the emission from zinc oxide films obtained by magnetron sputtering. The predominance of green emission related to donor–acceptor pairs, in which intrinsic defects, oxygen vacancies, played the role of donors and incorporated impurities acted as acceptors, was revealed. Also, the depth of the corresponding acceptor levels relative to the valence band was determined. It was found that copper and silver give the shallowest levels with binding energies of $3d^{10}$ states of 0.38 and 0.20 eV, respectively. The authors drew attention to the even lower binding energy of these acceptors in the $3d^9$ state characteristic of insulating ZnO films. However, the magnetron sputtering technique gave no way of obtaining films with a low electron density and good crystallinity. Therefore, it was of interest to study films obtained by other methods, containing an excess of oxygen with respect to stoichiometry, and with a varied concentration of dopants.

The aim of the present study was to analyze the influence exerted by doping with Group I acceptor impurities—copper and silver—taken in varied concentrations on the conductivity, photosensitivity, and luminescent properties of the material. The films studied were obtained using electron-beam evaporation with the composition of the ionic component controlled in the course of deposition. This technique does not require any subsequent high-temperature annealing of the films, which commonly leads to loss of oxygen [8].

2. EXPERIMENTAL

The luminescent and photoelectric properties of ZnO:Cu and ZnO:Ag films deposited by electron-beam evaporation onto amorphous substrates of thermally oxidized silicon (SiO_2) on a Leubold Haereus L-560 installation were studied. The composition of the ionic component was controlled in the course of deposition by applying a positive voltage to the substrate [8]. The films were doped by adding copper and silver oxides to

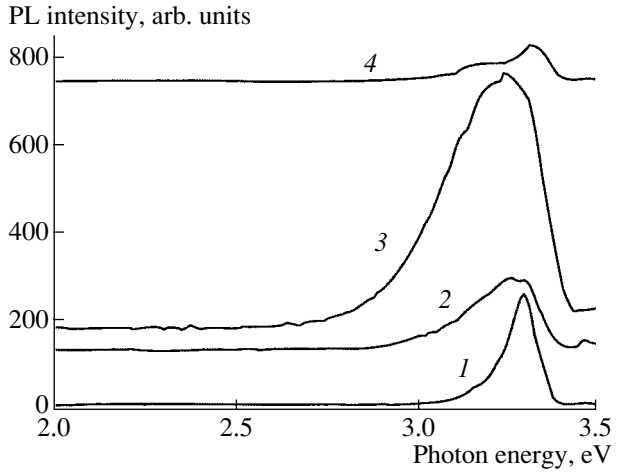

Fig. 1. PL spectra of (*1*) undoped ZnO films and (*2–4*) doped ZnO:Ag films at T = 80 K and impurity content of (*2*) 1, (*3*) 3, and (*4*) 5 at. %.

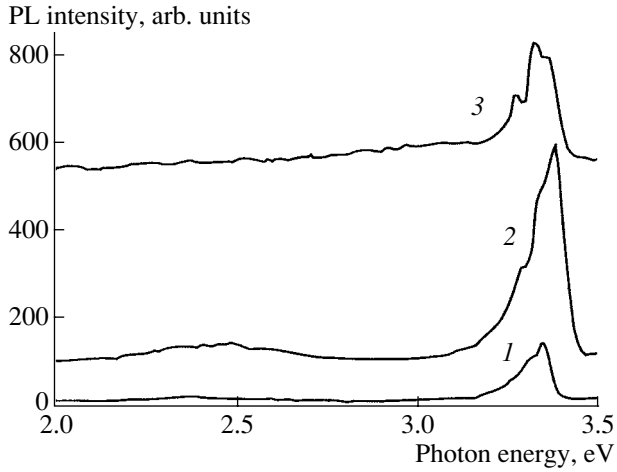

Fig. 2. PL spectra of doped ZnO:Cu films at T = 80 K and impurity content of (*1*) 1, (*2*) 3, and (*3*) 5 at. %.

the material of the ZnO target being sputtered in amounts of 1, 3, and 5 at. %. The PL spectra of the films were studied in liquid nitrogen under excitation by an LGI-505 pulsed nitrogen laser. The spectra were analyzed with an MDR-6 computer-controlled double monochromator, which ensured a spectral resolution of no worse than 1 meV for the slit widths used. The film thickness, measured with a quartz thickness monitor, was 0.5 μm. A JEM-2000FX transmission electron microscope was used to study the crystal structure and surface morphology of the films.

The photoconductivity was studied in the UV and visible spectral ranges under exposure to light of a Narva-2000 incandescence lamp, which was passed through a chopper, with a chopping frequency of 102 Hz, and an MDR-12 large-aperture monochromator.

3. RESULTS AND DISCUSSION

Figure 1 shows the PL spectra of an undoped zinc oxide film (curve *1*) and films doped with various amounts of silver (curves *2–4*). Pure ZnO films are characterized by the presence of a narrow line peaked at 3.30 eV. Doping leads to broadening of the UV line of emission from ZnO:Ag because of the increasing contribution from the long-wavelength part of the spectrum. Doping with up to 3 at. % Ag raises the total luminescence intensity. The intensity of luminescence from films with the highest content of silver (5 at. %) is much lower (Fig. 1, curve *4*), with two lines clearly seen at 3.17 and 3.33 eV.

The PL spectra of ZnO:Cu films at the same impurity concentrations (Fig. 2) differ in both the UV line positions and in the much narrower halfwidth of lines compared with ZnO:Ag films. In contrast to the spectra of pure zinc oxide, a fine structure is clearly seen in the given case. Three narrow lines peaked at 3.26, 3.31, and 3.35 eV, as well as a shoulder at longer wavelengths (3.05 eV), are observed for ZnO:Cu (5 at. %) films (Fig. 2, curve *3*). The same lines are revealed in the PL spectra of films with a lower copper content.

It is noteworthy that a green luminescence band, related to copper impurity in zinc oxide in early studies, is absent for both impurities. Previously, the authors of the present study attributed green emission to transitions from oxygen vacancies into the valence band or to those within the donor–acceptor pair, in which an oxygen vacancy is the donor and a shallow or intrinsic defect, the acceptor [7]. However, if oxygen excess is created in the process of film growth, then, as seen from the presented spectra, the green emission can be eliminated, with only edge and excitonic emission retained in the violet part of the spectrum. In this case, the broad long-wavelength bands at 3.17 eV for ZnO:Ag (Fig. 1, curve *4*) and 3.05 eV for ZnO:Cu (Fig. 2, curve *3*), labeled as edge emission, are due to electron transitions from the conduction band to the corresponding impurity acceptors. The narrower short-wavelength lines are due to recombination of bound excitons. It is noteworthy that only a single line of a bound exciton is observed at 3.33 eV at a high silver content (5 at. %), and three excitonic lines peaked at 3.26 (I_1), 3.31 (I_2), and 3.35 eV (I_3) are present in the spectrum when the copper concentration is the same. These lines cannot be phonon satellites, since their relative intensities depend on the content of copper. With account taken of the variable valence of copper, it seems reasonable to attribute the first two lines, I_1 and I_2, to recombination of bound excitons on Cu_{Zn} acceptors in different charge states ($3d^{10}$ and $3d^9$), and the I_3 line, to recombination of bound excitons on Cu_i donors. The intensity ratios of the given excitonic peaks for different contents of copper impurity can be used to determine which of the three possible kinds of defects is associated with copper atoms incorporated into the zinc oxide lattice. As for silver, the results of measurements (Fig. 1) indicate that

Resistivities of ZnO:Cu and ZnO:Ag films with different impurity concentrations

Type of impurity	Ag	Ag	Ag	Cu	Cu	Cu
Content, at. %	1	3	5	1	3	5
Resistivity, Ω cm	8.5×10^3	2.1×10^4	1.2×10^5	1.3×10^5	3.1×10^5	1.3×10^6

only a single excitonic peak, i.e., a single defect type (Ag_{Zn}), is present.

Since copper and silver are acceptor impurities in ZnO, it was of interest to study the conductivity of the films using the four-probe method. The table lists resistivities of films with a varied content of impurities. If account is taken of the fact that the resistivity of undoped zinc oxide films deposited under the same conditions is 0.77 Ω cm, it can be seen that doping leads to a pronounced increase in resistivity. It is noteworthy that incorporation of copper leads to a more pronounced (by an order of magnitude) increase in resistivity compared with the introduction of the same amount of silver impurity.

The deposition of insulating ZnO:Cu and ZnO:Ag films allows for the study of their photoconductivity spectra. The fact of the matter is that the dark conductivity of the undoped material is so high that exposing a film to light does not lead to any significant change in its conductivity, and nothing but noise is observed in the photoconductivity spectrum (Fig. 3, curve *1*). The increase in resistivity of ZnO:Ag films upon doping greatly improves the signal-to-noise ratio and yields an intense line of photosensitivity in the red spectral range, peaked at 1.8 eV, and a shoulder at 1.95 eV for the highest content of silver (Fig. 3, curve *4*). It is noteworthy that these films show pronounced absorption of visible light with a photon energy greater than 1.8 eV.

The photoconductivity of ZnO:Cu films shows peaks at 3.0, 3.16, and 3.5 eV and a peak at 2.75 eV for a copper content of 3 at. % (Fig. 4). It is seen immediately that the PL spectrum contains a line of green emission at 2.45 eV for the same impurity content (Fig. 2, curve *2*), which is related to oxygen vacancies [7]. Therefore, the photoconductivity in the visible part of the spectrum at 2.75 eV is, in all probability, due to electron transitions from oxygen vacancies into the conduction band. The shortest wavelength peak of photoconductivity at 3.5 eV, associated with carrier transition from the valence to the conduction band, correlates well with the band gap of zinc oxide. Two peaks in the edge region at 3.0 and 3.16 eV are most likely due to electron transitions from Cu_{Zn} acceptors in different charge states ($3d^{10}$ and $3d^9$) into the conduction band.

The unusual appearance of the photoconductivity spectra and the darkening of ZnO:Ag (5 at. %) films suggest that the films contain a second phase, i.e., silver oxide. To confirm this assumption, planar sections of the films were studied by transmission microscopy. The use of a JEM-2000FX transmission electron microscope revealed the presence in the film of 0.2- to 0.3-μm inclusions with an electron diffraction pattern characteristic of silver oxide. In films with copper, no

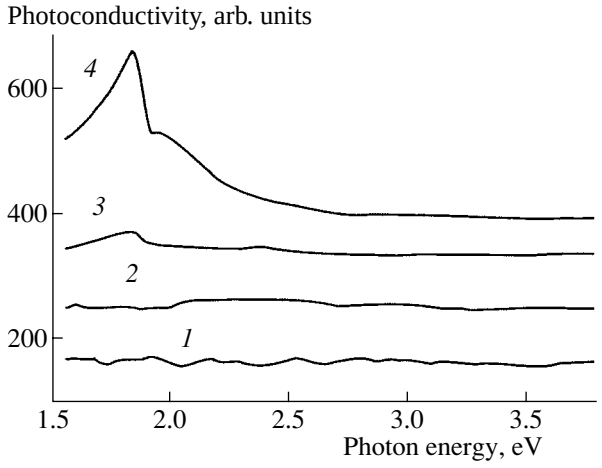

Fig. 3. Photoconductivity spectra of (*1*) undoped ZnO films and (*2–4*) doped ZnO:Ag films at T = 300 K and impurity content of (*2*) 1, (*3*) 3, and (*4*) 5 at. %.

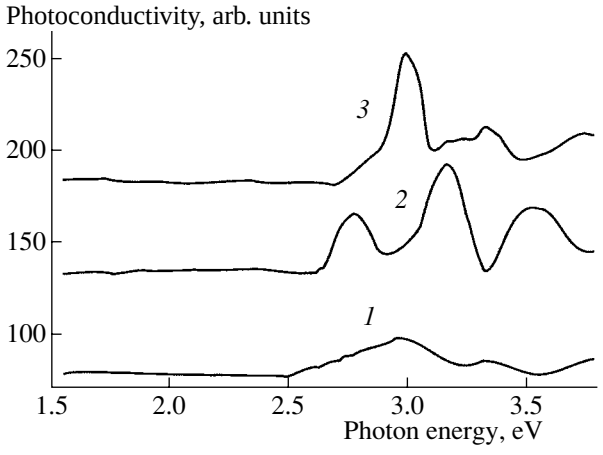

Fig. 4. Photoconductivity spectra of doped ZnO:Cu films at T = 300 K and impurity content of (*1*) 1, (*2*) 3, and (*3*) 5 at. %.

second phase was observed for any content of introduced impurity.

4. CONCLUSION

The doping of zinc oxide films with silver or copper impurity at high concentrations in the range from 1 to 5 at. % yielded high-resistivity layers with high photosensitivity in the visible (ZnO:Ag) and UV (ZnO:Cu) spectral ranges. Owing to enrichment with oxygen in the course of growth and impurity doping of the films, their PL spectra contained lines of edge and excitonic emission in the violet spectral range. The edge emission was due to electron transitions from the conduction band to acceptor levels, and the excitonic emission, to recombination of excitons bound on impurity defects.

Analysis of the PL and photoconductivity spectra suggests that the mechanisms by which these impurities are introduced are different. Copper atoms are incorporated in the form of point defects of three types: Cu_{Zn} acceptors in two charge states ($3d^{10}$ and $3d^{9}$) and Cu_i donors, whereas silver atoms are incorporated only as substitutional defects of Ag_{Zn} in a single charge state ($3d^{10}$), with part of the silver precipitated in the form of a second phase, silver oxide, with the silver content exceeding 3 at. %.

Incorporation of copper and silver into zinc oxide markedly raises the resistivity and photosensitivity of the films. This means that, when substituting zinc atoms in the crystal lattice, these impurities are rather effective acceptors. Copper yields a higher resistivity compared with silver. However, copper should be incorporated in the form of substitutional defects, Cu_{Zn} acceptors, rather than as interstitial defects, Cu_i donors. At high concentrations of copper impurity, it starts to self-compensate, forming defects of donor and acceptor types.

Such a strong difference in the behavior between copper and silver impurities in ZnO can be accounted for by the difference in their ionic radii: Cu^+, 0.098 nm; Cu^{2+}, 0.080 nm; and Ag^+, 0.113 nm [3]. The monovalent state of silver leads to a predominance of defects of a single type, Ag_{Zn} ($3d^{10}$). The much larger ionic radius of silver, compared with that of a Zn^{2+} ion (0.083 nm), hinders its egress into an interstitial position and gives rise to strains in the crystal lattice of zinc oxide, which are compensated for by the precipitation of the second phase.

5. ACKNOWLEDGMENTS

This study was financially supported by the Russian Academy of Sciences program “Low-Dimensional Quantum Structures” and by INTAS (grant no. 2002–0796).

REFERENCES

1. T. Yamamoto and H. Katayama-Yoshida, Jpn. J. Appl. Phys. **38**, L166 (1999).
2. M. Joseph, H. Tabata, and T. Kawai, Jpn. J. Appl. Phys. **38**, L1205 (1999).
3. K. Minegishi, Y. Kowai, Y. Kikuchi, *et al.*, Jpn. J. Appl. Phys. **36**, L1453 (1997).
4. A. N. Georgobiani, A. N. Gruzintsev, V. T. Volkov, and M. O. Vorob’ev, Fiz. Tekh. Poluprovodn. (St. Petersburg) **36**, 205 (2002) [Semiconductors **36**, 265 (2002)].
5. X. Guo, H. Choi, H. Tabata, and T. Kawai, Jpn. J. Appl. Phys. **40**, L177 (2001).
6. S. B. Zhang, S. H. Wei, and A. Zunger, Phys. Rev. B **63**, 075205 (2001).
7. A. N. Gruzintsev, V. T. Volkov, I. I. Khodos, *et al.*, Mikroélektronika **31**, 202 (2002).
8. A. N. Gruzintsev, V. T. Volkov, and L. N. Matveeva, Mikroélektronika **31**, 211 (2002).
9. *Physics and Chemistry of II–VI Compounds*, Ed. by M. Aven and J. S. Prener (North-Holland, Amsterdam, 1967; Mir, Moscow, 1970).

Translated by M. Tagirdzhanov

Semiconductors, Vol. 37, No. 3, 2003, pp. 263–265. Translated from Fizika i Tekhnika Poluprovodnikov, Vol. 37, No. 3, 2003, pp. 279–281.

ELECTRONIC AND OPTICAL PROPERTIES OF SEMICONDUCTORS

Arrangement of Arsenic Atoms in the PbTe Lattice

S. A. Nemov*, P. P. Seregin*, S. M. Irkaev, and N. P. Seregin****

** St. Petersburg State Polytechnical University, ul. Politekhnicheskaya 25, St. Petersburg, 195251 Russia*

*** Institute for Analytical Instrumentation, Russian Academy of Sciences, St. Petersburg, 198103 Russia*

Submitted July 1, 2002; accepted for publication July 3, 2002

Abstract—Mössbauer emission studies based on the ^{73}As(^{73}Ge) isotope showed arsenic impurity atoms in the PbTe lattice to be localized in both the anion and the cation sublattices, with the ^{73}Ge atoms formed in the radioactive decay of ^{73}As being electrically inactive in both positions. © *2003 MAIK "Nauka/Interperiodica".*

The recent discovery of two-electron centers with negative correlation energy in lead chalcogenides [1] has spurred interest in the nature of the impurity states formed in these compounds by Group V elements [2]. It appears [3] that As, Sb, and Bi impurities in lead chalcogenides act as donors and that the fraction of electrically active atoms is substantially smaller than unity. Two explanations may be forwarded to account for the latter observation: either a sizable fraction of the impurity atoms form electrically inactive complexes in the lattice or the impurity is distributed between the cation and the anion sublattices (where it acts as a donor or an acceptor, respectively). One can choose between these models if the arrangement of the impurity atoms in the lead chalcogenide lattices has been determined. In this study, such a determination was made for the case of arsenic impurity atoms in PbTe by Mössbauer emission spectroscopy based on the ^{73}As(^{73}Ge) isotope.

Figure 1 illustrates schematically the formation of the ^{73}Ge Mössbauer level following radioactive decay of the ^{73}As parent isotope [4]. As a result of electron capture by ^{73}As and neutrino emission, the recoil energy of the ^{73}Ge daughter atoms does not exceed the energy required to displace an atom from a normal lattice site [5]; one may therefore expect that radioactive transformation should not bring about displacement of germanium atoms from normal lattice sites and, hence, that the parameters of the ^{73}As(^{73}Ge) Mössbauer emission spectra should reflect the state of the ^{73}Ge atoms localized at the sites occupied by arsenic atoms.

The ^{73}As parent isotope was prepared using the ^{73}Ge(p, $2n$)^{73}As reaction. Carrier-free ^{73}As was obtained by a "dry chemistry" technique based on the high difference in volatility between the target and parent atoms [6]. To do this, the irradiated target (a single-crystal germanium film containing ~98% ^{74}Ge) was placed, after a three-month holding (to reduce the content of radioactive ^{73}As), into an evacuated quartz cell and its end containing the target was heated at 900 K for 5 h in a tubular furnace. After opening the cell, ~80% of the ^{73}As atoms were found sorbed at the inner walls of the quartz cell and the carrier-free ^{73}As was washed off by a nitric acid solution. The weight loss of the irradiated isotope-enriched material involved in this operation turned out to be ~1–2%, and it can be repeatedly used to prepare a cyclotron target.

The Mössbauer sources were prepared by fusing PbTe samples with the carrier-free ^{73}As; the concentration of impurity arsenic atoms did not exceed 10^{17} cm^{-3}. The starting PbTe samples were n- (with a lead excess, $n \approx 10^{18}$ cm^{-3}) and p-type (with tellurium excess, $p \approx 10^{18}$ cm^{-3}). The ^{73}As(^{73}Ge) Mössbauer spectra were measured using an SM-2201 commercial spectrometer at room temperature, with absorbers in the form of either a single-crystal Ge film or a film of fine-grained GeTe with a surface density of the ^{73}Ge isotope of 10 mg/cm^2 (the enrichment with the ^{73}Ge isotope was ~90%). Figures 2a and 2b display spectra obtained with such absorbers and a ^{73}As source (the source was a proton-irradiated single-crystal ^{74}Ge target cooled for

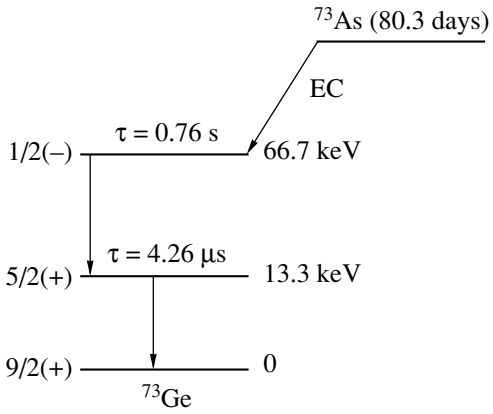

Fig. 1. ^{73}As decay scheme.

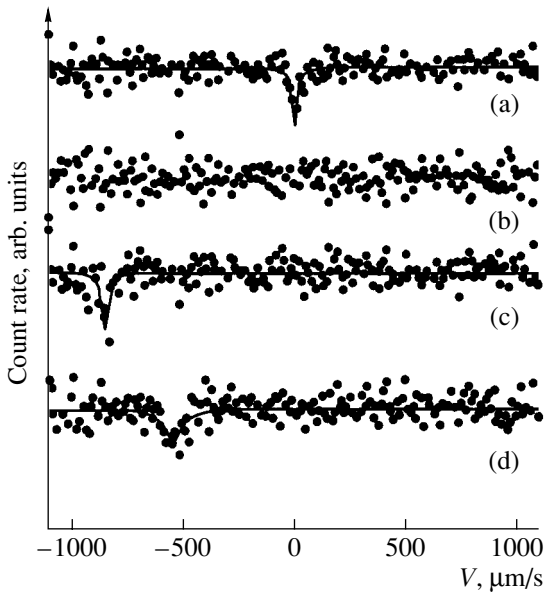

Fig. 2. Mössbauer emission spectra of the sources (a, b) Ge:^{73}As and (c, d) *n*-PbTe:^{73}As obtained at 297 K with the absorbers (a, c) ^{73}Ge and (b, d) ^{73}GeTe.

3 months and subsequently annealed at 500 K in a hydrogen environment for 5 h). The spectrum obtained with a ^{73}Ge absorber consisted of a single line with a full width at half-maximum of 30.8 ± 0.5 μm/s, which was significantly in excess of the natural width of the ^{73}Ge spectral line (~6.98 μm/s) [7] and should be attributed to the incomplete annealing of radiation defects in the target used as the Mössbauer source. No resonance absorption was detected in the case of the ^{73}GeTe absorber, which is apparently caused by the large isomer shift of the Mössbauer spectrum (at least above 1100 μm/s) [8].

Figures 2c and 2d show typical spectra of the *n*-type PbTe:^{73}As source obtained with these absorbers, and the results of processing of all spectra are listed in the table. All the spectra contain single lines, with their widths considerably exceeding the natural ^{73}Ge spectral line. This broadening is associated, at least in the case of the ^{73}GeTe absorber, with distortions of the cubic symmetry of the local environment of Ge atoms in the GeTe lattice. The absence of resonance absorption in Fig. 2b unambiguously implies that the spectra in Figs. 2c and 2d are related to two nonequivalent states of the ^{73}Ge daughter impurity atoms.

Parameters of ^{73}As(^{73}Ge) Mössbauer emission spectra in PbTe

Conduction	Absorber	Impurity center	*S*, μm/s	*G*, μm/s
n	Ge	$^{73}Ge^{0}$	–551	82
	GeTe	$^{73}Ge^{2+}$	–852	41
p	Ge	$^{73}Ge^{0}$	–542	78
	GeTe	$^{73}Ge^{2+}$	–863	45
Errors			±15	±5

Note: *S* is the position of the center of gravity of the spectrum of the source relative to that of the absorber; *G* is the FWHM of the spectrum.

The spectrum obtained with the ^{73}Ge absorber should be attributed to $^{73}Ge^{0}$ centers in the anion sublattice of PbTe (the local environment of these centers contains Pb atoms), with the $^{73}Ge^{0}$ atoms evidently formed from the ^{73}As atoms residing in the anion sublattice of PbTe. The spectrum obtained with the ^{73}GeTe absorber should be related to the $^{73}Ge^{2+}$ centers in the PbTe cation sublattice (Te atoms are present in the nearest environment of these centers), so that the $^{73}Ge^{2+}$ ions are evidently formed from the ^{73}As atoms in the cation sublattice of PbTe. Thus, one may conclude that As impurity atoms reside in PbTe in both the anion and the cation sublattices. While the fraction of electrically active arsenic atoms depends on the actual arsenic distribution between the sublattices, this fraction is always smaller than unity (this is deduced from the fact that part of the arsenic atoms reside in the anion sublattice even in *p*-type samples).

It should be pointed out that Ge impurity atoms in the cation sublattice of PbS and PbSe are two-electron donors with negative correlation energy [9]; however, as follows from the position of the $^{73}Ge^{2+}$ spectra being independent of the PbTe conduction type, Ge impurity atoms in the PbTe lattice are electrically inactive. Note that impurity atoms of Sn exhibit a similar behavior; indeed, Sn in PbS and PbSe forms two-electron donor centers with negative correlation energy, whereas Sn acts as an isovalent substitutional impurity in PbTe [1].

ACKNOWLEDGMENTS

This study was supported by the Russian Foundation for Basic Research (project no. 02-02-17306) and by the Ministry of Education of the Russian Federation (grant no. E 00-3.4-42).

REFERENCES

1. F. S. Nasredinov, S. A. Nemov, V. F. Masterov, and P. P. Seregin, Fiz. Tverd. Tela (St. Petersburg) **41**, 1987 (1999) [Phys. Solid State **41**, 1741 (1999)].
2. V. F. Masterov, F. S. Nasredinov, S. A. Nemov, *et al.*, Fiz. Tekh. Poluprovodn. (St. Petersburg) **31**, 1321 (1997) [Semiconductors **31**, 1138 (1997)]; V. F. Masterov, F. S. Nasredinov, P. P. Seregin, *et al.*, Fiz. Tekh. Poluprovodn. (St. Petersburg) **33**, 913 (1999) [Semiconductors **33**, 836 (1999)].

3. Yu. I. Ravich, B. A. Efimova, and I. A. Smirnov, *Semiconducting Lead Chalcogenides* (Nauka, Moscow, 1968; Plenum, New York, 1970).
4. *Radionuclide Decay Schemes. Radiation Energy and Intensity* (Énergoatomizdat, Moscow, 1987), p. 147.
5. L. Pfeiffer, R. S. Raghavan, C. P. Lichtenwalner, and A. G. Cullis, Phys. Rev. B **12**, 4793 (1975); L. Pfeiffer, T. Kovacs, G. K. Celler, *et al.*, Phys. Rev. B **27**, 4018 (1983).
6. S. I. Bondarevskiĭ, V. V. Eremin, and N. P. Seregin, in *Fundamental Studies in Technical Universities: Proceedings of V All-Russia Conference on Problems in Science and High School* (St. Petersburg, 2001), p. 121.
7. L. Pfeiffer, Phys. Rev. Lett. **38**, 862 (1977).
8. A. Svane, J. Phys. C: Solid State Phys. **21**, 5369 (1988).
9. V. F. Masterov, F. S. Nasredinov, S. A. Nemov, *et al.*, Fiz. Tekh. Poluprovodn. (St. Petersburg) **31**, 381 (1997) [Semiconductors **31**, 319 (1997)].

Translated by G. Skrebtsov

Semiconductors, Vol. 37, No. 3, 2003, pp. 266–270. Translated from Fizika i Tekhnika Poluprovodnikov, Vol. 37, No. 3, 2003, pp. 282–286.

ELECTRONIC AND OPTICAL PROPERTIES OF SEMICONDUCTORS

Polyamidine Supramolecular Structures—a New Class of Photosensitive Polymeric Semiconductors

E. L. Aleksandrova*, M. M. Dudkina, and A. V. Ten'kovtsev***

** Research Institute of Optical Materials Technology at Vavilov State Optical Institute All-Russia Research Center, Birzhevaya liniya 14, St. Petersburg, 199034 Russia*

*** Institute of Macromolecular Compounds, Russian Academy of Sciences, Bol'shoi proezd 31, St. Petersburg, 199004 Russia*

Submitted July 4, 2002; accepted for publication July 22, 2002

Abstract—Photophysical properties of a new class of polymers, polyamidines, are investigated in relation to their molecular structure. It is shown that the photosensitivity in the systems investigated is a consequence of the formation of supramolecular structures in them. These structures emerge due to the formation of an ordered system of hydrogen bonds. It is found that the materials mentioned are characterized by reasonably high quantum yields of photogeneration of charge carriers and photosensitivity at a level of 10^4 cm^2/J. © *2003 MAIK "Nauka/Interperiodica".*

1. INTRODUCTION

In recent decades, polymers have found wide application in the fabrication of optical carriers of information, specifically, photosensitive materials suitable for the development of electrophotographic and photothermoplastic recording media. The traditional approach to the synthesis of photoconducting polymer systems is associated with introducing photosensitive low-molecular compounds into a polymer matrix (fabrication of a host–guest system) or by obtaining polymers which are bonded covalently with photoactive fragments in the main or side chains. However, it was recently suggested that photosensitive polymer systems might be obtained due to the formation of supramolecular ensembles of photoactive components [1]. These ensembles emerge due to the existence of a system of ordered hydrogen bonds between the fragments of macromolecules. The formation of supramolecular ensembles affects the properties of the ground and excited states of individual particles; the cooperative character of the process gives rise to new photophysical properties. In such systems, a number of processes can be observed, for example, excitation energy transfer, photoinduced charge division, etc., which are usually not observed in other cases.

It is known that polymers, which contain amidine groups in the main chain, are capable of effective bicenter bonding with the formation of cyclic and linear supramolecular ensembles [2]. An example of such an ensemble is shown in Fig. 1. This circumstance leads to the formation of a quasi-conjugated system. Furthermore, the high basicity of amidine groups permits obtaining ionic complexes of the aforementioned polymers both with low-molecular compounds (electron donors or acceptors) and with dopants, which form complexes due to nonvalent bonding. This permits varying the photophysical properties of molecular ensembles due to charge transfer in the chains of their constituent macromolecules. Charge transfer is associated with the formation of cellular hydrogen-bonded systems with fragments that possess considerable π conjugation.

The purpose of this study is to investigate the photophysical properties of polyamidines, specifically, the

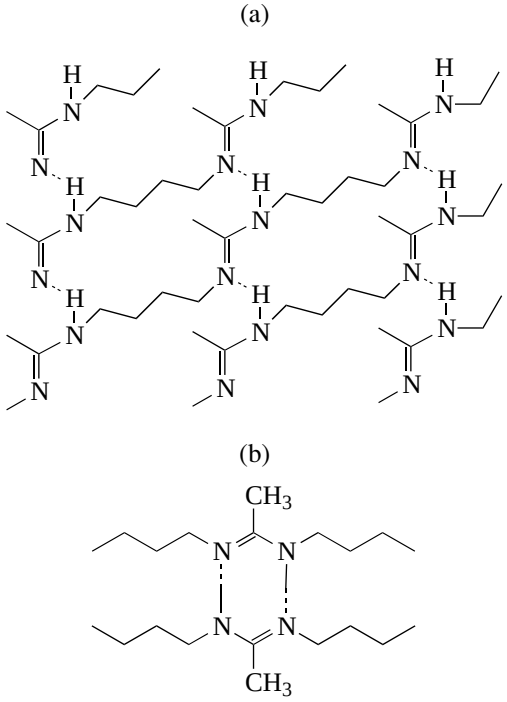

Fig. 1. Supramolecular structures of the polymers investigated: (a) linear and (b) cyclic.

photogeneration of charge carriers and the photosensitivity of recording media based on them.

2. OBJECTS OF INVESTIGATION

This investigation was carried out for a series of polyimidines which differ both in the structure of the main chain and the type of substituents in the amidine fragment (Fig. 2).

The choice of these structures was governed, on the one hand, by the possibility of considering the influence of basicity and, subsequently, the energy of hydrogen bonds both between amidine groups and chromophor molecules on the photophysical properties of complexes. On the other hand, the systematic increase in the number of π-conjugated fragments exhibiting the π-stacking effect, which leads to electron transfer between the noncovalent-bonded elements of the chain, will permit establishing the influence of this factor on the photoconductivity of the system as a whole.

The polymers were synthesized according to the known method [3].

As a compound which possesses a developed π-conjugation chain and is capable of ionic bonding with polyamidine molecules, 1.5-di(4-oxyphenyl)penta-1.4-dien-3-OH was used (Fig. 3).

This compound was chosen as the dopant, since the complexes of the compounds mentioned with polydecamethylene-acetamidine, according to our data, possess a low Schottky barrier. This manifests itself in their ability to exhibit third-order nonlinear optical effects [4]. 1.5-Di(4-oxyphenil)penta-1.4-dien-3-OH was synthesized according to the technique described previously [4].

Compounds which possess pronounced donor and acceptor properties were used as dopants capable of nonvalent complex formation with polyamidines as guests in a guest–host system. As donors, indole and anthracene molecules were used, and fullerene (C_{60} : C_{70} = 87 : 13) molecules were used as acceptors. The dopant concentration was 1 mol %.

The polymer complexes were obtained by mixing solutions of polyamidines with ethanol solutions of dopants. From the solutions obtained, films were molded by sprinkling onto a rotating substrate (glass with an ITO coating, 3000 rpm, 30 s). The films were dried in vacuum at room temperature to a constant weight. The film thickness was 1–5 μm.

3. MEASUREMENT PROCEDURE

The photosensitivity $S_{0.1}$ and the quantum yield of the carrier photogeneration η were measured in the electrophotographic mode. The decay kinetics of the surface potential $V(t)$ of the layer during illumination was measured; i.e., we measured the so-called photodischarge characteristic. The equienergetical spectrum with an average photon flux density of 10^{13} cm^{-2} s^{-1} was

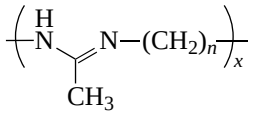

Ia_{10} (n = 10), Ia_6 (n = 6),

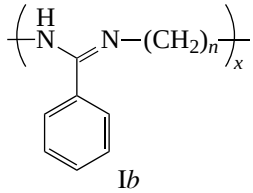

Ib

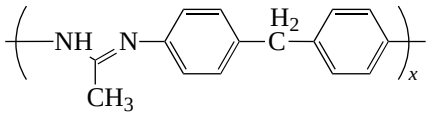

IIa

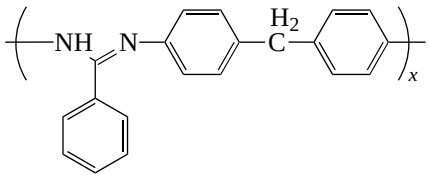

IIb

Fig. 2. Structures of polyamidines investigated.

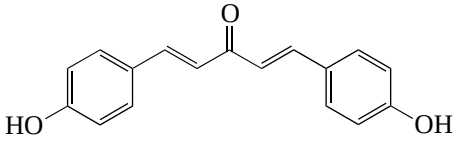

Fig. 3. Structure of the 1.5-di(4-oxyphenyl)penta-1.4-dien-3-OH doping impurity.

measured according to the procedure in [5, 6] in the spectral range of 400–900 nm for an electric-field strength $E = (0.2–1.0)E_0$. Here, E_0 is the limiting field strength for this material. The photodischarge characteristics $V(t)$ were measured at temperatures above and below the glass transition temperature of polymers T_{gl}. The temperature was monitored accurate to about 1% with the use of liquid-crystal indicators. The quantum yield of photogeneration was determined using the formula [5]

$$\eta = A\left(\frac{dV}{dt}\right)_{t=0}\frac{\varepsilon}{\alpha I\lambda d}, \quad (1)$$

where $\left(\frac{dV}{dt}\right)_{t=0}$ is the decay rate of the surface potential V of the layer at the instant of illumination at a wavelength λ and intensity I, α is the absorption coeffi-

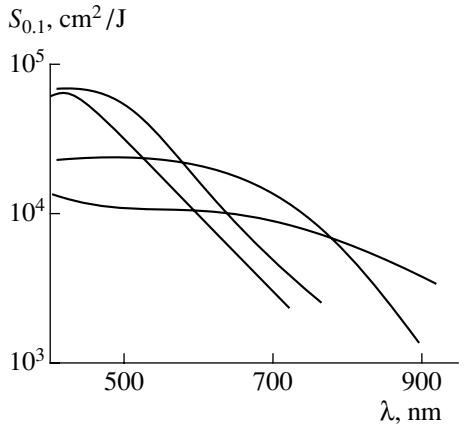

Fig. 4. Photosensitivity spectra of polyamidines.

cient, d is the layer thickness, and ε is the dielectric constant. The condition for the complete collection of carriers photogenerated in the polymer layer, which is necessary for the fulfillment of relationship (1), was monitored using the "photogeneration wedge" method [6], i.e., by measuring the field dependences of the quantum yield η/ε(V/d) for layers of various thicknesses in the range of 1–5 μm. The error in measuring the $S_{0.1}$ and η quantities was 10%.

The absorption spectra were measured using a Perkin-Elmer spectrophotometer in the spectral range of 400–1200 nm. The photosensitivity $S_{0.1}$ was determined from decay of the surface potential of the layer by 10% from the initial value ($dV/V = 0.1$) as a quantity inversely proportional to the exposure, which is necessary for attaining critical variation of the surface potential. The integral photosensitivity $S_{0.1}$ was determined from the same criterion ($\Delta V/V = 0.1$) upon exposure of the layers to the radiation of a KGM-150 halogen lamp with a power of 150 W.

Values of η/ε which are characteristic of the investigated polymers and are determined at temperatures above and below the glass transition temperature T_{gl}

Polymer* (T_{gl}, °C)	η/ε, 10^{-2}	
	$T < T_{gl}$	$T > T_{gl}$
Ia_{10}(60)	1.65	1.65
Ia_6(75)	1.41	1.41
Ib(95)	1.88	1.06
IIb(142)	2.12	0.35
IIa(158)	1.65	<0.01

Note: T_{gl} is the glass transition temperature.
* Negative charging of the layer to the limiting potential. The layer thickness is 1 μm.

4. RESULTS AND DISCUSSION

The investigation of the kinetics of the surface potential $V(t)$ before illumination of a layer at temperatures below the glass transition temperature showed that the relaxation rate of the surface potential in the absence of illumination is close to zero. This corresponds to low dark conductivity (dark resistance of the layer is about 10^9 Ω/□) for all polymers investigated.

Upon illuminating the samples, as can be seen from the photosensitivity spectra $S_{0.1}(\lambda)$ (Fig. 4), the magnitude of $S_{0.1}$ decreases monotonically, specifically, for the polymer Ia_{10}, from 2×10^4 to 3×10^3 cm^2/J, as λ increases from 400 to 950 nm.

Low-intensity long-wavelength peaks are observed in the electron absorption spectra of the films of the polyamidines investigated, for example, at 505–510 and 635–640 nm for Ia_{10}. These peaks are absent in the spectra of the ethanol solutions of the polymer. The emergence of these bands can be attributed to forbidden transitions in a quasi-conjugated system of hydrogen-bonded amidine groups (Fig. 1), whose existence in a solution of proton–donor solvent, specifically, ethanol, is impossible. This assumption is confirmed by calculations of the electron spectra of the trimer of an *N*,*N*'-dimethylacetamidine model compound using the ZINDO/S method, with optimization of the configuration using the STO-3G *ab initio* method. These calculations are indicative of the existence of a forbidden transition at 420 nm. The spectrum of the quantum yield of the carrier photogeneration η(λ) is characterized by a constant quantum yield, which is independent of λ in the visible spectral region, and its monotonical decrease at λ > 850 nm.

As can be seen from the data listed in the table, the η/ε quantity regularly increases at $T < T_{gl}$ in the series Ia_6–Ia_{10}–Ib–IIa–IIb. Such a variation in the photosensitive properties in the series of investigated polyamidines can be explained by the increasing degree of conjugation upon the introduction of the aryl substituents and the corresponding decrease in the ionization potential of the molecule and the electron work function. At temperatures above the glass transition temperature, the dielectric properties (ε) and photosensitivity ($S_{0.1}$) of the molecules of the Ia_{10} and Ib polymers remain virtually constant. However, for the IIb polymer, a relative decrease in η/ε by a factor of almost 2 is observed. As for the IIa polymer, the η/ε quantity decreases considerably by a factor of more than 10^2. These special features are apparently associated with a decrease in the basicity of the polymer in the series Ia_6–Ia_{10}–Ib–IIa–IIb, which leads to a weakening of the intermolecular hydrogen bonds and degradation of the supramolecular structure, which is responsible for the emergence of photoconductivity. The decrease in η/ε in the system Ia_{10}–1.5-di(4-oxyphenyl)penta-1.4-dien-3-OH by a factor of 1.7 also corroborates such an explanation for the observed features. In this case, the basicity of the dopant is sufficient for the protonation of the ami-

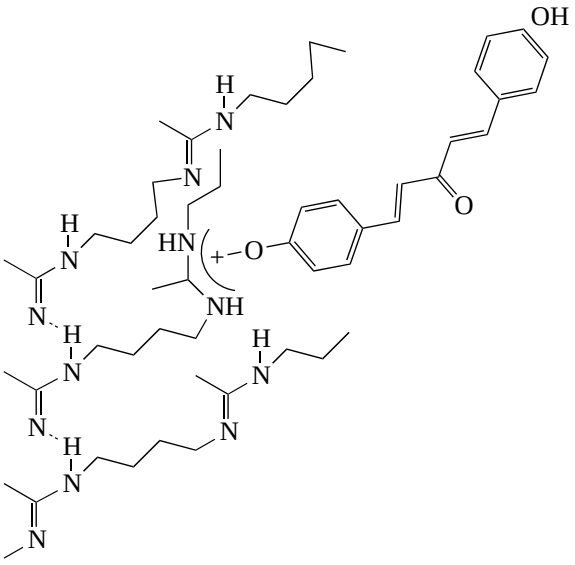

Fig. 5. Change of the supramolecular structure as a result of ionic doping.

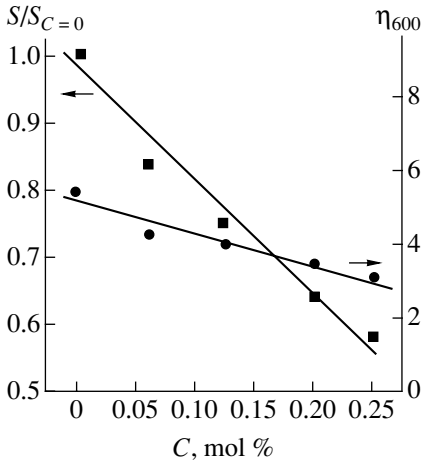

Fig. 6. Relative variation in the integrated photosensitivity for Ia_{10} polymer and quantum yields of photogeneration in relation to the concentration of the 1.5-di(4-oxyphenyl)penta-1.4-dien-3-OH dopant in the system.

dine groups of the polymer, which leads to the destruction of the system of hydrogen bonds and, consequently, quasi-conjugation in the supramolecular system (Fig. 5). The fact that a monotonic decrease in the photosensitivity is observed in the system as the relative dopant concentration increases also confirms the same inference (Fig. 6).

As can be seen from the data listed in the table, the quantum yield η/ε, as well as $S_{0.1}$, increase when going from aliphatic polyacetamidines to aromatic benzamidines. This is apparently the consequence of an increase in π-conjugation at temperatures below the glass transition temperature. However, at temperatures above the glass transition temperature, the η/ε quantity decreases sharply for the polymer samples which contain aromatic groups and remains practically constant for aliphatic polyamidines. We may assume that such behavior is associated with varying the system of hydrogen bonds and the transformation of linear structures (Fig. 1a), which are responsible for carrier transfer, into cyclic structures (Fig. 1b). The latter govern the photosensitivity of the system. This assumption is confirmed by the high (~10^4 cm^2/(V s) [8]) mobilities of charge carriers (holes) in polymer II*b*. This polymer contains dominant linear structures which are conductive to charge transport. The emergence of photoactive absorption in the long-wavelength region (at ~620 and 960 nm) for polymers I*a* and II*b*, which are capable of forming cyclic supramolecular structures, also confirms the above assumption.

Fullerene C_{60} is known to be an effective acceptor and can participate in complex formation [7]. The introduction of fullerene into the host polymers Ia_{10} and II*b* leads to a considerable (by a factor of 5) increase in dark conductivity and a decrease in the photosensitivity of these polymers by a factor of 2. Such behavior of the systems investigated is indicative of the preferentially donor character of polyamidine functional groups.

Indole is a typical donor molecule capable of complex formation. Its use as a dopant leads to an increase in the photosensitivity of the Ia_{10}–indole system by a factor of 5. However, the use of another dopant of this class, specifically anthracene, does not lead to variation in the photophysical properties. Such a distinction is apparently associated with the different character of interaction between the dopant molecules and a host polymer fragment. For additive anthracene, the absorption spectrum of the composite is the superposition of the spectra of polyamidine and anthracene. In contrast with this, a new absorption band at 400–800 nm emerges in the composite spectrum in the case of indole. This is indicative of the formation of a polymer–indole complex. The presence of NH groups, which can form hydrogen bonds with the functional groups of polymers, is apparently favorable for complex formation.

5. CONCLUSIONS

Thus, we may conclude that the suggested approach based on the formation of supramolecular structures that emerge due to an ordered system of hydrogen bonds between the functional groups of a polymer chain is an effective method for obtaining photoconducting media, specifically, polyamidine media, with a rather high photosensitivity ($\gtrsim 10^4$ cm^2/J). In combination with high carrier mobilities, as well as low glass transition temperatures, elastic modulus, and a high melt viscosity, this allows us to assume that such systems are promising for the development of transport

layers of electrophotographic devices and thermoplastic materials for information carriers.

ACKNOWLEDGMENTS

This study was supported by the Russian Foundation for Basic Research, project no. 01-03-32294.

REFERENCES

1. J.-M. Lehn, *Supramolecular Chemistry: Concepts and Perspectives* (VCH, Weinheim, 1995; Nauka, Novosibirsk, 1998).
2. F. Boehme, C. Klinger, H. Komber, *et al.*, J. Polym. Sci. **36**, 929 (1997).
3. A. V. Tenkovtsev, A. V. Yakimansky, M. M. Dudkina, *et al.*, Macromolecules **34**, 7100 (2001).
4. A. V. Ten'kovtsev, M. M. Dudkina, A. E. Trofimov, *et al.*, Zh. Prikl. Khim. (St. Petersburg) **74**, 1147 (2001).
5. I. A. Akimov, Yu. A. Cherkasov, and M. I. Cherkashin, *Sensitized Photoelectric Effect* (Nauka, Moscow, 1980).
6. E. L. Aleksandrova and Yu. A. Cherkasov, Opt. Spektrosk. **64**, 1047 (1988) [Opt. Spectrosc. **64**, 624 (1988)].
7. E. L. Aleksandrova, N. V. Kamanina, Yu. A. Cherkasov, *et al.*, Opt. Zh. **65** (8), 87 (1998) [J. Opt. Technol. **65**, 676 (1998)].
8. E. L. Aleksandrova, L. P. Kazakova, M. M. Dudkina, and A. V. Ten'kovtsev, in *Proceedings of III International Conference on Amorphous and Microcrystalline Semiconductor Classes* (St. Petersburg, 2002).

Translated by N. Korovin

Semiconductors, Vol. 37, No. 3, 2003, pp. 271–275. Translated from Fizika i Tekhnika Poluprovodnikov, Vol. 37, No. 3, 2003, pp. 287–291.

ELECTRONIC AND OPTICAL PROPERTIES OF SEMICONDUCTORS

Thermal Transport of Charge and Polarization of 1.2-eV Luminescence Broad Band in Uniaxially Strained *n*-GaAs:Te

A. A. Gutkin and M. A. Reshchikov

Ioffe Physicotechnical Institute, Russian Academy of Sciences, Politekhnicheskaya ul. 26, St. Petersburg, 194021 Russia

Submitted July 9, 2002; accepted for publication July 22, 2002

Abstract—The effect of temperature on the pressure-induced polarization of the photoluminescence broad band related to $V_{Ga}Te_{As}$ complexes in GaAs:Te is analyzed. It is shown that, within a certain temperature range, the pressure-induced difference in the activation energy of thermal emission of holes for dissimilarly oriented complexes leads to an abrupt increase in the integral polarization of radiation caused by recombination of free electrons with holes localized at these complexes compared to polarization at lower temperatures. In the samples subjected to 10-kbar pressure applied along the [111] axis, the described behavior of polarization was observed in the temperature range from 140 to 190 K. The results obtained validate the previously suggested model of a set of defects that give rise to the luminescence band under study. Fitting results of calculations to experimental data enabled us to correct the values of a number of the parameters of defects and to estimate a pressure-induced change in the activation energy of the thermal emission of holes from the defects with different orientation. © *2003 MAIK "Nauka/Interperiodica".*

1. INTRODUCTION

An external uniaxial strain in a semiconductor crystal violates the equivalence of similar-type anisotropic centers that are differently oriented with respect to the strain axis and shifts, by different values, the corresponding energy levels in the band gap. For centers with broad luminescence bands, such splitting of levels only slightly affects the emission spectrum but leads to an appreciable variation in the activation energy of the thermal emission from differently oriented centers. Thus, with an increase in temperature, the rate of thermal emission of carriers localized at the emitting centers, at first, becomes comparable with the rate of radiative capture of the opposite-sign carriers (and exceeds it) only for the centers with a certain orientation with respect to the strain axis. At a low level of luminescence excitation, the thermal emission of carriers from these centers is accompanied by their repeated capture by centers with any orientation with equal probability; therefore, in steady-state conditions, most emitting centers have an orientation corresponding to the highest activation energy of thermal emission of the carriers captured by these centers. Such transfer of charge carriers between the centers with a different orientation with respect to the strain axis results in their partial or complete removal from the luminescent recombination process and in the growth of the integral polarization of luminescence with temperature in a certain range due to the appearance of a prevalent orientation of recombination centers and an increase in the number of centers with this orientation.

A phenomenological theory of this phenomenon is suggested for the class of centers similar to the complexes responsible for the broad luminescence band with a peak at 1.2 eV in *n*-GaAs:Te [1–3]. In order to obtain further support for the model suggested in [3] and to correct a number of parameters of the model, we measured the dependences of the integral polarization of this band on temperature (up to $T \approx 215$ K) and pressure applied along the [111] direction (up to $P = 10$ kbar) and compared them to the results of calculation.

2. MODEL USED IN CALCULATIONS AND BASIC RELATIONS

As was shown in [3], the low-temperature ($T \lesssim 78$ K) behavior of the 1.2-eV photoluminescence (PL) band in *n*-GaAs:Te induced by either band-to-band excitation under uniaxial pressure or polarized resonant excitation can be explained by assuming that the emission is caused by two types of anisotropic centers with close spectral characteristics and optical dipole parameters. Defects of the first type are apparently isolated complexes composed of a gallium vacancy and tellurium $V_{Ga}Te_{As}$ characterized by Jahn–Teller distortions, which can change their orientation and align under uniaxial pressures applied in a certain direction; in contrast, the defects of the other type are devoid of such capability. As was determined in [3], the emitting optical dipole in each of the defects is oriented so that its axis is close to one of the ⟨111⟩ axes. For the sake of simplicity, splitting of the energy levels for differently oriented centers will be considered under the assump-

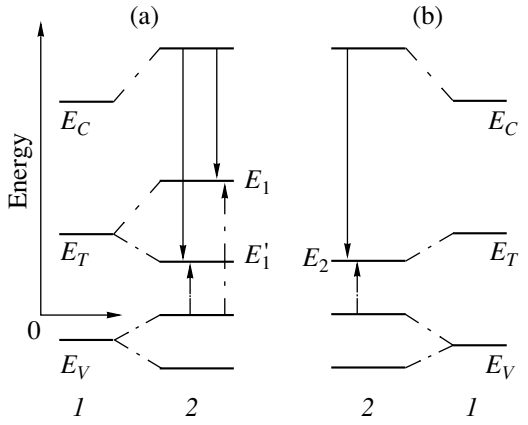

Fig. 1. Energy levels of $V_{Ga}Te_{As}$ (E_T) and the band gap boundaries (E_C and E_V) (*1*) in the absence of pressure and (*2*) under the uniaxial pressure along [111] axis (E_1, E_1', and E_2). The initial axis of complex and the direction of pressure are (a) not parallel and (b) parallel.

tion that the dipole axis is aligned with one of the trigonal axes of the crystal. In $V_{Ga}Te_{As}$ complexes, this axis does not coincide with the initial V_{Ga}–Te_{As} axis.

Let us first consider the integral polarization of radiation caused by recombination via the defects with reorienting and aligning distortions ($V_{Ga}Te_{As}$ complexes). When pressure is applied along the [111] axis, the complexes whose optical dipole has a different orientation with respect to the strain axis introduce different energy levels and the set of equivalent complexes separates into two groups, in one of which the initial V_{Ga}–Te_{As} axis does not coincide with the direction of pressure and, in the other, is parallel to it. In the first group, the complexes with configurations corresponding to different directions of the optical dipole have dissimilar energies, whereas the complexes of the second group remain equivalent even under pressure. Changes induced in the energy levels of complexes in reference to the allowed-band edges in these two cases are shown in Fig. 1.

In the first group of complexes, with pressure along the [111] axis, the binding energy of a hole is highest for the configuration with the optical dipole axis close to the direction of pressure [3]. We denote the activation energy of the thermal emission of holes from centers with this configuration by E_1, the activation energy for other configurations in the first group of complexes by E_1', and the corresponding energy for complexes of the second group by E_2 (Fig. 1).

Let us assume that, similar to the case with the absence of pressure, the capture cross sections of electrons and holes by the $V_{Ga}Te_{As}$ complex are independent of the orientation of defects and the direction of distortion and consider a system of defects in a stationary state characterized by a constant rate of electron–hole pair generation in a semiconductor strained along the [111] axis.

According to the conclusions drawn in [4], the distortion of a certain center may change its direction only when the center is in the absorbing state; i.e., the direction of the optical dipole axis in the emitting center is defined by the direction of this dipole in the absorbing state. Let N_1, N_1', and N_2 designate the total concentrations of defects, which, in the emitting state, are characterized by energies E_1, E_1', and E_2. The concentrations of these defects in the emitting state (the state when a hole is localized at a defect) is denoted by p_1, p_1', and p_2, respectively. It can be readily shown that, in low-excitation conditions ($p_1 \ll N_1$, $p_1' \ll N_1'$, and $p_2 \ll N_2$),

$$p_1' = p_1 \frac{1 + C_p N_V \tau \exp(-E_1/kT)}{1 + C_p N_V \tau \exp(-E_1'/kT)} \frac{N_1'}{N_1} \equiv p_1 B \frac{N_1'}{N_1}, \quad (1)$$

$$p_2 = p_1 \frac{1 + C_p N_V \tau \exp(-E_1/kT)}{1 + C_p N_V \tau \exp(-E_2/kT)} \frac{N_2}{N_1} \equiv p_1 B' \frac{N_1'}{N_1}. \quad (2)$$

Here, C_p is the hole capture coefficient, N_V is the effective density of states in the valence band under uniaxial pressure, τ is the characteristic time of recombination of the trapped holes with the conduction electrons, T is the temperature, and k is the Boltzmann constant.

Since the orientation of the dipole is close to the pressure axis for only one of three possible configurations of a first-group complex, we have

$$\frac{N_1'}{N_1} = 2\exp(-\Delta E'/kT) \equiv C, \quad (3)$$

where $\Delta E'$ is the energy difference for various configurations of the first-group complexes under [111] uniaxial pressure in the state that admits their reorientation and alignment. As was mentioned above, this state implies the capture of an electron [4]; therefore, $\Delta E'$ may differ from $E_1 - E_1'$. However, when there is a uniform distribution of complexes over the possible orientations of their initial axis (V_{Ga}–Te_{As}), we have

$$\frac{N_2}{N_1} = \frac{1 + 2\exp(-\Delta E'/kT)}{3} \equiv D. \quad (4)$$

In *n*-GaAs, the PL band associated with the considered defects stems from the radiative capture of electrons by the centers with a previously trapped hole. Thus, the integrated intensity of radiation I_{PL} is proportional to the total concentration of such centers, i.e., in the steady state,

$$I_{PL} \propto (p_1 + p_1' + p_2). \quad (5)$$

Note that centers with energy E_1 and various (but those permissible for this energy) orientations of the optical dipole axis equally contribute to p_1. A similar situation

takes place for the centers contributing to p_1' and p_2. Under these conditions, summing the intensities of radiation from the dipoles of different orientation and taking into account different concentrations p_1, p_1', and p_2 defined by (1)–(4), we can readily obtain the integrated intensity of light emitted within the studied band in the direction perpendicular to the pressure axis [111] with the electric field vector parallel $I_{PL}(\|)$ or perpendicular $I_{PL}(\perp)$ to this axis.

In order to reduce the number of parameters involved in the description of the system, we assume that

$$E_1' = E_2, \tag{6}$$

i.e., $B' = B$. This assumption is based on the fact that the orientation of optical dipoles of E_1' and E_2 centers is close to the ⟨111⟩ directions, which do not coincide with the [111] pressure direction; hence, the dipole and the pressure axes make nearly the same angle for the considered centers. Let A denote the fraction of centers with reorientable distortions in the total concentration of centers (N) contributing to the photoluminescence band; then,

$$I_{PL}(\|) \propto \frac{AN}{1 + B(4C+1)/3}\left\{\mu_2 + \frac{(2b+a)^2}{3}(1-2\mu_2) + CB\left[\mu_2 + \frac{a^2}{3}(1-2\mu_2)\right] + DB\left[\mu_2 + \frac{(2b-a)^2}{3}(1-2\mu_2)\right]\right\}, \tag{7}$$

$$I_{PL}(\perp) \propto \frac{AN}{1 + B(4C+1)/3}\left\{\mu_2 + \frac{(b-a)^2}{3}(1-2\mu_2) + CB\left[\mu_2 + \frac{1+b^2}{3}(1-2\mu_2)\right] + DB\left[\mu_2 + \frac{(b+a)^2}{3}(1-2\mu_2)\right]\right\}. \tag{8}$$

Here, μ_2 is the rotator fraction in a single-center emission and a and b are the components of a unit vector of the dipole axis along the axes of a local Cartesian coordinate system, which are aligned with the ⟨100⟩ directions and are governed by the orientation of the center so that

$$a = \sin\varphi, \quad b = \frac{\sqrt{2}}{2}\cos\varphi, \tag{9}$$

where φ is the angle of deviation of the emitting dipole axis from the [110] axis in the $(\bar{1}10)$ plane containing the dipole axis, the vacancy, and the tellurium atom.

We can now derive the corresponding intensities $I_{PL}^*(\|)$ and $I_{PL}^*(\perp)$ of light emitted by complexes that are not capable of reorienting or aligning distortions. On the assumption that these complexes feature nearly the same parameters of their optical dipoles and energy levels as those for the defects with reorientation of distortions [3], expressions (1) and (2) are also valid for them. However, in this case,

$$\frac{N_1'}{N_1} = 2, \quad \frac{N_2}{N_1} = 1. \tag{10}$$

Therefore, $I_{PL}^*(\|)$ and $I_{PL}^*(\perp)$ can be obtained from expressions (7) and (8) by substituting $1 - A$ for A, 2 for C, and 1 for D. The integral polarization ratio r_{111}^* includes contributions of both centers with and without reorientation in the form

$$r_{111}^* = \frac{I_{PL}(\|) + I_{PL}^*(\|)}{I_{PL}(\perp) + I_{PL}^*(\perp)}. \tag{11}$$

3. RESULTS AND DISCUSSION

The objects under study were *n*-GaAs:Te samples with an electron concentration of ~10^{18} cm^{-3}, similar to those studied in [3–6]. The photoluminescence spectrum under uniaxial strain was measured by a technique previously used [7, 8].

The resulting PL spectra of the considered 1.2-eV band under a pressure of $P = 10$ kbar applied along the [111] axis at different temperatures are shown in Fig. 2. The temperature dependence of the integral polarization ratio r_{111}^* at this pressure is shown in Fig. 3.

As the temperature increases starting from 2 K, the integral polarization induced by 10-kbar pressure along the [111] axis, at first, remains constant and then slightly decreases to $T \approx 130$ K. The latter decrease stems from a lower degree of alignment of distortions in Jahn–Teller centers ($V_{Ga}Te_{As}$ complexes) due to the appearance of configurations with an energy E_j'. A further increase in temperature in the range from 140 to 180 K leads to an abrupt increase in polarization (Fig. 3). However, the corresponding spectra of emission broaden only slightly in this temperature interval as a result of broadening of the long-wavelength edge (Fig. 2).

The pronounced increase in polarization of the studied band at temperatures above 140 K may be related to the redistribution, considered in Section 2, of the stationary concentration of holes at the centers that are differently oriented with respect to the pressure axis, i.e., to the thermal transfer of holes between the centers. In

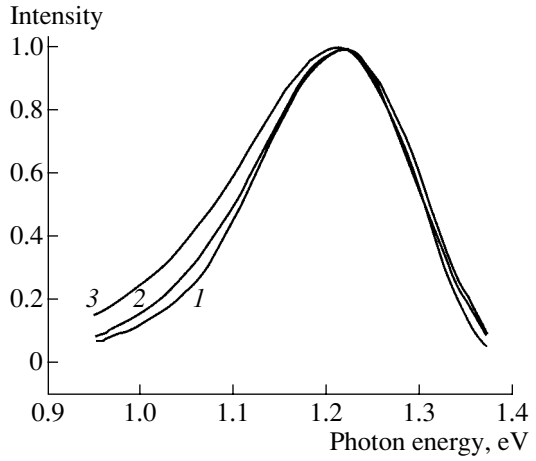

Fig. 2. The 1.2-eV band in *n*-GaAs:Te under a pressure P = 10 kbar along the [111] axis at (*1*) 78, (*2*) 135, and (*3*) 168 K.

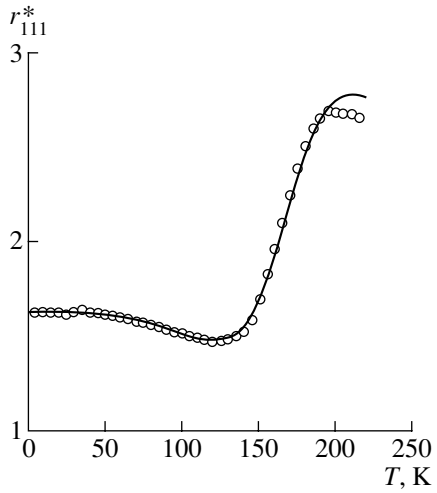

Fig. 3. Temperature dependence of the integral polarization ratio for the 1.2-eV band in *n*-GaAs:Te at 10-kbar pressure along the [111] axis. Circles represent experimental data; solid curve corresponds to the result of calculation at E_1 = 183 meV, E_2 = 150 meV, $\Delta E'$ = 25 meV, A = 0.4, μ_2 = 0.142, and $C_pN_V\tau = 7 \times 10^4$.

order to check the validity of the model of centers described in the previous section, we approximate the experimental dependences $r^*_{111}(T)$ by the curves calculated using formulas (7)–(11). We assume that, according to [3], $\varphi = 28°40'$ in (9) and choose the value of $C_pN_V\tau$ involved in the expressions for B (1) and (2) from the following considerations. In the absence of uniaxial pressure, $C_pN_V\tau$ for the studied defects is approximately 4×10^5 [6]. Since the 10-kbar pressure applied along the [111] axis results in an appreciable splitting of the valence-band top in GaAs and noticeably reduces the energy of light holes as compared to that of heavy ones [9], the effective density-of-state mass at a pressure of 10 kbar for the band involved in the thermal emission of holes from the studied defects decreases and approaches the mass of a light hole. Recalling that the ratio between the density-of-state masses for heavy and light holes in GaAs approximately equal 6, the value 4×10^5 in our case should be six times lower than that obtained in [6]. Thus, we assumed that $C_pN_V\tau = 7 \times 10^4$ for our calculations.

Furthermore, we take into account the fact that, at low temperatures (T = 2–30 K), no thermal transfer of holes occurs and no configurations with the energy E_1' can be realized in Jahn–Teller complexes at a pressure of 10 kbar. With respect to these circumstances, the integral polarization of the studied band $r^*_{111}(0)$ is governed only by the values μ_2 and A via the relationship [3]

$$A = \frac{r^*_{111}(0) - 1}{r^*_{111}(0) + 2} \frac{1}{(a+b)b} \frac{1 + \mu_2}{1 - 2\mu_2}. \qquad (12)$$

With a given $r^*_{111}(0)$ (Fig. 3), an arbitrary choice of μ_2 also defines the value of A.

Thus, it can be seen from expressions (1)–(4) and (7)–(12) that the description of the experimental dependence $r^*_{111}(T)$ in the range from 2 to 215 K requires specifying the following four parameters: μ_2, E_1, E_2, and $\Delta E'$. In particular, the value $\Delta E'$ is responsible for the low-temperature portion of the dependence $r^*_{111}(T)$ up to its abrupt increase, i.e., at $T \lesssim 120$ K (Fig. 3); the temperature of the increase is defined by E_2; and the largest polarization attained at high temperatures mainly depends on μ_2 and the ratio of E_1 to E_2.

Satisfactory agreement between the experimental and calculated dependences, similar to that presented in Fig. 3, was obtained for $\Delta E'$ = 25 meV, μ_2 = 0.14–0.20 (A = 0.4–0.5), E_1 = 183–190 meV, and E_2 = 150–146 meV. The values of $\Delta E'$, μ_2, and A correlate well with the results previously determined in other experiments [3, 5].

Energy splitting for centers with a different orientation relative to the pressure axis $E_1 - E_2$ ranges from 33 to 44 meV at P = 10 kbar and can be compared to the changes in the PL spectra at the same pressure and a temperature of 2 K. The large width of the band precludes direct observation of the pressure-induced splitting of its components. However, the experimental spectra of emission with an electric-field vector parallel and perpendicular to the [111] pressure axis are shifted with respect to each other by (34 ± 2) meV at P = 10 kbar. In terms of the model of nearly trigonal complexes considered in Section 2, this value represents the lower limit of splitting for two components corresponding to different orientations of a complex with respect to the pressure axis and is consistent with the value $E_1 - E_2$ given above. At the same time, if the bands corresponding to each of the polarizations are resolved into two components, whose amplitudes relate to each other in

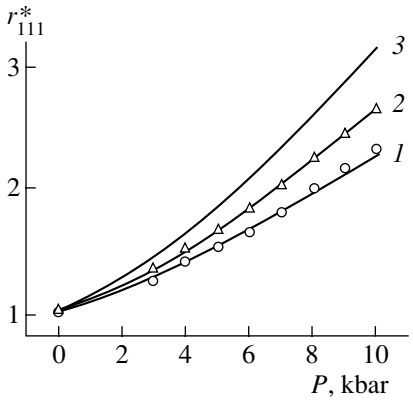

Fig. 4. Integral polarization ratio of 1.2-eV band in *n*-GaAs:Te as a function of pressure along the [111] axis. Circles correspond to experimental data points at (*1*) 173 and (*2*) 193 K. Curves show the results of calculation for (*1*) 173 and (*2*, *3*) 193 K. For $E_1(P)$ and $E_2(P)$ values, see text. $C_pN_V\tau$ is assumed to be equal to (*1*, *2*) 7×10^4 and (*3*) 4×10^5. Other parameters are the same as in Fig. 3.

terms of μ_2 and A, using the expressions known for trigonal centers and if the shape repeats that of the band in the absence of pressure [10], the resulting splitting turns out to be ~38 meV and $\mu_2 = 0.15$. These values are in good agreement with the data obtained above from fitting the calculated curve to the dependence $r^*_{111}(T)$.[1]

Expressions (7)–(11) may also be used to calculate the dependence $r^*_{111}(P)$ at a constant temperature. In this context, one may assume that, in the absence of pressure, $E_1 = E_2 = 170$ meV [6] and, as pressure increases, E_1 and E_2 increase linearly with P [9] and attain the above-mentioned values at $P = 10$ kbar; i.e., for $E_1(10\ \text{kbar}) = 183$ meV and $E_2(10\ \text{kbar}) = 150$ meV, $E_1(P) = (170 + 1.3P[\text{kbar}])$ meV and $E_2(P) = (170 - 2P[\text{kbar}])$ meV. In the strict sense, an increase in pressure from 0 to 10 kbar is accompanied by a change in $C_pN_V\tau$ from 4×10^5 at $p = 0$ to 7×10^4 at high pressures. However, at small P, when $C_pN_V\tau$ is far from the values corresponding to the mass of a light hole, the energy splitting for centers with different orientation is insignificant and the polarization induced by this energy difference is small. This is the reason why the deviation of $C_pN_V\tau$ from 7×10^4 introduces only a small error in r^*_{111}, which is confirmed by the calculations (Fig. 4). At higher pressures ($P \gtrsim 4$ kbar), the experimental data points are satisfactorily approximated by the curves calculated using expressions (7)–(11) at $C_pN_V\tau = 7 \times 10^4$ (Fig. 4). The same agreement was also obtained for other possible values of the parameters.

[1] The agreement between the experimental and calculated curves illustrated in Fig. 3 might also be achieved at $0 \le \mu_2 \le 0.14$. However, this would imply $E_1 - E_2 \le 30$ meV, which contradicts the data obtained in other experiments.

4. CONCLUSIONS

Our experimental results demonstrate that the model suggested in [3] for a set of reorientable and nonreorientable centers with close optical parameters and an emitting optical dipole oriented nearly along the ⟨111⟩ crystallographic direction adequately explains the polarization properties of the photoluminescence band associated with these centers both at low and comparatively high (up to 215 K) temperatures. The quantitative analysis of the influence of temperature on a change in the integral polarization of radiation in this band under uniaxial pressure enabled more accurate determination of the parameters of these centers and estimation of a change in the activation energy of the thermal emission of holes from the emitting centers with different orientation of the optical dipole under a uniaxial pressure applied along the [111] axis.

REFERENCES

1. E. W. Williams and H. B. Bebb, in *Semiconductors and Semimetals*, Ed. by R. K. Willardson and A. C. Beer (Academic, New York, 1972), Vol. 8, p. 321.
2. H. G. Guislain, L. De Wolf, and P. Clauws, J. Electron. Mater. **7**, 83 (1978).
3. A. A. Gutkin, M. A. Reshchikov, and V. E. Sedov, Fiz. Tekh. Poluprovodn. (St. Petersburg) **34**, 1201 (2000) [Semiconductors **34**, 1151 (2000)].
4. A. A. Gutkin, M. A. Reshchikov, and V. E. Sedov, Z. Phys. Chem. (Munich) **200**, 217 (1997).
5. N. S. Averkiev, A. A. Gutkin, and M. A. Reshchikov, Fiz. Tekh. Poluprovodn. (St. Petersburg) **33**, 1323 (1999) [Semiconductors **33**, 1196 (1999)].
6. A. A. Gutkin, M. A. Reshchikov, and V. E. Sedov, Fiz. Tekh. Poluprovodn. (St. Petersburg) **31**, 1062 (1997) [Semiconductors **31**, 908 (1997)].
7. A. A. Gutkin, M. A. Reshchikov, and V. R. Sosnovskiĭ, Fiz. Tekh. Poluprovodn. (St. Petersburg) **27**, 1516 (1993) [Semiconductors **27**, 838 (1993)].
8. N. S. Averkiev, A. A. Gutkin, E. B. Osipov, *et al.*, Fiz. Tekh. Poluprovodn. (Leningrad) **25**, 58 (1991) [Sov. Phys. Semicond. **25**, 33 (1991)].
9. R. N. Bhargava and M. I. Nathan, Phys. Rev. **161**, 695 (1967).
10. A. A. Gutkin and A. V. Ermakova, in *Proceedings of International Conference on Optics, Optoelectronics, and Technologies, Ul'yanovsk, 2002* (Ul'yan. Gos. Univ., Ul'yanovsk, 2002), p. 22.

Translated by A. Sidorova

Semiconductors, Vol. 37, No. 3, 2003, pp. 276–282. Translated from Fizika i Tekhnika Poluprovodnikov, Vol. 37, No. 3, 2003, pp. 292–298.

ELECTRONIC AND OPTICAL PROPERTIES OF SEMICONDUCTORS

Thermoelectric Figure of Merit in Solid Solutions with Phonon Scattering by Off-Center Impurities

E. A. Gurieva*, P. P. Konstantinov*, L. V. Prokof'eva*, Yu. I. Ravich, and M. I. Fedorov***

** Ioffe Physicotechnical Institute, Russian Academy of Sciences, St. Petersburg, 194021 Russia*

*** St. Petersburg State Technical University, St. Petersburg, 195251 Russia*

Submitted July 23, 2002; accepted for publication September 6, 2002

Abstract—The Seebeck coefficient and the electrical and thermal conductivities (S, σ, and κ) of ternary $PbTe_{1-x}Se_x$ ($x = 0.1$ and 0.3) and quaternary $PbTe_{1-2x}Se_xS_x$ ($x = 0.025$, 0.05, 0.1, and 0.15) solid solutions have been studied. Polycrystalline samples with an electron density of $(0.5–5.0) \times 10^{18}$ cm^{-3} were used; their quality was monitored by comparing the measured and calculated mobility values at 85 K. A considerable decrease in mobility and an anomalous trend in the $\sigma(T)$ curve near 77 K were revealed in quaternary alloys with $x \gtrsim 0.1$; for $x = 0.15$, unusual behavior of $\kappa(T)$ was also found. According to estimates, the lattice thermal conductivity of this material is temperature-independent in the 80- to 300-K temperature range. This means that a reduction in phonon–phonon scattering with an increase in temperature is completely compensated by an increase in the scattering on impurities. The observed anomalies of $\sigma(T)$ and $\kappa(T)$ are considered assuming the possible of off-center location of sulfur atoms at the lattice sites. The thermoelectric figure of merit Z of the studied alloys has been determined in the range 80–300 K. In spite of decreasing mobility, the maximum Z was obtained in a quaternary compound with $x = 0.1$: at 300 K, $Z_{max} = 2 \times 10^{-3}$ K^{-1} with a carrier density of $\sim 3 \times 10^{18}$ cm^{-3}; at 175 K, $Z_{max} = 1.5 \times 10^{-3}$ K^{-1} with the density decreasing to 5×10^{17} cm^{-3}. The obtained data indicate that the introduction of off-center impurities rises Z at $T \lesssim 300$ K. © *2003 MAIK "Nauka/Interperiodica".*

Currently, ever increasing attention is being drawn to the development of thermoelectric devices for cooling below room temperature. To a large extent, progress in this area is determined by the properties of thermoelectric materials used in these devices.

According to the relation between the dimensionless thermoelectric figure of merit ZT, which determines refrigeration efficiency and the thermoelectric material parameters

$$ZT \propto \text{const}(m/m_0)^{3/2}\mu\kappa_L^{-1}T^{5/2},$$

a decrease in the operating temperature directly reduces ZT. Therefore, to make this dependence weaker, it is necessary to create, in the material, conditions for a sufficiently steep rise of the mobility μ and a weak decrease of the lattice thermal resistivity ($1/\kappa_L$) with decreasing temperature. Conventionally, solid solutions are used for this purpose. This was indeed a way to considerably improve the thermoelectric characteristics of the Bi_2Te_3 compound. The development of highly efficient thermoelectric materials based on the ternary solid solutions $(BiSb)_2Te_3$ and $Bi_2(TeSe)_3$ allowed for the deriving and wide spread of thermoelectric coolers for the room-temperature range. A current problem consists in defining the trends in the variation of solid solution compositions, which is necessary in order to provide high Z in the low-temperature range. The material must have a low carrier density and be characterized by optimum scattering of electrons and phonons on impurities.

We present the study of some general trends that are important in the search for efficient low-temperature materials. As the object of study, solid solutions based on n-PbTe were chosen in view of the following reasons. The cermet technology is successfully used in the fabrication of these materials for thermoelectric applications; it provides for the reliable and reproducible fabrication of homogeneous polycrystalline samples with a prescribed composition and doping level with optimum thermoelectric properties. Wide-range variation of the carrier density is possible, including the low-doping range, which is the working range in the case in question. The electrical and thermal properties of PbTe and its alloys are well understood [1–4]; this simplifies monitoring of sample quality and analysis of the obtained data.

Ternary and quaternary solid solutions, $PbTe_{1-x}Se_x$ with $x = 0.1$ and 0.3, and $PbTe_{1-2x}Se_xS_x$ with $x = 0.025$, 0.05, 0.1, and 0.15, have been studied. The first system was one of the first objects that demonstrated the efficient application of solid solutions for raising the thermoelectric figure of merit in semiconductors at room temperature. The maximum thermoelectric figure of merit obtained in these alloys at 300 K was $Z = 1.9 \times 10^{-3}$ K^{-1} for $x = 0.3$ [5]; for $x = 0.1$, the value was some-

Table 1. The parameters of samples at $T = 85$ K

Sample no.*	Composition	n, 10^{18} cm^{-3}	μ	μ_{imp}	μ_{calcd}	μ_{calcd}/μ
			cm^2 V^{-1} s^{-1}			
1	PbTe	0.5	20125	–	–	–
2	$PbTe_{0.95}Se_{0.025}S_{0.025}$	0.5	16250	82000	16210	1.0
3	$PbTe_{0.9}Se_{0.05}S_{0.05}$	0.5	14000	40680	13480	0.96
4	$PbTe_{0.8}Se_{0.1}S_{0.1}$	0.63	7540	18100	9670	1.28
5	$PbTe_{0.70}Se_{0.15}S_{0.15}$	0.5	5000	13000	7850	1.57
6	$PbTe_{0.9}Se_{0.1}$	0.55	17270	47760	14230	0.82
7	$PbTe_{0.7}Se_{0.3}$	0.61	9530	14760	8620	0.90
8	$PbTe_{0.9}Se_{0.05}S_{0.05}$	2.0	8820	21700	10520	1.19
9	$PbTe_{0.9}Se_{0.05}S_{0.05}$	5.0	7500	13170	7170	0.96
10	$PbTe_{0.8}Se_{0.1}S_{0.1}$	2.0	5230	10630	7000	1.34
11	$PbTe_{0.8}Se_{0.1}S_{0.1}$	3.3	3750	8180	5640	1.5
12	$PbTe_{0.9}Se_{0.1}$	1.4	12500	31570	12780	1.02
13	$PbTe_{0.9}S_{0.1}$	0.49	9180	–	–	–
14	$PbTe_{0.8}Se_{0.1}S_{0.1}$	0.45	7360	–	–	–
15	$PbTe_{0.8}Se_{0.1}S_{0.1}$	3.8	3450	–	–	–
16	$PbTe_{0.8}Se_{0.1}S_{0.1}$	6.8	2920	–	–	–
17	$PbTe_{0.8}Se_{0.1}S_{0.1}$	16	1920	–	–	–
18	$PbTe_{0.8}Se_{0.1}S_{0.1}$	34	1000	–	–	–
19	$PbTe_{0.8}Se_{0.1}S_{0.1}$	52	820	–	–	–

Note: Sample numbers in the table correspond to curve numbers in figures.

what lower. The intriguing feature of the second system of solid solutions is that the effect of Se and S impurities on the phonon scattering in a multicomponent material does not conform to the additivity rule [6]. The lattice thermal resistivity appears to be higher than the half-sum of the lattice thermal resistivities of the corresponding ternary compounds with an impurity concentration equal to their total concentration in the quaternary solid solution. The aim of the present study is to reveal the correlations between Z values in ternary alloys with a varying composition at $T < 300$ K, to determine to what extent the nonadditivity of the impurity thermal resistivity affects the thermoelectric figure of merit of a multicomponent solid solution and, correspondingly, to evaluate the prospects of applying multicomponent solid solutions in coolers.

An optimum electron density of about 5×10^{17} cm^{-3}, which provides the highest Z value in these materials at $T < 300$ K, was obtained by introducing a slight excess of Pb. Higher electron densities were created by introducing Cl. The Seebeck coefficient and the electrical and thermal conductivity were measured in the temperature range of 77–300 K. The parameters of samples at 85 K are listed in Table 1. To verify that the electron mobility was no lower than the values typical for the materials under study, we calculated the mobility determined by scattering on neutral impurity centers, using the data [2], and determined the calculated total mobility on the assumption that the phonon-limited mobility in alloys equals the mobility in PbTe produced by the same technology. It was assumed that the electron scattering on isoelectronic substitution impurities occurs via interaction with the short-range potential of impurity atoms and that the interaction coefficient defined previously for a single composition of a solid solution [2] retains its value in other compounds of this system. This value was 9.5×10^{-35} erg cm^{-3} for $PbTe_{1-x}Se_x$ and 10.5×10^{-35} erg cm^{-3} for $PbTe_{1-2x}Se_xS_x$. The calculated electron mobilities listed in Table 1 correlate fairly well with the experimental data for the majority of solid solutions. The largest difference (about 1.3–1.5 times) is observed for quaternary solid solutions with $x \gtrsim 0.1$, whose electrical conductivity increases as the temperature decreases much more slowly than in other materials (Fig. 1), and its absolute value is considerably reduced when the overall impurity content reaches 20 at. % or more. To confirm that this result is not an anomaly, but reflects the inherent properties of these materials, we studied the temperature dependence of the electrical conductivity for an additional set of samples with $x = 0.1$ and an electron density in the range of 4.5×10^{17}–5×10^{19} cm^{-3}. These results (Fig. 2) clearly indicate a special feature—a region of rising resistivity when the temperature decreases in the range of about

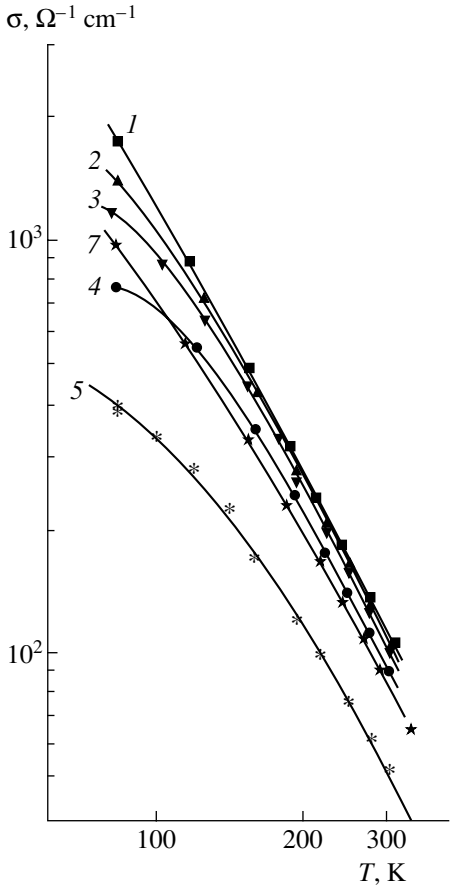

Fig. 1. Temperature dependences of the electrical conductivity of solid solutions of various composition (see Table 1) with an electron density of $\sim 5 \times 10^{17}$ cm^{-3}.

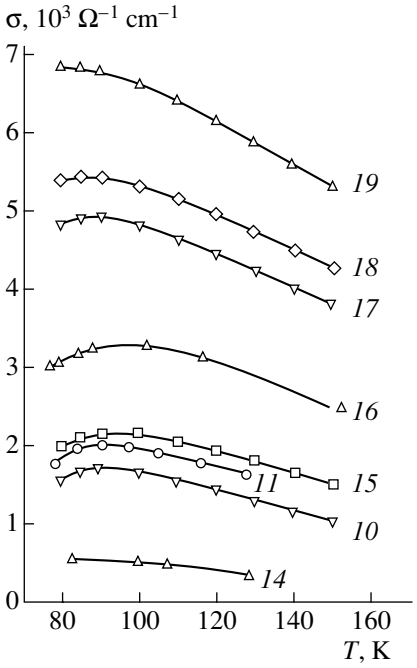

Fig. 2. Temperature dependences of the electrical conductivity of the $PbTe_{0.8}Se_{0.1}S_{0.1}$ solid solution with an electron density of 4.5×10^{17}–5.2×10^{19} cm^{-3} (see Table 1).

77 K. This feature vanishes as the electron density increases, and it was not observed in the sample with the highest density, at least in the studied temperature range. In the sample with the lowest electron density, this feature could be expected at temperatures below 77 K. Though this special feature is not large, it does exceed the possible experimental error.

Different mechanisms can define the increase in conductivity as the temperature rises. When the concentration of Se and S scattering centers is about 20 at. %, the approximation in which scattering on the short-range potential of each impurity atom is considered independently should presumably be replaced by the concept of electron scattering on a random potential profile. A random profile with a characteristic magnitude of about 0.03 eV was used to account for an increase and maximum of the $\sigma(T)$ function of PbTe doped with 12–20 at. % In, with an electron density on the order of 10^{18} cm^{-3} [7, 8]. However, in the $PbTe_{0.8}Se_{0.1}S_{0.1}$ solid solution, $\sigma(T)$ increases in a wide range of carrier densities (see Fig. 2) corresponding to a chemical potential variation from 0.03 eV to about 0.15 eV [1, 9]. At such a high chemical potential, the increase in electron energy with temperature is only slight and the cause for the electron scattering by the potential profile becoming less pronounced upon heating is eliminated.

Furthermore, the effect in question is not observed in solid solutions containing only Se, though the Se content may rise up to 30 at. %. Therefore, the rise of $\sigma(T)$ is associated with some specific property of the S impurity which is not shared by Se. The ionic radius of sulfur is much smaller than that of Se, or especially Te, whose lattice sites they occupy. The relatively small size of S ions may lead to the off-center position of this impurity with respect to the lattice sites at low temperatures. There are several alternative off-center positions for impurities, with possible tunneling between them. As a result, tunneling states are formed with closely spaced energy levels [10–12]. These tunneling states have specific properties; in particular, they scatter carriers similarly to impurities responsible for the Kondo effect [13–16]. In the Kondo effect, the resistivity increases logarithmically as the temperature decreases.

Another effect related to the off-center position of an impurity is the formation of a random dipole structure [17]. The random dipole structure can provoke even stronger low-temperature carrier scattering than the Kondo effect. Thus, the off-center position of S atoms can qualitatively account for the observed portion of a rise in electrical conductivity as a function of temperature in $PbTe_{1-2x}Se_xS_x$ solid solutions at high x.

We now return to the obtained experimental data. Figures 1 and 3–5 show the temperature dependences of the electrical and thermal conductivity and the See-

beck coefficient of solid solutions and *n*-PbTe, and also the thermoelectric figure of merit *Z*, calculated from the experimental data. Since the electron densities in samples of different compositions with the lowest level of doping are close and the effective masses do not differ significantly [18], the scatter in the Seebeck coefficient is no more than 10% (curves *1–7* in Fig. 3). Quantitative differences in the electrical and thermal conductivity of these samples are due to different isoelectronic impurities and somewhat different electron densities. For the lowest-density compositions under discussion, the *Z* values at 300 K are close (with the exception of a quaternary solid solution with $x = 0.15$) and greatly exceed the corresponding *Z* value for PbTe (dashed curves in Fig. 5). With temperature decreasing, a distinct dependence on the alloy composition appears in the behavior of *Z*. Comparison of the experimental data in the temperature range under study allows us to make several conclusions. In the $PbTe_{1-x}Se_x$ system, the optimum composition changes: the composition with $x = 0.3$ is no longer the best. This is due to the fact that the effect of impurities on mobility increases strongly as the temperature decreases. In the solid solution with $x = 0.3$, this effect becomes too strong for the observed change in the lattice thermal conductivity; therefore, the maximum in the composition dependence of the μ/κ_L ratio shifts to lower *x*. For this reason, a smaller addition of Se is more efficient, but it does not provide the best result either. The maximum benefit in *Z* was obtained in a quaternary system for the compounds with 5–10 at. % Se and S; at 175 K, $Z_{max} = 1.5 \times 10^{-3}$ K^{-1}. The thermoelectric figure of merit of the $PbTe_{0.7}Se_{0.15}S_{0.15}$ solid solution at 300 K is considerably lower; this is associated with the above-mentioned stronger reduction in mobility. However, owing to the fact that the thermal conductivity of this material increases only slightly as the temperature decreases and then decreases somewhat (Fig. 4), the value of *Z* rises considerably and its value at the maximum does not differ from those values for the other materials under study. This is the first time the above-described variation of the thermal conductivity with temperature in these materials has been observed. Estimates of the lattice thermal resistivity at 85 and 300 K, which have a sufficiently high accuracy owing to the small contribution of electrons to the total thermal conductivity of the material, indicate that its value in these materials remains virtually invariable at 133 cm K W^{-1}. At the same time, the corresponding value for PbTe at 85 K is an order of magnitude lower.

Thus, the contribution of additional thermal resistivity associated with the introduction of impurities is very large in this material. The additional phonon scattering in solid solutions with a high sulfur content may be due to the resonance interaction of phonons with the excitations related to the possible off-center positioning of S atoms. This scattering is similar to that observed in glasses. Generalization of the above-mentioned idea of tunneling states has lead to the concept of soft atomic potentials [19], from which follows the existence of tunneling states, along with other types of localized excitations. In contrast to tunneling systems, the transitions between potential wells in relaxation systems occur via thermal activation, rather than via tunneling.

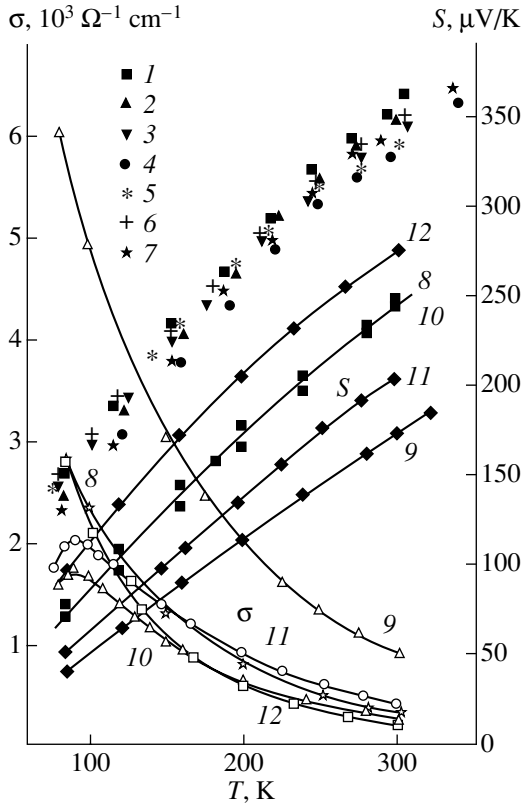

Fig. 3. Temperature dependences of the electrical conductivity and the Seebeck coefficient of $PbTe_{1-x}Se_x$ and $PbTe_{1-2x}Se_xS_x$ solid solutions at different electron densities (see Table 1).

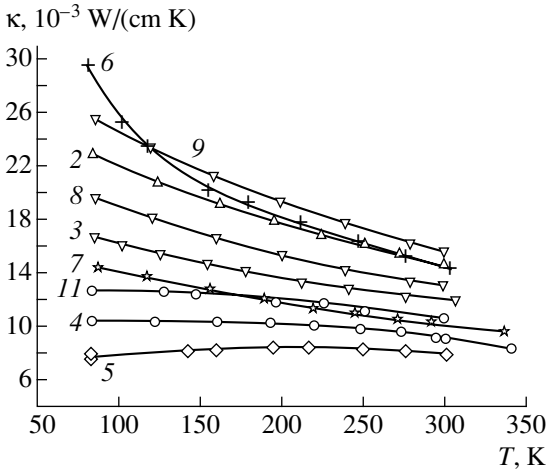

Fig. 4. Temperature dependences of the thermal conductivity of solid solutions with different compositions (see Table 1).

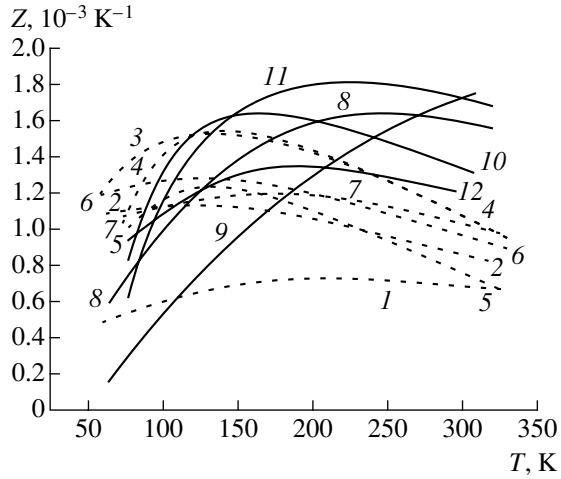

Fig. 5. The thermoelectric figure of merit of $PbTe_{1-x}Se_x$ and $PbTe_{1-2x}Se_xS_x$ solid solutions with different electron densities (see Table 1).

Quasi-local low-frequency oscillators become important at higher excitation energies.

The interaction of heat-carrying phonons with the listed systems results in a rise in thermal conductivity as the temperature increases, which can be compensated for by its decrease due to standard phonon–phonon scattering. Experimental studies of the thermal conductivity of glasses [20] and mixed crystals with off-center impurities based on potassium halides [21] have revealed a plateau in the temperature dependence at ~10 K; in a partially crystallized opal matrix, the plateau extends from 50 to 230 K [22], which is comparable with that observed in our study.

Therefore, the Kondo-like maximum in the temperature dependence of the electrical conductivity and especially the specific behavior of the heat conductivity with temperature may have the same origin, specifically, the off-center position of sulfur atoms (in more exact terms, the soft potentials characterizing the states of S atoms).

To obtain additional information about the variation of the thermoelectric figure of merit with composition at $T < 300$ K, we studied samples with a higher electron density. Figures 3 and 4 present data on the thermoelectric properties of solid solutions of various compositions with an electron density of $(1–5) \times 10^{18}$ cm^{-3}; the corresponding $Z(T)$ curves are shown in Fig. 5. These data indicate unambiguously that the optimum composition for the low-temperature range is the quaternary compound with $x = 0.1$, in spite of the much stronger decrease in mobility mentioned above. At room temperature, the maximum value of Z in this material is as high as 2×10^{-3} K^{-1} at an electron density of $\sim 3 \times 10^{18}$ cm^{-3}. In a multicomponent solid solution with $x = 0.05$, the absolute value of Z_{max} is lower but the $Z_{max}(T)$ dependence has a much gentler slope in the low-temperature range, because the specific low-temperature electron scattering is not observed in this material.

The reason for high Z_{max} values in the multicomponent alloy with $x = 0.1$ is the high value of the additional lattice thermal resistivity related to the phonon scattering on off-center impurities. At room temperature, the impurity thermal resistivity is 59 cm K W^{-1}, while the phonon component is 50 cm K W^{-1}; at 85 K, the impurity resistivity increases even more (90 cm K W^{-1}) owing to the enhanced additional scattering of phonons. This compensates for the decrease in the phonon–phonon scattering (W_{ph} falls to ~13 cm K W^{-1}) and maintains a rather high value of the overall lattice thermal resistivity in this material, compared with that in the ternary alloys.

The additional increase in the thermal resistivity, related to the introduction of off-center impurities, is also inherent to other systems of PbTe-based solid solutions, in particular, to the multicomponent Pb(Sn)Te(Se) system [23]. Nevertheless, there is no real prospect of obtaining the higher thermoelectric figure of merit in this material at low temperature, because the phonon scattering on tin impurity atoms is weaker than that on sulfur [4]. Therefore, to strongly suppress the lattice thermal conductivity in Pb(Sn)Te(Se) alloys, it is necessary to introduce additional components at high concentrations. However, since this reduces the band gap and, correspondingly, the effective electron mass, any significant increase in Z cannot be achieved. The experimental study of the thermoelectric characteristics of $(PbTe)_{1-x}(SnSe)_x$ with $x = 0.1$ and 0.15 at room temperature confirms this suggestion. Table 2 compares the parameters of these alloys with quaternary $PbTe_{1-2x}Se_xS_x$ ($x = 0.1$) for a fixed value of the Seebeck coefficient. Indeed, the band gap and, correspondingly,

Table 2

Sample no.	Composition	S, μV K^{-1}	n, 10^{18} cm^{-3}	μ, cm^2 V^{-1} s^{-1}	κ	κ_L	μ/κ_L	Z, 10^{-3} K^{-1}
					10^{-3} W cm^{-1} K^{-1}			
20	$(PbTe)_{0.9}(SnSe)_{0.1}$	–155	5.0	1425	17.3	11.5	1.53	1.58
21	$(PbTe)_{0.85}(SnSe)_{0.15}$	–157	4.6	126	14.7	9.9	1.64	1.56
22	$PbTe_{0.8}Se_{0.1}S_{0.1}$	–155	5.8	950	12.3	8.0	1.47	1.65

the effective mass in the first two alloys are lower than those in the sulfur-containing solid solution, because the concentrations are lower and the electron mobilities are higher. Nevertheless, the rise in mobility does not considerably improve the ratio μ/κ_L (with respect to the μ/κ_L value in PbTe), because the lattice thermal conductivity in these materials is higher than that in the solid solution with Se and S. In this situation, Z does not exceed the Z value in the $PbTe_{0.8}Se_{0.1}S_{0.1}$ solid solution at all, due to a decreasing effective electron mass. As concerns the additional lattice thermal resistivity upon doping with Sn and Se, the obtained data indicate that this effect, in contrast to the data of [23], is considerably weaker than the effect related to Se and S. This is presumably due to a higher probability of the off-center positioning for sulfur atoms, compared with that for tin, at low temperature. It is not by chance that a rise in the lattice thermal resistivity with decreasing temperature was observed in ternary $PbTe_{1-z}S_z$ but was not observed in ternary alloys with tin [4]. It is necessary to note that ternary $PbTe_{1-z}S_z$ solid solutions are of no interest as objects for raising the thermoelectric figure of merit; the negative factors are a very low solubility of PbS in PbTe [24] and a strong decrease in mobility. For example, the total lattice thermal resistivity of $PbTe_{0.9}S_{0.1}$ (sample 13, Table 1) with an electron density of $\sim 5 \times 10^{17}$ cm^{-3}, on the one hand, and of the quaternary solid solution $PbTe_{0.9}Se_{0.05}S_{0.05}$, on the other hand, demonstrates virtually the same value and temperature behavior, but the electron mobility in the first material is considerably lower. Therefore, Z does not exceed 1.2×10^{-3} K^{-1} in the range 80–300 K.

The results obtained concerning the increasing thermoelectric figure of merit in multicomponent alloys with an off-center impurity might be of interest for deriving efficient low-temperature thermoelectric materials based on $Bi(Sb)_2Te(Se)_3$. It had generally been assumed until now that, even if the effect of different impurities on the phonon scattering in these materials does deviate from the additivity rule, the deviation is toward weaker phonon scattering in a solid solution with two different impurities. This conclusion was based on the study of the thermal conductivity in these materials with various compositions in the range 77–300 K [25]. It is worth noting, however, that comparison of the lattice thermal resistivity in ternary and quaternary solid solutions was performed at different values of the total concentration of impurity atoms. Since the dependence of the lattice thermal conductivity on the impurity concentration becomes sublinear in this range of compositions, the thermal resistivity of a quaternary lattice, calculated under the assumption of additivity of impurity effects, was always higher than the experimentally observed value. Accurate treatment of the experimental data yields results similar to those obtained for PbTe-based solid solutions. Therefore, the low-temperature study of the thermoelectric figure of merit in multicomponent solid solutions based on bismuth and antimony chalcogenides and, in particular, the conventional n-type $Bi_2(TeSe)_3$ solid solution moderately doped with sulfur should attract further attention.

ACKNOWLEDGMENTS

This study was supported by the program “Integration” (project no. 75).

REFERENCES

1. Yu. I. Ravich, B. A. Efimova, and I. A. Smirnov, *Semiconducting Lead Chalcogenides* (Nauka, Moscow, 1968; Plenum, New York, 1970).
2. E. A. Gurieva, B. A. Efimova, and Yu. I. Ravich, Fiz. Tekh. Poluprovodn. (Leningrad) **8**, 1261 (1974) [Sov. Phys. Semicond. **8**, 819 (1974)].
3. G. T. Alekseeva, B. A. Efimova, L. M. Ostrovskaya, and M. I. Tsypin, Fiz. Tekh. Poluprovodn. (Leningrad) **4**, 1322 (1970) [Sov. Phys. Semicond. **4**, 1122 (1971)].
4. G. T. Alekseeva, B. A. Efimova, and Yu. A. Logachev, Fiz. Tekh. Poluprovodn. (Leningrad) **9**, 128 (1975) [Sov. Phys. Semicond. **9**, 83 (1975)].
5. T. S. Stavitskaya, Candidate’s Dissertation (Leningrad, 1968), p. 19.
6. G. T. Alekseeva, B. A. Efimova, L. V. Prokof’eva, and L. S. Stil’bans, Izv. Akad. Nauk SSSR, Neorg. Mater. **3**, 320 (1967).
7. S. N. Lykov, Yu. I. Ravich, and I. A. Chernik, Fiz. Tekh. Poluprovodn. (Leningrad) **11**, 1731 (1977) [Sov. Phys. Semicond. **11**, 1016 (1977)].
8. Yu. I. Ravich and S. A. Nemov, Fiz. Tekh. Poluprovodn. (St. Petersburg) **36**, 3 (2002) [Semiconductors **36**, 1 (2002)].
9. I. N. Dubrovskaya and Yu. I. Ravich, Fiz. Tekh. Poluprovodn. (Leningrad) **8**, 1455 (1966).
10. P. W. Anderson, B. I. Halperin, and C. M. Varma, Philos. Mag. **25**, 1 (1972).
11. W. A. Phillips, J. Low Temp. Phys. **7**, 351 (1972).
12. R. W. Cochran, R. Harris, J. O. Strom-Olson, and M. J. Zuckermann, Phys. Rev. Lett. **35**, 676 (1975).
13. Kh. A. Abdullin, V. N. Demin, and A. I. Lebedev, Fiz. Tverd. Tela (Leningrad) **28**, 1020 (1986) [Sov. Phys. Solid State **28**, 570 (1986)].
14. A. I. Dmitriev, G. V. Lashkarev, V. I. Litvinov, *et al.*, Pis’ma Zh. Éksp. Teor. Fiz. **45**, 304 (1986) [JETP Lett. **45**, 383 (1986)].
15. A. I. Dmitrieva, V. I. Lazorenko, and G. V. Lashkarev, Fiz. Tverd. Tela (Leningrad) **31**, 272 (1989) [Sov. Phys. Solid State **31**, 1255 (1989)].
16. S. Katayama, S. Maekawa, and H. Fukuyama, J. Phys. Soc. Jpn. **56**, 697 (1987).
17. A. I. Lebedev and I. A. Sluchinskaya, Pis’ma Zh. Éksp. Teor. Fiz. **46**, 425 (1987) [JETP Lett. **46**, 536 (1987)].

18. E. A. Gurieva, B. A. Efimova, Yu. I. Ravich, and L. V. Buzyleva, Fiz. Tekh. Poluprovodn. (Leningrad) **5**, 1715 (1971) [Sov. Phys. Semicond. **5**, 1499 (1971)].
19. D. A. Parshin, Fiz. Tverd. Tela (St. Petersburg) **36**, 1809 (1994) [Phys. Solid State **36**, 991 (1994)].
20. R. C. Zeller and R. O. Pohl, Phys. Rev. B **4**, 2029 (1971).
21. F. C. Bauman, J. P. Harrison, W. D. Seward, and R. O. Pohl, Phys. Rev. **159**, 691 (1967).
22. V. N. Bogomolov, N. F. Kartenko, L. S. Parfen'eva, *et al.*, Fiz. Tverd. Tela (St. Petersburg) **41**, 348 (1999) [Phys. Solid State **41**, 313 (1999)].
23. G. A. Alekseeva and Yu. A. Logachev, Izv. Akad. Nauk SSSR, Neorg. Mater. **17**, 172 (1981).
24. N. Kh. Abrikosov and L. E. Shelimova, *Semiconducting Materials Based on IV–VI Compounds* (Nauka, Moscow, 1976), p. 137.
25. E. A. Gurieva, V. A. Kutasov, and I. A. Smirnov, Fiz. Tverd. Tela (Leningrad) **6**, 2453 (1964) [Sov. Phys. Solid State **6**, 1945 (1964)].

Translated by D. Mashovets

Semiconductors, Vol. 37, No. 3, 2003, pp. 283–287. Translated from Fizika i Tekhnika Poluprovodnikov, Vol. 37, No. 3, 2003, pp. 299–303.

ELECTRONIC AND OPTICAL PROPERTIES OF SEMICONDUCTORS

Effect of Annealing in Zn Vapor and Liquid Zn on Photoluminescence of High-Purity Polycrystalline ZnTe

V. S. Bagaev*, V. V. Zaĭtsev, Yu. V. Klevkov, V. S. Krivobok, and E. E. Onishchenko

Lebedev Physical Institute, Russian Academy of Sciences, Moscow, 119991 Russia

** e-mail:bagaev@sci.lebedev.ru*

Submitted July 24, 2002; accepted for publication September 6, 2002

Abstract—The photoluminescence from high-purity polycrystalline ZnTe has been studied. The evolution of the emission spectra upon annealing in Zn is analyzed. The effect of impurity aggregation is observed in the initial samples. This effect gives rise to an undulatory spectrum on the long-wavelength wing of the line associated with emission from an acceptor-bound exciton. It is demonstrated that annealing leads to homogenization of the impurity distribution, which results in the appearance of a rich structure of two-hole transitions. An analysis of these lines yields the energies of the ground and excited states of Li and Cu acceptor impurities. © *2003 MAIK "Nauka/Interperiodica".*

1. INTRODUCTION

ZnTe is a promising material for modern optoelectronics. Owing to its wide band gap (2.26 eV at room temperature), it is, in particular, widely used as a barrier material in designing various low-dimensional structures (quantum dots, quantum wells, superlattices) on the basis of II–VI semiconductor compounds [1, 2], which are of both scientific and practical interest. Among practical applications of the bulk material, mention should be made of recent first reports on the development of ZnTe light-emitting diodes with reproducible parameters for the green spectral range [3]. It is noteworthy that in this study, as in many other investigations, ZnTe was grown from melt. As is known, the composition of the thus-obtained material deviates from stoichiometry, and a rather labor-consuming procedure has to be carried out in order to eliminate this disadvantage. In contrast to [3], our study is concerned with pure polycrystalline ZnTe prepared using techniques for the synthesis, sublimation purification, and growth at crystallization temperatures below 700°C; these techniques were developed at our laboratory. The technology we employed yields polycrystals with a nearly stoichiometric composition and with a lower concentration of intrinsic point defects compared with the concentration of residual impurities. In addition to containing a small number of point defects (intrinsic and impurity-related), the polycrystals we studied were characterized by a rather large size (up to several millimeters) of their grains, in which the dislocation density did not exceed 10^3 cm^{-2}. It was precisely due to these factors which resulted in the samples being characterized by a high quantum efficiency of photoluminescence (PL) at low temperature, which is associated both with intrinsic emission and with optical transitions of varied nature related to residual impurities. Our study of the emission spectra of polycrystalline samples immediately after their growth and upon annealing in Zn revealed quite a number of interesting features, which we will describe in the present communication.

2. EXPERIMENTAL

Polycrystalline ZnTe samples, 25 mm in diameter, textured in the [111] direction, and having an average grain size of 1.5–2.0 mm, were produced by the method of free growth from the vapor phase at a temperature of ~600°C in a dynamic vacuum. The starting stock comprised purified ZnTe with a composition brought as close as possible to stoichiometry (the $P_{\min}$ point in the P–x section of the phase diagram at ~600°C). Two polycrystalline blocks were prepared from a disk by means of cleavage. One of the blocks was annealed in saturated Zn vapor at ~700°C for 70 h, and the other, in liquid Zn at the same temperature for 95 h. All PL measurements were done on freshly cleaved surfaces. The main type of extended defects in the samples studied were grain boundaries and twins. The dislocation density did not exceed 10^3 cm^{-2}.

PL spectra were mainly measured at a temperature of $T = 5$ K under optical excitation by a 20-mW He–Cd laser (emission wavelength $\lambda = 441.6$ nm) with its beam focused at a spot 300 μm in diameter. The spectra were analyzed using a DFS-24 double monochromator with a resolution no worse than 0.1 meV. The signal from the photomultiplier was recorded in the photon counting mode.

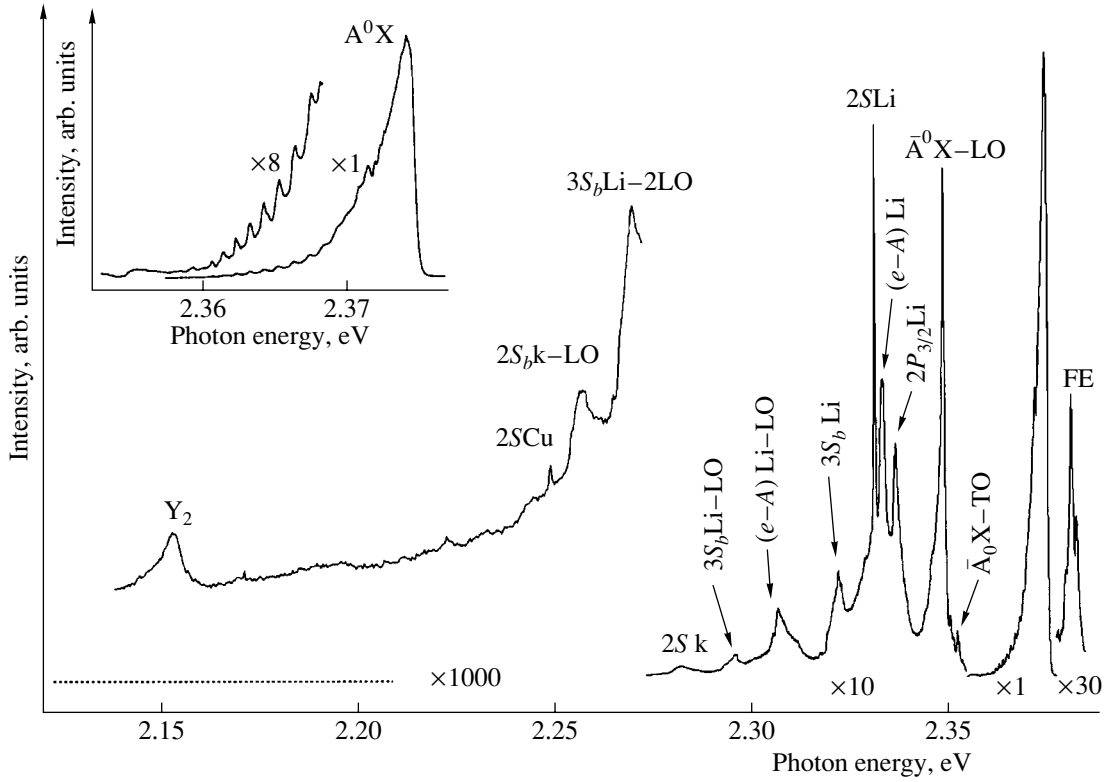

Fig. 1. Emission spectrum of the initial polycrystal measured at $T = 5$ K. Insert: fragment of spectrum with undulations in the region of the $\bar{A}^0$ X line.

3. RESULTS AND DISCUSSION

The PL spectrum of the initial sample (Fig. 1) is, on the whole, similar, with respect to the set of lines observed, to the emission spectrum of a high-quality single crystal with a low impurity content. This is indicated by the presence in the spectra of the near-bandgap emission associated with free excitons (FE), the occurrence of two-hole transitions related to only three substitutional acceptors (Li, Cu, and an unidentified *k*-acceptor [4]), and the lack of emission from vacancy–impurity complexes [5]. Now, we will specify the designations adopted in the present communication for the identification of various lines. In the first place, this deals with the emission from neutral-acceptor-bound excitons. An optical transition, in which a hole on the acceptor remains after annihilation of a bound exciton in the ground state of the impurity, corresponds to the brightest line, commonly designated as A^0X. In sufficiently perfect crystals, so-called two-hole transitions (THT) appear at relatively low impurity concentrations. In these transitions, after annihilation of a bound exciton, the hole remains on the acceptor in one of the excited states of the impurity. The common designation for THT lines is FA, where A corresponds to an impurity on which the transition occurs, and F, to the state of the hole after exciton recombination. The classification of these states is performed in conformity with theoretical studies [6, 7]. As shown below, analysis of THT lines yields the energies of both the ground and the excited states of an acceptor.

Let us now discuss some features observed in the spectrum shown in Fig. 1. First of all, we should note the unusual shape of the line designated as $\bar{A}^0$ X, whose peak position coincides with the positions of the A^0X lines for Li and Cu acceptors [4]. It would be expected that, since the impurity concentration in our samples did not exceed 10^{15} cm^{-3} according to mass-spectrometric data, the A^0X emission line must be narrow (with a linewidth less than 1 meV) and symmetric (the possible splitting of A^0X, caused by the so-called *J–J* coupling [4], is not discussed here). However, it can be seen from Fig. 1 that $\bar{A}^0$ X is rather strongly broadened and has an asymmetric profile with a "tail" in the long-wavelength part. In addition, an undulatory structure appears on the long-wavelength wing of the $\bar{A}^0$ X line. Effects of this kind are commonly observed in doped crystals with an impurity concentration of ~10^{17} cm^{-3}. For the sample studied here, characterized by a low content of residual impurities, these effects apparently result from impurity aggregation in local regions of the crystal. Additional evidence in favor of this assumption is that a forbidden transition involving the excitation of

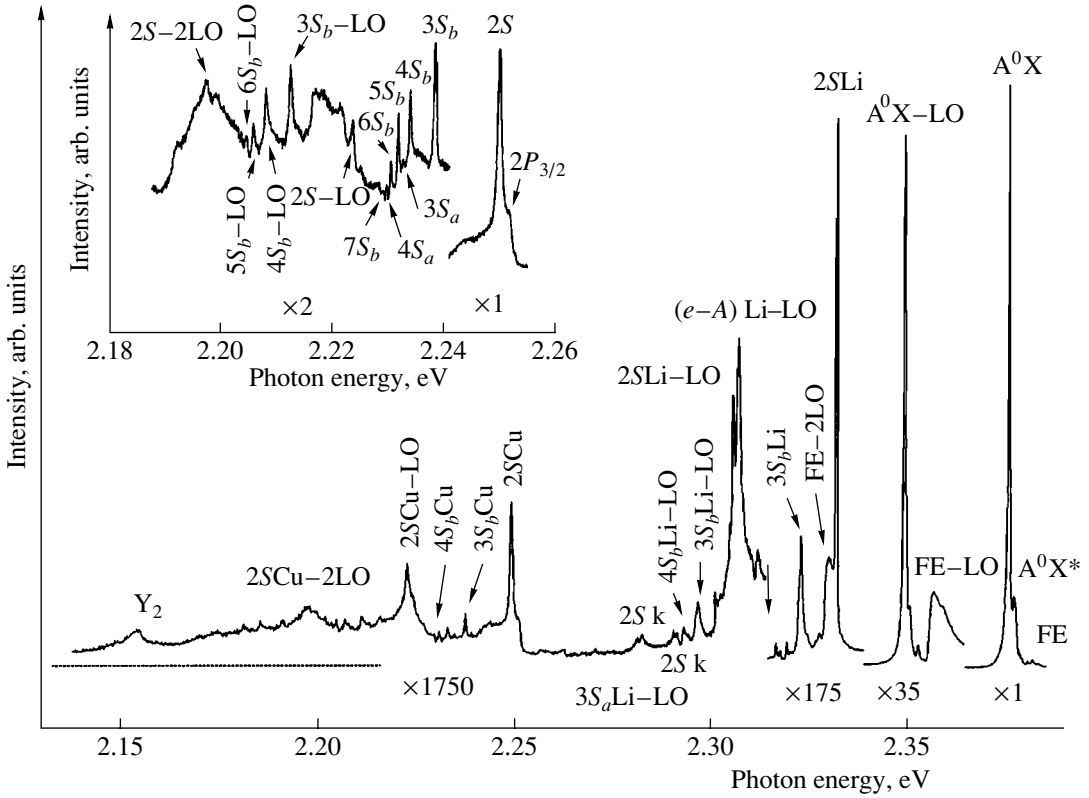

Fig. 2. Emission spectrum of a polycrystal annealed in Zn vapor and measured at $T = 5$ K. Insert: fragment of spectrum in the range of THT transitions on Cu.

a hole to the $2P_{3/2}$ state is seen in the spectrum of THT for Li impurity.

Let us consider in more detail the undulatory structure in the long-wavelength part of $\bar{A}^0$ X (Fig. 1, insert). There is currently no common concept concerning the nature of undulations in ZnTe. According to one viewpoint, the undulatory structure is due to fluctuations of closely spaced pairs of acceptors as the distance between them changes [8]. Another viewpoint posits that the appearance of undulations is due to the transfer of a bound exciton between neutral acceptors, which is accompanied by emission of an acoustic phonon [9]. The second viewpoint is supported by the lack of undulations in transmission spectra. It is noteworthy that undulations are not seen in the spectrum even at $T > 20$ K.

The spectra of a sample annealed in Zn vapor are shown in Fig. 2. It can be seen that annealing leads to homogenization of the spatial distribution of impurities. This is confirmed by the appearance of a much richer structure associated with THT transitions for both Li and Cu, and by the disappearance of the forbidden $2P_{3/2}$Li transition associated with impurity aggregation in unannealed samples. The insert of Fig. 2 shows a fragment of the spectrum with THT transitions on Cu, which was obtained with an order-of-magnitude longer accumulation time.

Annealing of polycrystals in liquid Zn leads to a strongly different transformation of the PL spectrum of the initial samples (see Fig. 3). First, the THT lines associated with Cu completely disappear, which may be due to segregation of Cu. Second, the intensity of emission related to near-bandgap transitions markedly increases, with the structure shown in the insert of Fig. 3 appearing in the emission spectra near the bottom of the excitonic band. This structure can only be accounted for in terms of the polariton model. This is indicated by the presence in the spectrum of lines associated with emission corresponding to upper (X_U) and lower (X_L) polariton branches, which were previously observed in ZnTe crystals [10]. In addition, one more line, X_M, is observed between X_U and X_L. Its appearance may be due to the presence of a third polariton branch [11], whose existence is due to the fact that, as in all crystals with a zinc-blende structure and cubic symmetry, the two upper valence subbands are degenerate at the point Γ ($k = 0$). It is also noteworthy that a D^0X line, associated with emission from a donor-bound exciton, appears in the PL spectrum.

The rich structure of THT transitions, which appears upon annealing, enables analysis of the acceptor states of Li and Cu impurities (the brightest lines are shown in

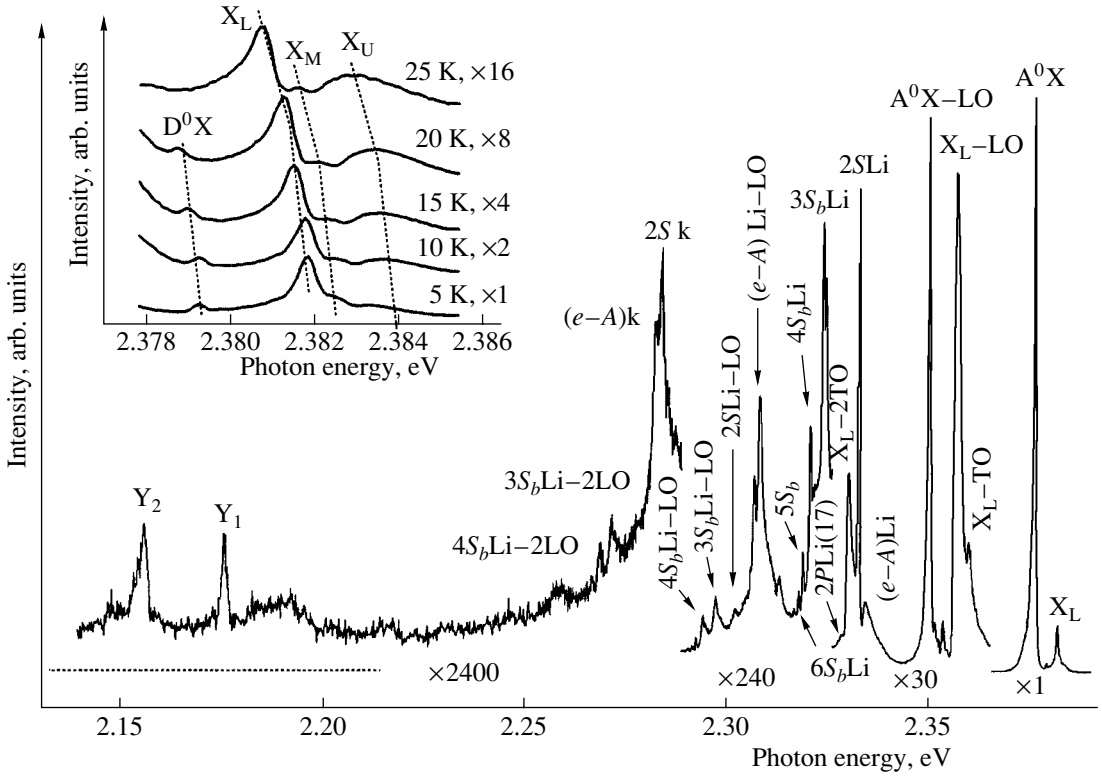

Fig. 3. Emission spectrum of a polycrystal annealed in liquid Zn and measured at T = 5 K. Insert: spectra exhibiting a polariton structure of emission at the bottom of the excitonic band.

the spectra). It is noteworthy that, because of the degeneration of the valence band in ZnTe, the acceptor states are not hydrogen-like. For example, at $n \geq 3$, the acceptor states allowed in THT transitions are represented by the following linear combinations: $nS_{3/2b} = \alpha_n S + \beta_n D$, and $nS_{3/2a} = \alpha_n S - \beta_n D$, where n is the principal quantum number, and S, D are hydrogen functions [6, 7] (the index 3/2, representing the total momentum of a state, is dropped in the spectra for the sake of brevity). The results obtained in our analysis of the acceptor states on the basis of the positions of the THT lines, performed according to the method described in [4], are listed in the table together with the results of recent theoretical calculations. It is noteworthy that the THT lines $6S_b$Cu, $4S_a$Cu, $3S_a$Li, and $7S_b$Li are observed for the first time. The asterisked experimental values in the table were taken from [4]. The THT line $2P_{5/2}(\Gamma_8)$Li is close in position to a brighter line, which is an 2LO replica of the free-exciton line, and, therefore, its position cannot be determined adequately.

Experimental and theoretical [6, 7] energies of the ground and excited states for Li and Cu acceptors

State	Li		Cu	
	experiment	theory	experiment	theory
$1S_{3/2}$	60.5	60.7	148	142.8
$2P_{3/2}$	21.7	23.5	23.8	23.5
$2S_{3/2}$	17.0	17.6	22.1	23.7
$2P_{3/2}(\Gamma_8)$	–	15.8	15.6*	15.8
$2P_{5/2}(\Gamma_7)$	12.5	12.5	12.7*	12.5
$3S_{3/2b}$	8.9	8.6	10.2	10.2
$4S_{3/2b}$	5.8	5.2	5.8	6.0
$3S_{3/2a}$	3.8	3.8	4.5	4.0
$5S_{3/2b}$	3.1	3.4	3.6	3.7
$6S_{3/2b}$	2.0	2.5	2.4	2.7
$4S_{3/2a}$	1.3(?)	2.0	2.0	2.0
$7S_{3/2b}$	0.9(?)	1.8	1.0	1.9

* Data of [4].

To conclude, we mention briefly the lines Y_1 and Y_2 observed in the long-wavelength part of the spectra shown in Figs. 1–3. Lines of this kind have been discussed (see, e.g., [12, 13], and their relationship with dislocations has been demonstrated. Their specific feature of interest is the presence of very weak phonon replicas, which is characteristic of extended defects. It is noteworthy that, to date, the nature of these lines has not been elucidated.

4. ACKNOWLEDGMENTS

This study was supported by the Russian Foundation for Basic Research (project nos. 01-02-16500, 02-02-17324, and 00-02-17355), the program "Leading Scientific Schools" (grant no. 00-15-96568), and the Program of the Russian Academy of Sciences for the Support of Scientific Projects of Young Scientists.

REFERENCES

1. V. V. Zaĭtsev, V. S. Bagaev, and E. E. Onishchenko, Fiz. Tverd. Tela (St. Petersburg) **41** (4), 582 (1999) [Phys. Solid State **41**, 647 (1999)].
2. C. Gourgon, B. Eriksson, L. S. Dang, *et al.*, J. Cryst. Growth **138**, 590 (1994).
3. K. Sato, T. Asahi, M. Hanafusa, *et al.*, Phys. Status Solidi A **180**, 267 (2000).
4. H. Venghaus and P. J. Dean, Phys. Rev. B **21**, 1596 (1980).
5. P. J. Dean, Czech. J. Phys., Sect. B **30**, 272 (1980).
6. M. Said, M. A. Kanehisa, M. Balkanski, and Y. Saad, Phys. Rev. B **35**, 687 (1987).
7. M. Said and M. A. Kanehisa, J. Cryst. Growth **101**, 488 (1990).
8. E. Molva and N. Magnea, Phys. Status Solidi B **102**, 475 (1980).
9. B. Monemar, N. Magnea, and P. O. Holtz, Phys. Rev. B **33**, 7375 (1986).
10. M. S. Brodin and M. G. Matsko, Solid State Commun. **35**, 375 (1980).
11. E. Koteles, in *Excitons*, Ed. by E. I. Rashba and M. Sturge (North-Holland, Amsterdam, 1982; Nauka, Moscow, 1985), Chap. 3.
12. A. V. Kvit, S. A. Medvedev, Yu. V. Klevkov, *et al.*, Fiz. Tverd. Tela (St. Petersburg) **40** (5), 850 (1998) [Phys. Solid State **40**, 924 (1998)].
13. K. Wolf, A. Naumov, T. Reisinger, *et al.*, J. Cryst. Growth **135**, 113 (1994).

Translated by M. Tagirdzhanov

Semiconductors, Vol. 37, No. 3, 2003, pp. 288–293. Translated from Fizika i Tekhnika Poluprovodnikov, Vol. 37, No. 3, 2003, pp. 304–309.

ELECTRONIC AND OPTICAL PROPERTIES OF SEMICONDUCTORS

The Role of Tin in Reactions Involving Carbon Interstitial Atoms in Irradiated Silicon

L. I. Khirunenko*, O. A. Kobzar', Yu. V. Pomozov, M. G. Sosnin, and N. A. Tripachko

Institute of Physics, National Academy of Sciences of Ukraine, pr. Nauki 144, Kiev, 03028 Ukraine

** e-mail: lukh@iop.kiev.ua*

Submitted August 6, 2002; accepted for publication September 6, 2002

Abstract—The influence of doping with Sn on reactions proceeding with the involvement of interstitial C atoms in Si was studied. It is shown that Sn atoms in Si are effective sinks for interstitial C atoms (C_I); as a result, in Sn-doped Si, formation of C_IO_I and C_IC_S centers is not observed in the course of annealing of C_I centers; rather, C_ISn_S centers are formed. The C_IO_I and C_IC_S centers appear in Si:Sn only after annealing of the formed C_ISn_S complexes. It is ascertained that C_I atoms can occupy two different interstices around Sn atoms. The process of radiation-defect formation in Si:Sn was simulated in the approximation of quasi-chemical reactions. Expressions for dependences of concentrations of main radiation defects on the Sn content were derived; the results of calculations were compared with experimental data. © *2003 MAIK "Nauka/Interperiodica"*.

1. INTRODUCTION

It is well known that Sn and C are isovalent substitutional impurities in Si. Doping with these elements gives rise to an appreciable local perturbation of the lattice; however, the signs of resulting strains in the cases of Sn and C are opposite (the covalent radii are R_{Sn} = 1.44 Å for Sn, R_C = 0.77 Å for C, and R_{Sn} = 1.17 Å for Si). Tin atoms in irradiated silicon interact actively with vacancies (V) with the formation of SnV centers [1, 2], which reduces the efficiency of production of vacancy-containing radiation defects [3–5]. According to the Watkins exchange mechanism [6], substitutional carbon atoms (C_S) are pushed from the lattice sites to interstices by silicon self-interstitials (Si_I); the following reaction takes place: $C_S + Si_I \longrightarrow C_I + Si_S$ [6, 7]. The C_I centers are annealed out by diffusion at temperatures near 300 K. In the course of diffusion, a substantial fraction of C_I atoms in silicon grown by the Czochralski method become located in the vicinity of interstitial oxygen atoms O_I with the eventual formation of $C3$ (C_IO_I) centers [8, 9]. The C_I atoms also interact actively with substitutional carbon (which leads to the formation of C_IC_S centers), with elements of Groups III and V, and with other atoms [10–12]. The efficiency of formation of particular C_I-containing centers depends on the impurity types in as-grown crystals and on the concentration of components comprising the defect. One can affect the probabilities of the reactions by introducing competing reactions for the capture of interstitial carbon.

The effect of tin on the parameters of silicon has been investigated in considerable detail. However, the data on the effect of doping with tin on reactions involving interstitial atoms in irradiated silicon are virtually lacking in the available publications. It has been noted [13, 14] that tin does not affect the reactions with the involvement of interstitial carbon in silicon; in particular, it does not affect the production rate of C_IO_I centers. New bands were observed in studies of Si:Sn using infrared absorption spectroscopy [15, 16]; these bands were related to centers formed owing to interaction of substitutional tin atoms Sn_S with C_I interstitial atoms.

In this paper, we report new data on the effect of doping silicon with tin on the processes that concern radiation-defect formation and involve interstitial carbon atoms.

2. EXPERIMENTAL

We studied single-crystal *n*-Si:P samples grown by the Czochralski method. The phosphorus concentration was $(3–4) \times 10^{14}$ cm^{-3}. The tin concentration was determined from the results of neutron-activation analysis and with the use of a JCXA-733 X-ray microprobe analyzer and ranged from about 2×10^{18} to about 2×10^{19} cm^{-3}. The carbon concentration was estimated at 2.3×10^{16}–2.9×10^{17} cm^{-3} using the results from measuring the absorption band at 607 cm^{-1}. All the studied samples contained almost the same oxygen concentration [$(5–6) \times 10^{17}$ cm^{-3}]. In order to reveal the special features of the effect of doping with tin on the processes of radiation-defect formation, we used (for the sake of comparison) silicon samples that contained no tin but contained carbon and oxygen with concentrations comparable to those mentioned above.

1063-7826/03/3703-0288$24.00 © 2003 MAIK "Nauka/Interperiodica"

The samples were irradiated with 5-MeV electrons at a temperature of about 80 K; a microtron was used as the electron source. The irradiation dose was (2–5) × 10^{17} cm^{-2}. The samples were transported (without warming up) to a cryostat for measurements or to a special chamber for annealing. We studied the absorption spectra of the samples immediately after irradiation and after subsequent isochronous (20 min) annealing in the temperature range T_a = 80–550 K with a step of 5–20 K; these spectra were measured using an IFS-113v Fourier spectrometer at temperatures T = 300 and 10 K in the spectral range of 8000–500 cm^{-1} with a spectral resolution of 0.5 cm^{-1}.

3. RESULTS

Our studies have shown that doping of silicon with tin does not result in appreciable changes in the initial electrical and optical parameters of silicon. It was shown previously that perturbation of oxygen (of an Si_2O quasi-molecule) by neighboring tin atoms gives rise to additional absorption lines in the spectral region corresponding to interstitial oxygen [17]. We observed a similar effect in studying the absorption spectrum of substitutional carbon C_S in Si:Sn samples. We observed three new bands peaked at 642.8, 591.1, and 562.4 cm^{-1} (Fig. 1) in the absorption spectra of Si:Sn in the vicinity of the 607-cm^{-1} band, which corresponds to the vibrational mode of C_S. The intensities of these bands increase with both an increase in the carbon content and an increase in the tin concentration in the samples. This circumstance suggests that the observed bands correspond to a vibration of C_S perturbed by tin atoms located within the nearest coordination shells. The presence of three bands can be caused by the nonequivalent arrangement of C_S and Sn_S atoms.

In Fig. 2, we show absorption spectra measured at T = 10 K for the Si:Sn samples with an Sn concentration of 1.9×10^{19} cm^{-3} immediately after irradiation at $T \approx 80$ K. As can be seen from Fig. 2, absorption spectra in the range under investigation for Si:Sn immediately after irradiation are identical to the well-known spectra for Si; i.e., no additional bands are observed in the spectra of Si:Sn compared to the spectra of the reference Si samples. The most intense bands at ~922 and ~932 cm^{-1} correspond to local vibrational modes of C_I, whereas the band peaked at ~6903 cm^{-1} corresponds to an electron transition related to the C_I center [5]. In the course of heat treatment of irradiated silicon at temperatures T_a = 250–300 K, the C_I centers are annealed out; simultaneously, C_IO_I and C_IC_S complexes come into existence [8, 9, 18]. In contrast to nominally undoped silicon, six new bands at the wave numbers of 873.5, 888.9, 985.3, 1025.3, 6915, and 6875 cm^{-1} were observed in the absorption spectra in Si:Sn crystals heat-treated at $T_a \gtrsim 250$ K in the course of annealing out of C_I centers; bands corresponding to C_IO_I and C_IC_S centers were not observed (Fig. 2, curve *2*). Studies of the samples with various concentrations of tin and carbon showed that the intensities of all six absorption bands depend on concentrations of both carbon and tin; i.e., the higher these concentrations, the more intense are the bands.

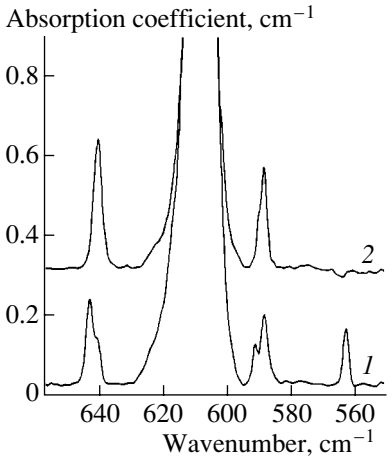

Fig. 1. Absorption spectra of (*1*) Si:Sn and (*2*) Si at T = 10 K.

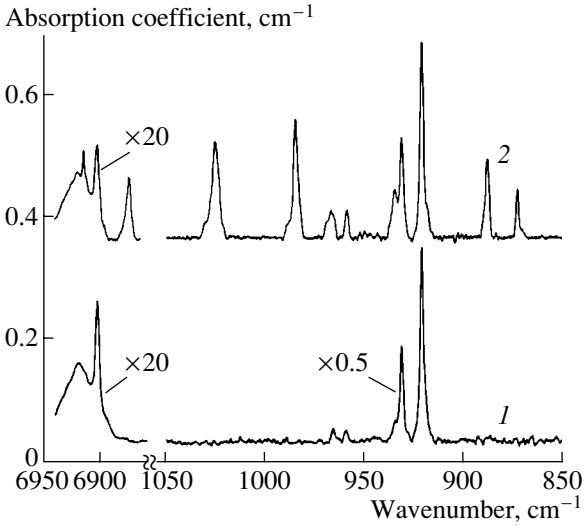

Fig. 2. Absorption spectra of Si:Sn irradiated at 80 K with electrons with a dose of 5×10^{17} cm^{-2} (*1*) before and (*2*) after annealing at T_a = 255 K. The spectra were measured at T = 10 K; the Sn concentration was 1.9×10^{19} cm^{-3}.

The absorption bands peaked at 888.9, 985.3, and 6915 cm^{-1} simultaneously attain the highest intensity at an annealing temperature $T_a \approx 260$ K; at $T_a > 270$ K, these bands begin to anneal out synchronously. Transformation of the absorption spectra in the course of isochronous annealing is illustrated in Fig. 3 for the bands peaked at 888.9 and 985.3 cm^{-1}. All three bands are simultaneously annealed out at $T_a \approx 280$ K. In the course of annealing of the bands peaked at 888.9, 985.3, and 6915 cm^{-1}, the C_I centers anneal out in Si:Sn in the same way as they do in Si that is not doped with

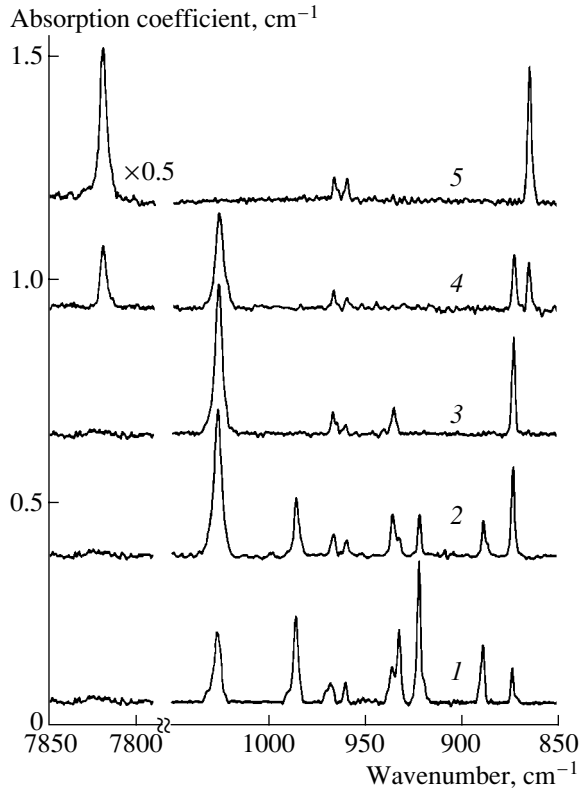

Fig. 3. Isochronous annealing of electron-irradiated Si:Sn with an Sn concentration of 1.9×10^{19} cm^{-3}. The annealing temperatures T_a = (*1*) 260, (*2*) 273, (*3*) 305, (*4*) 353, and (*5*) 383 K.

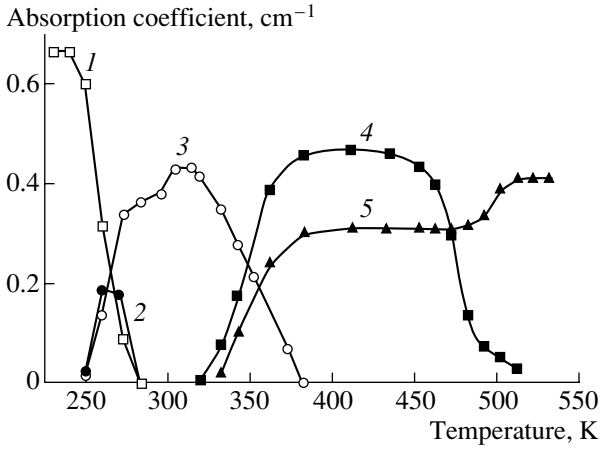

Fig. 4. Transformation of radiation defects in the course of annealing of irradiated Si:Sn. The curves correspond to the (*1*) C_I, (*2*) (C_ISn_S)*, (*3*) $(C_ISn_S)^{2N}$, (*4*) C_IC_S, and (*5*) C_IO_I centers.

Sn. The identity of the behavior of the absorption bands peaked at 888.9, 985.3, and 6915 cm^{-1} during heat treatment indicates that these bands are related to the same center.

Intensities of absorption bands peaked at 873.5, 1025.3, and 6875 cm^{-1} increase steadily as the temperature of heat treatment increases and attain a maximum when the C_I centers are completely annealed out. In Fig. 3, we show the results of isochronous annealing for the bands peaked at 873.5 and 1025.3 cm^{-1}. As can be seen from Fig. 3, C_IO_I and C_IC_S centers are not observed after the C_I centers were completely annealed out. It is noteworthy that, in the Si:Sn samples, the temperature corresponding to the annealing of C_I centers gradually decreases as the tin concentration increases. The C_I centers are annealed out at a temperature of 300 K in Si that does not contain Sn; in contrast, this temperature decreases to ~295 and 285 K for Si:Sn with Sn concentrations $N_{Sn} = 2 \times 10^{18}$ and 1.9×10^{19} cm^{-3}, respectively. Apparently, the promotion of annealing of the C_I centers is related to elastic-stress fields, which arise owing to the difference in covalent radii between silicon and tin atoms.

The lack of bands corresponding to the C_IO_I and C_IC_S centers in the absorption spectrum of Si:Sn samples after the C_I centers were annealed out and the dependence of intensities of new additional absorption bands on the C concentration suggest that, in the annealed Si:Sn samples (in contrast to those containing no Sn), the major fraction of C_I atoms are involved in the formation of the centers responsible for the observed additional absorption bands.

Intensities of the absorption bands peaked at 873.5 and 1025.3 cm^{-1} begin to decrease at heat-treatment temperatures $T_a \gtrsim 323$ K; these bands are annealed out synchronously at $T_a \approx 383$ K (Fig. 3, curves *4*, *5*). It is worth noting that, as the temperature of measurements is elevated to about 300 K, the bands peaked at 873.5 and 1025.3 cm^{-1} shift to lower frequencies, with their peaks now being located at 865.5 and 1010.4 cm^{-1}, respectively. The absorption band peaked at 6875 cm^{-1} is annealed out similarly to those at 873.5 and 1025.3 cm^{-1}. The pattern of annealing of the bands peaked at 873.5, 1025.3, and 6875 cm^{-1} (as in the case of the bands at 888.9, 985.3, and 6915 cm^{-1}) is independent of the Sn concentration within the entire range under consideration. The simultaneous appearance of the absorption bands corresponding to the C_IO_I and C_IC_S centers is observed in the course of annealing of the bands peaked at 873.5, 1025.3, and 6875 cm^{-1}. In Fig. 3 (curves *4*, *5*), we show the most intense bands for these centers, i.e., a band at 865.7 cm^{-1} for C_IO_I and a band at 7819.7 cm^{-1} for C_IC_S.

We estimated the ratio between concentrations of the C_I and C_IO_I centers for Si crystals without Sn and Si crystals doped with Sn, with the initial concentrations of C and O being comparable in both types of crystals. In order to assess the concentrations of the aforementioned centers, we used the areas under the corresponding absorption peaks. The results show that the above ratio is the same for Si and Si:Sn; i.e., the resulting concentration of C_IO_I centers is independent of the Sn concentration in the samples.

The complete pattern of transformation of radiation defects as a result of annealing in the temperature range of T_a = 230–550 K is illustrated in Fig. 4 for the samples with an Sn concentration of 1.9×10^{19} cm^{-3}. As can be seen from Fig. 4, an increase in the concentration of centers related to the absorption bands peaked at 873.5, 1025.3, and 6875 cm^{-1} is observed as the bands at 888.9, 985.3, and 6915 cm^{-1} are annealed out. An increase in the concentration of C_IO_I centers at $T_a \gtrsim$ 473 K occurs owing to the release of C_I atoms as a result of annealing of C_IC_S complexes. The pattern of transformation of the centers in the course of annealing is the same for all concentrations of Sn under consideration.

4. DISCUSSION

Absorption bands peaked at 873.5, 1025.3, and 6875 cm^{-1} were observed previously [15, 16] and, according to the suggested model, were attributed to C_ISn_S centers. The first two bands were related to local vibrations of C_ISn_S and the third band was related to an electronic transition. In theoretical analysis of a model for C_ISn_S centers [16], possible positions of interstitial carbon atoms in the first coordination sphere and in the second and third coordination shells centered at a tin atom were considered. It is assumed that the configuration $(C_ISn_S)^{2N}$ is the most stable; in this configuration, a C_I atom is located within the second coordination shell around an Sn_S atom. In this case, two nonequivalent arrangements of interstitial carbon atoms in reference to a substitutional tin atom Sn_S may take place; in one of these, the system has the lowest energy (assumed to be equal to zero in [16]), whereas, in the second configuration, the energy of the system is higher by 0.25 eV, so that this configuration is expected to be less stable. The location of C_I atoms within the third coordination shell centered at an Sn atom is close in energy to the second case and yields a defect with an energy that is higher by 0.3 eV than the lowest value. The arrangement of an interstitial C atom within the first coordination sphere centered at an Sn atom is, energetically, the least favorable (the energy increases to 0.5–0.8 eV). Absorption bands peaked at 873.5, 1025.3, and 6875 cm^{-1} are related [16] to the $(C_ISn_S)^{2N}$ configuration, which corresponds to the lowest energy, and to C_I atoms located within the second coordination shell centered at an Sn atom. Adhering to the model suggested previously [15, 16] and taking into account special experimental features of the behavior of all six additional absorption bands, we can attribute new bands peaked at 888.9, 985.3, and 6915 cm^{-1} to a less stable arrangement of interstitial C atoms $(C_ISn_S)^*$ within the second or third coordination shells centered at an Sn atom. An increase in the concentration of the centers related to the absorption bands at 873.5, 1025.3, and 6875 cm^{-1}, which occurs simultaneously with annealing of the bands at 888.9, 985.3, and 6915 cm^{-1} and does not affect the special features of annealing of the C_I centers, indicates that the C_ISn_S centers are transformed from the configuration $(C_ISn_S)^*$ into the configuration $(C_ISn_S)^{2N}$ in the course of annealing.

As follows from aforementioned experimental data, the presence of Sn atoms in the Si lattice profoundly affects the process of transformation of radiation defects during annealing of Si irradiated at 80 K. We now use the approximation of a quasi-chemical reaction to analyze the experimentally observed transformation of radiation defects in the course of annealing. We will separately analyze two annealing stages in Si:Sn: the stage of annealing of interstitial C atoms and the stage of annealing of C_ISn_S centers. In the course of annealing of interstitial carbon in nominally undoped silicon, the following reactions controlling defect formation are prevalent:

$$C_I + O_I \longrightarrow C_IO_I, \tag{1}$$

$$C_I + C_S \longrightarrow C_IC_S. \tag{2}$$

According to the obtained experimental data, the process of radiation-defect formation in Si:Sn involves the following additional reactions:

$$C_I + Sn_S \longrightarrow (C_ISn_S)^{2N}, \tag{3}$$

$$C_I + Sn_S \longrightarrow (C_ISn_S)^*. \tag{4}$$

Reactions (3) and (4) describe the formation of two nonequivalent types of C_ISn_S centers, which correspond either to the 873.5, 1025.3, and 6875 cm^{-1} bands or to the 888.9, 985.3, and 6915 cm^{-1} bands, respectively.

A system of kinetic equations corresponding to the above reactions can be written as

$$\frac{dN_{C_I}}{dt} = -k^{2N}_{C_I, Sn_S}N_{C_I}N_{Sn_S} - k^*_{C_I, Sn_S}N_{C_I}N_{Sn_S} - k_{C_I, O_I}N_{C_I}N_{O_I} - k_{C_I, C_S}N_{C_I}N_{C_S}, \tag{5}$$

$$\frac{dN_{(C_ISn_S)^{2N}}}{dt} = k^{2N}_{C_I, Sn_S}N_{C_I}N_{Sn_S}, \tag{6}$$

$$\frac{dN_{(C_ISn_S)^*}}{dt} = k^*_{C_I, Sn_S}N_{C_I}N_{Sn_S}, \tag{7}$$

$$\frac{dN_{C_IO_I}}{dt} = k_{C_I, O_I}N_{C_I}N_{O_I}, \tag{8}$$

$$\frac{dN_{C_IC_S}}{dt} = k_{C_I, C_S}N_{C_I}N_{C_S}, \tag{9}$$

where N_i denote the concentrations of corresponding components, and the coefficients $k_{i,j}$ account for the probabilities of interactions between the components i and j.

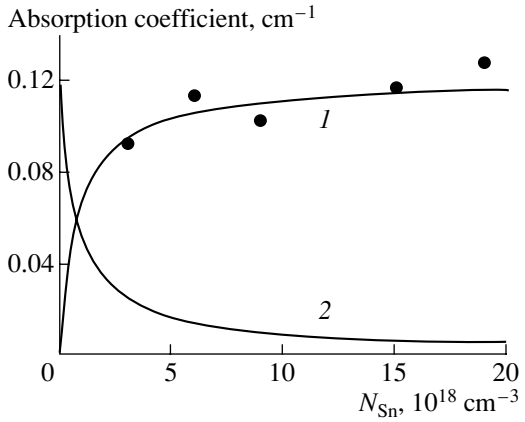

Fig. 5. Dependences of concentrations of the (*1*) C_ISn_S and (*2*) C_IO_I centers on the Sn concentration in Si; the dependences were plotted using expressions (10) and (12). The dots represent experimental data for the band peaked at 1025.3 cm^{-1}.

We then integrate Eqs. (5)–(9), taking into account that $N_{C_I} \ll N_{Sn_S}$ and also that the major fraction of interstitial C atoms become involved in the formation of complexes with Sn_S in the course of annealing (consequently, the O_I and C_S concentrations remain constant at this annealing stage); as a result, we obtain the following expressions for concentrations of the centers:

$$N_{(C_ISn_S)^{2N}} = N_{C_I} \times \frac{k^{2N}_{C_I,Sn_S} N_{Sn_S}}{(k^{2N}_{C_I,Sn_S} + k^{*}_{C_I,Sn_S})N_{Sn_S} + k_{C_I,O_I}N_{O_I} + k_{C_I,C_S}N_{C_S}}, \quad (10)$$

$$N_{(C_ISn_S)^{*}} = N_{C_I} \times \frac{k^{*}_{C_I,Sn_S} N_{Sn_S}}{(k^{2N}_{C_I,Sn_S} + k^{*}_{C_I,Sn_S})N_{Sn_S} + k_{C_I,O_I}N_{O_I} + k_{C_I,C_S}N_{C_S}}, \quad (11)$$

$$N_{C_IO_I} = N_{C_I} \times \frac{k_{C_I,O_I} N_{O_I}}{(k^{2N}_{C_I,Sn_S} + k^{*}_{C_I,Sn_S})N_{Sn_S} + k_{C_I,O_I}N_{O_I} + k_{C_I,C_S}N_{C_S}}, \quad (12)$$

$$N_{C_IO_S} = N_{C_I} \times \frac{k_{C_I,C_S} N_{C_S}}{(k^{2N}_{C_I,Sn_S} + k^{*}_{C_I,Sn_S})N_{Sn_S} + k_{C_I,O_I}N_{O_I} + k_{C_I,C_S}N_{C_S}}. \quad (13)$$

It can be seen from an analysis of expressions (10)–(13) that the formation of the C_IO_I and C_IC_S centers is bound to be suppressed by Sn impurity, which is exactly what is observed in our experiments.

As was mentioned above, C_IO_I and C_IC_S centers are formed when C_ISn_S centers are annealed. This process can be described by the following reactions:

$$(C_ISn_S)^{2N} \xrightarrow{\tau^{2N}} C_I + Sn_S, \quad (14)$$

$$(C_ISn_S)^{*} \xrightarrow{\tau^{*}} C_I + Sn_S, \quad (15)$$

$$C_I + O_I \longrightarrow C_IO_I, \quad (16)$$

$$C_I + C_S \longrightarrow C_IC_S. \quad (17)$$

A system of kinetic equations corresponding to these reactions can be written as

$$\frac{dN_{(C_ISn_S)^{2N}}}{dt} = -\frac{dN_{(C_ISn_S)^{2N}}}{\tau^{2N}}, \quad (18)$$

$$\frac{dN_{(C_ISn_S)^{*}}}{dt} = -\frac{dN_{(C_ISn_S)^{*}}}{\tau^{*}}, \quad (19)$$

$$\frac{dN_{C_I}}{dt} = \frac{N_{(C_ISn_S)^{2N}}}{\tau^{2N}} + \frac{N_{(C_ISn_S)^{*}}}{\tau^{*}} - k_{C_I,O_I}N_{C_I}N_{O_I} - k_{C_I,C_S}N_{C_I}N_{C_S}, \quad (20)$$

$$\frac{dN_{C_IO_I}}{dt} = k_{C_I,O_I}N_{C_I}N_{O_I}, \quad (21)$$

$$\frac{dN_{C_IO_S}}{dt} = k_{C_I,O_S}N_{C_I}N_{C_S}, \quad (22)$$

where the time constants τ^{2N} and τ^{*} correspond to the disintegration rates of the $(C_ISn_S)^{2N}$ and $(C_ISn_S)^{*}$ centers, respectively.

Taking into account the initial concentrations of defects (10)–(13), we use Eqs. (18)–(22) to obtain the following expressions for concentrations of the C_IO_I and C_IC_S centers:

$$N_{C_IO_I} = \frac{k_{C_IO_I}N_{C_I}N_{O_I}}{k_{C_I,O_I}N_{O_I} + k_{C_I,C_S}N_{C_S}}, \quad (23)$$

$$N_{C_IO_S} = \frac{k_{C_I,C_S}N_{C_I}N_{O_S}}{k_{C_I,O_I}N_{O_I} + k_{C_I,C_S}N_{C_S}}. \quad (24)$$

As can be seen from (23) and (24), the final concentrations of the C_IO_I and C_IC_S centers are bound to be independent of the Sn concentration in the samples.

In Fig. 5, we show the obtained theoretical dependences of concentrations of the $(C_ISn_S)^{2N}$ and C_IO_I centers on the Sn concentration in the samples; these dependences were plotted according to expressions (10) and (12). Corresponding dependences for the $(C_ISn_S)^{2N}$ and $(C_ISn_S)^{*}$ complexes are similar and differ only by the constant factor. This is also true for the C_IO_I and C_IC_S centers. We compared the results of calculations with experimental data for C_IC_S centers (dots at the curve correspond to the intensity at the peaks of the absorp-

tion bands). As can be seen, there is satisfactory agreement between theoretical and experimental dependences. It is impossible to conduct a similar comparison for the C_IO_I and C_IC_S centers, since the bands corresponding to these centers are not observed experimentally in the absorption spectra even for the lowest Sn concentration in Si. In fact, the absorption coefficient (estimated from the theoretical dependence) at the peak of the band corresponding to the C_IO_I center is equal to ~ 0.03 cm^{-1} for the lowest Sn concentration in our experiments; this value of the absorption coefficient is below the sensitivity threshold of the measurements.

5. CONCLUSIONS

Thus, the results reported in this paper indicate that Sn atoms in irradiated Si act as effective traps for interstitial C atoms (C_I). As a result of this interaction, C_ISn_S complexes are formed. Notably, C_I atoms can be found in two different configurations in reference to substitutional Sn atoms. As a result of interaction between C_I and Sn_S atoms, the efficiency of introduction of the centers containing interstitial C is appreciably lowered. A theoretical consideration of the transformation of major radiation defects in the course of annealing yields results that are in qualitative agreement with experimentally observed dependences of the concentration of the centers under investigation on the content of Sn in the samples.

REFERENCES

1. G. D. Watkins, *Radiation Damage in Semiconductors*, Ed. by P. Baruch (Dunod, Paris, 1965), p. 97.
2. G. D. Watkins, Phys. Rev. B **12**, 5824 (1975).
3. G. D. Watkins, Phys. Rev. **155**, 802 (1967).
4. A. Brelot, IEEE Trans. Nucl. Sci. **19**, 220 (1972).
5. G. Davies, A. S. Oates, R. C. Newman, *et al.*, J. Phys. C: Solid State Phys. **19**, 841 (1986).
6. E. V. Lavrov and M. Fanciulli, Physica B (Amsterdam) **302–303**, 263 (2001).
7. E. V. Lavrov, M. Fanciulli, M. Kaukonen, *et al.*, Phys. Rev. B **64**, 125212 (2001).
8. G. D. Watkins, Phys. Rev. B **12**, 4383 (1975).
9. A. Nylandsted Larsen, J. J. Goubet, P. Mejlholrn, *et al.*, Phys. Rev. B **62**, 4535 (2000).
10. A. Brelot and J. Charlemagne, *Radiation Effects in Semiconductors*, Ed. by J. W. Corbett and G. D. Watkins (Gordon and Breach, London, 1971), p. 161.
11. V. B. Neĭmash, M. G. Sosnin, B. M. Turovskiĭ, *et al.*, Fiz. Tekh. Poluprovodn. (Leningrad) **16**, 901 (1982) [Sov. Phys. Semicond. **16**, 577 (1982)].
12. B. G. Svensson, J. Svensson, J. L. Lindström, *et al.*, Appl. Phys. Lett. **51**, 2257 (1987).
13. R. C. Newman and A. R. Bean, Radiat. Eff. **8**, 189 (1971).
14. J. M. Trombetta and G. D. Watkins, Appl. Phys. Lett. **51**, 1103 (1987).
15. R. C. Newman and A. R. Bean, Radiat. Eff. **8**, 189 (1971).
16. M. T. Asom, J. L. Benton, R. Sauer, and L. C. Kimerling, Appl. Phys. Lett. **51**, 256 (1987).
17. L. W. Song, X. D. Zhan, B. W. Benson, and G. D. Watkins, Phys. Rev. Lett. **60**, 460 (1988).
18. L. C. Kimerling, M. T. Asom, J. L. Benton, *et al.*, Mater. Sci. Forum **38–41**, 141 (1989).

Translated by A. Spitsyn

Semiconductors, Vol. 37, No. 3, 2003, pp. 294–301. Translated from Fizika i Tekhnika Poluprovodnikov, Vol. 37, No. 3, 2003, pp. 310–317.

SEMICONDUCTOR STRUCTURES, INTERFACES, AND SURFACES

Layer Structure of $Zn_{1-x}Cd_xSe$ Films Grown by Vapor-Phase Epitaxy from Metal–Organic Compounds on $Cd_{0.92}Zn_{0.08}S(0001)$ Substrates

V. P. Martovitsky*, V. I. Kozlovsky*, P. I. Kuznetsov, Ya. K. Skasyrsky*, and G. G. Yakushcheva***

** Lebedev Institute of Physics, Russian Academy of Sciences, Leninskiĭ pr. 53, Moscow, 119991 Russia*
e-mail: vikoz@mail1.lebedev.ru

*** Institute of Radio Engineering and Electronics (Fryazino Branch), Russian Academy of Sciences, pl. Vvedenskogo 1, Fryazino, Moscow oblast, 141190 Russia*

Submitted April 25, 2002; accepted for publication May 15, 2002

Abstract—The structure of $Zn_{1-x}Cd_xSe$ films, which were grown by vapor-phase epitaxy from metal–organic compounds on a $Cd_{0.92}Zn_{0.08}S(0001)$ substrate, was investigated by X-ray diffractometry. For both cubic and hexagonal phases, asymmetric reflections were selected. These reflections make it possible not only to reliably determine the presence of these phases in the film, but also to estimate the dimensions of coherent X-ray scattering regions and (or) variation in the lattice parameters in the intergrowth plane. The ZnSe films preferentially consist of twinned interlayers of the cubic phase, 200–250 Å thick, and with a low content of the hexagonal phase. In contrast, the hexagonal phase with a small number of cubic interlayers predominates in CdSe films. The thickness of the interlayers of the cubic phase in $Zn_{1-x}Cd_xSe$ decreases, whereas the concentration of the hexagonal phase increases for low x values with an approximately identical development of both phases for $x = 0.15$–0.20. © *2003 MAIK "Nauka/Interperiodica"*.

1. INTRODUCTION

The ZnSe-based quantum-well structures with ZnCdSe quantum wells (QWs) were used for the development of the first injection laser, which emits in the green spectral region [1]. However, further efforts to improve this type of laser were confronted by the serious problem of the degradation of the structures [2]. As one of the ways to solve this problem, it was suggested that QW structures with a hexagonal crystal lattice (of the wurtzite type) be used instead of structures with a cubic lattice (of the sphalerite type), which were used previously [3, 4]. The formation of defects of the "dark spot" type is believed to proceed more slowly due to a lesser number of planes of easy glide for dislocations in the lattice compared with the more symmetric cubic lattice. The first studies concerned with obtaining hexagonal structures were carried out using (111)-oriented perfect III–V substrates [4–10]. If grown in the [111] direction, the hexagonal wurtzite structure differs from the cubic sphalerite structure only in the mutual arrangement of the third layer with respect to the first two. For this reason, the growth of a hexagonal structure on a cubic substrate is most probable for this direction. However, due to a slight distinction between the lattices in this direction, the formation of stacking faults and even layer growth with the formation of interlayers of the cubic and hexagonal phases can be expected [11, 12].

Another approach for obtaining hexagonal structures is the growth of II–VI compounds on hexagonal substrates. As such substrates, ZnMgSSe [13, 14] or, more recently, CdSSe and ZnCdS [15, 16] have been suggested for this purpose. To obtain hexagonal heterostructures, it is best to avoid using the basal orientation of the substrate. The reason for this is that the difference between the hexagonal and cubic polymorphs is small for growth in the ⟨0001⟩ direction, similarly to the ⟨111⟩ direction for the substrate with a cubic structure. However, for a number of applications, for example, as the active medium of a laser electron-beam tube [17], it is necessary to retain the symmetry of the grown structure relative to the normal to the substrate. In this case, growth on substrates with a near-basal orientation is necessary. It is assumed that the influence of the substrate structure on the film structure will also be strong for the basal orientation in the case of layer-by-layer growth, where the atoms are preferentially incorporated into the growth steps.

The emission properties of the heterostructure, as well as their stability during prolonged device operation, depend on the quality of the crystalline structure. One of the effective methods for investigating the crystalline structure is X-ray diffractometry. However, during investigation of the ⟨111⟩-oriented films for the cubic substrate or ⟨0001⟩-oriented films for the hexagonal substrate, the problem of determining the microstructure of these films emerges. The reason for this is

that the interplanar spacings for these directions are almost identical for both polymorphs of the crystal lattice. The simplest method for separating the hexagonal and cubic phases in the films, which are homogeneous over the surface, is ϕ-scanning of the sample using the unchangeable position configuration of the source and a counter of the X-ray radiation pulses [10]. If the sample is rotated by 360°, the dependence of the detector signal on the rotation angle for the cubic structure should have three peaks, whereas this dependence for the hexagonal structure should have six peaks. However, the cubic structure with 60°-rotation twins, which are located in close proximity to each other in the neighborhood on the substrate surface, will also yield six peaks [10]. A similar result is also expected for the film consisting of twin interlayers alternating along the growth direction.

In this study, the structural characteristics of ZnSe, CdSe, and $Zn_{1-x}Cd_xSe$ films, which were grown by vapor-phase epitaxy from metal–organic compounds (MOCVD) on $Cd_{0.92}Zn_{0.08}S(0001)$ substrates, are investigated. It is demonstrated that the ZnSe films consist of twin interlayers 200–250 Å thick with a cubic crystalline structure, which are separated by thin interlayers of the hexagonal phase. In contrast, the CdSe films are formed by thicker (300–400 Å) hexagonal interlayers and thin interlayers of one of the components of the cubic phase. Upon an increase in x from 0 to 0.15, a decrease in the thickness of the cubic interlayers and an increase in the thickness of the hexagonal interlayers are observed. At $x > 0.2$, the hexagonal phase becomes dominant.

2. FILMS UNDER INVESTIGATION

The ZnSe, CdSe, and $Zn_{1-x}Cd_xSe$ epilayers 0.5–1 μm thick were grown on $Cd_{0.92}Zn_{0.08}S(0001)B$ substrates in a horizontal quartz reactor by the MOCVD technique at a hydrogen pressure close to atmospheric. For comparison, several growth processes were carried out on GaAs(111) and GaAs(001) substrates, and several CdS films were grown on $Cd_{0.92}Zn_{0.08}S(0001)B$ substrates. The metal–organic compounds were used for epitaxy: diethylzinc ($ZnEt_2$), dimethylcadmium ($CdMe_2$), diethyl sulfide (Et_2S), and dimethyl selenide (Me_2Se). The growth was carried out with a low excess of Group VI elements in the vapor phase with respect to Group II elements. The substrate temperature was varied from 435 to 495°C. To fabricate the substrates, CdZnS single crystals with a diameter of 50 mm were used. The crystals were grown from the vapor phase by the free-growth technique [18]. The density of low-angle boundaries was 10–15 cm^{-1}, whereas the dislocation density outside of these boundaries did not exceed 10^4 cm^{-2}. The (0001)-oriented wafers were cut from single crystals. The wafers were further ground and polished mechanically with a gradual decrease in the grain size of the diamond powder and then etched in a $CrO_3/HCl/H_2O$ polishing solution. Prior to epitaxy, the substrates were kept for 10 min in a hydrogen flow at the growth temperature so as to cleanse the surface of oxides.

The films grown on the CdZnS(0001)B substrates, according to optical microscopy observations, had predominantly smooth surfaces with various growth patterns. For the ZnSe and $Zn_{1-x}Cd_xSe$ films with $x < 0.15$, the majority of growth patterns were represented by three-edged pyramids. For the CdSe and $Zn_{1-x}Cd_xSe$ films, the growth patterns for $x > 0.2$ were predominantly represented by sharp-peaked and truncated hexahedral pyramids. Furthermore, growth defects in the form of lines, which often had a fine structure, were observed at the surface of the majority of such films.

The ZnCdSe films under investigation which were grown on CdZnS(0001) substrates had a significantly lower intensity of photoluminescence (PL) and cathodoluminescence (CL) both at room temperature and lower (T = 14 K) compared with the films of the same composition which were grown on the GaAs(001) substrates and almost the same PL intensity as the films grown on the GaAs(111) substrates. The PL was investigated through pulse excitation from an LG-21 N_2 laser with a pulse power of 1.5 kW. The CL was observed for an electron energy of 3–30 keV and a current density from 0.1 mA/cm^2 to 2 A/cm^2. The low-temperature CL spectra are shown in Fig. 1. A series of lines is observed in the CL spectrum of the ZnSe film grown at a low temperature (T_{gr} = 470°C). These are lines of free exciton emission (FE) and donor-acceptor pairs (DAP), which are inherent to the cubic polymorph of a crystal lattice, and long-wavelength emission in the range of 500–700 nm, where a broad line peaked at 510 nm can be resolved. When the growth temperature is increased to T_{gr} = 494°C, the FE and DAP lines in the emission spectrum of the ZnSe film vanish, whereas the line peaked at 510 nm becomes more clearly pronounced. The emission spectra of the ZnCdSe films contain two broad emission bands. The first band, located at a shorter wavelength (I_z), is the analogue of the line peaked at 510 nm in the spectrum of the ZnSe film grown at a high temperature. This line shifts to longer wavelengths as the composition parameter x increases. The second line is related to recombination via deep levels formed by film defects. We assume that the first emission band is caused by the recombination of the localized electron and hole, which are spatially separated due to the layered structure of the ZnCdSe films under investigation.

3. PROCEDURE FOR X-RAY INVESTIGATIONS

Structural investigations were carried out using a DRON-2.0 X-ray diffractometer with a graphite monochromator in both θ and (θ–2θ) scanning modes for various azimuthal angles ϕ of sample rotation around the normal to the growth surface. To reduce the width of asymmetrical reflections, an additional vertical slit 0.1 mm wide was positioned immediately in front of

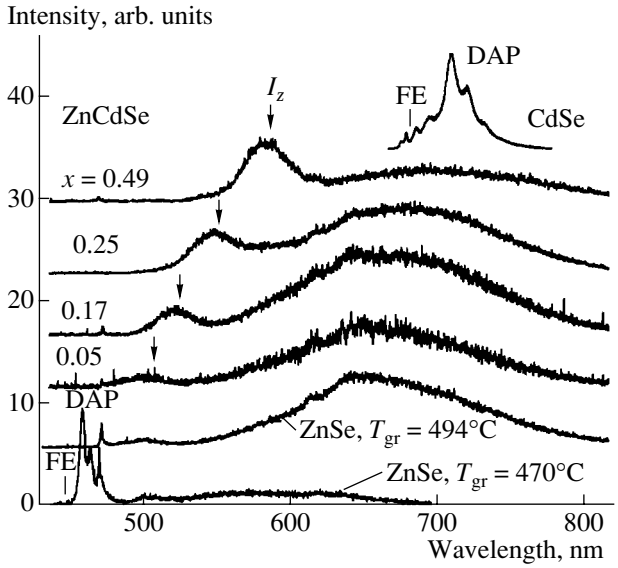

Fig. 1. Low-temperature cathodoluminescence spectra of ZnSe, CdSe, and $Zn_{1-x}Cd_xSe$ for various values of x. T = 14 K, the electron energy 10 keV, and the current density 0.1 mA/cm^2.

the sample under investigation. As the reference point for the search and recording of the asymmetrical reflections from the film, neighboring asymmetrical reflections of the substrate with the hexagonal structure were used. It seemed to us that it was evidently insufficient to estimate the concentrations of the hexagonal and cubic phases from the shifts and broadening of the (220) and (440) reflections, as was done in studies [19, 20]. To detect the presence of one or another phase in the film with confidence, we analyzed all possible reflections that can be used for the separate phase determination in the configuration of X-ray reflection from the surface under investigation. Due to strong X-ray absorption in this configuration, only the reflections whose Bragg angle exceeds the tilt angle of the reflecting plane to the growth surface can be observed.

Figure 2 shows fragments of a Boldyrev polar diagram for the ⟨111⟩ direction of the cubic structure and the ⟨0001⟩ direction of the hexagonal structure. In Fig. 2, the normals to the planes are shown. Reflections from these planes can actually be observed in the reflection configuration for the $Zn_{1-x}Cd_xSe$ films with the use of Cu radiation. In this diagram, each of the concentric circles, starting from the smallest one, corresponds to a deviation of 10° from the [111] direction of the cubic phase or from the [0001] direction of the hexagonal phase. The angular distance between the neighboring straight lines in the Boldyrev diagram is equal to 30°. Since only the reflections from vertical or close to vertical planes can be detected using a DRON-2.0 diffractometer, the normals to these planes should be positioned in the horizontal straight line. Sample rotation around the [111] direction permits one to draw out the normal to each possible reflecting plane of the crystal to

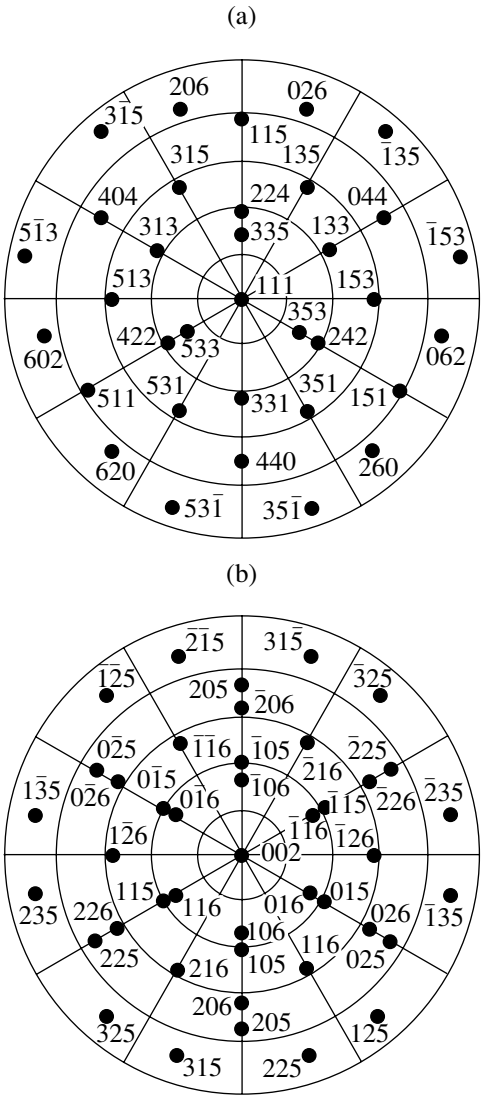

Fig. 2. Gnomonic projections for ZnSe in a form of polar Boldyrev diagrams of (a) the cubic phase, which consists of two twin components, along the [111] direction; and (b) the hexagonal phase along the [002] direction. The normals are shown to only the planes, which manifest themselves in the reflection configuration with the use of Cu radiation.

the horizontal straight line. The indices of normals to the planes of the hexagonal structure in the four-index representation {*hkil*} are used; three of these indexes {*hkl*} are shown in Fig. 2. The attribution of the reflection under investigation to the cubic or hexagonal phase was determined under the simultaneous fulfillment of two conditions. These conditions are as follows: (i) coincidence of the reflection peak in the (θ–2θ) scanning mode with the calculated value for one or another phase and (ii) proximity of the experimental asymmetry angle of the reflecting plane to the calculated value. A slight discrepancy between the calculated and experimental tilt angles of the reflecting plane (~0.1°) can emerge due to tetragonal distortion of the film lattice. This distortion is caused by lattice mismatch and different ther-

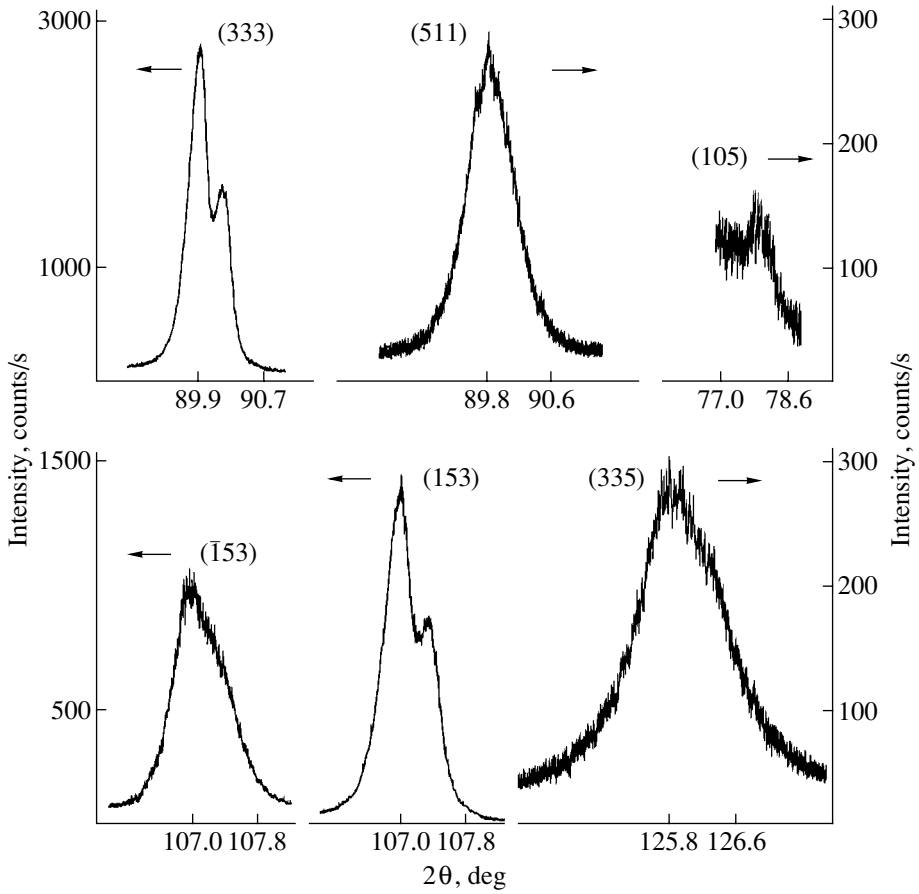

Fig. 3. Diffraction profiles of the symmetrical (333) reflection, asymmetrical (511), (153), ($\bar{1}53$), and (335) reflections of the cubic phase, and the weak (105) reflection of the hexagonal phase of the ZnSe film (sample 737).

mal expansion coefficients for the film and the substrate.

Our preliminary results demonstrated that the reflections from the $Zn_{1-x}Cd_xSe$ films with the sphalerite structure are twinned and correspond to the rotation of the lattices of twin components relative to each other by 360° (or 180°) around the [111] direction. This means that for the single-crystal film, each system of asymmetrical reflections should triply manifest itself on its rotation by 360° around the [111] direction. In contrast with this, for the twinned structure, the same system of reflections should sextuply manifest itself. Due to this, for example, if the (511) plane is in the vertical (reflecting) position, the (440) plane of another twin component will simultaneously be in the vertical position. After rotation of the structure by 60°, the (440) planes of the first component and the (511) planes of the second component will be in the reflecting position. However, in this case, only the system of {153} planes with an asymmetry angle of 28.56° exists. This system repeats in 60° intervals for each component; i.e., both twin components reflect X-rays as a single-crystal without twins, similarly to the case of the (333) symmetrical reflection, only for this system. In the case of this system of {153} planes, thin hexagonal interlayers should also be in the reflecting position. Note the existence of one more system of $\{\bar{1}53\}$ reflections with a slope angle to the [111] direction of 46.91°. For this system, the diffraction conditions are satisfied simultaneously for only one of the twin components.

4. RESULTS OF X-RAY INVESTIGATIONS

Figure 3 shows the reflections recorded in the (θ–2θ) scanning mode from the ZnSe film obtained at an elevated growth temperature (T_{gr} = 495°C). Compared with the symmetrical (333) reflection, broadening of the asymmetrical (511) reflection of the film with a sphalerite structure is clearly observed. Note that the angle positions of these reflections are almost identical; as a result, the distinction in reflection broadening is especially pronounced. The peak of the (511) reflection is shifted by 0.1° to smaller angles due to the tetragonal compression of the film lattice along the [111] direction. This tetragonal distortion is partly caused by a larger thermal expansion coefficient of the ZnSe film compared with the substrate [21], as well as by a partial compensation of the lattice mismatch between the film

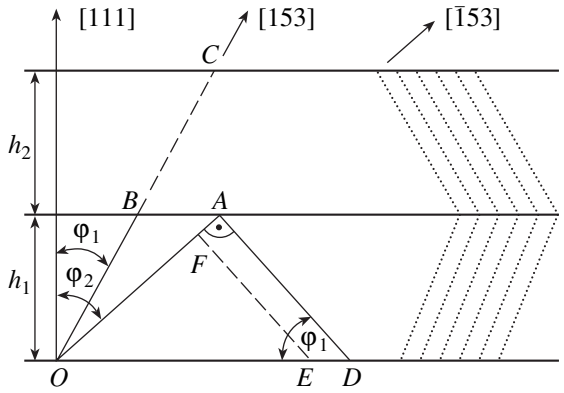

Fig. 4. Increase in the length of X-ray coherent scattering for the common (153) reflection of two twin components (*OC*) compared with the *OA* length for the ($\bar{1}$53) reflection, for which only one of two twin components is reflecting.

and the substrate in the intergrowth plane due to elastic strain. For the same angle position ϕ, a (440) reflection of approximately the same intensity and degree of broadening is observed. After sample rotation by 60° around the normal to the growth plane, one more pair of broadened (511) and (440) reflections is observed. The low-intensity (105) reflection from the film fragments with the hexagonal structure also manifests itself.

The results obtained permit us to assume that the layered structure of the ZnSe film consists of alternating twin cubic interlayers and thin hexagonal interlayers. In fact, if the cubic film grows along the [111] direction, the growth of a hexagonal interlayer with an odd number of atomic layers transforms the subsequent fragment with a cubic structure into a twinning position relative to the fragment of the structure, which grew prior to the growth of the hexagonal interlayer [22]. The thicknesses of these interlayers can be estimated from the broadening of the reflections, if broadening is caused by the small dimensions of the coherent scattering region. However, for the (001)-oriented films, both for III–V compounds [23, 24] and for II–VI compounds [25], it was shown that the reflections of the films, which were grown on severely lattice-mismatched substrates, broaden mainly due to the existence of microstresses at the film–substrate interface. These stresses are caused by nonuniform defect distribution along two orthogonal, [110] and [1$\bar{1}$0], directions. This distribution depends heavily on the direction of substrate misorientation from the exact (001) crystallographic plane.

The contributions to broadening of the asymmetrical reflections of both the finite interlayer thickness (h) of each of the twin components and variations of the lattice parameter of the film in the plane of intergrowth with the substrate can be estimated. To this end, we measured the profiles of reflections with various asymmetry angles of reflecting planes. Figure 4 schematically represents a fragment of the film with two twin components h_1 and h_2 thick, which are separated by one hexagonal atomic layer. Let the asymmetry angle be $\varphi = \varphi_1$, the thickness of the twin interlayer be h_1, and the diffraction vector be directed along the *OA* line. From simple geometric relationships, the length of X-ray coherent scattering equals $L = h_1/\cos\varphi_1$. In this case, reflection broadening $\beta(2\theta)$, which is determined by the finite dimensions of the coherent scattering region, can be determined from the formula [26]

$$\beta(2\theta) = \frac{\lambda}{L\cos(\theta)} = \frac{\lambda\cos(\varphi_1)}{h_1\cos(\theta)}, \qquad (1)$$

where $\lambda = 1.54056$ Å is the X-ray radiation wavelength. It can be seen from formula (1) that broadening should increase with decreasing angle φ. In contrast, broadening of reflections should increase with φ if this broadening is caused mainly by the presence of microstresses at the film–substrate interface. It can be seen from simple geometric relationships in Fig. 4 that variation in the *OD* vector in the (111) plane by *ED* leads to variation in the *OA* vector along the diffraction direction by *AF*, i.e., proportionally to the sine of the slope angle φ of the reflecting plane. In this case, broadening of reflections should increase as the asymmetry angle of reflecting planes increases.

The profiles of the ($\bar{1}$53), (153), and (335) reflections with asymmetry angles of 46.91°, 28.56°, and 14.42° are also shown in Fig. 3. Although the (153) reflection has a lower asymmetry angle relative to the ($\bar{1}$53) reflection with the same Bragg angle, both twin components are in the reflecting position, as was mentioned above in Section 3. For this reason, the size of the coherent scattering region should be no less than the *OC* segment in Fig. 4, which exceeds the *OA* segment by a factor of more than 1.5. In this case, we assume that the thicknesses of twin interlayers h_1 and h_2 are approximately equal. If the thickness of hexagonal interlayers between all twins does not exceed one atomic layer, the entire film thickness for the (153) reflection will reflect X-rays as an indivisible single crystal. Thus, the widths of the symmetrical (333) reflection and asymmetrical (153) reflection, which are common for two twin components, are small. Alternatively, broadening of other asymmetrical reflections, which increases as the asymmetry angle decreases, is substantial. This allows us to conclude that the contribution of thin cubic interlayers to the broadening of the reflections of the ZnSe films is decisive. From formula (1), it is possible to estimate the thickness of these interlayers. Substituting the experimental values $\beta(2\theta) = 0.49°$ for the (511) reflection with the angles $\theta = 44.9°$ and $\varphi = 38.94°$, we obtain the estimate h = 200 Å. Approximately the same interlayer thickness follows from the use of physical broadening of the ($\bar{1}$53) and (353) reflections. However, for the (153) reflection, which is common for twins, with $\beta(2\theta) = 0.20°$, $\theta = 53.5°$, and $\varphi = 28.56°$, we obtain the estimate

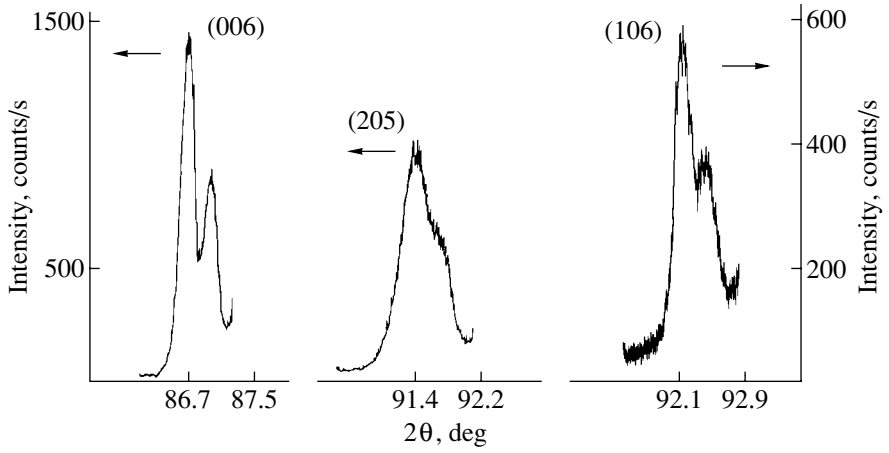

Fig. 5. Diffraction profiles of the symmetrical (006) reflection and asymmetrical (205) (φ = 37°) and (106) (φ = 17.44°) reflections of the CdS film, in which the layer structure detected by the X-ray diffraction technique is absent.

$h_{(153)}$ = 650 Å. The latter value exceeds the thickness of separate twin interlayers by a factor of more than 3, which is in good agreement with the low content of the hexagonal phase in the film.

A comparison of diffraction reflections of the ZnSe films which were obtained at lower temperatures shows that the peak from the hexagonal phase of the film first vanishes with a simultaneous small increase in broadening of the (511) and (440) reflections. With a further decrease in the growth temperature to T_{gr} = 440°C, rocking curves for all reflections of the film broaden. In this case, the intensities of the reflections of one of the twin components exceed those for the other one by a factor of 2–3.

The profiles of the (006), (205), and (106) reflections of the CdS film grown on the $Cd_{0.92}Zn_{0.08}S$ substrate are shown in Fig. 5. A layered structure which broadens the asymmetric reflections is not observed for this film. Thus, even though the film consists of interlayers, their average thickness exceeds 1000 Å. In this case, broadening of asymmetrical reflections depends only on the variation in the lattice parameters in the intergrowth plane and is proportional to the sine of the slope angle of the reflecting plane to the growth surface. For this reason, the (106) reflection with a low slope angle φ = 17.44° relative to the basal plane (0001) is broadened much less than the (205) reflection with a larger slope angle φ = 37.01°. Such behavior was observed previously both for III–V films [23, 24] and for II–VI films [25]. From the physical broadening, β(2θ) = 0.28°, of the (205) reflection, it is possible to estimate the variation of the lattice parameter of the film in the intergrowth plane:

$$\frac{\Delta a}{a} = \frac{\beta(2\theta)}{4\tan\theta\sin\varphi}. \qquad (2)$$

This quantity equals 2.1×10^{-3}. In this case, the overall difference between the relaxed lattice parameter of the CdS film (4.1458 Å) and the lattice parameter of the $Cd_{0.02}Zn_{0.08}S$ substrate (4.1245 Å) in the intergrowth plane is equal to $\Delta a_0/a_0 = 5.2 \times 10^{-3}$. A part of this discrepancy (1.6×10^{-3}) is removed owing to the elastic strain of the film, due to which the ratio of the lattice parameters for the film c/a = 1.6254 is larger compared with that of the substrate (c/a = 1.6186).

Figure 6 shows the profiles of two asymmetrical reflections of the hexagonal phase of the CdSe film which was grown on the $Cd_{0.92}Zn_{0.08}S$(0001) substrate. The widths of the (205) and (106) reflections with asymmetry angles of 37° and 17.4°, respectively, are approximately equal, and a weak (331) reflection from the CdSe cubic phase exists. This permits us to assume that the layered structure with an alternation of thick hexagonal interlayers with thin cubic interlayers, as well as variations in the lattice parameters of the film in the intergrowth plane, is simultaneously present in this film. Note that the (205) reflection of the hexagonal phase for the CdSe film is less broadened compared with the (511) reflection of the cubic phase for the ZnSe film in Fig. 3; both reflections have almost the same Bragg angle. Thus, larger dimensions of the coherent scattering region along the [001] direction are observed for the CdSe films. These dimensions can be estimated from the half-widths of the observed asymmetrical reflections as 350–400 Å. The symmetrical (006) reflection of the CdSe film has the same profile as the reflection of the ZnSe film with a separation of the $K_{\alpha1}$–$K_{\alpha2}$ doublet. However, the peak is shifted to smaller angles due to the larger lattice parameter. It is interesting that, despite the substantially larger lattice mismatch for the CdSe–$Cd_{0.92}Zn_{0.08}S$ system ($\Delta a_0/a_0$ = 4.48%) compared with the CdS–$Cd_{0.92}Zn_{0.08}S$ system ($\Delta a_0/a_0$ = 0.52%), the tetragonal distortion of the CdS and CdSe films is approximately identical owing to elastic strain. Another special feature of the CdSe film is that the cubic interlayers of only one of the two twin components predominate in it. This allows us to assume that there is ordered growth of hexagonal interlayers

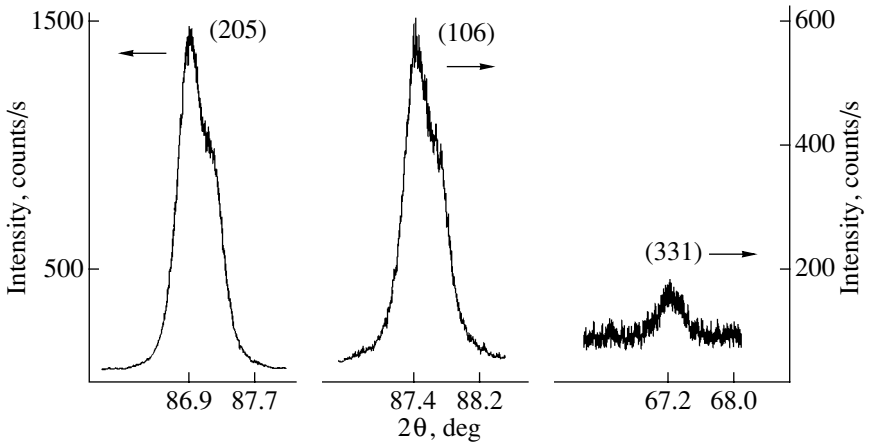

Fig. 6. Diffraction profiles of the asymmetrical (205) and (106) reflections of the hexagonal phase and the (331) reflection of the cubic phase of the CdSe film. Approximately equal widths of the first two reflections and the presence of the cubic phase are indicative of the contribution of both the layer structure of the film and variations in the lattice parameter in the intergrowth plane to broadening of reflections.

with the predominance of an even number of monolayers. The reason for this is that both twins with approximately equal intensities should otherwise be observed statistically.

The investigation of the structure of the $Zn_{1-x}Cd_xSe$ films showed that the content of the hexagonal phase in the range of $0 < x < 0.15$ increases much more rapidly than the content of the cubic phase in the composition range of $0.5 < x < 1$. In this case, the width of interlayers of the prevalent phase regularly decreases. For example, for the film containing 5% of Cd, the dimensions of the coherent scattering region decrease by a factor of approximately 2 compared with the pure ZnSe films. Simultaneously, the structural quality of the film somewhat worsens, which manifests itself in the broadening of the rocking curves of the film and a substantial decrease in the intensity of large-angle reflections. For compositions with $x = 0.15$–0.2, the films grow with the equiprobable formation of interlayers of both cubic and hexagonal phases. It seems to be difficult to determine the exact x value for these substrates due to the superposition of the peak of the hexagonal phase onto the peak of the substrate. It should be noted that a sphalerite–wurtzite structural transition in the $Zn_xCd_{1-x}Se$ crystals was observed for $x = 0.3$–0.5 [27], whereas in the $Zn_{1-x}Mg_xSe$ system it was observed for $x = 0.18$–0.19 [28]. A certain shift of the phase transition to smaller x values in our epilayers compared with the single crystals is apparently associated with the lower temperatures of film growth and the influence of the substrate structure.

5. CONCLUSION

In this study, a novel X-ray diffraction technique for the determination of the concentrations of the cubic and hexagonal phases in $Zn_{1-x}Cd_xSe$ films is developed. The technique also permits one to estimate the interlayer thickness and microstresses from an analysis of the broadening of several asymmetrical reflections simultaneously. It is found that the ZnCdSe films grown by the MOCVD technique contain interlayers of both types in the entire composition range. For pure ZnSe, a cubic structure of twin interlayers is prevalent, whereas a hexagonal structure with the cubic interlayers of one of the twin components is dominant for pure CdSe. The equiprobable growth of both interlayers is observed at $x = 0.15$–0.20. The profiles of reflections of the CdS films are also measured. For these films, a layered structure, which can be detected by this technique, is not observed.

The layered structure of the ZnCdSe films probably leads to spatial carrier separation, which can be the cause of the weak luminescence of these films. Additional investigations of the influence of the layer structure of the films on their optical properties are required.

ACKNOWLEDGMENTS

This study was supported by the comprehensive program of the Presidium of the Russian Academy of Sciences “Low-Dimensional Quantum Structures”; the Federal program “Physics of Solid-State Nanostructures”; the program “Leading Scientific Schools”, project no. 00-15-96624; the research program “NATO for Peace,” grant no. SfP974355; and the Russian Foundation for Basic Research, project no. 01-02-16409.

REFERENCES

1. M. A. Haase, J. Qiu, J. M. DePuydt, and H. Cheng, Appl. Phys. Lett. **59**, 1272 (1991).
2. S. Itoh, K. Nakano, and A. Ishibashi, J. Cryst. Growth **214/215**, 1035 (2000).
3. M. C. Tamargo, L. Zeng, W. Lin, *et al.*, in *Proceedings of 2nd International Symposium on Blue Laser and Light*

Emitting Diodes, Chiba, 1998 (Ohmsha, Tokyo, 1998), p. 703.

4. A. Jia, T. Furushima, M. Kobayashi, *et al.*, J. Cryst. Growth **214/215**, 1085 (2000).
5. Y. Endoh, Y. Kawakami, T. Taguchi, and A. Hiraki, Jpn. J. Appl. Phys. **27**, L2199 (1988).
6. M. P. Halsall, J. E. Nicholls, J. J. Davies, *et al.*, Surf. Sci. **228**, 41 (1990).
7. D. R. T. Zahn, G. Kudlek, U. Rossow, *et al.*, Adv. Mater. Opt. Electron. **3**, 11 (1994).
8. M. Hetterich, S. Petillon, W. Petri, *et al.*, J. Cryst. Growth **159**, 81 (1996).
9. I. V. Bradley, J. P. Creasey, and K. P. O'Donnell, J. Cryst. Growth **184/185**, 728 (1998).
10. H. Umeya, K. Kitamura, A. Jia, *et al.*, J. Cryst. Growth **214/215**, 192 (2000).
11. N. Matsumura, J. Ueda, and J. Saraie, Jpn. J. Appl. Phys. **39**, L1026 (2000).
12. B. V. Novikov, N. R. Grigorieva, R. V. Grigoriev, *et al.*, Phys. Status Solidi B **229**, 69 (2002).
13. W. Lin, M. C. Tamargo, J. Steiner, *et al.*, J. Cryst. Growth **212**, 83 (2000).
14. W. Lin, M. C. Tamargo, H. Y. Wei, *et al.*, J. Vac. Sci. Technol. B **18**, 1711 (2000).
15. V. I. Kozlovsky, V. P. Martovitsky, Ya. K. Skasyrsky, *et al.*, Phys. Status Solidi B **229**, 63 (2002).
16. V. I. Kozlovsky, Ya. K. Skasyrsky, P. I. Kuznetsov, *et al.*, Kratk. Soobshch. Fiz., No. 1, 29 (2002).
17. V. N. Ulasyuk, *Quantoscopes* (Radio i Svyaz', Moscow, 1988).
18. A. A. Davydov, V. N. Ermolov, S. V. Neustroev, and L. P. Pavlova, Neorg. Mater. **28**, 42 (1992).
19. N. R. Grigor'eva, R. V. Grigor'ev, E. P. Denisov, *et al.*, Fiz. Tverd. Tela (St. Petersburg) **42**, 1570 (2000) [Phys. Solid State **42**, 1613 (2000)].
20. E. P. Denisov, A. G. Areshkin, D. L. Fedorov, and S. G. Konnikov, Fiz. Tverd. Tela (St. Petersburg) **39**, 49 (1997) [Phys. Solid State **39**, 41 (1997)].
21. *Acoustical Crystals*, Ed. by M. P. Shaskol'skaya (Nauka, Moscow, 1982).
22. N. V. Belov, *Structure of Ionic Crystals and Metal Phases* (Akad. Nauk SSSR, Moscow, 1947).
23. B. R. Bennet and J. Del Alamo, Appl. Phys. Lett. **58**, 2979 (1991).
24. R. S. Goldman, H. H. Wieder, and K. L. Kavanagh, Appl. Phys. Lett. **67**, 344 (1995).
25. X. B. Zhang and S. K. Hark, J. Cryst. Growth **234**, 373 (2002).
26. S. S. Gorelik, L. N. Rastorguev, and B. A. Skakov, *X-Ray Diffraction and Electron–Optical Analysis* (Metallurgiya, Moscow, 1970).
27. A. S. Nasibov, P. V. Shapkin, Yu. V. Korostelin, *et al.*, Solid State Commun. **78**, 521 (1991).
28. F. Firszt, A. Cichos, P. Diuzewsld, *et al.*, Solid State Commun. **108**, 367 (1998).

Translated by N. Korovin

Semiconductors, Vol. 37, No. 3, 2003, pp. 302–306. Translated from Fizika i Tekhnika Poluprovodnikov, Vol. 37, No. 3, 2003, pp. 318–322.

ELECTRONIC AND OPTICAL PROPERTIES OF SEMICONDUCTORS

Properties of Shallow-Level D^--Centers in Polar Semiconductors

N. I. Kashirina*, V. D. Lakhno*, V. V. Sychev, and M. K. Sheinkman***

** Institute of Semiconductor Physics, National Academy of Sciences of Ukraine, Kiev, 03028 Ukraine*
e-mail: lak@impb.psn.ru
*** Institute of Mathematical Problems in Biology, Russian Academy of Sciences, Pushchino, 142290 Russia*
Submitted June 4, 2002; accepted for publication July 9, 2002

Abstract—The energy of the lowest singlet and triplet terms of shallow-level D^- centers (two electrons bound at a singly charged Coulomb center) in semiconductors with ion bonding is theoretically analyzed. Electron–phonon interaction is described by the Fröhlich Hamiltonian. The D^--center energy is calculated by the Buĭmistrov–Pekar method of canonical transformations for an arbitrary coupling force with phonons. It was shown that, for the entire range of electron–phonon interaction parameters, the Buĭmistrov–Pekar method gives the lowest values of the ground-state energy of the D^- centers and the free bipolaron in comparison with the best available numerical computations of these values which were performed using direct variational methods. The calculations showed the absence of both bound metastable triplet states, corresponding to the lowest triplet term of a D^- center, and a bipolaron for the entire range of parameters of electron–phonon interaction. This is consistent with the Hill theorem concerning the absence of bound excited states of an H^- ion. © *2003 MAIK "Nauka/Interperiodica".*

INTRODUCTION

Two-electron D^- centers in semiconductors (in Si and Ge [1–3], in GaAs, InP, and InSb [4]) are observed when studying the frequency dependence of photoconductivity in the far-infrared region. An atomic analogue of the considered system is the negative ion of hydrogen, H^-, with an ionization energy equal to 0.0555 Ry. If chemical shift and electron–phonon interaction are disregarded, the D^- centers in crystal have the same energy but measured in the effective rydberg Ry* = $m^*e^4/2\varepsilon_0^2\hbar^2$ (where m^* is the effective electron mass, and ε_0 is the static dielectric constant of the crystal). Taking the interaction with phonons into account can result in a significant increase in the binding energy of a two-electron system in crystal in comparison with the value of 0.0555 Ry* [5, 6]. In alkali halide crystals, the F' centers are similar to a D^- center [7].

Recently, studies of the energy structure of two-electron systems have also been extended to low-dimensional systems, including quantum dots [8, 9] and clusters [10, 11]. The energy levels of quasi-two-dimensional systems, which are similar to the D^- centers [14–17] and bipolarons [18] in isotropic crystals, have been studied both experimentally [12, 13] and theoretically. This is partly connected with the fact that interest in similar systems has considerably increased recently in relation to the development of nanotechnologies and the possibility of developing quantum computers based on electron spin resonance [19–21], particularly in Ge–Si structures [21].

In the first studies [7, 22] devoted to the calculation of the energy of two-electron formations, electronic correlations were disregarded that considerably lowered the binding energy of a D^- center. Nevertheless, the Buĭmistrov–Pekar method [22] for calculating the energy of one- and two-electron states in crystals with an arbitrary coupling force of the electron system with phonons is, in our opinion, one of the simplest and most effective methods for calculating the energy spectrum of electron systems in the solid state.

Due to its simplicity, this method is used quite frequently for calculating the energy of specific systems for both one- and two-electronic states in crystals with an arbitrary coupling force of electrons with phonons [5, 23–25]. Nevertheless, it is generally believed that the Buĭmistrov–Pekar method yields less precise values of the energy of two-electron systems in comparison with the method of optimized canonical transformation suggested by Adamowski [6], which presently gives the lowest values for the energy of two-electron systems (bipolarons and D^- centers or bound bipolarons). We will show that with a fairly flexible trial electron wave function (WF), which accounts for interelectronic correlations (direct dependence of the WF on the electron–electron distance), the method of the Buĭmistrov–Pekar yields lower values than the Adamowski method for the entire range of parameters of electron–phonon interaction. The latter circumstance makes it possible to use the above method combined with a tested set of wave functions, which are convenient for analytical calculations, for reliable computation of the energy of two-electron systems (D^- centers, bipolarons, and exchange-coupled

pairs of paramagnetic centers) in anisotropic crystals and in low-dimensional systems with an arbitrary constant of electron–phonon coupling. Previously, this set of functions [26] was tested during the calculation of the bipolaron energy in crystals with an anisotropic effective mass and dielectric constant under conditions of strong electron–phonon coupling.

2. BASIC RELATIONS

In what follows, we use the Feynman system of units in which $\hbar = 1$, $\omega = 1$, and $2m^* = 1$. Hence, $\hbar\omega$ is a unit of energy and $L_0 = \sqrt{\hbar/2m^*\omega_0}$ is a unit of length. The Hamiltonian of the D^- center (or bound bipolaron in [6]) can be written as

$$H = \sum_{\mathbf{k}} a_k^+ a_k + \frac{\beta}{r_{12}} + \sum_{j=1}^{2}\left[-\nabla_j^2 - \frac{\gamma}{r_j} - \sum_{\mathbf{k}}\sqrt{\frac{4\pi\alpha}{V}}\frac{1}{k}(a_k - a_{-k}^+)\exp(i\mathbf{k}\mathbf{r}_j)\right], \quad (1)$$

$$\alpha = \frac{e^2}{2\hbar\omega}\left(\frac{1}{\varepsilon_\infty} - \frac{1}{\varepsilon_0}\right)\frac{1}{L_0}, \quad L_0 = \sqrt{\hbar/2m^*\omega_0},$$

$$\beta = \frac{e^2}{\hbar\omega\varepsilon_\infty L_0} = \frac{2\alpha}{1-\eta}, \quad \gamma = \frac{e^2}{\hbar\omega\varepsilon_0 L_0} = \frac{2\alpha\eta}{1-\eta},$$

where $\mathbf{r}_j$ is a radius vector of the jth electron with an effective mass m^* and r_{12} is the electron–electron distance. We assume that the Coulomb charge is concentrated at the origin. The effect of polarization of a crystal on the Coulomb field of a static charge is taken into account by introducing the static dielectric constant ε_0. The optical dielectric constant ε_∞ is included in the operator of the electron–electron interaction, and a_k^+ (a_k) is the creation (annihilation) operator of a longitudinal optical phonon with a wave vector $\mathbf{k}$. We assume that the phonon frequency is independent of $\mathbf{k}$ and is equal to ω; α is the Fröhlich dimensionless coupling constant, and V is the crystal volume.

2.1. The Buĭmistrov–Pekar Method Applied to Two-Electron Systems in Polar Crystals with Intermediate Electron–Phonon Coupling

In a present-day representation, the Buĭmistrov–Pekar method amounts to application of the canonical transformation $\exp(\alpha S)H\exp(-\alpha S)$ with the unitary operator

$$S = \sum_{\mathbf{k}}[F_{\mathbf{k}}^*(\mathbf{r}_1, \mathbf{r}_2)a_k - F_k(\mathbf{r}_1, \mathbf{r}_2)a_k^+],$$

where $F_k(\mathbf{r}_1, \mathbf{r}_2)$ is a function of the coordinates of the electronic system, to the Hamiltonian (1). Then, the following expressions are valid:

$$\exp(S)a_k\exp(S) \longrightarrow a_k + F_k,$$
$$\exp(S)a_k^+\exp(S) \longrightarrow a_k^+ + F_k^*.$$

After averaging over the phonon variables, we obtain the following functional:

$$H = \frac{\beta}{r_{12}} + \sum_{j=1}^{2}\sum_{\mathbf{k}}\nabla_j F_k^*\nabla_j F_k + \sum_{j=1}^{2}\sum_{\mathbf{k}}\left\{-\nabla_j^2 - \frac{\gamma}{r_j} + V_k[F_k\exp(i\mathbf{k}\mathbf{r}_j) + F_k^*\exp(i\mathbf{k}\mathbf{r}_j)]\right\} + \sum_{\mathbf{k}}F_k F_k^*. \quad (2)$$

Expression (2) is initial for further calculations. Let us choose the function F_k as

$$F_k = C_k + \gamma_k f(\mathbf{r}_1, \mathbf{r}_2), \quad (3)$$

where C_k and γ_k are the variational parameters.

Having substituted (3) in (2) and variating over C_k and γ_k (in contrast to the Buĭmistrov–Pekar method [6], the parameters C_k and γ_k are selected in a specified analytical form), we obtain the following expression for the functional of the ground state of a two-electron system:

$$E_{Bp} = J_S + J_i, \quad (4)$$

$$J_i = -\sum_{\mathbf{k}}V_k^2\frac{\tilde{U}_k^2}{2k^2 + U_k\omega_k}, \quad (5)$$

$$\tilde{U}_k = \langle\Psi_{12}|f_k(\mathbf{r}_1, \mathbf{r}_2)L_k^*(\mathbf{r}_1, \mathbf{r}_2)|\Psi_{12}\rangle - \langle\Psi_{12}|f_k(\mathbf{r}_1, \mathbf{r}_2)|\Psi_{12}\rangle\langle\Psi_{12}|L_k^*(\mathbf{r}_1, \mathbf{r}_2)|\Psi_{12}\rangle, \quad (6)$$

$$L_k^*(\mathbf{r}_1, \mathbf{r}_2) = \exp(-i\mathbf{k}\mathbf{r}_1) + \exp(-i\mathbf{k}\mathbf{r}_2), \quad (7)$$

$$U_k = \langle\Psi_{12}|f_k(\mathbf{r}_1, \mathbf{r}_2)f_k^*(\mathbf{r}_1, \mathbf{r}_2)|\Psi_{12}\rangle - \langle\Psi_{12}|f_k(\mathbf{r}_1, \mathbf{r}_2)|\Psi_{12}\rangle\langle\Psi_{12}|f_k^*(\mathbf{r}_1, \mathbf{r}_2)|\Psi_{12}\rangle. \quad (8)$$

Here, J_i is an addition appropriate for intermediate coupling, and J_S corresponds to the D^--center functional in the limit of strong electron–phonon coupling:

$$J_S = \bar{T}_{12} + \beta\bar{V}_{ee} - \gamma\bar{V}_e + \sum_{\mathbf{k}}V_k^2|\langle\exp(-i\mathbf{k}\mathbf{r}_1) + \exp(-i\mathbf{k}\mathbf{r}_2)\rangle|^2, \quad (9)$$

$$\bar{T}_{12} = -\int\Psi_{12}(\Delta_1 + \Delta_2)\Psi_{12}d\tau, \quad (10)$$

$$\bar{V}_{ee} = \int \frac{|\Psi_{12}|^2}{r_{12}} d\tau, \quad (11)$$

$$\bar{V}_e = \int \frac{|\Psi_{12}|^2}{r_1} d\tau + \int \frac{|\Psi_{12}|^2}{r_2} d\tau. \quad (12)$$

2.2 The Functional of the Ground State of a Two-Electron System

Choosing $f_k(\mathbf{r}_1, \mathbf{r}_2) = L_k^*(\mathbf{r}_1, \mathbf{r}_2)$ and, hence, $\tilde{U}_k = U_k$, we obtain

$$J_i = -\sum_{\mathbf{k}} V_k^2 \frac{U_k^2}{2k^2 + U_k \omega_k}. \quad (13)$$

In the specific case of the absence of electronic correlations, when the WF of an electronic system can be written as the product of one-electron WFs $\Psi(\mathbf{r}_1, \mathbf{r}_2) = \psi(\mathbf{r}_1)\psi(\mathbf{r}_2)$, relation (13) yields

$$J_i = -\sum_{j=1}^{2} \sum_{\mathbf{k}} V_k^2 \frac{[1 - F_k^2(\mathbf{r}_j)]^2}{k^2 + [1 - F_k^2(\mathbf{r}_j)]\omega_k}, \quad (14)$$

where

$$F_k(\mathbf{r}_j) = \int \psi(\mathbf{r}_j) \exp(i\mathbf{k}\mathbf{r}_j) \psi^*(\mathbf{r}_j) d\tau_j.$$

Having substituted (14) in (4), we obtain a functional coinciding with formula (18) from the Buĭmistrov and Pekar paper [22].

With a more general choice of the WF (a nonmultiplicative form corresponding to a consideration of electronic correlations), it is necessary to use a more general functional in which the addition, which is appropriate for intermediate coupling J_i, is defined by expression (13).

In a recent publication [27], which was concerned with the two-center bipolaron of intermediate coupling, the electron WF was selected in the form of a symmetrized product of the polaron wave functions centered at different points, i.e., in a nonmultiplicative form (the Heitler–London method applied to a bipolaron). Thus, the functional with a J_i addition defined by Eq. (14) was used for variation. This is correct only for the specific case when the WFs of a two-electron system are chosen as the product of one-electron WFs. Notably, Mukhomorov [27] varied the incorrect functional and performed erroneous numerical calculations. The correct formulas for calculating the bipolaron energy using the Buĭmistrov–Pekar method were given in [24]; however, the trial function chosen in [24] for the entire range of electron–phonon interaction parameters yielded a higher bipolaron energy in comparison with the results in [28].

3. NUMERICAL CALCULATIONS

Let us choose a two-electron WF as a linear combination of Gaussian orbitals:

$$\Psi(\mathbf{r}_1, \mathbf{r}_2) = \frac{1}{\sqrt{N_{12}}} \sum_{i=1}^{N} C_i [1 + (-1)^S P_{12}] \times \exp(-a_{1i} r_1^2 - 2a_{2i} \mathbf{r}_1 \mathbf{r}_2 - a_{3i} r_2^2), \quad (15)$$

where P_{12} is an interchange operator for the electron coordinates; and the exponent is equal to $S = 0$ and 1 for singlet and triplet states of a two-electron system, respectively. The WF of a polaron and F center is chosen as

$$\Psi_p(\mathbf{r}) = \frac{1}{N_1} \sum_{i=1}^{n} C_i \exp(-a_i r^2), \quad (16)$$

where C_i, a_i, a_{1i}, a_{2i}, and a_{3i} are variational parameters; $\mathbf{r}$ are the electron coordinates in a polaron; $\mathbf{r}_1$ and $\mathbf{r}_2$ are coordinates of the first and second electron in a bipolaron, respectively; and N_{12} and N_1 are normalization factors.

In the limit $\eta \longrightarrow 0$ ($\eta = \varepsilon_\infty/\varepsilon_0$, where ε_∞ and ε_0 are optical and static dielectric constants, respectively) the coupling of electrons to the Coulomb core weakens and the D^- center becomes equivalent to a one-center bipolaron or to a Pekar bipolaron. The one-center configuration of a bipolaron can be considered as an elementary two-electron system in a crystal. At the same time, the functional of this system includes the most complex component describing nonlocal interaction of the two-electron system with the phonon field. From this point of view, the addition of interaction with the field of static charge only insignificantly complicates the numerical calculations of the energy spectrum of a bound polaron or D^- center.

Bipolaron energies E_{Bp}, calculated using the system of Gaussian functions (15) ($S = 0$), are summarized in Table 1. For the entire domain of existence of a bipolaron, the Buĭmistrov–Pekar method yields the lowest ground-state energies for a free bipolaron and the widest region of existence for a bound bipolaron in comparison with the best numerical calculations of these parameters performed using direct variational methods [28]. For comparison, numerical calculations of E_{Bp}^{A}, performed in [28], are also listed in Table 1. The number of terms $N = 5$ in the WF (15) used for calculating the bipolaron energy.

When considering a bound bipolaron in a system, an additional parameter describing the interaction of electrons with the field of static charge appears. Let us express the energy of the D^- center as a function of two dimensionless parameters: the Fröhlich electron–phonon coupling constant $\alpha = e^2/(2r_0\hbar\omega)\tilde{\varepsilon}$ (where $1/\tilde{\varepsilon} = 1/\varepsilon_\infty - 1/\varepsilon_0$, $r_0 = \sqrt{\hbar/2m^*\omega}$, $\hbar\omega$ is the frequency of long-

Table 1. The ground-state energy of a free bipolaron for various parameters α

η	α							
	6		7		9		20	
	E_{Bp}	E_{Bp}^{A}	E_{Bp}	E_{Bp}^{A}	E_{Bp}	E_{Bp}^{A}	E_{Bp}	E_{Bp}^{A}
0	–12.703	–12.601	–16.234	–16.067	–24.927	–24.652	–111.928	–110.504
0.01	–12.595	–12.487	–16.053	–15.91	–24.650	–24.354	–110.497	–109.064
0.1			–14.598	–14.500	–22.068	–21.756	–96.878	–95.335

Note: The parameters E_{Bp}^{A} are taken from [28].

Table 2. The ground-state energy of the D^--center (bound bipolaron) in $\hbar\omega$ units

Crystal	α	R	$\hbar\omega$, meV	E^-	E_0	E_B^-	E_B^0	E_B^-/E_B^0
CdTe	0.272	0.657	21.08	–1.266	–0.965	0.029	0.693	0.042
CdS	0.529	0.783	38.0	–1.931	–1.363	0.039	0.834	0.047
ZnSe	0.45	0.924	31.4	–1.926	–1.428	0.048	0.978	0.049
AgBr	1.64	1.68	15.4	–5.656	–3.818	0.198	2.178	0.091
				-5.637^{L}	-3.817^{L}	0.180^{L}	2.177^{L}	0.083^{L}
						0.132^{A}	2.166^{A}	0.061^{A}
AgCl	1.9	1.90	24.4	–6.668	–4.483	0.285	2.583	0.110
				-6.643^{L}	-4.482^{L}	0.261^{L}	2.582^{L}	0.101^{L}
				-6.662^{A}		0.202^{A}	2.560^{A}	0.078^{A}
CdF_2	2.53	1.274	50.0	–7.357	–4.510	0.317	1.98	0.016

Note: Superscripts L and A indicate the results of calculations in [5] and [6], respectively.

wavelength longitudinal optical phonons, and m^* is the effective electron mass) and the ratio of the effective rydberg to $\hbar\omega$ given by

$$R = m^* e^4/2\varepsilon_0^2\hbar^3\omega = (e^2/2r_0\hbar\omega\varepsilon_0)^2.$$

As an example, Table 2 lists the energies of the ground state of the D^- ($S = 0$) and D^0 centers: E^- and E^0, respectively, for a number of crystals. The binding energy is designated as E_B. All energies are expressed in $\hbar\omega$. The superscripts L and A define the parameters obtained in [5] and [6], respectively. The number of terms in expressions (15) and (16) for the WF, which were used to calculate the energy of D^- and D^0 centers, equals 12.

In order to assess the flexibility of the WFs used for calculating the energy of two-electron systems, we used these WFs to calculate the ground-state energy of the negative hydrogen ion H^- (this atomic system is the closest analogue of a bipolaron in atomic physics). This energy is equal to –1.055470 [$N = 28$ in (15)], whereas the precise value is equal to –1.055502 [29].

The possibility of forming metastable triplet states of D^- centers should be considered separately. This matter has assumed great importance because the absence of bound triplet states of D^- centers (similar to the absence of bound excited states of the H^- ion [30]) is one of the basic conditions for realizing the detection of the spin state of a two-electron system in quantum computers operating on the basis of electron spin resonance [21]. The scheme proposed in [21] can be briefly described as follows: the application of an electric field along the line connecting a singlet-state exchange-coupled pair of shallow-level paramagnetic centers can cause the controlled charge transfer to one of the Coulomb centers and the formation of a D^- center. In the triplet state, a similar combination is impossible. Donors remain neutral, and there is no charge transfer between centers. Due to this circumstance, the spin state of the two-electron system can be observed.

Variatonal calculations with the use of a system of functions (15) for $S = 1$ showed that, for the entire range of parameters of electron–phonon interaction, including the region of extremely strong coupling ($\alpha > 20$), the relation $E_p + E_D \le E_{Dt}$ is valid, where E_p, E_D, E_{Dt} are the energies of a polaron, a neutral donor, and a D^- center in the triplet state, respectively. Thus, electron–phonon interaction in the continuous approximation does not lead to the formation of a metastable triplet state of the D^- center. This is a close analogy to the the-

orem concerning the absence of bound excited states of a negative hydrogen ion H^- [30]. Our calculations showed that the bound state of the triplet bipolaron that formed as a result of coupling to optical phonons is also energetically unfavorable. Our test calculations of the orthohelium energy, with the use of the system of functions (15) for $S = 1$, show that there is good agreement with the experimental values of the orthohelium energy.

It should be noted that an external magnetic field gives rise to upper excited states of the D^- center [31]. Calculations of the triplet states of the D^- center in spherical quantum dots were performed in [8].

4. CONCLUSIONS

The chosen system of Gaussian functions in combination with the Buĭmistrov–Pekar method of calculations yields lower D^- center energies and enables one to perform calculations of the energy spectrum of more complex two-electron systems, such as exchange-coupled pairs of paramagnetic centers, and also obtain reliable values of the ground-state energy of paramagnetic centers and their complexes in anisotropic crystals and low-dimensional systems.

ACKNOWLEDGMENTS

This study was supported by the Russian Foundation for Basic Research, project no. 01-07-90317.

REFERENCES

1. S. Narita, J. Phys. Soc. Jpn. **49**, 173 (1980).
2. P. J. Dean, J. R. Hayes, and W. F. Flood, Phys. Rev. **161**, 711 (1967).
3. P. Gross, M. Gienger, and K. Lassmann, Jpn. J. Appl. Phys. Part 1 **26**, 673 (1987).
4. C. J. Armistead, S. P. Najda, and R. A. Stradling, Solid State Commun. **53**, 1109 (1985).
5. D. M. Larsen, Phys. Rev. B **23**, 628 (1981).
6. J. Adamowski, Phys. Rev. B **39**, 13061 (1989).
7. S. I. Pekar, *Investigations on Electron Theory of Crystals* (GITTL, Moscow, 1951; Report AEC-tr-5575, U.S. Atomic Energy Commission, 1963).
8. B. Szafran, B. Stebe, J. Adamowski, and S. Bednarek, Phys. Rev. B **60**, 15558 (1999).
9. B. Szafran, J. Adamowski, and B. Stebe, J. Phys.: Condens. Matter **10**, 7575 (1998).
10. V. D. Lakhno, Izv. Ross. Akad. Nauk, Ser. Fiz. **60**, 65 (1996).
11. V. D. Lakhno, Izv. Ross. Akad. Nauk, Ser. Fiz. **62**, 1091 (1998).
12. S. Holmes, J. P. Cheng, B. D. McCombe, and W. Schaff, Phys. Rev. Lett. **69**, 2571 (1992).
13. Z. X. Jiang, B. D. McCombe, J.-L. Zhu, and W. Schaff, Phys. Rev. B **56**, R1692 (1997).
14. D. M. Larsen and S. Y. McCann, Phys. Rev. B **45**, 3485 (1992).
15. J. M. Shi, F. M. Peeters, and J. T. Devreese, Phys. Rev. B **51**, 7714 (1995).
16. I. K. Marmorkos, V. A. Schweigert, and F. M. Peeters, Phys. Rev. B **55**, 5065 (1997).
17. J. M. Shi, F. M. Peeters, G. A. Farias, *et al.*, Phys. Rev. B **57**, 3900 (1998).
18. S. Mukhopadhyay and A. Chatterjee, J. Phys.: Condens. Matter **8**, 4017 (1996).
19. A. Barenco, D. Deutsch, and A. Ekert, Phys. Rev. Lett. **74**, 4083 (1995).
20. D. Loss and D. P. DiVincenzo, Phys. Rev. A **57**, 120 (1998).
21. R. Vrijen, E. Yablonovitch, K. Wang, *et al.*, Phys. Rev. A **62**, 012306 (2000).
22. V. M. Buĭmistrov and S. I. Pekar, Zh. Éksp. Teor. Fiz. **32** (5), 1193 (1957) [Sov. Phys. JETP **5**, 970 (1957)].
23. R. S. Brandt and F. C. Brown, Phys. Rev. **181**, 1241 (1969).
24. P. Zh. Baĭmatov, D. Ch. Khuzhakulov, and Kh. T. Sharipov, Fiz. Tverd. Tela (St. Petersburg) **39** (2), 284 (1997) [Phys. Solid State **39**, 248 (1997)].
25. S. A. McGill, K. Cao, W. B. Fowler, and G. G. DeLeo, Phys. Rev. B **57**, 8951 (1998).
26. N. I. Kashirina, E. M. Mozdor, É. A. Pashitskiĭ, and V. I. Sheka, Izv. Ross. Akad. Nauk, Ser. Fiz. **52** (8), 127 (1995).
27. V. K. Mukhomorov, Opt. Spektrosk. **86**, 50 (1999) [Opt. Spectrosc. **86**, 41 (1999)].
28. J. Adamowski and S. Bednarek, J. Phys.: Condens. Matter **4**, 2845 (1992).
29. A. J. Thakkar and V. H. Smith, Jr., Phys. Rev. A **15**, 1 (1977).
30. R. N. Hill, Phys. Rev. Lett. **38**, 643 (1977).
31. D. M. Larsen, Phys. Rev. B **20**, 5217 (1979).

Translated by I. Kucherenko

Semiconductors, Vol. 37, No. 3, 2003, pp. 307–311. Translated from Fizika i Tekhnika Poluprovodnikov, Vol. 37, No. 3, 2003, pp. 323–327.

SEMICONDUCTOR STRUCTURE, INTERFACES, AND SURFACES

On the Modification of a Silicon Surface Studied by Scanning Tunneling Microscopy

V. M. Kornilov* and A. N. Lachinov

Institute of Molecular and Crystal Physics, Ufa Research Center, Russian Academy of Sciences, Ufa, 450075 Russia

** e-mail: kornilov@anrb.ru*

Submitted February 7, 2002; accepted for publication September 10, 2002

Abstract—The results of investigating the surface of Si with a thin oxide layer by scanning tunneling microscopy in air are reported. The tunneling current is shown to represent a superposition of several components. This circumstance makes it possible to suggest that a pseudoprofile is detected instead of the true surface image. The principal laws in modifying the pseudoprofile are established. In the case of positive or negative polarity of a sample, the image is observed in the form of indentations or protrusions, respectively. The electron nature of the modification under observation is suggested, and this suggestion is corroborated by the possibility of implementing write–erase–write cycles for the image of the same surface section. The mechanism of modifying the Si surface is discussed for the model of the insulator–oxide–semiconductor structure, in which an adsorbate layer may serve as an insulator. © *2003 MAIK "Nauka/Interperiodica".*

1. INTRODUCTION

The interface between Si and SiO_2 has a number of unique electrical properties, which are largely responsible for the rapid development of silicon microelectronics. The features of the charge storage and transfer near this interface made it possible to develop a wide variety of semiconductor devices: MIS transistors, charge-coupled devices, nonvolatile memory, etc. [1]. All of these facts help to maintain an interest in investigating interface properties using a wide variety of methods.

In this context, it is very interesting to investigate the processes of redistribution of charge at the Si–SiO_2 interface and to detect them on the nanometer scale. To attain this purpose, scanning tunneling microscopy (STM) seems to be one of the most convenient methods in that it allows for the fact that a set of electrical parameters related to a certain point of the sample corresponds to each point of the STM image. Under the conditions of ultrahigh vacuum and a specially cleansed surface, the case of direct tunneling to unoccupied states is implemented and the obtained STM image shows the best correlation with the surface morphology.

Even the first STM studies of Si in air indicated that an oxide on the Si surface significantly impedes the measurement and maintaining of the tunneling current [2]. This circumstance makes it necessary to use various methods of etching and passivating the Si surface [3–5]. In any event, a necessary stage involves removing a SiO_2 layer, owing to which it is possible to obtain information only about the geometrical parameters of the surface under investigation. However, more recently, the possibility of investigating physical properties of the Si–SiO_2 interface by STM methods was justified theoretically [6].

In study [7], the electric-field induction of the current contrast on Si surfaces with thin oxide layers was experimentally investigated. The technique used (the constant-height mode) requires a very high surface quality, which restricts the possibilities of this method to small areas whose roughness is lower than the atomic roughness.

In studies [8, 9], the possibility of modifying a passivated Si surface upon STM investigations in air was shown. The modified sections had the form of indentations on the surface. It was suggested that O ions from the adsorbate layer migrate over the surface and chemically combine with Si atoms in the areas where the tunneling current is located. At the same time, it was shown in [10] that the local oxidation of the Si surface in ultrahigh vacuum leads to the appearance of protrusions. Recent studies [11, 12] show that the mechanism of the processes occurring on a silicon surface during STM investigations has not been completely clarified, although the effect itself is very interesting from the viewpoint of the possibility of ultrahigh-density data writing.

In this context, we posed the problem of studying the mechanism of the processes leading to the modification of the Si surface during STM investigations of Si in air depending on the scanning parameters.

2. EXPERIMENTAL

For the experiment, we used single-crystal *n*-Si (100) wafers intended for the production of integrated circuits. The Si surface, which was polished during the

1063-7826/03/3703-0307$24.00 © 2003 MAIK "Nauka/Interperiodica"

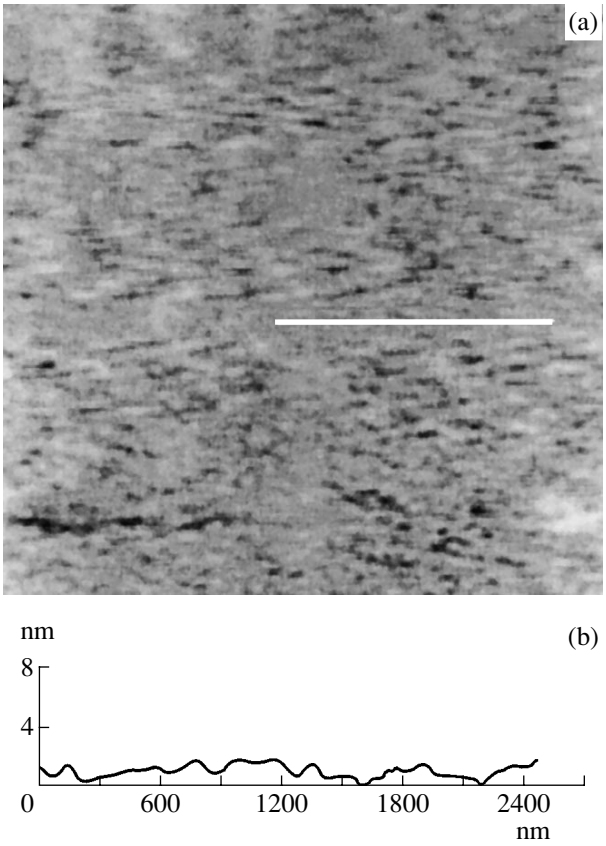

Fig. 1. (a) Typical image of the initial (unmodified) surface of *n*-Si(001) with a native SiO_2 oxide layer and (b) the surface profile corresponding to the line in the image. The polarity of the sample is negative, the scan size is 5.7×5.7 μm^2, and the scanning parameters are $U = -3.54$ V and $I = 0.08$ nA.

manufacturing process, was subjected to no additional treatment. In this case, it is known that there is a native SiO_2 layer on the surface with a thickness on the order of several nanometers. While on the subject of the Si surface, in what follows, we mean just this situation.

This study was performed using an SMM-2000T scanning multimode microscope [13], which provides for a coordinate resolution in air down to 0.3 nm in the surface and down to 0.1 nm along the *z* axis perpendicular to the surface. The tunneling current *I* was varied from 0.01 to 160 nA, and the voltage *U* across the needle–sample gap ranged from 0 to ±10 V. The probe was made of a Pt wire, and the probe tip was formed by a bevel cut.

3. RESULTS

In Fig. 1, we show the STM image of the initial Si surface. The thickness of the oxide film on Si, which was close to the tunneling depth, enabled us to use the mode for maintaining a constant tunneling current; however, the quality of the obtained surface image was low. The analysis of the results of multiple measurements showed that, apparently, it makes sense to speak about detecting a peculiar pseudoprofile. In this case, the current flowing through the system can be represented in the form of a superposition of several components. The first component is the direct-tunneling current; the second component is caused by Fowler–Nordheim tunneling (in relatively strong fields); and the third component is due to the leakage currents in the sample surface (for low given currents). Varying the scanning parameters, we can isolate a particular com-

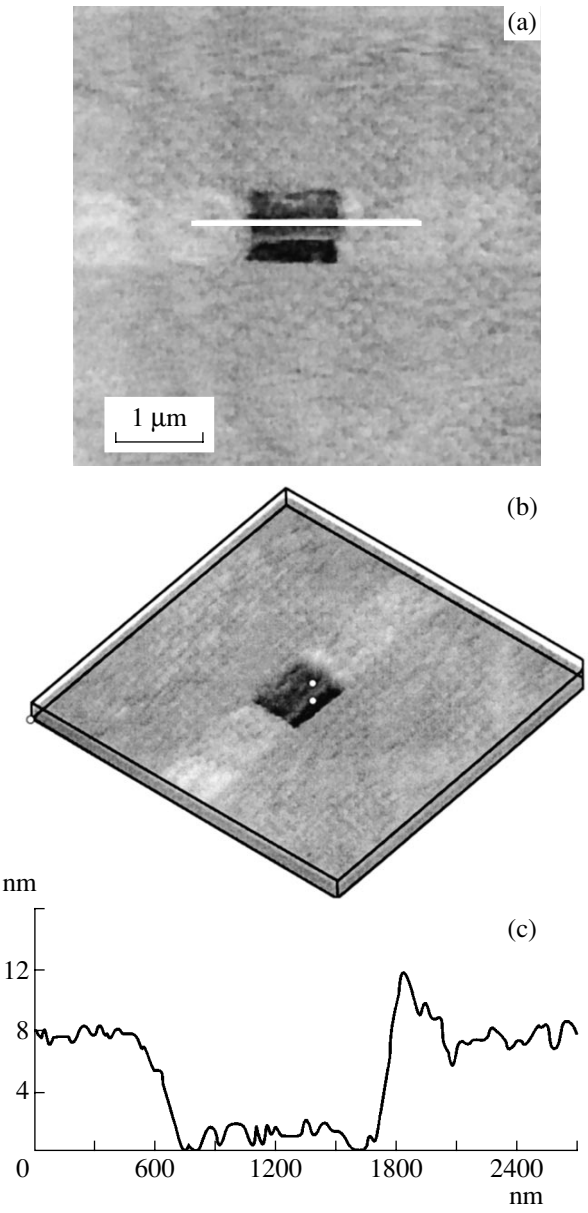

Fig. 2. Image of the Si surface modified at the positive polarity of the sample: (a) morphology, (b) three-dimensional representation, and (c) profile. The modification voltage is +4.5 V, and the reading voltage is +3.26 V. The total scan size is 5.86×5.86 μm^2, the modified-section size is 0.9×0.9 μm^2, and the average depth is 6–8 nm.

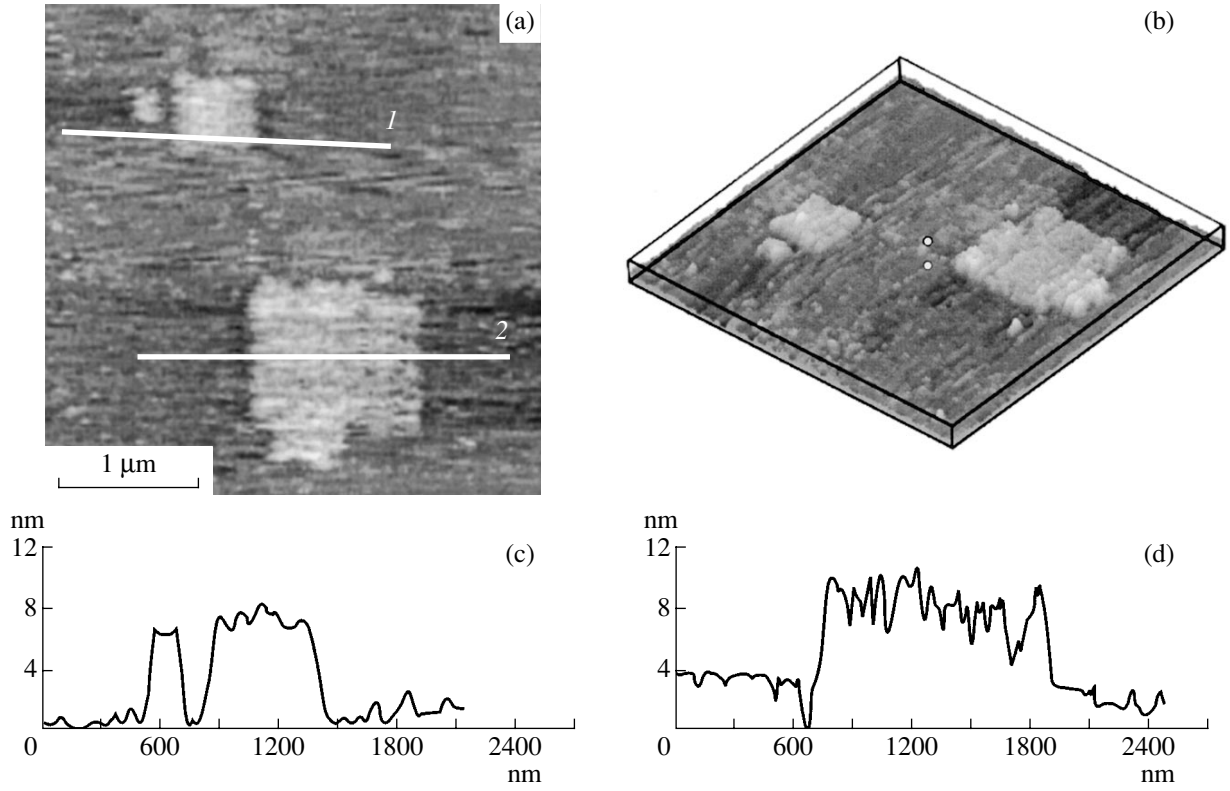

Fig. 3. Image of the Si surface at the negative polarity of the sample: (a) morphology, (b) three-dimensional representation, (c) profile along line *1*, and (d) profile along line *2*. The modification voltage is –4.5 V, and the reading voltage is –3.34 V. The total scan size is 3.5×3.5 μm^2; the sizes of the modified sections are 0.2×0.2, 0.5×0.5, and 1×1 μm^2; and the average depth is 5–8 nm.

ponent of the detected current in the form of a feature in the pseudoprofile image. The possibility of forming the pseudoprofile is corroborated by the existence of an extended section (plateau) in the removal curve obtained from the STM investigations in air [14].

In Fig. 2, we show a typical image of the modified section on the Si surface. The sequence of operations for obtaining this image was as follows. We preliminarily scanned a relatively small section of the surface (the modification mode). Then, we scanned a larger area containing the modified section (the read mode). It was established that there is a relationship between the scanning parameters at which a stable observation of the image is possible: a voltage of 3 V < U_{vis} < 6 V and a current of 10 pA < I < 100 pA. The modification of the sample-surface profile occurred when the applied voltage exceeded a certain threshold value $U_{thr} \approx 2.8$–3.0 V. The best results were obtained under the condition that the modification voltage exceeded the reading voltage by more than $\Delta U \approx 0.4$ V.

In the process of measuring, it was established that the formation of an indentation in the STM image occurred under positive voltage across the sample and at a scanning voltage $U_s > U_{thr}$. The obtained feature was observed when scanning the surface section of a larger area at a voltage U_{vis} of the same polarity, provided that $U_s > U_{vis} > U_{thr}$.

If the polarity changed (minus at the sample), the section scanned with an elevated voltage was read as a protrusion. In Fig. 3, we show the final result of the successive modification of several sections of various sizes. The image of three marks in Fig. 3 is the result of

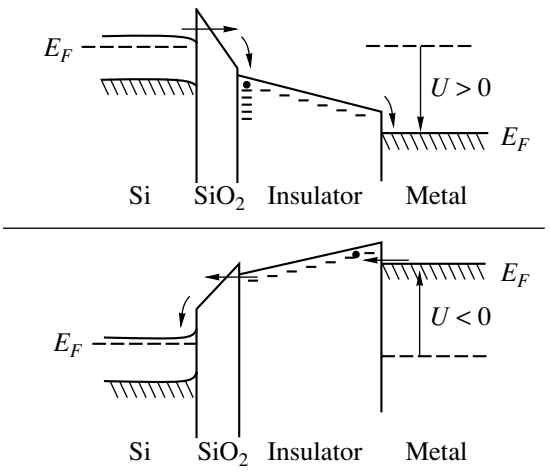

Fig. 4. Band diagrams plotted for a multilayer experimental configuration at the negative (upper figure) and positive (lower figure) polarities of the voltage U across the sample. The arrows indicate the direction of the charge-carrier motion. E_F is the Fermi level.

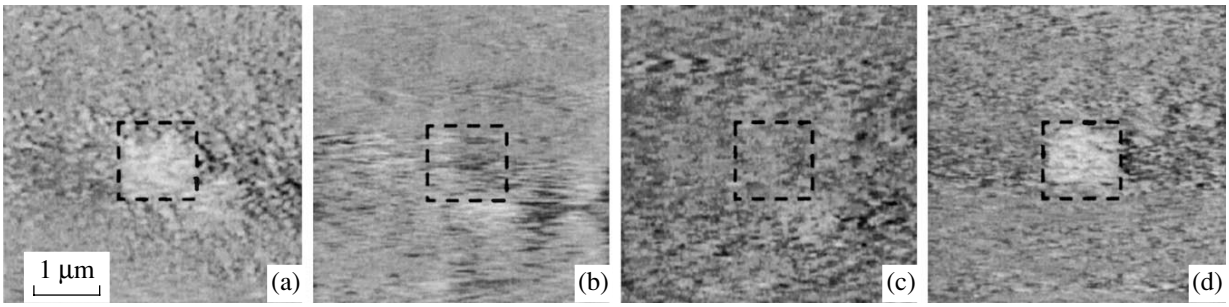

Fig. 5. Illustration of the possibility of rewriting information at the same section of the sample surface. The scan size is 5.8 × 5.8 μm^2; the modified place is outlined by the dashed line. (a) Image of the modified section of the Si surface, the writing voltage is –4.5 V, the reading voltage is –3.14 V; (b) the same section, the reading voltage is +3.3 V; (c) the same section, the reproduction voltage is – 3.14 V; (d) the image of a new mark formed at the place of the previous mark under the conditions similar to case (a).

implementation of the step-by-step modification of the surface. During each stage, only one mark was "drawn." Thereafter, its image was controlled during the next scanning of a larger area, as was described above. Thus, we first obtained the image of one mark, then of two marks, and, finally, of three marks.

It should be noted that the scanning parameters were similar (in magnitude) in the cases of operation with a differing polarity of the sample. However, a substantial distinction consisted in the nature of the obtained image. In the case of negative polarity, the modified profile was revealed as protrusions on the surface and was somewhat structured; i.e., the observed protrusions usually involved finer elements (Fig. 3, profile). For the positive polarity, the image arises in the form of an indentation and there is no similar structurization (Fig. 2, profile).

Apparently, one can write and read graphic information on the Si surface by means of the STM, with the nature of the surface modification being dependent on the polarity of the operation voltage.

4. DISCUSSION

It is evident that, operating with the STM images obtained in air, it is necessary to take into account the presence of the layer of molecules adsorbed on the sample surface. Apparently, the adsorbate layer on the surface of oxidized Si represents an additional potential barrier; thus, in the general case, we deal with metal–insulator–oxide–semiconductor structures (STM probe–adsorbate layer–SiO_2 layer–Si). It is well known that such structures are used as elements of energy-independent memory based on the injected-charge capture in the insulator layer [1]. The charge captured in the insulator may substantially influence the parameters of tunneling through the whole system. This circumstance must correspondingly affect the STM image.

Let us consider the schematic representation of the energy-barrier diagram shown in Fig. 4 [1] for such a system. With a negative polarity of the semiconductor, the *n*-Si surface operates in the enhancement mode. The scanning at an elevated voltage leads to the situation where the charge carriers (electrons in this case) tunnel through the oxide layer according to the Fowler–Nordheim law. Some portion of them is captured by traps in the adsorbate layer, and some portion is involved in the formation of the through tunneling current. It is noteworthy that the scanning voltage in both modification and reading modes must be higher than the potential barrier at the Si–SiO_2 interface (3.2 eV).

When there is positive polarity of the sample, the surface layer becomes depleted or even inversed, which may substantially reduce the probability of tunneling from the probe to the sample.

From the suggested model for modifying the charge state of the interface, it follows that this state can be changed by changing the sample polarity. In other words, we suggest that it is possible to control the written information, implementing the write–read, write–erase, and write–read cycles by altering the polarity and, correspondingly, changing the profile shape. It should be noted that the write–read cycles were always performed using the same polarity. An attempt to read an image section scanned at another polarity usually resulted in the distortion of the image or in the failure of microscope operation.

We succeeded in implementing the possibility of rewriting the data by changing the polarity as follows (Fig. 5). First, the image of a modified section of the surface was obtained under negative polarity (the square mark in Fig. 5a). This section was then scanned at under positive polarity (Fig. 5b). In this case, the mark was found to be gradually destroyed. Subsequent scanning under negative polarity (Fig. 5c) showed that there was no mark. In Fig. 5d, the image of a new mark written in the place of the preceding one (see Fig. 5a) is shown.

5. CONCLUSIONS

Thus, we report the following results. First, the nature of modification depends on the polarity of the applied voltage (under negative polarity of the sample,

a protrusion is formed; under positive polarity, this is an indentation). Second, the manifestation of this effect heavily depends on the relationship between the writing and reading parameters. This fact points to the charge nature of the observed modifications. Third, we show the possibility of rewriting data, which is unlikely in the case of electrochemical modification of the surface because the process of formation of SiO_2 is irreversible under these conditions.

Apparently, the modification of the Si surface during the STM investigation cannot be explained only by electrochemical processes such as depassivation and oxidation. On the surface under investigation, a structure of the insulator–oxide–semiconductor type is formed, in which the adsorbate layer plays the role of insulator. The carriers injected through the oxide layer are captured and localized in the insulator layer. The STM methods make it possible to stimulate the injection processes and to detect alternations that arise in the charge distribution in the surface region of the $Si–SiO_2$ system.

REFERENCES

1. S. Sze, *Physics of Semiconductor Devices* (Wiley, New York, 1981; Mir, Moscow, 1984), Vols. 1 and 2.
2. A. A. Bukharaev, A. V. Nazarov, V. Yu. Petukhov, and K. M. Salikhov, Pis'ma Zh. Tekh. Fiz. **16** (6), 8 (1990) [Sov. Tech. Phys. Lett. **16**, 207 (1990)].
3. M. S. Khaĭkin, A. M. Troyanovskiĭ, V. S. Édel'man, *et al.*, Pis'ma Zh. Éksp. Teor. Fiz. **44**, 193 (1986) [JETP Lett. **44**, 245 (1986)].
4. V. V. Levenets, V. I. Beklemishev, E. P. Kirilenko, *et al.*, Jpn. J. Appl. Phys. **34**, 1723 (1995).
5. D. V. Vyalykh and S. I. Fedoseenko, Fiz. Tekh. Poluprovodn. (St. Petersburg) **33**, 708 (1999) [Semiconductors **33**, 654 (1999)].
6. M. I. Sumetskii and H. U. Baranger, Appl. Phys. Lett. **66**, 1352 (1995).
7. A. V. Yukhnevich, O. P. Losik, V. L. Kuznetsov, and A. V. Panenko, Poverkhnost, No. 8, 95 (2001).
8. J. A. Dagata, J. Schneir, H. H. Harary, *et al.*, Appl. Phys. Lett. **56**, 2001 (1990).
9. L. N. Bolotov, V. A. Kozlov, I. V. Makarenko, and A. N. Titkov, Fiz. Tekh. Poluprovodn. (St. Petersburg) **27**, 1375 (1993) [Semiconductors **27**, 760 (1993)].
10. J. W. Lyding, T.-C. Shen, J. S. Hubacek, *et al.*, Appl. Phys. Lett. **64**, 2010 (1994).
11. J. A. Dagata, T. Inoue, J. Itoh, and H. Yokoyama, Appl. Phys. Lett. **73**, 271 (1998).
12. G. Abadal, F. Perez-Murano, N. Barniol, and X. Aymerich, Appl. Phys. A **66**, 791 (1998).
13. *Scanning Multimode Microscope SMM-2000T* (ZAO KPD, Tekhnopark MIÉT, Zelenograd, 1997).
14. S. Yu. Vasil'ev and A. V. Denisov, Zh. Tekh. Fiz. **70**, 100 (2000) [Tech. Phys. **45**, 99 (2000)].

Translated by V. Bukhanov

Semiconductors, Vol. 37, No. 3, 2003, pp. 312–313. Translated from Fizika i Tekhnika Poluprovodnikov, Vol. 37, No. 3, 2003, pp. 328–329.

LOW-DIMENSIONAL SYSTEMS

Phonon Spectra of $(GaAs)_n(Ga_{1-x}Al_xAs)_m$ Superlattices According to the Keating Model

E. N. Prykina*, Yu. I. Polygalov, and A. V. Kopytov

Kemerovo State University, ul. Krasnaya 6, Kemerovo, 650043 Russia

**e-mail: Selena@rsl.kemsu.ru*

Submitted March 25, 2002; accepted for publication June 25, 2002

Abstract—Phonon spectra of $(GaAs)_n(Ga_{1-x}Al_xAs)_m$ superlattices were calculated using the Keating model with allowance made for long-range forces. The calculated summed longitudinal acoustical branches are consistent with observed experimental Raman doublets. The tendency towards a shift to higher frequencies of longitudinal optical modes as the number of GaAs monolayers increases, which is observed both in calculations and in experiments, is caused by localization of these modes within the GaAs layer. *© 2003 MAIK "Nauka/Interperiodica".*

Experimental data on the phonon spectrum of GaAs/GaAlAs(001) superlattices (SLs) have been reported in a large number of publications. The GaAs/GaAlAs system is one of the best experimentally studied heterostructures and represents a model object for investigations. To date, the phonon spectrum of the above SLs has been calculated on the basis of simple models (such as the linear-chain model, the dielectric continuous model, and the elastic-continuum model), which do not adequately account for special features of the SL phonon spectrum.

In this paper, we report the results of studying the special features of vibrational modes in $(GaAs)_n(Ga_{1-x}Al_xAs)_m$ SLs according to the Keating model with allowance made for long-range Coulomb forces. We used this model previously to analyze the lattice vibrations in strained ZnSe/ZnS, ZnSe/ZnTe, and ZnS/ZnTe SLs [1].

In order to simulate disorder in calculations of phonon spectra in solid solutions and in SLs based on these solid solutions, one has to use a large supercell, which can involve computational difficulties. In this study, we use the approximation of a pseudounit cell composed of $(1 - x)$Ga, xAl, and As atoms [2, 3]. In Table 1, we list the calculated frequencies of summed longitudinal acoustical (LA) phonons in the $(GaAs)_{15}(Ga_{0.7}Al_{0.3}As)_3$ SL; for the sake of comparison, experimental values of corresponding frequencies are also listed. In Table 1, k is the number of the branch of summed phonons and, for a specified k, the signs "∓" correspond to two dispersion branches, which are experimentally observed as doublets in the Raman spectra [4]. It can be seen that the calculated phonon frequencies are in good agreement with frequencies of experimentally observed Raman doublets.

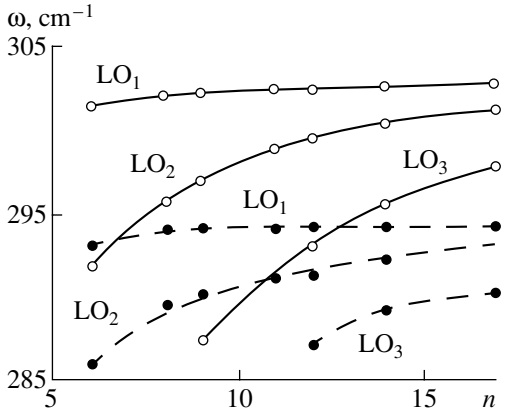

Dependences of frequencies of longitudinal optical (LO) phonons in a $(GaAs)_n(Ga_{1-x}Al_xAs)_m$ superlattice on the number of monolayers n. Open circles correspond to the results of calculations based on the Keating model. Filled circles represent experimental data [5].

1063-7826/03/3703-0312$24.00 © 2003 MAIK "Nauka/Interperiodica"

Table 1. Frequencies of summed LA phonons in the $(GaAs)_{15}(Ga_{0.7}Al_{0.3}As)_3$ superlattice (the frequencies are expressed in cm^{-1})

k	Our calculation	Experiment [4]
–1	29	26
+1	33	31
–2	58	57
+2	62	63
–3	88	89
+3	90	94

Table 2. Frequencies of LO phonons in a $(GaAs)_n(Ga_{1-x}Al_xAs)_m$ superlattice in the range of GaAs vibrations (the frequencies are expressed in cm^{-1})

Superlattice parameters			LO_1		LO_2		LO_3	
n	m	x	our calculation	experiment [5]	our calculation	experiment [5]	our calculation	experiment [5]
6	4	0.123	302	293	291	286		
8	6	0.126	302	294	292	289.5		
9	9	0.147	302	294	297	290		
11	11	0.15	302	294	299	291	292	
12	7	0.141	303	294	299	291	293	287
14	14	0.15	303	294	300	292	296	289
17	12	0.145	303	294	301	–	298	290

In the figure, we show the calculated and experimental [5] frequencies of longitudinal optical (LO) vibrations in a $(GaAs)_n(Ga_{1-x}Al_xAs)_m$ SL in relation to the number of monolayers n. The values of m, mole fraction x, and the number of monolayers n correspond to those in Table 2. An analysis of the frequencies of vibrational modes LO_1, LO_2, and LO_3 calculated by us shows that the tendency toward a shift of the phonons under investigation to higher frequencies, which is observed both in experiments and in calculations, is caused by localization of these phonons in the GaAs layer.

REFERENCES

1. E. N. Prykina, Yu. I. Polygalov, and A. V. Kopytov, Fiz. Tekh. Poluprovodn. (St. Petersburg) **35**, 89 (2001) [Semiconductors **35**, 91 (2001)].
2. I. Lee, S. M. Goodnick, M. Gulia, *et al.*, Phys. Rev. B **51**, 7046 (1995).
3. I. F. Chang and S. S. Mitra, Adv. Phys. **20**, 359 (1971).
4. M. V. Klein, *Raman Spectroscopy: Sixty Years on Amsterdam* (1989), p. 203.
5. B. Jusserand and D. Paquet, Phys. Rev. B. **30**, 6245 (1984).

Translated by A. Spitsyn

Semiconductors, Vol. 37, No. 3, 2003, pp. 314–316. Translated from Fizika i Tekhnika Poluprovodnikov, Vol. 37, No. 3, 2003, pp. 330–333.

LOW-DIMENSIONAL SYSTEMS

Luminescence from ZnO Quantum Dots Deposited with Synthetic Opal

A. N. Gruzintsev*, V. T. Volkov*, G. A. Emel'chenko, I. A. Karpov**, V. M. Masalov*, G. M. Mikhaĭlov*, and E. E. Yakimov***

** Institute of Microelectronic Technology and Ultrahigh-Purity Materials, Russian Academy of Sciences, Chernogolovka, Moscow oblast, 142432 Russia*

e-mail: gran@ipmt-hpm.ac.ru

*** Institute of Solid State Physics, Chernogolovka, Moscow oblast, 142432 Russia*

Submitted June 25, 2002; accepted for publication June 27, 2002

Abstract—Photoluminescence from ZnO layers of varied thickness deposited onto the surface of synthetic opal has been studied. Narrow peaks of luminescence in the excitonic spectral range, related to quantum confinement of the electron wave functions, have been observed. The formation of ZnO quantum dots (QD) within the opal voids in the second subsurface layer has been confirmed by atomic force microscopy and by studying the angular dependence of the luminescence spectra. © *2003 MAIK "Nauka/Interperiodica".*

1. INTRODUCTION

Along with their applications as passive photonic crystals, synthetic opals can be used as matrices for the formation of 3D arrays of nanoscale electronic devices. For example, studies of opal–Pt–Si nanocomposites [1, 2] have demonstrated that 3D-ordered Schottky barriers can be formed on the inner surface of opal voids. Later, electron microscopy was used to show the formation of GaN crystals in the opal voids [3]. The study of optical reflection confirmed that 3D ordering is retained in opal–GaN composites.

However, in studying 3D-ordered nanostructures of this kind, their luminescent properties are of primary interest. The reason is that the existence of a photonic gap in the visible spectral range and the quantum confinement of the electron wave functions can allow substantial modification and improvement of the emission characteristics of these structures. The aim of this study was to investigate the luminescent properties of a spatially coherent array of QDs and profiled ZnO layers which were obtained with the use of synthetic opal.

The fabrication of high-quality nanostructures based on ZnO films, with prevalent emission in the UV region, is necessary for the design of high-power semiconductor light sources for this spectral range. This semiconductor is characterized by a wide (3.4 eV [4]) band gap, direct interband transitions, and low resistivity, which allows for its application to semiconductor LEDs [5], transparent contacts, and windows of solar cells [6, 7]. Being completely analogous to GaN in its optical, electrical, and crystal lattice parameters, ZnO is much easier to fabricate and exhibits a higher reliability in operation. Earlier [8], we observed stimulated UV (397 nm) luminescence from ZnO films on oxidized silicon under excitation with a nitrogen laser. Depending on their crystal structure and defect properties, ZnO films can serve as the basis for the production of structures with an intense emission band in the range of electron–hole recombination at room temperature. We discuss the effect of quantum confinement of the carrier wave functions on the intensity and spectral characteristics of this emission in ZnO deposited on a synthetic opal substrate.

2. EXPERIMENTAL

Synthetic opals with spheres 279 nm in diameter forming a regular face-centered cubic lattice and deposited onto a glass substrate were used (Fig. 1). ZnO films with thicknesses of 90, 300, and 600 nm were deposited on opals via high-vacuum electron beam sputtering in an L-560 (Leubold Haereus) machine. The microstructure of the obtained layers was studied by atomic force microscopy (AFM). The photoluminescence (PL) spectra of ZnO–opal films were recorded at liquid nitrogen temperature under pulsed excitation with an LGI-505 nitrogen laser. The spectra were analyzed using a computerized MDR-6 double-grating monochromator, which provided a spectral resolution of no worse than 1 meV for the slits used. The ZnO film thickness was measured with a profilometer after deposition onto that section of glass where no synthetic opal had been deposited.

3. RESULTS AND DISCUSSION

Figure 2 shows the PL spectra of ZnO–opal films with the smallest thickness of 90 nm. The luminescence was detected at a varied angle θ with respect to the normal to the opal surface, while the angle between the exciting laser beam and the axis of the collector lens

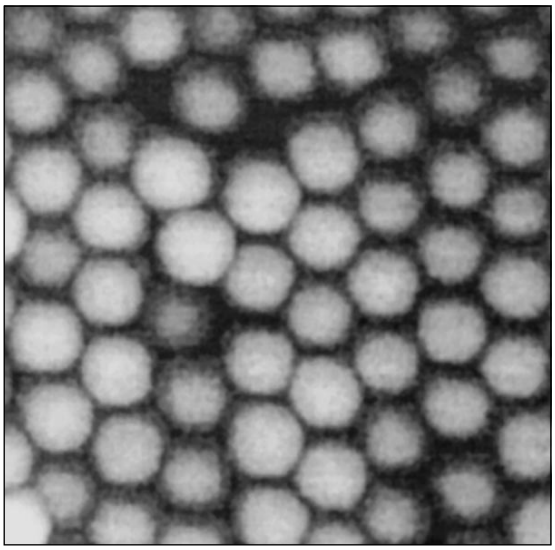

Fig. 1. AFM image of the surface of synthetic opal on glass used as a substrate in the deposition of ZnO layers of varied thickness. The scan field size is 1960×1960 nm^2.

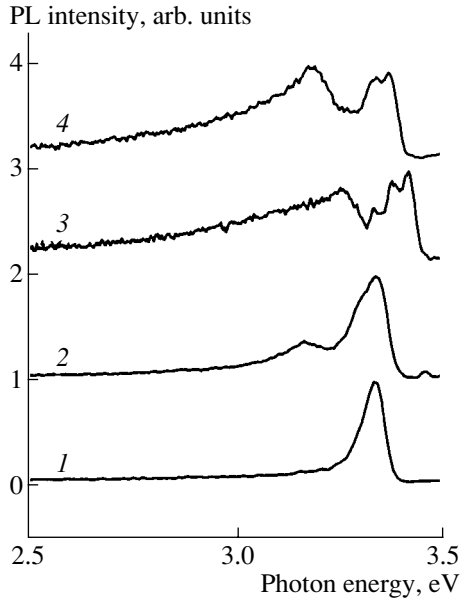

Fig. 2. PL spectra of 90-nm-thick ZnO films on (*1*) glass and (*2–4*) ZnO–opal structures. The detection angle θ: (*2*) 20°, (*3*) 35°, (*4*) 45°. The angle θ is counted off from the normal to the film surface. The temperature of experiment was 80 K.

remained constant at 45°. For comparison, curve *1* represents the PL spectrum of a ZnO film of the same thickness, but deposited onto glass without opal. In the latter case, only an excitonic peak at 3.33 eV is observed. In the PL spectra recorded at 35° and 45° (curves *3* and *4*), the excitonic peak splits into several narrow lines peaked at 3.33, 3.373, and 3.413 eV and shifts to shorter wavelengths. This effect can be attributed to quantum confinement of the electron wave functions in ZnO QDs, which are formed within the opal voids in the second subsurface layer.

According to AFM data, the lateral size of these QDs is less than 40 nm (Fig. 1). The QDs are effectively excited with the nitrogen laser at the detection angles of 35°–45°. The lack of the shortest wavelength peak at 3.413 eV in curve *4* (Fig. 2) can be attributed to the reabsorption of luminescence in the upper opal spheres covered with ZnO. These ZnO islands are significantly larger (280 nm) and exhibit characteristic PL spectra (curve *2*) without narrow peaks related to quantum confinement. Only the surface ZnO–opal spheres, which shade the QDs located in the second subsurface layer, are excited at a detection angle of 20°. Along with a common excitonic line at 3.33 eV, this spectrum shows long-wavelength edge luminescence at 3.16 eV, which is related to imperfections of the crystal structure.

Deeper scrutiny of the ZnO–opal spatial structure with a ZnO layer of small thickness under the experimental arrangement for PL detection shows that QDs in the second subsurface layer can be excited with a nitrogen laser only at detection angles θ over 30°. At lower angles, the spheres of the first surface layer of opal (also covered with ZnO) shade the QDs from the exciting laser beam. Therefore, the PL spectrum recorded at a detection angle of 20° (Fig. 2, curve *2*) represents the luminescence from upper hemispheres of the surface of opal spheres covered with a ZnO layer. As the size of these hemispheres is large, quantum confinement of electron wave functions does not occur and the excitonic emission is not split into several narrow lines typical of QDs. A comparison of the shapes of spectral lines recorded from these hemispheres (curve *2*) and from the films on glass (curve *1*) shows that the crystal structure of ZnO on the hemispheres is more amorphous, which is indicated by the broadening of the excitonic peak and appearance of red (3.16 eV) emission. The AFM data show that the surface of ZnO on the opal spheres is piecewise-planar (like a soccer ball), rather than spherical. Each planar fragment (of 30–60 nm in size) of this surface probably represents a single-crystal ZnO grain.

The increase in the film thickness to 300 nm results in a considerable modification of the PL spectra of the ZnO–opal structure (Fig. 3). It is necessary to note that, in this case, the deposited ZnO film is solid, as indicated by AFM. As seen, the PL spectra are virtually independent of the excitation and detection angles (curves *2–4*), but differ slightly from the spectrum of planar ZnO films of the same thickness deposited on the common glass (curve *1*). For planar films, the excitonic peak at 3.339 eV is significantly narrower. For films on opal, the luminescence peak is shifted to 3.30 eV and two shoulders are observed in the short- and long-wavelength regions. This broadening can be unambiguously attributed to the deterioration of the crystal structure of 300-nm-thick ZnO on opal, in contrast to the case of the glass substrate. In the case of the opal

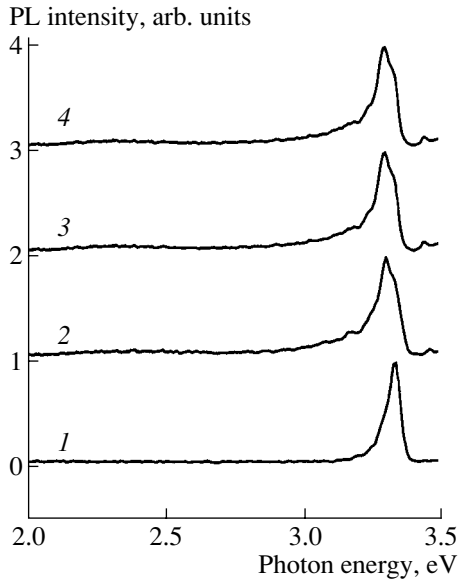

Fig. 3. PL spectra of 300-nm-thick ZnO films. The designations and temperature are the same as in Fig. 2.

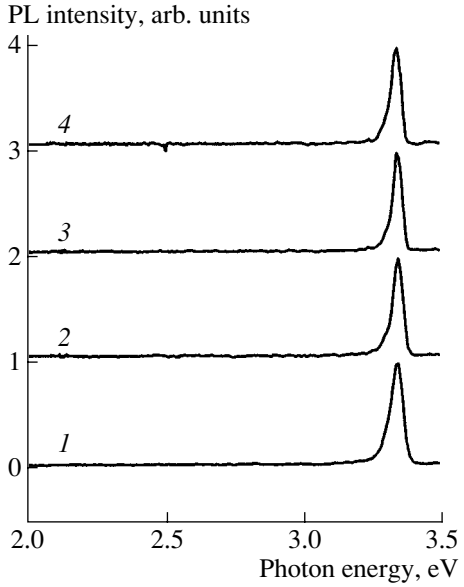

Fig. 4. PL spectra of 600-nm-thick ZnO films. The designations and temperature are the same as in Fig. 2.

substrate, the structure of the semiconductor material is more amorphous; this results in the broadening of the excitonic emission peak.

The surface of ZnO films on opal is smoothed even more when the film thickness increases to 600 nm. Figure 4 shows typical PL spectra of films deposited on opal and glass; they are virtually identical. Only a narrow peak of excitonic luminescence at 3.339 eV is observed. Since the exciting radiation of the nitrogen laser (337.1 nm) is completely absorbed by the upper ZnO layer with a thickness of 100–200 nm, it can be concluded that the opal substrate has no effect on the crystallinity and stoichiometry of the surface layer of thick films.

4. CONCLUSIONS

ZnO–opal structures with a thin (90 nm) zinc oxide layer demonstrate UV excitonic photoluminescence from QDs formed in the second subsurface layer. When the layer thickness increases to 300 and 600 nm, the ZnO layer becomes solid, rather than being composed of separate QDs, and the effect of quantum confinement on electronic states disappears.

The process of semiconductor QD formation with the use of an external mask of opal spheres is fundamentally different from QD self-arrangement in solid solutions [9]. In our case, the scatter in the QD size is much narrower and the arrangement of QDs (within the opal voids) is spatially coherent. The suggested technology for QD formation enables subsequent elimination of the opal matrix by selecting an appropriate etchant composition, with only fragments of ZnO semiconductor material remaining on the substrate.

ACKNOWLEDGMENTS

This study was supported by INTAS (project no. 2002-0796).

REFERENCES

1. V. N. Bogomolov, N. A. Feoktistov, V. G. Golubev, *et al.*, J. Non-Cryst. Solids **266–269**, 1021 (2000).
2. C. Diaz-Guerra, J. Piqueras, V. G. Golubev, *et al.*, Appl. Phys. Lett. **77**, 3194 (2000).
3. V. G. Golubev, D. A. Kurdyukov, A. V. Medvedev, *et al.*, Fiz. Tekh. Poluprovodn. (St. Petersburg) **35**, 1376 (2001) [Semiconductors **35**, 1320 (2001)].
4. Y. Chen, D. M. Bagnall, Z. Zhu, *et al.*, J. Cryst. Growth **181**, 165 (1997).
5. Y. R. Ray, W. J. Kim, and H. W. White, J. Cryst. Growth **219**, 419 (2000).
6. A. N. Georgobiani, A. N. Gruzintsev, V. T. Volkov, and M. O. Vorob'ev, Fiz. Tekh. Poluprovodn. (St. Petersburg) **36** (3), 284 (2002) [Semiconductors **36**, 265 (2002)].
7. J. R. Tuttle, M. A. Contreras, T. J. Gillespie, *et al.*, Prog. Photovoltaics **3**, 235 (1995).
8. A. N. Gruzintsev, V. T. Volkov, K. Bartkhou, and P. Benalul, Fiz. Tekh. Poluprovodn. (St. Petersburg) **36**, 741 (2002) [Semiconductors **36**, 701 (2002)].
9. N. N. Ledentsov, V. M. Ustinov, V. A. Shchukin, *et al.*, Fiz. Tekh. Poluprovodn. (St. Petersburg) **32**, 385 (1998) [Semiconductors **32**, 343 (1998)].

Translated by D. Mashovets

Semiconductors, Vol. 37, No. 3, 2003, pp. 317–321. Translated from Fizika i Tekhnika Poluprovodnikov, Vol. 37, No. 3, 2003, pp. 334–338.

LOW-DIMENSIONAL SYSTEMS

Structure of Energy Quantum Levels in a Quantum Dot Shaped as an Oblate Body of Revolution

G. G. Zegrya, O. V. Konstantinov, and A. V. Matveentsev

Ioffe Physicotechnical Institute, Russian Academy of Sciences, Politekhnicheskaya ul. 26, St. Petersburg, 194021 Russia

Submitted July 2, 2002; accepted for publication July 4, 2002

Abstract—It was shown that the electron energy spectrum in a disk-shaped potential well is characterized by two types of levels. One is characterized by a quantum number corresponding to carrier motion mainly along the disk axis. Energy intervals between such levels are large. As a rule, only a single electron level of this type can fit into the InAs quantum dot with GaAs surroundings. The second-type levels form a substructure with quantum numbers corresponding to carrier rotation about the polar axis and motion along the major disk axis. The distances between such levels are rather short. The theory makes it possible to determine the number of such levels as a function of the disk thickness and diameter and the conditions of the quantum dot transition into the quantum well with a large number of substructure levels. © *2003 MAIK "Nauka/Interperiodica".*

1. INTRODUCTION

As is known, quantum dot (QD) arrays offer advantages over quantum wells (QWs) in the context of their application as an active laser medium [1]. It is assumed that only one quantum level fits into an ideal QD. In this case, the shape of the cluster forming such a quantum dot should be compact, such as a sphere, cube, etc. However, experimental observations of InAs QD arrays on a GaAs substrate show that InAs QDs are strongly oblate disk-shaped clusters, which, in principle, can have many levels. If the disk diameter is sufficiently large, it corresponds to a QW fragment with transverse motion bands split into a substructure of levels. In this study, we qualitatively investigate the multiplicity of such a substructure. To this end, we considered two models, which allow an analytical solution for the electron energy in the disk-shaped object in the case of the parabolic dispersion relation in InAs. One model deals with a cluster shaped as an ellipsoid of revolution (Fig. 1a). Within this model, we developed a method for constructing a quasi-spherical system of ellipsoidal coordinates, which allows complete separation of variables, as this takes place in the spherical coordinate system. However, the application of the orthogonal quasi-spherical system is valid only for sufficiently strong oblateness, i.e., for a large major-to-minor axis ratio of the ellipsoid. The known ellipsoidal coordinates described, e.g., in [2] do not allow complete separation of variables, since two coordinates analogous to the radius and polar angle remain linked. However, in the actual case of an ideal QD with a single level, the ellipsoid oblateness can be weak. Therefore, to substantiate the applicability of the quasi-spherical system with weak oblateness, we used the cylindrical QD model allowing an exact solution. In this case, the QD is a QW fragment formed by cutting out a cylindrical surface impermeable to carriers from the QW. Figure 1b shows such a cylinder. The boundary conditions at the cylinder face are the same as in the QW. The wave function at the lateral surface of the cylinder is assumed to be zero. Then, variables are separated in the cylindrical system of coordinates, which results in a simple exact solution for the energy spectrum. This gives grounds to reject one of the solutions for the quasi-spherical approximation. The wave function of this solution is constant with respect to the polar angle, and such a state is the lowest in energy. Comparison with the exact solution for the cylinder shows that this solution is unnecessary. It should be disregarded, since it appears due to the inapplicability of the quasi-spherical approximation at weak oblateness.

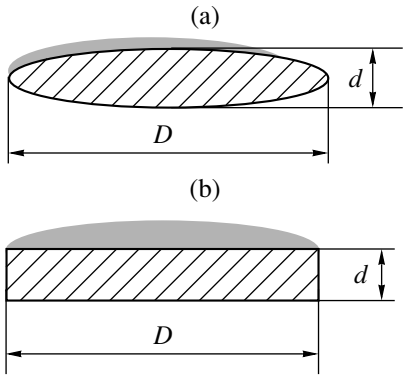

Fig. 1. Cross sections of oblate bodies of revolution with the diameter D and the largest thickness d: (a) ellipsoid and (b) cylinder (tablet).

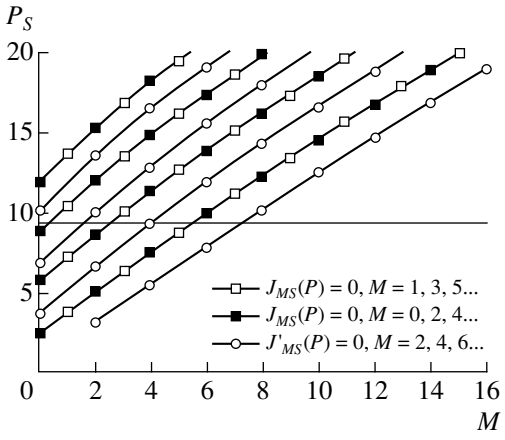

Fig. 2. Dependences of the roots of the Bessel functions or their derivatives on the order *M*. The curve parameter is the root index. Open and filled squares correspond to the even- and odd-index roots of the Bessel functions, respectively. Circles correspond to the even-index roots of the derivatives of the Bessel functions. The numbers of open symbols and squares (open and filled) below the cutoff line are equal to the numbers of levels in the ellipsoid and the cylinder, respectively.

2. QUANTUM LEVELS IN A CYLINDRICAL QUANTUM DOT

Let us consider the Schrödinger equation in the case of the parabolic dispersion relation of an electron,

$$-\frac{\hbar^2}{2m}\nabla^2\Psi = E\Psi, \tag{1}$$

where m is the effective mass of a carrier in the QD material. The Laplacian in the cylindrical system of coordinates is written as

$$\nabla^2\Psi = \frac{\partial^2\Psi}{\partial z^2} + \frac{1}{R}\frac{\partial}{\partial R}\left(R\frac{\partial\Psi}{\partial R}\right) + \frac{1}{R^2}\frac{\partial^2\Psi}{\partial\varphi^2}. \tag{2}$$

We seek a wave function written as the product of three functions,

$$\Psi = \exp(iM\varphi)\mathrm{J}_M(pR)\cos(kz), \tag{3}$$

where $\mathrm{J}_M(pR)$ is the Bessel function, and k and p are related to the energy,

$$E = E(k) + E(p), \quad E(k) = \frac{\hbar^2k^2}{2m}, \quad E(p) = \frac{\hbar^2p^2}{2m}. \tag{4}$$

The Bessel function index M should be an integer (M = 0, 1, 2, 3, …) because of the periodicity of the wave function with respect to the angle φ. The first term $E(k)$ is the energy of levels for electron motion along the z axis. The motion is described by the wave function $\cos(kz)$. The energy spectrum has long intervals between levels and is determined from the known QW equation

$$\tan(ka) = \frac{q}{k}, \quad q^2 = \frac{2m_B}{\hbar^2}[\Delta E - E(k)], \tag{5}$$

where $a = d/2$ is the halved thickness of the cylinder, m_B is the mass of electrons and holes in GaAs, and q is the falloff exponent in GaAs. Solution (5) is characterized by the index f. In the example we suggested, the corresponding potential steps at the heterojunction are ΔE_c = 0.70 eV and ΔE_v = 0.38 eV at T = 0 K. We take the effective electron and hole masses as $m_c = 0.027m_0$ and $m_v = 0.41m_0$ in InAs, and $m_{cB} = 0.065m_0$ and $m_{vB} = 0.45m_0$ in GaAs. Then, the solution of Eq. (5) yields ka = 0.730 and 0.850 at a cylinder thickness of 24 and 30 Å, respectively. These thicknesses correspond to the energy $E(k)$ = 0.523 and 0.453 eV. The energy gaps

$$I(k) = \Delta E - E(k) \tag{6}$$

define the energy $E(p)$ intervals corresponding to the motion transverse to the cylinder. The wavevector p is defined by the boundary condition of the lateral wall impermeability at $R = b = D/2$ for electrons and holes,

$$\mathrm{J}_M(pb) = 0. \tag{7}$$

The term $E(p)$ describes the substructure of energy levels. The solution to Eq. (7),

$$P = pb \tag{8}$$

is illustrated by the diagram in Fig. 2. The abscissa axis is the order M of the Bessel function, the ordinate axis is the root P. Filled and open squares are the even- and odd-index roots of the Bessel function. The solid curve connects all the squares with a fixed number S of the root P_S of the Bessel function. Similar curves are given in Figs. 126–128 of the handbook [3]. We note that the index S is the third quantum number of the problem in the set (f, M, S). We ascertained that the dependence $P_S(M)$ can be described by the approximate formula

$$P_S(M) = M - 1 + 3S + \sqrt{S(0.55M + 0.2)}, \quad M = 0, 1, 2, 3, \ldots, \tag{9}$$

where S = 1, 2, 3,… . These formulas do not yield errors when determining the number of states, whereas the roots themselves are characterized by an error of a few percent at small M and S and of fractions of a percent at larger M and S. Thus, the basic structure is characterized by the quantum number f, and the substructure depends on two quantum numbers, M and S.

The number of levels in the QD with a given diameter D is defined by the ordinate of the P cutoff line parallel to the abscissa axis. The cutoff line ordinate is given by

$$P = \frac{D}{2\hbar}\sqrt{2mI(k)}, \tag{10}$$

where $I(k)$ is the energy gap defined by formula (6). At the thickness d = 30 Å and the diameter D = 300 Å, when I = 0.25 eV, we obtain P = 9.35, which yields ten levels in the cylindrical QD. According to this scheme, using the diagram in Fig. 2, we constructed the histograms of the total number of levels in the cylinder, shown in Fig. 3a.

3. INTRODUCTION OF ELLIPSOIDAL CURVILINEAR COORDINATES

Let the QD surface shape be given by the following equation of the ellipsoid of revolution:

$$\frac{x^2+y^2}{b^2}+\frac{z^2}{r^2}=1, \quad b=nr, \tag{11}$$

where r and b are the ellipsoid minor and major semiaxes, respectively; and n is the oblateness degree. We introduce a quasi-spherical system of coordinates, in which the ellipsoid surface has a spherical shape, r = const, inscribed into the initial ellipsoid of revolution,

$$x=nr\sin\theta\cos\varphi, \quad y=nr\sin\theta\sin\varphi, \quad z=r\cos\theta. \tag{12}$$

This system of curvilinear coordinates is not orthogonal. To verify that this is the case, the squared unit length should be written as

$$ds^2=dx^2+dy^2+dz^2, \tag{13}$$

where dx, dy, dz are the differentials of the Cartesian coordinates related to the curvilinear coordinates r, θ, φ by relations (12). Calculating the squared length differential, we obtain it in the form

$$ds^2=dr^2+r^2d\theta^2+n^2r^2\sin^2\theta d\varphi^2+(n^2-1)\times[\sin\theta dr+r\cos\theta d\theta]^2. \tag{14}$$

One can see from this formula that the curvilinear coordinates r and θ are mutually orthogonal at n = 1. However, the curvilinear coordinates become orthogonal at $n \gg 1$ as well. To make sure that this is the case, we change variables, introducing the cylindrical radius ρ

$$\rho=r\sin\theta, \quad d\rho=\sin\theta dr+r\cos\theta d\theta \tag{15}$$

instead of the polar angle θ. Then we obtain

$$ds^2=dr^2+r^2d\theta^2+n^2\rho^2d\varphi^2+(n^2-1)d\rho^2. \tag{16}$$

The term $r^2d\theta^2$ should be written in terms of the differentials dr and $d\rho$. However, we shall consider the limiting case of a strongly oblate ellipsoid, $n \gg 1$. Then, the term $r^2d\theta^2$ may be disregarded, and the curvilinear coordinates r, ρ, φ become orthogonal, since the squared arc length contains no cross products of differentials of curvilinear coordinates,

$$ds^2=dr^2+n^2d\rho^2+n^2\rho^2d\varphi^2. \tag{17}$$

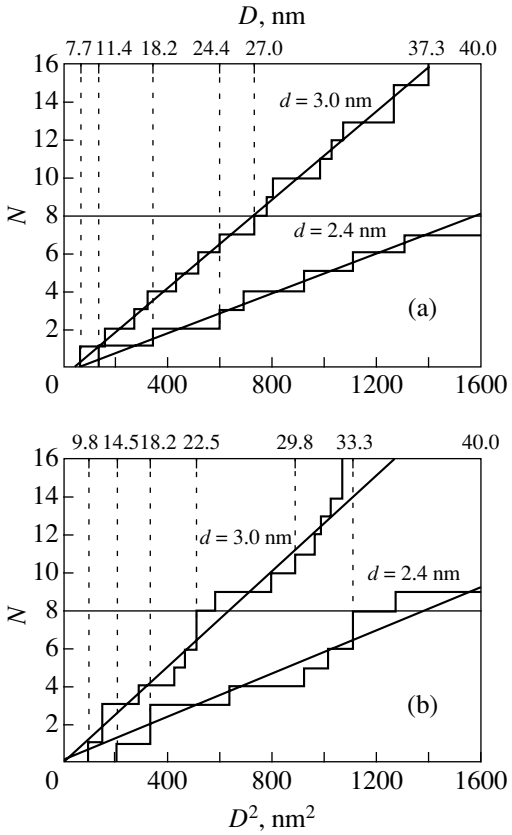

Fig. 3. Dependences of the number N of electron levels on the squared diameter for an InAs cluster in the GaAs host material in the parabolic approximation for the energy spectrum of electrons in InAs in the cases of (a) cylinder and (b) ellipsoid. The upper and lower curves correspond to the thickness d = 3 and 2.4 nm.

In formula (17), the Lamé coefficients [4] are at the squared differentials of the curvilinear coordinates. In these coordinates, the Lamé coefficients are written as

$$H_r=1; \quad H_R=n; \quad H_\varphi=n\rho. \tag{18}$$

Using the Lamé coefficients, one can readily construct the Laplacian for a strongly oblate ellipsoid ($n \gg 1$). According to the method described in [5], we derive the following Laplacian:

$$\nabla^2\Psi=\frac{\partial^2\Psi}{\partial r^2}+\frac{1}{n^2}\left[\frac{1}{\rho}\frac{\partial}{\partial\rho}\left(\rho\frac{\partial\Psi}{\partial\rho}\right)+\frac{1}{\rho^2}\frac{\partial^2\Psi}{\partial\varphi^2}\right]. \tag{19}$$

This operator is similar to Laplacian (2) of the cylindrical systems of coordinates with the substitution $z \longrightarrow r$, $R \longrightarrow n\rho$. The Laplacian outside the QW has the same form. We note that operator (19) can be derived from the initial operator of the kinetic energy in the Cartesian frame of reference only for an isotropic quadratic dispersion relation of electrons, i.e., in the parabolic approximation.

4. SEPARATION OF VARIABLES IN THE QUASI-SPHERICAL COORDINATES

The solution to Schrödinger equation (1) with Laplacian (19) will have a form similar to (3),

$$\Psi = \exp(iM\varphi)J_M(pn\rho)\cos(kr), \qquad (20)$$

where k and p are the discrete components of the wave vector, defined by the boundary conditions of the problem. The boundary conditions with respect to the variable r consist in the continuity of the wave function and its derivative with respect to the normal at the sphere surface, $r = a$, which results in Eq. (5) being the same as in the QW case. The boundary conditions with respect to the variables φ and ρ are the conditions of the wave function cyclicity. Since the wave function is periodic with respect to the variable φ, the quantum number M should be an integer, $M = 0, 1, 2, 3, \ldots$. The energy E, by analogy with Eq. (4), is the sum of two terms. The first term $E(k)$ is the energy of the levels corresponding to the carrier motion over the radius r. The spectrum of these energies, given by Eq. (5), will be a basic structure with long intervals between levels. The second term $E(p)$ describes the substructure of levels and corresponds to the carrier motion along the direction at angles φ and θ. We now discuss the cyclicity conditions with respect to θ. To this end, we change the reference point of the polar angle. We substitute the variable θ with θ': $\theta' = \frac{\pi}{2} - \theta$, $\rho = r\cos\theta'$. The limits of variation of these parameters are $-\pi/2 < \theta' < \pi/2$ and $-a < \rho < a$. If M is even, the solution will describe the even function $\Psi(\rho) = -\Psi(-\rho)$. Then, the boundary condition at $\theta' = \pi/2$ ($\rho = 0$) consists in the requirement that the derivative be continuous. Since the function should be even with respect to the angle θ', the derivative should vanish at $\theta' = \pi/2$, i.e., at $\rho = 0$; otherwise, the function will have a kink. If M is odd, the solution will describe the odd function $\Psi(\rho) = -\Psi(-\rho)$. Thus, we obtain the following dispersion relations:

$$\begin{aligned} J'_M(P) &= 0, \quad M = 0, 2, \ldots; \\ J_M(P) &= 0, \quad M = 1, 3, \ldots . \end{aligned} \qquad (21)$$

Each root is characterized by the index S: $P \equiv P_S(M)$, $S = 1, 2, 3, \ldots$. The first roots will be as follows: $P_1(0) = 0$, $P_1(2) = 3.05$, $P_2(0) = P_1(1) = 3.83$, $P_1(4) = 5.32$, and $P_1(3) = 6.38$ [6]. It should be emphasized that, the equation for the derivative has a zero root, $P_1(0) = 0$, which will correspond to zero energy for the motion along the major axis. As was mentioned above, this root is unnecessary; hereafter, the case with $M = 0$ will be disregarded. To simplify the determination of roots of Eqs. (21), we write the approximate formula for the dimensionless roots of the derivative of the Bessel function $P_{S'}(M)$,

$$P_{S'}(M) = M - 3.1 + 3.07S' + \sqrt{S'(0.55M + 0.2)}, \quad M = 2, 4, \ldots . \qquad (22)$$

For odd M, the root is defined by formula (9). These formulas do not yield an error when determining the number of states (see Fig. 2), whereas the roots themselves at small M and $S(S')$ are characterized by a certain error. For these cases, the exact values of the roots are listed above. Each curve in Fig. 2 corresponds to a certain root index S, $S' = 1, 2, 3$. Thus, the roots of Eqs. (21) correspond to circles and filled squares. The latter are also solutions to Eq. (7).

5. RESULTS OF CALCULATIONS

The results calculated using the models under consideration are shown in Figs. 3a–3b. Figure 3a shows the dependence of the number N of electron levels in the cylindrical QD on the squared diameter of the cylinder. The dependence represents a histogram, since the number of levels is a discrete quantity. If the squared diameter is plotted on the horizontal axis, the histogram median is a straight line. Moreover, at $N > 100$, the dependence $N(D^2)$ is virtually no different from this straight line. This fact has a simple physical meaning: the number of levels is proportional to the disk area. For convenience, the diameter is plotted as the upper supplementary horizontal axis. The bottom and top histograms correspond to cylinder thicknesses of 2.4 and 3.0 nm, respectively. The diameters corresponding to one, two, and three levels are projected by dashed lines onto the upper horizontal axis at the points 11.4, 18.2, and 24.4 nm for the cylinder thickness of 2.4 nm. Eight levels appear at a diameter of 40 nm. An ideal QD with a single quantum level exists only in the diameter range from 114 to 182 Å. We note that these conclusions are more likely illustrative than strictly quantitative, since the parabolic approximation was used for the dispersion relation of electrons in InAs. As for a cylinder 30 Å thick, the range of ideal QD diameters narrows and extends from 77 to 116 Å. Therefore, the condition for ideal QD existence crucially depends on the diameter and, in particular, on cylinder thickness. Figure 3b shows similar histograms for the ellipsoid of revolution. The ellipsoid with a diameter in the range from 145 to 182 Å and a thickness of 24 Å is an ideal QD. If the thickness is 30 Å, this range decreases and extends from 96 to 120 Å, which confirms the above-stated conclusion on the crucial dependence of the number of levels of a QD substructure on thickness. The physical meaning of this dependence consists in the fact that the level corresponding to the carrier motion along the short axis deepens as the QD thickness increases; therefore, a larger number of substructure levels can be found in the energy range from this level to the continuous spectrum edge. Summarizing the discussion of the

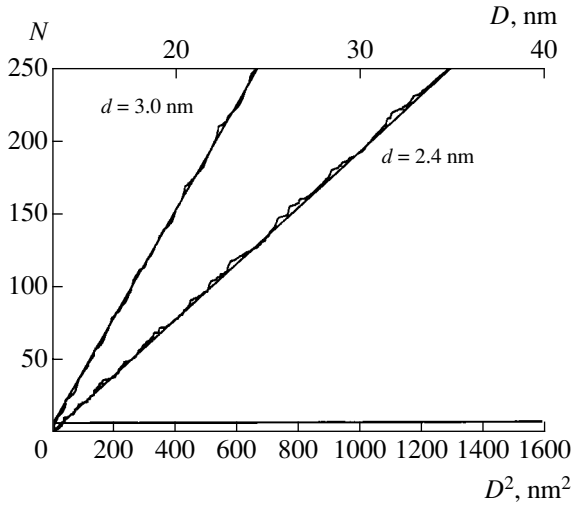

Fig. 4. Dependences of the number N of hole levels on the squared diameter for the InAs cluster in the GaAs host constructed within the parabolic approximation of the hole energy spectrum in InAs in the case of an ellipsoid. The upper and lower curves correspond to the thickness $d = 3$ and 2.4 nm, respectively. The effective hole masses in InAs and GaAs are $m = 0.41m_0$ and $0.45m_0$, respectively. The band offset is $\Delta E_v = 0.38$ eV.

multiplicity of levels, we note that all of the advantages of a QD over a QW are lost when the number of substructure levels is large. Furthermore, other disadvantages arise, which are caused by a large number of carriers inside the QD, since the density of carriers in the QD can be higher than in the QW. If QD occupancy with carriers is high, the Auger recombination rate of carriers in the QD will rapidly increase with the QD sizes. Therefore, the quantum yield of radiative recombination will decrease with the number of populated electron levels.

We now discuss the case of a single bound state in a QD. In publications which deal [7, 8] with the theory of QD levels the QD shape was approximated by a sphere. It was assumed that the lowest state of QD carriers is described by a wave function with a single node at the well center. In the case of the parabolic dispersion relation, this level cannot fit into the well if the QD parameters are selected close to the experimentally observed ones [9]. Therefore, it was necessary to employ the nonparabolic dispersion relation, which was done in [8]. The nonparabolic approximation allows the existence of a bound state with a single node at the spherical QD center. The number of levels in the cluster increases as the parabolic approximation is substituted with the nonparabolic one, since this, roughly speaking, corresponds to a significant increase in the effective mass. Therefore, here we presented only the lower estimate for the number of levels in the cluster. Taking into account the nonparabolicity of the conduction band, the number of substructure levels in a cluster with a given thickness and diameter will undoubtedly increase.

Figure 4 shows a histogram of the dependences of the number of hole levels in the ellipsoid on the squared diameter; this histogram is similar to that in Fig. 3 for electrons. The horizontal straight line at the bottom is drawn at the level $N = 8$. It is evident that the number of hole levels is enormous in comparison with the number of electron levels at the same diameter. Thus, this cluster is almost never a QD for holes. As indicated above, these histograms are straight lines.

ACKNOWLEDGMENTS

We would like to thank A.V. Subashiev for constructive criticism.

REFERENCES

1. N. N. Ledentsov, V. M. Ustinov, V. A. Shchukin, *et al.*, Fiz. Tekh. Poluprovodn. (St. Petersburg) **32**, 385 (1998) [Semiconductors **32**, 343 (1998)].
2. G. A. Korn and T. M. Korn, *Mathematical Handbook for Scientists and Engineers*, 2nd ed. (McGraw-Hill, New York, 1968; Nauka, Moscow, 1974).
3. E. Jahnke, F. Emde, and F. Lösch, *Tables of Higher Functions*, 7th ed. (Teubner, Stuttgart, 1968; McGraw-Hill, New York, 1960; Nauka, Moscow, 1977).
4. V. M. Levin and Yu. I. Grosberg, *Differential Equations of Mathematical Physics* (Gostekhizdat, Moscow, 1951).
5. V. I. Smirnov, *A Course of Higher Mathematics* (GITTL, Moscow, 1954; Addison-Wesley, Reading, Mass., 1964), Vol. 2.
6. *Handbook of Mathematical Functions*, 2nd ed., Ed. by M. Abramowitz and I. A. Stegun (Dover, New York, 1971; Nauka, Moscow, 1979).
7. L. V. Asryan and R. A. Suris, Semicond. Sci. Technol. **11**, 554 (1996).
8. V. P. Evtikhiev, O. V. Konstantinov, and A. V. Matveentsev, Pis'ma Zh. Tekh. Fiz. **27** (6), 65 (2001) [Tech. Phys. Lett. **27**, 248 (2001)].
9. V. P. Evtikhiev, O. V. Konstantinov, E. Yu. Kotel'nikov, *et al.*, Pis'ma Zh. Tekh. Fiz. **27** (16), 40 (2001) [Tech. Phys. Lett. **27**, 683 (2001)].

Translated by A. Kazantsev

Semiconductors, Vol. 37, No. 3, 2003, pp. 322–328. Translated from Fizika i Tekhnika Poluprovodnikov, Vol. 37, No. 3, 2003, pp. 339–345.

LOW-DIMENSIONAL SYSTEMS

Investigation of the Physical Properties of Semiconductor Nanostructures Using Samples with Laterally Nonuniform Layers: 1. Photoluminescence

Yu. V. Khabarov

Institute of Radio Engineering and Electronics, Russian Academy of Sciences, Moscow, 101999 Russia

Submitted August 29, 2002; accepted for publication August 30, 2002

Abstract—A new technique for the experimental investigation of semiconductor structures is suggested and implemented. The technique is based on an analysis of correlations in the spectra of samples with laterally nonuniform layers. A molecular-beam-epitaxy-grown sample containing $Al_xGa_{1-x}As$–GaAs and GaAs–$In_yGa_{1-y}As$ quantum wells (QWs) and a modulation doped $Al_xGa_{1-x}As$–GaAs heterojunction was studied by photoluminescence (PL) spectroscopy at 77 K. The dependences of the PL spectra on the parameters describing sample nonuniformity were analyzed, which made it possible to characterize the processes of the charge-carrier redistribution in the structure and to reveal a number of specific features in the PL of narrow GaAs QWs. In the entire range of the nonuniformity-related variation in the semiconductor structure parameters, the values of the optical transition energies determined experimentally agree with those calculated theoretically and may serve as a basis for estimating these parameters. It is shown in this study that the suggested approach is highly informative, which stems from the capacity for precision control over the technologically adjustable parameters of the structure within the same sample. © *2003 MAIK "Nauka/Interperiodica".*

1. INTRODUCTION

Quantum-confinement structures (QCSs) possess diverse physical properties and form the basis for the emergence of new areas of semiconductor electronics, which stimulates considerable interest in their investigation. In particular, studies of the relationship between the physical properties of QCSs and their structural parameters are of specific importance due to a high variability of the latter.

It is standard practice to study the dependence of physical characteristics of semiconductor nanostructures on the structure parameters (such as thicknesses of the quantum-confinement layers, composition of the particular layers, etc.) using a series of laterally uniform samples in which one of the parameters is varied.

Recently, a new approach to the investigation of physical processes in multilayer semiconductor structures was suggested [1]. It is based on the study of correlations in the spectra of structures with intentionally introduced lateral nonuniformity. Instead of a series of uniform samples in which a particular parameter is varied, a single sample with built-in lateral variation of this parameter is used. Records of the sample spectra taken locally over its surface yield a multidimensional set of parameters that represents the nonuniformity profile and is sufficient for analysis of the correlation relationships between the characteristics of the phenomenon under study (e.g., the photoluminescence (PL) spectra) and the parameters describing sample nonuniformity.

2. DISCUSSION OF THE METHOD

The suggested method of correlative spectroscopy relies on the study of multilayer semiconductor structures composed of laterally uniform layers and layers with correlated lateral nonuniformities. Along with the subsystem to be investigated, the structure must contain an auxiliary subsystem that provides information on the character of the built-in nonuniformity. It is assumed that experimental analysis of these structures will be carried out by different spectroscopic techniques, making it possible to observe both the spectral features related to the subsystem under study and those related to the auxiliary subsystem and to specify the value of the varied parameter in each local area of the nonuniform sample. Thus, there is no need either for additional diagnostic techniques or for technological estimates to determine the value of the varied parameter; this implies that exact positioning of the measurement area is also not necessary. Subsequent analysis of the correlation relationships between the parameters of the spectra enables one to follow the behavior of the characteristics of the structure under study in the field of the built-in nonuniformity.

The diagram in Fig. 1 serves to illustrate the discussion of the suggested technique by the simple example of a structure containing two laterally nonuniform layers: layer *1* to be studied and auxiliary layer *2*. For this representative structure, the nonuniformity of the layers in the cross section of Fig. 1 consists in the dependence of their thicknesses on the coordinate *X*. The thickness

1063-7826/03/3703-0322$24.00

ratio does not change with X, which imposes correlation between the two layers. Let us assume that the goal of this study is to find the dependence of some spectral parameter S_1 characterizing layer *1* on the layer thickness w_1, $S_1 = f_1(w_1)$. The spectra recorded locally over different areas of the sample yield a set of values S_{1i} of the parameter under study corresponding to different coordinates X_i. The values of the layer thickness w_{1i} for each X_i remain unknown. To determine these, the auxiliary layer *2* is introduced into the structure. There should be a spectral parameter S_2, characterizing layer *2*, whose dependence on the layer thickness w_2 is known ($S_2 = f_2(w_2)$). A quantum well (QW) may serve as such a layer, since the dependence of the quantum-state energies in a QW on the main QW structure parameters has been well investigated [2, 3]. The two sets of spectral parameters obtained can then be used to determine a correlation relationship $S_{1i} = f_k(S_{2i})$, where S_{2i} represent values of the parameter S_2 at points with coordinates X_i. This relationship represents the dependence of the parameter S_1 on the thickness w_1, so long as both the dependence $S_2 = f_2(w_2)$ and the ratio w_1/w_2 are known. Thus, S_2 can be treated as a generalized thickness parameter, and the shape of the sought-for dependence $S_{1i} = f_1(w_{1i})$ can be reconstructed from the above data.

The correlation relationships thus obtained approximate the actual functional relationships to a certain level of accuracy, which is determined by the degree to which the influence of the intentionally varied parameter on the characteristics under study dominates over the influence of other parameters that determine the background. These can be possible nonideality of conditions at the substrate, variation in the parameters of nominally uniform layers, local structural defects, etc. All of these are factors that commonly affect the results of analysis of uniform samples. It should be noted that the efficiency of the suggested technique relies on the high level of uniformity of those layers that are not intended to be nonuniform. Thus, the application of this method still requires that the technological processes used to grow the structures meet stringent requirements in terms of layer uniformity.

3. PHOTOLUMINESCENCE. EXPERIMENTAL DETAILS

We used the correlative-spectroscopy method to examine an epitaxial AlGaAs/GaAs/InGaAs QW structure using steady-state PL spectroscopy as a measurement technique. PL spectroscopy, which offers high accuracy in the analysis of the energies of electron states and yields information on the occupation of the energy subbands, became one of the main tools for studying quantum states in QCSs [2–6]. The usefulness of the PL technique is further enhanced by the availability of such modifications as PL excitation spectroscopy, time-resolved PL spectroscopy, and PL spectroscopy in an electric or magnetic field; all of these can be exploited in the context of the correlative-spectroscopy method.

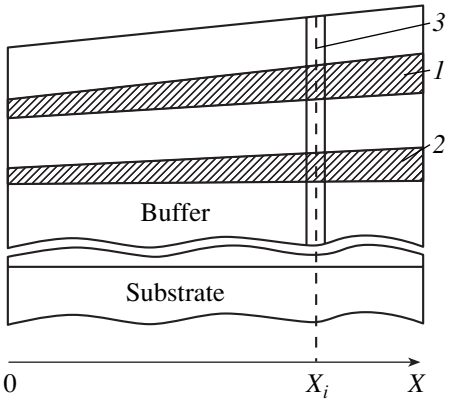

Fig.1. A schematic layout of the simplest sample configuration suitable for the investigation by the correlative spectroscopy method: (*1*) laterally nonuniform layer *1*, (*2*) auxiliary laterally nonuniform layer *2*, and (*3*) the area of local spectral measurements.

A multilayer sample grown for this study contained several QCSs on a semi-insulating 76-mm-diameter GaAs substrate. A technologically defined nonuniformity was intentionally introduced into all of the sample layers (except the buffer). This kind of nonuniformity implies that many parameters vary simultaneously; thus, when interpreting the experimentally determined relationships, it was necessary to recognize whether or not some of them have a dominant effect on the measurement results.

The sample was grown by molecular-beam epitaxy in a Riber-32P unit. The layer sequence is shown in Fig. 2. First, a buffer layer was deposited on the GaAs substrate. Then, two GaAs–$In_yGa_{1-y}As$–GaAs QWs of different widths (denoted as QW_D and QW_E) were grown; the upper GaAs barrier layer, along with the subsequent doped and undoped AlGaAs layers, formed a modulation-doped heterojunction (MDHJ) separating the two upper $Al_xGa_{1-x}As$–GaAs–$Al_xGa_{1-x}As$ QWs (denoted as QW_B and QW_C); the meaning of the subscripts *B*, *C*, *D*, and *E* will be explained below. The structure was capped by a layer of $Al_xGa_{1-x}As$ with an increased Al content and by a thin GaAs layer. To obtain nonuniform layers, the rotation of the substrate was stopped after growing the buffer layer; all subsequent layers were deposited without substrate rotation. The resulting lateral nonuniformity was determined by the dependence of the epitaxial growth conditions on the coordinate on the substrate surface, related to the spatial distribution of the molecular fluxes in the plane of the growing sample. In particular, the local thickness of a particular layer of the structure was determined by the local growth rate and the layer exposure duration; thus, the ratio of the local thicknesses of the layers formed under similar conditions was defined technologically by the ratio of the corresponding growth dura-

GaAs,	5 nm
$Al_xGa_{1-x}As$, $x^* = 0.41$,	50 nm
$Al_xGa_{1-x}As$, $x^* = 0.27$,	50 nm
GaAs,	2.5 nm, QW_B
$Al_xGa_{1-x}As$, $x^* = 0.27$,	50 nm
GaAs,	8.5 nm, QW_C
$Al_xGa_{1-x}As$, $x^* = 0.27$,	70 nm
$Al_xGa_{1-x}As$ + Si, $x^* = 0.27$,	12 nm
$Al_xGa_{1-x}As$, $x^* = 0.27$,	12 nm
GaAs,	10 nm
$In_yGa_{1-y}As$, $y^* = 0.13$,	4 nm, QW_D
GaAs,	50 nm
$In_yGa_{1-y}As$, $y^* = 0.19$,	12 nm, QW_E
GaAs,	800 nm, buffer layer
GaAs,	substrate

Fig. 2. A schematic structure layout of the sample under study. The indicated values of the layer thicknesses and ternary-alloy composition are estimates corresponding to the central part of the wafer.

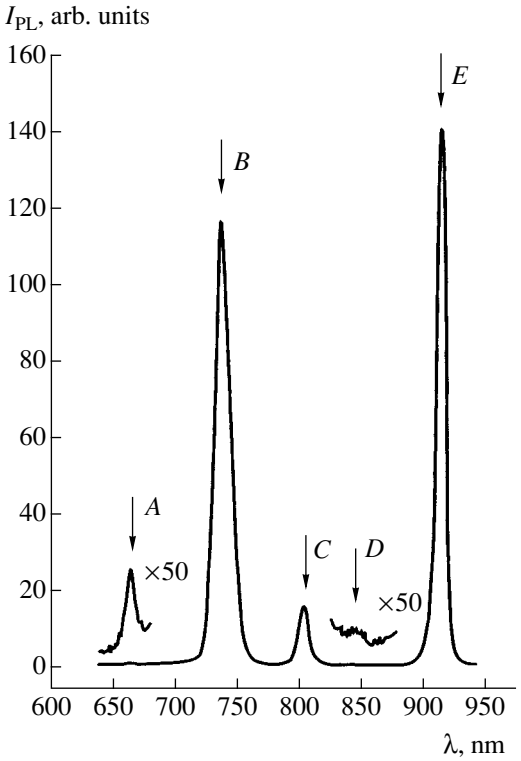

Fig. 3. A typical photoluminescence spectrum recorded in the central part of the wafer. Arrows indicate the positions of bands *A*, *B*, *C*, *D*, and *E*.

tions. To give an idea of the thickness and the composition of laterally nonuniform layers, in Fig. 2 we cite the estimated layer thicknesses (determined from the growth durations) in the central part of the wafer (i.e., close to the axis) and the averaged parameters x^* and y^* characterizing the composition of ternary-alloy layers (determined from the ratio of the molecular fluxes in the growth process). At the same time, these estimates indicate the parameters of uniform layers that can be grown in a similar process carried out with substrate rotation, which eliminates the influence of the spatial nonuniformity of the molecular fluxes on the parameters of the deposited layers.

The PL spectra were recorded at liquid-nitrogen temperature in the wavelength range of 580–1000 nm. An Ar^+-ion laser emitting at 488 nm was used as the excitation source; the laser beam was focused on the sample surface at a spot of 50 μm in diameter, and the excitation density was as high as 200 W/cm^2. The PL emission was analyzed by an automated spectrometer based on an MDR-23 monochromator; a cooled FEU-62 photomultiplier operating in the photon-counting mode was used as the photodetector. To record the spectra over the entire surface of 76-mm-diameter semiconductor wafers at liquid-nitrogen temperature, an optical cryostat of special design was used.

According to the principles of the method described above, the PL spectra were recorded at different spots over the surface of the nonuniform sample and the behavior of the spectral parameters related to different components of the structure (the QWs) as a function of the parameter characterizing the nonuniformity was analyzed.

The PL spectra from two groups of spots were recorded. The spots of group *1* were arranged along the wafer diameter oriented close to the direction of the layer-thickness gradient; the spots of group *2* were located randomly over the rest of the surface.

4. EXPERIMENTAL RESULTS AND DISCUSSION

Intense PL was observed at all of the spots examined. This indicates that the crystal quality of the grown layers is sufficiently high, in spite of the considerable nonuniformity in the growth conditions. Data describing variation in layer parameters will be given below. A typical spectrum, recorded at the central part of the wafer, is shown in Fig. 3. Along with strong bands *B*, *C*, and *E* corresponding to the emission from QW_B, QW_C, and QW_E (see Fig. 2), the spectrum contains weak bands *A*, corresponding to the edge emission from $Al_xGa_{1-x}As$ barrier layers with a low Al content, and *D*,

corresponding to the emission from QW_D. Emission from the $Al_xGa_{1-x}As$ layer with a high Al content ($x^* = 0.41$) was not observed.

The spectral position of bands *B*, *C*, and *E* varied considerably, depending on the location of a measurement spot. At the same time, in the spectra recorded at spots from group *1*, the position of band *A*, which depends on the composition of $Al_xGa_{1-x}As$ layers, varied insignificantly and remained within the range of 1.83–1.86 eV; this resulted from appropriate "focusing" of the Ga and Al molecular sources. Thus, in all subsequent estimates, the composition of these layers was assumed to be constant.

Band *C*, corresponding to the wider GaAs QW_C, was observed in all recorded spectra. In the spectra measured at spots from group *1*, the energy position of its peak varied monotonically; under the conditions of insignificantly small variations in the barrier-layer composition, this corresponds to a monotonic variation in the width of the QW_C and, consequently, relative variations in the thicknesses of all other layers (except In-containing QWs) proportional to the corresponding growth durations. This means that the energy position of band *C* can be considered as a parameter characterizing the thicknesses of the structure layers at each particular location. Thus, in handling experimental data in this study, this parameter was used as a generalized thickness parameter.

Estimates for the width and composition of In-containing QWs at the measurement spots were obtained from a calculation using experimentally determined values for corresponding PL band peak positions. The calculation was performed within the context of a model utilizing a numerical solution of the Schrödinger equation in the envelope-function approximation. The energy $\Delta E = E_{e1} - E_{hh1}$ of the transition $e1$–$hh1$ between the first electron level E_{e1} in the conduction band and the first hole level E_{hh1} in the valence band was calculated. The calculation was similar to that carried out in [5], and a number of assumptions were made. It was assumed that the shape of the QWs is rectangular and not affected by the built-in electric field. The effective masses of the charge carriers (electrons and heavy holes) in $In_yGa_{1-y}As$ QWs were evaluated using the relationships $m_e^*(y) = (0.0665 - 0.044y)m_0$ and $m_{hh}^*(y) = (0.62 - 0.22y)m_0$ (where m_0 is the free-electron mass); next, it was assumed that the effective masses m_e and m_{hh} in the barrier layers are equal to those in the QWs. The relation $E_g(y) = 1.508 - 1.214y + 0.264y^2$ was used to describe the dependence of the $In_yGa_{1-y}As$ band gap on the In content, and the conduction-band offset ratio $\Delta E_c/\Delta E_g$ was assumed to be 0.7 (here, ΔE_c is the conduction-band offset and ΔE_g is the band-gap difference at the interface). The exciton binding energy was assumed to be 7 meV [5].

The calculation of the GaAs–$Al_xGa_{1-x}As$ QWs was carried out both for the cases of abrupt and stepwise interfaces. The value corresponding to the average energy position of spectral band *A* (1.85 eV) was used as an estimate for the band gap in $Al_xGa_{1-x}As$ barrier layers. It was assumed that the conduction-band offset ratio $\Delta E_c/\Delta E_g = 0.6$. The electron and heavy-hole effective masses were determined from the relation $m_e^*(x) = (0.0665 - 0.0835x)m_0$ and $m_{hh}^*(x) = (0.51 - 0.2x)m_0$, respectively [4]. The dependence of the exciton binding energy on the QW width was taken from [6].

The experimentally determined energy positions of the QW emission peaks, along with the results of calculating the QW parameters, are shown in Fig. 4a. Experimental points describing the spectral positions of bands *B*, *D*, and *E* are represented by curves *1*, *2*, and *3*, respectively; the abscissa is the energy position E_C of the peak of band *C*. The calculated relationship between the width of QW *C* and the corresponding emission photon energy plotted on the abscissa is represented by curve *1* in Fig. 4b. The width of the QW_E calculated from the experimental values of the transition energies (see curve *3* in Fig. 4a) is shown in Fig. 4b by curve *2*. The calculation, taking into account the nonuniformity of the QW composition, was based on the known ratios of the layer growth durations and the dependence of the $In_yGa_{1-y}As$ layer thickness on the In content *y*. The values of this parameter for QW_E, yielded by the same calculation, are given by curve *3* (Fig. 4b). Corresponding estimates for QW_D can be obtained in a similar way.

4.1. Photoluminescence of AlGaAs–GaAs–AlGaAs Quantum Wells

A large spread observed in the energy positions of bands *B* and *C* (E_B and E_C, respectively) is evidence of considerable variation in the layer thicknesses in the sample under study. For example, from the range of variation in the experimental values of E_C in Fig. 4a, one can estimate that the width of QW_C varies between 2.5 and 14 nm (cf. curve *1* in Fig. 4b). This means that we have a set of pairs of AlGaAs–GaAs–AlGaAs QWs whose widths vary greatly and the ratio of widths is constant (determined by the technological parameters). The energies of quantum states in QWs are sensitive to a number of characteristics of the semiconductor crystal, such as the built-in electric field, the band-structure parameters, and the interface morphology. The degree of this sensitivity depends on the QW width, and, thus, the shape of the experimental curve $E_B = f(E_C)$ should carry information on these characteristics. Thus, we calculated theoretical curves $E_B = f(E_C)$, which represent a correlation between the energies of the transitions $e1$–$hh1$ in QW_B and QW_C, for different values of certain parameters (see Fig. 4a, curves *4*, *5*).

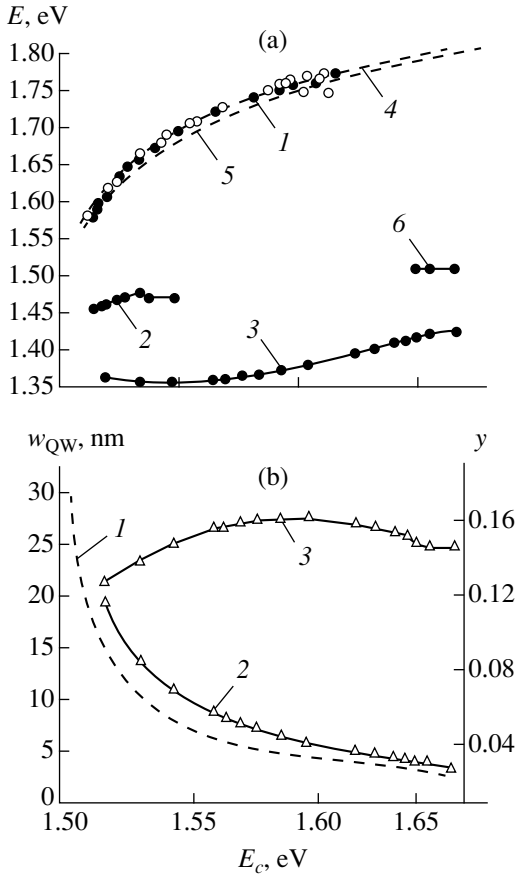

Fig. 4. Experimental and theoretical values of the PL band energy positions and the QW parameters in a nonuniform structure plotted as functions of the QW_C emission energy. (a) Experimental peak energies of bands (*1*) *B*, (*2*) *D*, and (*3*) *E*; energies of the optical transition *e*1–*hh*1 in QW_B calculated for w_C/w_B = 3.8 and 3.4 (curves *4* and *5*, respectively). Curve *6* represents the experimental values of the GaAs emission energy. (b) (*1*) Calculated relationship between the width of QW_C and its emission energy; (*2*) $In_yGa_{1-y}As$ layer width and (*3*) in content *y* estimated for QW_E by calculation based on experimental data. Experimental points corresponding to spots from group *1* are shown by filled circles and those from group *2*, by open circles; points obtained by calculation are shown by open triangles.

Good agreement can be seen in Fig. 4a between the experimental curve *1*, relating the energy positions of bands *B* and *C*, and the theoretical curve *4*. The latter was calculated assuming that the built-in electric field equals 5×10^3 V/cm and the ratio of the widths of QW_C and QW_B is w_C/w_B = 3.8, which is somewhat larger than the ratio of the growth durations for these layers (t_C/t_B = 3.4). The scatter of experimental points on the right-hand side of curve *1* is mainly introduced by those corresponding to spots from group *2* on the wafer surface. This scatter may be related to small variations in the barrier-layer composition, since the energies of quantum states in narrow QWs are highly sensitive to structure parameters.

If the ratio of the QW width is assumed to be equal to the ratio of growth durations (i.e., w_C/w_B = 3.4), calculation yields results represented by curve *5* (Fig. 4a). This curve noticeably deviates from the experimental points. Apparently, this discrepancy stems from the assumption that interfaces between the layers forming the QW are perfectly abrupt. As indicated by the calculation, the energy of the *e*1–*hh*1 transition in a symmetric QW with a mean width *w* and slanted (stepwise) interfaces (in other words, a trapezium-shaped QW) is higher than that in a rectangular QW of the same width, and the difference increases with decreasing *w*. Such an energy shift may be thought of as originating from an additional decrease in the width of the narrower QW (QW_B), which means an effective increase in the ratio w_C/w_B illustrated by curve *5*. In the case under consideration, the model of a trapezium-shaped QW may account for the small-scale interface fluctuations averaged over the exciton wave function [2]. Similarly, changing the value of the electric-field strength used in the calculation or disregarding the exciton binding energy, one obtains theoretical curves that deviate in a specific way from the experimental one.

Thus, the presented results of calculations ensure that it is possible to describe the layer parameters in a nonuniform structure by models yielding sufficiently close agreement with the experiment over the entire nonuniformity field and in a broad range of parameter variation. This, in turn, means that analysis of a single sample based on experimental data only (without any need to rely on technology-based estimates of the layer parameters) enables one to get information on the nature of the observed optical transitions and the character of the interfaces and to estimate the values of certain parameters, such as the strength of the built-in electric field in the structure, etc.

The suggested approach made it possible to obtain a detailed picture of the variation in the PL band intensity in the field of the nonuniformity under study; the results are shown in Fig. 5.

The intensity of band *B*, related to the narrower QW_B, behaves unusually with an increase in the thickness parameter (see curve *1*). Starting from zero, it increases; goes through a clearly defined maximum corresponding to a QW width of 2–2.2 nm; and then decreases by almost an order of magnitude, reaching the intensity level of band *C*. On the scale of these changes, the latter remains nearly constant in the entire range of parameter variation (curve *2*). Qualitatively, this general pattern does not change when the data obtained from the spots of group *2* are included (Fig. 5). It is difficult to explain such a behavior of the PL intensity by the changes in the overlap of the charge-carrier wave functions in the QW subjected to the built-in electric field: in this case, stronger variations should be observed in the wider QW_C. Apparently, the observed rise in intensity is related to the filling of the QWs by charge carriers: the process of redistribution of the

charge carriers from the barrier layers to the QWs depends nonmonotonically on the thickness parameter. In the context of this study, both the barrier thickness and the QW width are included in the thickness parameter. It cannot be decided which of them is the dominant factor that governs the variation in the PL intensity. However, this uncertainty can be avoided if, e.g., the parameters of the barrier layers of the structure are kept constant and only the QW layer remains laterally nonuniform.

The rightmost portion of curve *1* in Fig. 5 corresponds to the thinnest QW in which the PL is still observed. The absence of experimental points in curve *1* of Fig. 4a to the right of $E_C = 1.64$ eV means that band *B* disappears from the spectra measured at the spots with sufficiently small widths of QW *B*. The process of this gradual disappearance can be seen in Fig. 5 as a region of linear decrease in the intensity of band *B* in the right-hand side of curve *1* followed by a short region with a more gentle slope of the curve in the range of the lowest intensities; very small steps in the thickness parameter can be made to trace this decrease in detail. The entire region of the linear decrease in intensity corresponds to the variation of the thickness of the QW_C by 2 nm (see curve *1* in Fig. 4b); consequently, the effective width of the QW_B varies by about 0.6 cm. Supposedly, the decrease is caused by a reduction in the region where exciton states may exist, which takes place as the interfaces of a QW with a smeared Al-distribution profile are brought closer and closer together. The rightmost portion of curve *1* in Fig. 5 corresponds to the case where the energies of the quantized electron states are close to the barrier energy and the processes of the tunneling escape of charge carriers from the QW subjected to a built-in electric field become important. Probably, this region of low PL intensity corresponds to the breakup of a two-dimensional potential well for electrons into separate islands where carrier confinement is still possible.

The observed features of the PL in narrow QWs, whose energy states are most sensitive to variations in structure parameters, can be used to obtain some estimates. For example, let us assume that the end of the region of a linear decrease in the PL intensity, which reflects the "closing" of the QW interfaces, corresponds to the limiting case of a trapezium-shaped QW, a triangular QW. Then, in the context of the adopted theoretical model, we find that the conduction-band offset ratio at the interface $\Delta E_c/\Delta E_g = 0.612$, which agrees well with the commonly accepted value of 0.6 [2]. To obtain this result, we used the experimental values of the energy of the edge PL in AlGaAs barrier layers (E_A = 1.85 eV) and the energies E_B and E_C corresponding to the intersection of the linearly decreasing region of curve *1* in Fig. 5 with the abscissa axis ($E_B^* = 1.757$ eV, $E_C^* = 1.597$ eV); the ratio of the mean QW widths was assumed to be $w_B/w_C = 3.4$; and, finally, it was assumed

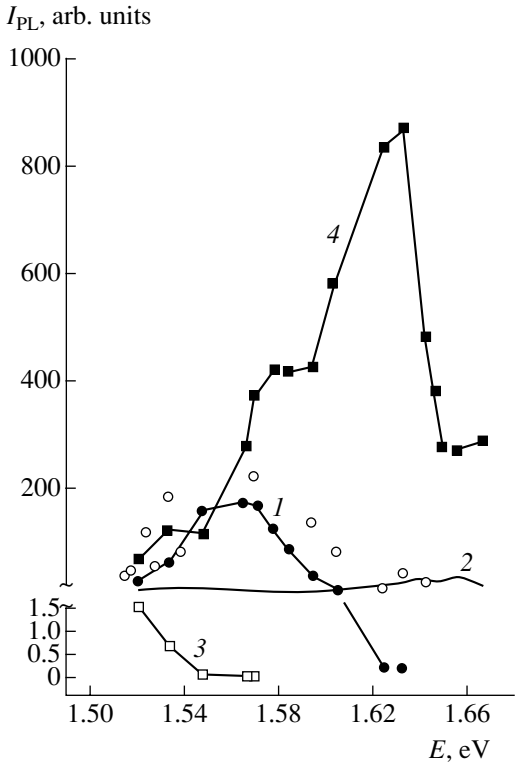

Fig. 5. Experimentally measured intensities of the spectral bands *B*, *C*, *D*, and *E* (curves *1*, *2*, *3*, and *4*, respectively) plotted as functions of the QW_C emission energy. For band *B*, experimental points corresponding to spots from group *1* are shown by filled circles and those from group *2*, by open circles.

that the stepwise potential profile at the QW interfaces consists of five steps at each interface.

The detailed investigation of special features of the PL in narrow QWs was not the purpose of this study. We only conclude from the above results that the suggested approach is highly informative in studying the influence of technologically defined parameters on the properties of QCSs. This approach is most promising for the investigation of the processes of a threshold and resonance nature, where the possibility of precise variation of the parameters is especially important.

4.2. Photoluminescence of In-*Containing Quantum Wells*

Now, let us consider the PL of In-containing QWs. First, it should be noted that the emission from the QW_E (band *E*), which is the most deeply located one, is the most intense over virtually the entire wafer surface (see Fig. 5, curve *4*). In contrast, the PL intensity of QW_D is very low (Fig. 5, curve *3*). Band *D* rapidly decreases with an increase in the thickness parameter and, similarly to band *B*, disappears from the spectra; it is not observed over the greater part of the wafer.

Evidently, the special features of the PL of In-containing layers are determined by a built-in electric field created by the MDHJ. This field tends to push the holes away from the heterojunction in the direction of the In-containing QWs and the buffer layer. A QW may serve as an effective sink for holes, which creates the conditions for intense radiative recombination from the well. Most probably, it is this process of carrier capture by the QW_E that explains the high intensity of band *E* in the spectra. Notably, the intensity of band *E* depends nonmonotonically on the thickness parameter (see Fig. 5, curve *4*), while the variation of In content in the layers is insignificant (Fig. 4b, curve *3*); this can be related to the "optimization" of charge-carrier capture by the QW_E with changes in the geometric parameters of the MDHJ–QW_E system due to variation in the barrier-layer thicknesses. For the QW_D, which is narrower, shallower, and located in a stronger electric field due to its proximity to the MDHJ, the capture conditions are different; this is responsible for the low level of PL intensity there.

It should be noted that, as a rule, the features related to emission from GaAs barrier layers, including the buffer layer, are not observed in the spectra. A weak band near 1.508 eV is observed only in a small region of the wafer corresponding to the thinnest layers (see Fig. 4a, curve *6*). In the same region, a decrease in emission from QW_E takes place (Fig. 5, curve *4*). These findings also indicate that the processes of redistribution of the photoexcited charge carriers from GaAs barrier layers into the QWs are, in general, sufficiently effective and depend on the parameters characterizing sample nonuniformity. The possibility of achieving low levels of PL from GaAs layers may be useful in studying the PL from various semiconductor structures in the spectral region of the edge emission of GaAs, where buffer-layer PL represents a background that hinders measurement of the PL from the structure under study; e.g., this is the case for investigations of PL from δ-doped layers [3].

Thus, it can be concluded that the suggested approach for investigating laterally nonuniform structures can be sufficiently informative in the studies of the processes of charge-carrier redistribution under the influence of a built-in electric field within a crystal and, in particular, of carrier capture by QWs.

5. CONCLUSIONS

Thus, studying the photoluminescence of a single nonuniform sample on the basis of the correlative-spectroscopy method indicated the possibility of multiparameter characterization of the structure of a semiconductor sample, demonstrated the possibility of investigating a number of processes with precise control over sample parameters, revealed the features of the PL of narrow QWs, and provided information on charge-carrier redistribution in a structure with QWs. It can be concluded that a variant of the method considered in this paper can be applied to the investigation of quantum-confinement structures. The results obtained indicate that the new method suggested for studying semiconductor structures is promising and, certainly, is not limited to the issues considered here.

ACKNOWLEDGMENTS

I thank V.A. Petrov for numerous and useful discussions, and A.V. Guk for his help in sample preparation.

REFERENCES

1. Yu. V. Khabarov, RF Patent No. 2,168,238 (2001).
2. M. A. Herman, D. Bingerg, and J. Christen, J. Appl. Phys. **70** (2), R1 (1991).
3. J. Wagner, A. Fischer, and K. Ploog, Phys. Rev. B **42**, 7280 (1990).
4. L. Pavesi and M. Guzzi, J. Appl. Phys. **75**, 4779 (1994).
5. S. V. Evstigneev, R. M. Imamov, A. A. Lomov, *et al.*, Fiz. Tekh. Poluprovodn. (St. Petersburg) **34**, 719 (2000) [Semiconductors **34**, 693 (2000)].
6. G. Bastard, C. Delalande, Y. Guldner, and P. Voison, in *Advances in Electronics and Electron Physics*, Ed. by P. W. Hawkes (Academic, San Diego, 1988), Vol. 72.

Translated by M. Skorikov

Semiconductors, Vol. 37, No. 3, 2003, pp. 329–335. Translated from Fizika i Tekhnika Poluprovodnikov, Vol. 37, No. 3, 2003, pp. 346–352.

LOW-DIMENSIONAL SYSTEMS

Conductivity of One-Dimensional Semiconductor with Periodic Potential

S. D. Beneslavskiĭ, A. A. Elistratov*, and S. V. Shibkov**

Institute of Cryptography, Communication, and Computer Science, Academy of Federal Security Service, Moscow, 117602 Russia

** e-mail: elist@interset.ru*

*** e-mail: shibkovsv72@mail.ru*

Submitted September 2, 2002; accepted for publication September 18, 2002

Abstract—The kinetic equation for the electron distribution function in a one-dimensional semiconductor with a spatial-periodic potential in the presence of a weak pulling electric field was analytically solved in the limiting case of the infinite length of carrier energy relaxation. An explicit expression for the conductivity of the system was derived for a sinusoidal potential profile with an arbitrary amplitude. It was shown that the singularities in the electron distribution function, arising in the asymptotic limit, are smoothed in the region of finite lengths of energy relaxation. A comparison with the results of an opposite (local) mode shows that conductivity in the significantly nonlocal case is lower at any potential amplitude. *© 2003 MAIK "Nauka/Interperiodica".*

1. INTRODUCTION

As is known, the kinetic coefficients of a conductor can be analytically calculated only in exceptional cases. In particular, metal or semiconductor conductivity may be explicitly calculated in the region of applicability of the quasi-classical approximation by solving the linearized kinetic Boltzmann equation in the case of an isotropic dispersion relation for carriers and dominant elastic or quasi-elastic scattering mechanisms. In this case, the conductivity and other linear kinetic coefficients are expressed in terms of the momentum relaxation time $\tau_p(\varepsilon)$ (averaged in a certain way) characterized by a power-law dependence on the particle energy [1]. It is important that the problem of the nonequilibrium energy distribution of carriers does not emerge within the linear-response approach, since the Joule heat is proportional to the squared electric field. This is valid only for spatially homogeneous systems; the situation drastically changes in the case of nonuniform potential fields. Indeed, built-in fields locally perform work as electric current flows, with consequent nonequilibrium arising in the energy distribution of carriers. In this case, the kinetic problems can be solved in the quasi-hydrodynamic limit, where the characteristic scale of potential-field nonuniformity significantly exceeds both the momentum and energy relaxation lengths [2].

In this paper, we suggest a method for calculating the conductivity of a spatial-periodic one-dimensional (1D) semiconductor structure in the limit inverse to the hydrodynamic one. Explicit calculations can be carried out in the asymptotic case of an infinite length l_e of energy relaxation (referred to as the "cooling" length) for any relation between the structure period L and the momentum path length l_p. The choice of a 1D model is justified for mathematical reasons; furthermore, practical examples of quasi-1D semiconductor systems are well known [3, 4]. We restrict ourselves to the system's parameter range in which the quasi-classical kinetic equation is applicable; i.e., we do not consider localization and quantum tunneling effects, as well as miniband structure formation [5]. It is evident that all of these essentially quantum effects cease to exist at rather high temperatures. Specific calculations are carried out for a model with the conventional dispersion relation for electrons; the interaction between carriers and 1D acoustical phonons is considered as the basic scattering mechanism. In the limit $l_e \longrightarrow \infty$, the problem is solved exactly; however, the distribution function is found to be singular in a certain energy range. In the case of finite l_e, an elliptic differential equation was derived for the electron distribution function dependent on the coordinate and energy; a corresponding boundary-value problem was formulated. The problem can only be solved numerically. However, in the limit $l_e \gg L$, consideration of the finiteness of the cooling length regularizes the solution singularities having no effect on integral quantities, in particular, those that do not significantly change the conductivity. In addition, the results were compared to those obtained in the local limit. The conductivity in the hydrodynamic region appears higher than that in the nonlocal mode at any amplitude of the periodic potential.

2. MODEL AND BASIC EQUATIONS

Let us consider a nondegenerate system of electrons in a 1D semiconductor characterized by the macroscopic potential profile $U(x) = U(x + L)$ with the period L

1063-7826/03/3703-0329$24.00 © 2003 MAIK "Nauka/Interperiodica"

significantly exceeding both the lattice constant and the de Broglie wavelength. The dispersion relation of electrons is conventional, $\varepsilon_p = p^2/2m$. As the basic mechanism of scattering, we consider the interaction with 1D acoustical phonons, whose spectrum is given by the formula $\omega = sq$, where s is the velocity of sound. If the temperature condition $T \gg ms^2$ is met, electron scattering by phonons is quasi-elastic, as in the three-dimensional (3D) case [6, 7], with the consequent relation $l_e \gg l_p$ between the momentum and energy path lengths. We consider the density of electrons to be sufficiently low, so that we may disregard their scattering by each other. The kinetic equation linearized over the external ("pulling") electric field is written as

$$\frac{p}{m}\frac{\partial f_1}{\partial x} - \frac{\partial U}{\partial x}\frac{\partial f_1}{\partial p} + eE\frac{\partial f_0}{\partial p} = I_{st}(f_1), \quad (1)$$

where $f_0 = \exp[(\mu - \varepsilon)/T]$ is the equilibrium function with the chemical potential μ, $\varepsilon = p^2/2m + U(x)$ is the total energy, f_1 is a linear addition to the distribution function in the field E, and $I_{st}(f_1)$ is a collision integral that is a linear functional of f_1. To describe the electron–phonon interaction, we employ the deformation potential approximation. In the range of validity of the inequality $ms^2 \ll T$, the collision integral in Eq. (1) allows equal probability of forward and backward scattering. An analogue of this in the 3D case is electron–phonon scattering isotropy.

Let us represent the sought-for addition to the distribution function as the sum of even and odd (with respect to the momentum) components,

$$f_1(x, p) = f_{1s}(x, p) + f_{1a}(x, p),$$

where $f_{1s}(x, p) = f_{1s}(x, -p)$ and $f_{1a}(x, p) = -f_{1a}(x, -p)$. The symmetry of Eq. (1) allows us to write the system

$$\upsilon\frac{\partial f_{1s}}{\partial x} - \frac{\partial U}{\partial x}\frac{\partial f_{1s}}{\partial p} + eE\frac{\partial f_0}{\partial p} = I_{st}(f_{1a}), \quad (2)$$

$$\upsilon\frac{\partial f_{1a}}{\partial x} - \frac{\partial U}{\partial x}\frac{\partial f_{1a}}{\partial p} = I_{st}(f_{1s}), \quad (3)$$

where $\upsilon = p/m$ is particle velocity.

The scattering quasi-elasticity allows us to write the right-hand side of Eq. (2) in the relaxation time approximation and the collisional term in Eq. (3) in the differential form (see [8])

$$I_{st}(f_{1a}) = -\frac{f_{1a}}{\tau(\varepsilon_p)}, \quad (4)$$

$$I_{st}(f_{1s}) = \frac{1}{\rho(\varepsilon_p)}\frac{\partial}{\partial\varepsilon_p}\rho(\varepsilon_p)D(\varepsilon_p)\left(\frac{\partial f_{1s}}{\partial\varepsilon_p} + \frac{f_{1s}}{T}\right), \quad (5)$$

where

$$\rho(\varepsilon_p) = [\pi\hbar\upsilon(\varepsilon_p)]^{-1} = (\pi\hbar)^{-1}(m/2\varepsilon_p)^{1/2}$$

is the density of electron states, and $D(\varepsilon_p)$ is the effective diffusivity over the energy axis and defined by the conventional relation

$$D(\varepsilon_p) = \frac{1}{2}\left\langle\frac{\delta(\Delta\varepsilon_p)^2}{\delta t}\right\rangle.$$

It is evident that $\tau(\varepsilon_p) \propto \varepsilon_p^{1/2}$ and $D(\varepsilon_p) \propto \varepsilon_p^{1/2}$ in the model under consideration, which is caused by the energy dependence of the density of the levels in the 1D system. Hence, the product $\rho(\varepsilon_p)D(\varepsilon_p) = \text{const}$.

In the set of Eqs. (2) and (3), it is convenient to introduce variable coordinates and the total energy $\varepsilon = \varepsilon_p + U(x)$:

$$\upsilon[\varepsilon - U(x)]\left(\frac{\partial f_{1s}}{\partial x} + eE\frac{\partial f_0}{\partial\varepsilon}\right) = -\frac{f_{1a}}{\tau[\varepsilon - U(x)]}, \quad (6)$$

$$\upsilon[\varepsilon - U(x)]\left(\frac{\partial f_{1a}}{\partial x}\right) = D[\varepsilon - U(x)]\left(\frac{\partial^2 f_{1s}}{\partial\varepsilon^2} + \frac{1}{T}\frac{\partial f_{1s}}{\partial\varepsilon}\right), \quad (7)$$

where

$$\upsilon[\varepsilon - U(x)] = 2[\varepsilon - U(x)]/m^{1/2};$$

when writing the right-hand sides, the D properties indicated above were used.

3. EXTREMELY NONLOCAL MODE

We now consider the zeroth approximation with respect to the inelasticity of electron–phonon scattering (i.e., the case of infinitely long energy relaxation); then, $D \equiv 0$ in Eq. (7). Under this condition, it is evident that f_{1a} is a function of the total energy ε, which (together with the oddness condition for the momentum) causes f_{1a} to vanish for all the states with $\varepsilon < U_{max}$, i.e., for finite trajectories. In the region $\varepsilon > U_{max}$, the odd component of the distribution function is nonzero; in general, it can be written as

$$f_{1a}(x, p) = f_{1a}(\varepsilon)\,\mathrm{sgn}(p)\theta(\varepsilon - U_{max}). \quad (8)$$

To determine $f_{1a}(\varepsilon)$, we rewrite Eq. (6), introducing the momentum path length $l = \upsilon\tau$ as

$$\frac{\partial f_{1s}}{\partial x} + eE\frac{\partial f_0}{\partial\varepsilon} = -\frac{f_{1a}(\varepsilon)}{l[\varepsilon - U(x)]}. \quad (9)$$

Having integrated Eq. (9) over the structure period, taking into account the periodicity condition, we obtain

$$-e\frac{\partial f_0}{\partial\varepsilon}\int_0^L E(x)dx = f_{1a}(\varepsilon)\int_0^L\frac{dx}{l[\varepsilon - U(x)]}. \quad (10)$$

For the sake of convenience, we introduce the quantities averaged over the period and we rewrite Eq. (10) as

$$-e\frac{\partial f_0}{\partial\varepsilon}\langle E\rangle = f_{1a}(\varepsilon)\langle l^{-1}(\varepsilon)\rangle$$

and, in final form,

$$f_{1a}(\varepsilon) = -e\langle E\rangle\langle l^{-1}(\varepsilon)\rangle^{-1}\frac{\partial f_0}{\partial\varepsilon} = \frac{e\langle E\rangle\langle l^{-1}(\varepsilon)\rangle^{-1}}{T}e^{\mu-\varepsilon/T}. \quad (11)$$

The electric current is conventionally written as

$$j_1 = e\int_{-\infty}^{+\infty}\upsilon f_{1a}(x,p)\frac{dp}{2\pi\hbar} = \frac{e}{\pi\hbar}\int_{U_{\max}}^{\infty} f_{1a}(\varepsilon)d\varepsilon. \quad (12)$$

We draw attention to the fact that the form of function (8) necessarily provides the fulfillment of the current continuity conditions $\partial j/\partial x = 0$.

Having substituted Eq. (11) into Eq. (9), we obtain an equation for determining $f_{1s}(x, \varepsilon)$; this equation is easily solved:

$$f_{1s}(x,\varepsilon) = -e\frac{\partial f_0}{\partial\varepsilon}\int E(x)dx - f_{1a}(\varepsilon)\int l^{-1}[\varepsilon - U(x)]dx + \varphi(\varepsilon). \quad (13)$$

We will briefly dwell upon the problem of choosing the integration limits in Eq. (13) and the values of the formally arising arbitrary function $\varphi(\varepsilon)$ of energy. We restrict ourselves to the case of the even potential $U(x)$. Then, from symmetry considerations, one readily sees that $f_{1s}(x, \varepsilon) = -f_{1s}(-x, \varepsilon)$. Hence, it is convenient to set the lower limit of integrals (13) equal to zero; then $\varphi(\varepsilon)$ automatically vanishes,

$$f_{1s}(x,\varepsilon) = -e\frac{\partial f_0}{\partial\varepsilon}\int_0^x E(x')dx' - f_{1a}(\varepsilon)\int_0^x l^{-1}[\varepsilon - U(x')]dx'. \quad (14)$$

Having separated the constant component from $E(x)$,

$$\langle E\rangle = \frac{1}{L}\int_0^L E(x)dx,$$

the variable term $E(x) - \langle E\rangle$ may be eliminated by redefining the potential $U(x)$.

Finally, expression (14) is reduced to the form

$$f_{1s}(x,\varepsilon) = -e\frac{\partial f_0}{\partial\varepsilon}Ex - f_{1a}(\varepsilon)\int_0^x l^{-1}[\varepsilon - U(x')]dx', \quad (15)$$

where we set $E \equiv \langle E\rangle$ for brevity.

For the scattering mechanism under consideration, we have $l \propto \varepsilon_p$; therefore, the explicit expression for the path length can be conveniently written as

$$l[\varepsilon - U(x)] = l_T\frac{\varepsilon - U(x)}{T}, \quad (16)$$

where l_T is the path length of electrons possessing a thermal velocity.

In the region of finite motion $\varepsilon < U_{\max}$, where $f_{1a} \equiv 0$, the following simple result follows from Eq. (15):

$$f_{1s}(x,\varepsilon) = -e\frac{\partial f_0}{\partial\varepsilon}Ex = \frac{eEx}{T}e^{(\mu-\varepsilon)/T}.$$

It corresponds to the weak redistribution of particles in potential wells, which is caused by an electric field; in other words, it describes an emerging polarization of bound electrons.

Further calculation requires specification of the potential form. We consider the case of the harmonic potential profile,

$$U(x) = U_0\cos 2\pi\frac{x}{L}. \quad (17)$$

The finite and infinite motion regions correspond to $\varepsilon < U_0$ and $\varepsilon > U_0$, respectively. Using expressions (16) and (17), we reduce Eq. (11) to the form

$$f_{1a}(\varepsilon) = \frac{eE}{T^2}l_T f_0\sqrt{\varepsilon^2 - U_0^2}.$$

Hence, Eq. (15) can be written as

$$f_{1s}(x,\varepsilon) = \frac{eEL}{T}\left[\frac{x}{L} - \frac{1}{\pi}\arctan\left(\sqrt{\frac{\varepsilon+U_0}{\varepsilon-U_0}}\tan\pi\frac{x}{L}\right)\right]f_0. \quad (18)$$

The solutions obtained are characterized by a number of interesting features. The curves $f_{1s}(x)$ are shown in Fig. 1 for $U_0/T = 1/2$. One can see from Eq. (18) and Fig. 1 that $f_{1s}(x)$ is singular at $\varepsilon \longrightarrow U_0$ and $x \longrightarrow 0$.

The carrier behavior near the potential energy maxima $U(x)$ ($x = 0, L, 2L, \ldots$) is formally similar to the hydrodynamic case, which takes place when a nonviscous fluid flows around a body, and is referred to as a tangential discontinuity. When $\varepsilon \longrightarrow U_0$, the derivatives $(\partial f_{1a}/\partial\varepsilon)$ and $(\partial f_{1s}/\partial x)$ approach infinity, and the function f_{1s} itself has a discontinuity at the point (0, 0) (see Fig. 2).

The consideration of nonequilibrium additions in the approximation of quasi-elastic scattering of electrons should eliminate the nonanalyticity of the distribution function f_{1s} in the region of the separatrix (the line $\varepsilon = U_0$ separating the regions of finite and infinite motion) and the points of periodic potential maxima.

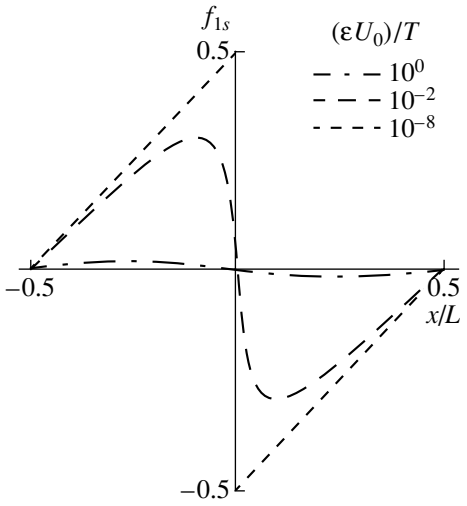

Fig. 1. Dependences $f_{1s}(x)$ of the even component of the nonequilibrium addition to the distribution function at various electron energies ε (extremely nonlocal case).

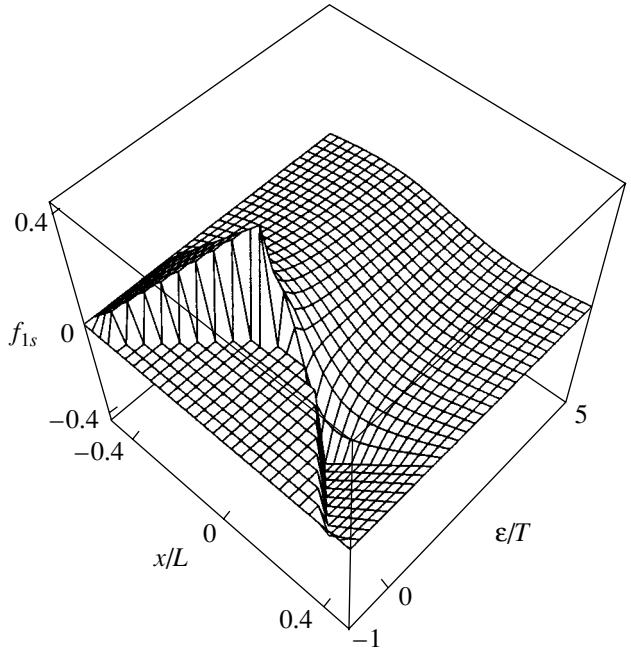

Fig. 2. General form of the dependence $f_{1s}(x, \varepsilon)$.

Let us calculate the current density (12) within this model:

$$j_1 = \left[\frac{e^2 l_T}{\pi\hbar} e^{\mu/T} \int_{V_0}^{\infty} \sqrt{y^2 - V_0^2}\, e^{-y} dy\right] E = \frac{e^2 l_T}{\pi\hbar} e^{\mu/T} |V_0| \mathrm{K}_1(|V_0|) E, \quad (19)$$

where $V_0 = U_0/T$ and $\mathrm{K}_1(|V_0|)$ is the Macdonald function. To reveal the behavior of the chemical potential appearing in Eq. (19), we use the condition for a constant number of particles. Integrating Eq. (19) over x in the interval $[0, L]$ in the case of the presence and absence of periodic potential and equating the found expressions, we obtain

$$e^{\mu/T} \int_0^L e^{-V(x)} dx = L e^{\mu/T} \int_0^1 e^{-V_0 \cos 2\pi t} dt = L e^{\mu/T} \mathrm{I}_0(V_0) = L e^{\mu_0/T},$$

where μ and μ_0 is the chemical potential of electron gas at $V_0 \neq 0$ and $V_0 = 0$, respectively; and $\mathrm{I}_0(V_0)$ is the modified Bessel function. In final form, the current is written as

$$j_1 = \left[\frac{e^2 l_T}{\pi\hbar} e^{\mu_0/T} \frac{|V_0| \mathrm{K}_1(|V_0|)}{\mathrm{I}_0(V_0)}\right] E = j_0 \frac{|V_0| \mathrm{K}_1(|V_0|)}{\mathrm{I}_0(V_0)}, \quad (20)$$

where j_0 is the current density in the absence of the periodic potential. We estimate this expression in two extreme cases.

(i) In the case of $U_0 \gg T$, we use asymptotic expansion for the Bessel and Macdonald functions and obtain

$$j_1 = j_0 \pi |V_0| e^{-2|V_0|}.$$

One can see that the current density in the case of a deep potential well is exponentially small in comparison with the spatially homogeneous case, which is caused by a small number of carriers with an energy sufficient for overcoming the high potential barrier.

(ii) In the case of $U_0 \ll T$, when there are small arguments, we use the expansion of the Bessel and Macdonald functions and obtain the following expression valid with an accuracy up to the second-order terms:

$$j_1 = j_0 \left\{1 + \left[(C-1) + \ln\frac{|V_0|}{2}\right] \frac{|V_0|^2}{2}\right\}. \quad (21)$$

Here, $C \approx 0.577$ is the Euler constant.

4. QUASI-ELASTIC SCATTERING OF CARRIERS

We introduce the inelasticity parameter $\delta = (2ms^2/T)(L/l_T)^2$. In the case of quasi-elastic scattering of electrons at acoustical phonons ($\delta \ll 1$), the kinetic equation can be transformed as follows. Substituting expressions (4) and (5) into Eqs. (2) and (3), we find the

expression for f_{1a} from Eq. (2) and substitute it into Eq. (3); as a result, we obtain

$$-\upsilon\left(\frac{\partial}{\partial x}+F_0\frac{\partial}{\partial\varepsilon_p}\right)\tau\upsilon\left(\frac{\partial f_{1s}}{\partial x}+F_0\frac{\partial f_{1s}}{\partial\varepsilon_p}+eE\frac{\partial f_0}{\partial\varepsilon_p}\right) = \frac{2ms^2T}{l_T}\upsilon\frac{\partial}{\partial\varepsilon_p}\left(\frac{\partial f_{1s}}{\partial\varepsilon_p}+\frac{f_{1s}}{T}\right). \quad (22)$$

Let us estimate the energy-range width near the separatrix ($\varepsilon = U_0$), where the solution to Eq. (22) significantly differs from the values given by the expression obtained in the extremely nonlocal mode. This difference is caused by the additional term which appears in Eq. (22), is proportional to δ, and corresponds to the collision integral in the quasi-elastic limit. Let us consider the asymptotic behavior of the terms in Eq. (22) using expression (18) as the function f_{1s}. Simple analysis yields the following condition:

$$\frac{\varepsilon}{T} \gg \frac{\sqrt{\delta}}{4\pi\sqrt{V_0}};$$

if this condition is met, deviations of the solution from the values given by function (18) become vanishingly small. It is evident that, in the strongly nonlocal case $\delta \ll 1$, solution (18), obtained in the limit $\delta = 0$, is valid to a good accuracy over almost the entire energy region.

For the energy region

$$\varepsilon/T \le \delta^{1/2}/(4\pi V_0^{1/2}),$$

Eq. (22) was numerically solved with the following relevant boundary conditions: the function f_{1s} and its derivative with respect to x are periodic, the sought-for solution is transformed into Eq. (18) at $\varepsilon/T \longrightarrow \infty$, and the flux in the energy space is zero at $\varepsilon = U(x)$. As a result, the dependence $f_{1s}(x/L, \varepsilon/T)$ was obtained at various δ ($x/L = 1/4$) (see Fig. 3). One can see that consideration of the quasi-elasticity of carrier scattering by phonons eliminates the nonanalyticity in the energy dependence of f_{1s}.

5. LOCAL LIMIT

Let us solve the kinetic problem for a spatial-periodic structure using the conventional approach, referred to as the hydrodynamic approximation [7].

In this inverse, extremely local case, in order to retain the above quasi-elasticity condition of electron scattering by long-wavelength acoustical phonons, we should restrict ourselves to the case where the dimensionless phonon energy ms^2/T still remains low (this is always valid for the relaxation mechanism under study), but where the period L is much longer than the free path length l. Introducing the dimensionless variable $y = \varepsilon/T$ and taking into account the fact that the inequality $\delta \gg 1$ is valid at the above-mentioned relations between the length and energy scales, we obtain Eq. (22) in the zero approximation with respect to $1/\delta$ in the form

$$\frac{\partial^2 f_{1s}}{\partial y^2}+\frac{\partial f_{1s}}{\partial y} = 0.$$

Taking into account the fact that the function should be normalizable and recalling relation (9) between f_{1a} and f_{1s}, as well as expression (12) for the current density, we obtain

$$f_{1s}(x,\varepsilon) = \frac{eE}{T}\left(x-\frac{L}{\mathrm{I}_0(V_0)}\int_0^{x/L} e^{V_0\cos 2\pi t}dt\right)f_0.$$

The coordinate dependence of f_{1s} at various amplitudes of the periodic potential is shown in Fig. 4. Notably, the dependence on the spatial coordinate in the hydrody-

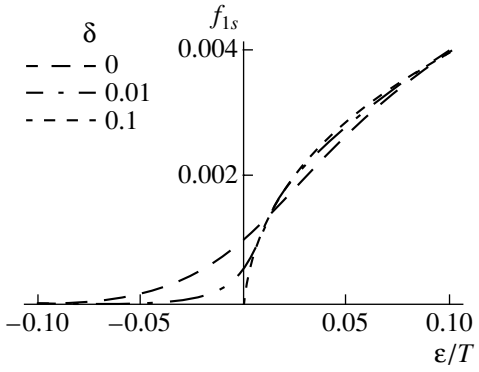

Fig. 3. Dependence $f_{1s}(\varepsilon/T)$ at the point $x = L/4$ at various anelasticity parameters δ.

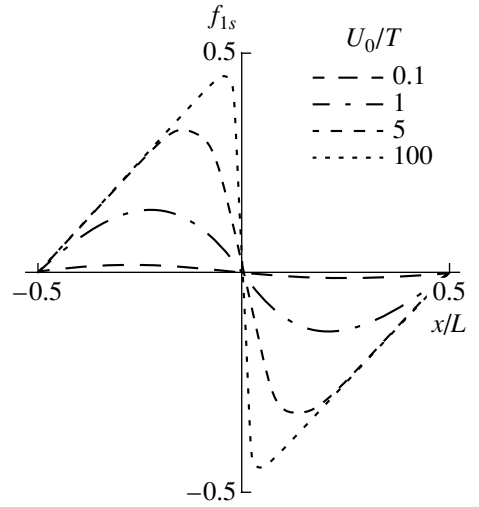

Fig. 4. Dependences $f_{1s}(x, \varepsilon = 0)$ at various amplitudes of the periodic potential U_0 in the local mode.

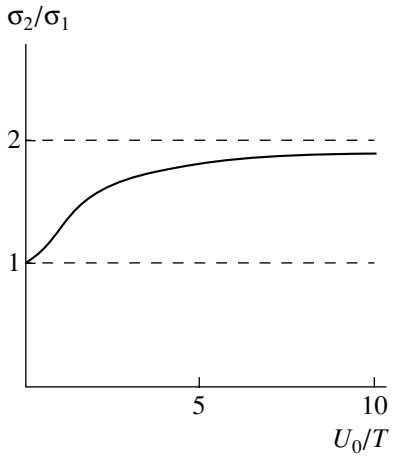

Fig. 5. Dependence of the ratio of conductivities in the extremely local and nonlocal modes on the potential U_0 amplitude.

namic limit coincides with that in the case of extremely nonlocal electron–phonon interaction at sufficiently large amplitudes of the periodic potential.

Taking into account the fact that the number of particles remains constant as the chemical potential varies (similar to expression (20)), we obtain the expression for the current density:

$$j_2 = \frac{e^2 l_T e^{\mu_0/T}}{\pi\hbar[\mathrm{I}_0(V_0)]^2}E = \frac{j_0}{[\mathrm{I}_0(V_0)]^2}. \qquad (23)$$

As in the nonlocal mode, we consider expression (23) in extreme cases.

(i) At large values $V_0 \gg 1$, using the asymptotic expansion of the Bessel function, we obtain the expression

$$j_2 = j_0 2\pi|V_0|e^{-2|V_0|},$$

which, up to a numerical factor, coincides with the corresponding expression in the nonlocal case.

(ii) At small values $V_0 \ll 1$, with an accuracy reaching second-order terms, we have

$$j_2 = j_0\left(1 - \frac{|V_0|^2}{2}\right).$$

In comparison with the spatially homogeneous case, the decrease in conductivity is not as abrupt as in the extremely nonlocal situation (see expression (21)). This is because the physics of the phenomenon, in the case of local interaction leading to Maxwell distribution at the periodic potential amplitudes $V_0 \ll 1$, does not differ greatly from the kinetic problem of small deviations from thermodynamic equilibrium in weak fields.

A comparison of current density expressions (20) and (23), which were derived in the extremely nonlocal case and in the hydrodynamic approximation, shows that $j_1 < j_2$ at both small and large periodic potential amplitudes. As V_0 increases, the ratio j_2/j_1 of currents asymptotically tends to 2 (see Fig. 5). Thus, a system of particles interacting nonlocally with scatterers is characterized by a higher resistance to current transport than a system of carriers in local equilibrium with a phonon thermostat, which is not in itself obvious from general considerations.

6. CONCLUSION

One of the results of this study is a technique suggested for solving kinetic problems in a spatially inhomogeneous system when there are long characteristic path lengths of particles. A similar approach can be applied to systems with a large number of dimensions, as well as when considering problems in diffusion, thermoelectric phenomena, and some other situations.

The numerical solution of the Boltzmann equation showed that a gradual increase in the degree of inelasticity of electron–phonon interaction leads to the involvement of carriers localized in the elastic case in the current transport. This process is characterized by a diffusive energy exchange between two electron subsystems. Energy relaxation results in "smearing" of the singularities near the potential maxima and at the interface between the finite and infinite regions.

In conclusion, we discuss the possibility of comparing the results of this study with experimental data. The conductivity calculation procedure developed in this study presumes a one-dimensional dynamics of carriers, which requires quantization of the transverse motion of particles in actual systems. In this case, the one-dimensionality condition is not necessary for the phonon subsystem.

Actual systems with quasi-one-dimensional conduction are sufficiently well known [9]. A recent example of such a system can be represented by nanostructures of lead phthalocyanine molecules, whose kinetic characteristics were considered in [10]. The periodic potential in quasi-one-dimensional systems can be implemented, e.g., in the course of initiation of the charge density wave, and in the passage of a strong acoustic wave, or an intentionally selected structure of an electrostatic field.

REFERENCES

1. V. L. Bonch-Bruevich and S. G. Kalashnikov, *Physics of Semiconductors*, 2nd ed. (Nauka, Moscow, 1990).
2. *Proceedings of 1st All-Union Telavi School–Seminar on Nonequilibrium Quasi-Particles in Solids* (Tbilisi Gos. Univ., Tbilisi, 1979).
3. G. Crüner, Rev. Mod. Phys. **60**, 1129 (1988).

4. L. I. Glazman, G. V. Lesovik, D. E. Khmel'nitskiĭ, and R. I. Shekhter, Pis'ma Zh. Éksp. Teor. Fiz. **48** (3), 218 (1988) [JETP Lett. **48**, 238 (1988)].
5. V. Ya. Demikhovskiĭ and G. A. Vugal'ter, *Physics of Quantum Low-Dimensional Structures* (Logos, Moscow, 2000).
6. E. M. Conwell, *High Field Transport in Semiconductors* (Academic, New York, 1967; Mir, Moscow, 1970).
7. V. Denis and Yu. Pozhela, *Hot Electrons* (Mintis, Vilnius, 1971).
8. B. I. Davydov, Zh. Éksp. Teor. Fiz. **6**, 463 (1936).
9. M. E. Gershenzon, Yu. B. Khavin, and A. L. Bogdanov, Usp. Fiz. Nauk **168** (2), 200 (1998) [Phys.–Usp. **41**, 186 (1998)].
10. N. A. Poklonskiĭ, E. F. Kislyakov, D. I. Sagaĭdak, *et al.*, Pis'ma Zh. Tekh. Fiz. **27** (5), 17 (2001) [Tech. Phys. Lett. **27**, 180 (2001)].

Translated by A. Kazantsev

Semiconductors, Vol. 37, No. 3, 2003, pp. 336–339. Translated from Fizika i Tekhnika Poluprovodnikov, Vol. 37, No. 3, 2003, pp. 353–357.

AMORPHOUS, VITREOUS, AND POROUS SEMICONDUCTORS

Spectra of Photoluminescence from Silicon Nanocrystals

É. B. Kaganovich*, É. G. Manoĭlov, I. R. Basylyuk, and S. V. Svechnikov

Institute of Semiconductor Physics, National Academy of Sciences of Ukraine, Kiev, 03028 Ukraine

**e-mail: dept_5@isp.kiev.ua*

Submitted May 7, 2002; accepted for publication June 17, 2002

Abstract—The evolution of time-resolved photoluminescence (PL) spectra in Au-doped nanocrystalline silicon films produced by laser ablation has been studied. The PL spectra with a relaxation time of nanoseconds are broad; they lie in the energy range 1.4–3.2 eV with a peak at 2.4–2.8 eV. At the longest times of tens of microseconds, the spectra become narrower, with a peak at 1.6 eV. At intermediate times, two bands are observed: low-energy (1.6 eV) and high-energy, with the peak shifting from 2.7 to 2.1 eV with time increasing. The data are discussed in terms of quantum confinement, dielectric amplification, and manifestation of kinetically coupled electron–hole and exciton subsystems. Ions and atoms of gold passivate dangling bonds on the Si surface and serve as catalysts for the oxidation of nanocrystals. The similarity between recombination processes responsible for the visible PL in oxidized *por*-Si layers and in the studied Au-doped films is discussed. © *2003 MAIK "Nauka/Interperiodica".*

1. INTRODUCTION

Silicon nanocrystals (NC) dispersed in a dielectric medium, typically in silicon oxide SiO_x ($0 < x \leq 2$), attract much interest owing to their efficient photoluminescence (PL) in the visible spectral range at room temperature and the possibility of observing quantum-confinement effects. Porous silicon (*por*-Si) and nanocrystalline silicon (*nc*-Si) films, exhibiting PL in the visible spectral range, belong to low-dimension structures. The majority of studies of PL in *nc*-Si have been concerned with static spectra of PL from *por*-Si produced by anodizing; and a far smaller number, with spectra of time-resolved PL (TRPL) from *nc*-Si films produced by glow discharge decomposition, sputtering, ion implantation, spark discharge, laser pyrolysis of silane, laser ablation, etc. PL spectra are, as a rule, complex, covering wide ranges on the energy ($h\nu$ = 1.4–3.2 eV) and time scales ($\tau = 10^{-12}$–10^{-3} s) [1–5]. The PL spectra of Si nanocrystals, in which the fast nonradiative recombination channel associated with neutral dangling bonds on the NC surface ($D^\times$-bonds) is suppressed, are more informative with respect to recombination mechanisms. In *por*-Si produced by chemical etching, the formation conditions ensure passivation of $D^\times$-bonds by hydrogen, oxygen, and hydroxy ions. Special efforts in the passivation of $D^\times$-bonds should be made to reveal the features concealed in *nc*-Si PL spectra by the surface nonradiative-recombination channel.

In our previous study [6], we demonstrated the possibility of making the nonradiative recombination time longer, improving the PL intensity and stability, and reducing the density of traps in *nc*-Si films deposited by pulsed laser ablation (PLA) by passivating $D^\times$-bonds with gold in the course of film formation. In the present study, the TRPL spectra of these films are analyzed, including their evolution with the PL relaxation time and their dependence on the size of Si nanocrystals, and the mechanism of the effect of gold is elucidated. Our aim is to investigate the recombination mechanisms responsible for the PL spectra of Au-doped *nc*-Si films fabricated by PLA and to reveal the recombination processes common to these films and other nanocrystalline Si films.

2. EXPERIMENTAL

Photoluminescent films were obtained by PLA in vacuum. The insert in Fig. 1 schematically shows the vacuum chamber. The beam I of a Q-switched Nd^{3+}:YAG laser, emitting at 1.06 μm with a 10-ns pulse width, 20-J cm^{-2} energy density, and 25-Hz repetition rate, scanned the target V in the form of a single-crystal Si (*c*-Si) wafer. The deposition was carried out in the atmosphere of an inert gas (He, Ar) under a pressure of 10^{-1}–20 Pa. Films of the first type were deposited from the direct flux of particles from the erosion plume IV onto the substrate III placed opposite to the target in parallel to its plane [7]. Films of the second type were deposited from the reverse flux of the torch particles onto the substrate IV lying in the plane of the target [8]. In the latter case, selection of Si nanocrystals by their size occurred, with coarser NC formed closer to the axis of the erosion torch. For doping *nc*-Si films with gold, a thin (~80 nm) gold layer was deposited onto the *c*-Si target. The film growth rate was 10–20 nm min^{-1}. During deposition onto a substrate placed in the plane of the target, the film thickness decreased from ~1500 to ~300 nm with the distance from the erosion torch axis increasing to 10–12 mm. The substrates were *c*-Si, glassy ceramics, quartz, mica, etc.

The PL was excited with a nitrogen laser with a 337-nm wavelength and 8-ns pulse width. The signal was recorded stroboscopically in the photon counting mode at room temperature. The minimum gate width for the photon accumulation was 250 ns. The PL relaxation times below 250 ns were estimated using an oscilloscope.

3. RESULTS AND DISCUSSION

Figure 1 shows the thickness-normalized PL spectra of films of the second type, recorded at four points of a film at distances of 2, 4, 6, and 8 mm from the torch axis, with the corresponding decreasing size of nanocrystals (curves *1–4*, respectively). The spectra for films of the first type are shown in Fig. 2 (curve *1*). The spectra are broad, lie in the photon energy range $h\nu$ = 1.4–3.2 eV, and exhibit wide peaks at 2.4–2.6 eV with shoulders at low (1.8–2.2 eV) and high energies (2.8–3.0 eV). The PL relaxation time τ does not exceed 50 ns, which indicates that the radiative recombination is strongly overlapped with the nonradiative process. With the NC size decreasing, the PL intensity I_{PL} increases and the spectral peak shifts from 2.45 to 2.55 eV (Fig. 1a), which is indicative of the quantum confinement effect. Spectral broadening is attributed to scatter of the sizes and shapes of nanocrystals and the diversity of dielectric properties in their environment.

The PL relaxation time in gold-doped films was three orders of magnitude higher, up to several tens of microseconds. Since the quantum efficiency of films was not higher than several percent and correlation was observed between the intensity I_{PL} and the PL relaxation time τ at temperatures $T > 150$ K [9], τ is defined by the nonradiative recombination time τ_{nR}. The increase in τ_{nR} upon the passivation of NCs with gold is due to the high electron affinity (2.3 eV) and ionization energy (9.26 eV) of Au atoms. Therefore, not only positive ions, but also gold atoms effectively capture electrons from $D^{\times}$-bonds at the surface of Si nanocrystals, which are thus passivated.

The temporal evolution of TRPL spectra, revealed owing to saturation of $D^{\times}$-bonds with gold, is shown in Figs. 1b, 3, and 4 for films of the second type, and in Fig. 2 for those of the first type. It can be seen that, in both cases, the spectral behavior is about the same and comparable with that observed in *por*-Si containing oxidized material, characterized by effective visible PL [1–5]. At a relaxation time of 250 ns, the spectral peaks fall in the high-energy (2.0–2.8 eV) range, whereas with time increasing they shift to a lower energy (2.0–2.5 eV). Two bands are observed, at low (1.6 eV) and high (2.0–2.4 eV) energies. The intensity of the low-energy band is higher at maximum relaxation times of several tens of microseconds, and the high-energy band dominates at shorter times.

In Au-doped films of the second type, the high-energy spectral peak shifted to the blue spectral region with decreasing NC size at PL relaxation times $0 < \tau < 250$ ns (Fig. 1b). At the same time, a red shift was observed in the range 250 ns $< \tau \le 750$ ns, with the peak position of this band depending on the NC size only slightly at $\tau > 750$ ns (Fig. 3). The position of the low-energy peak was virtually independent of the NC size (Figs. 3 and 4).

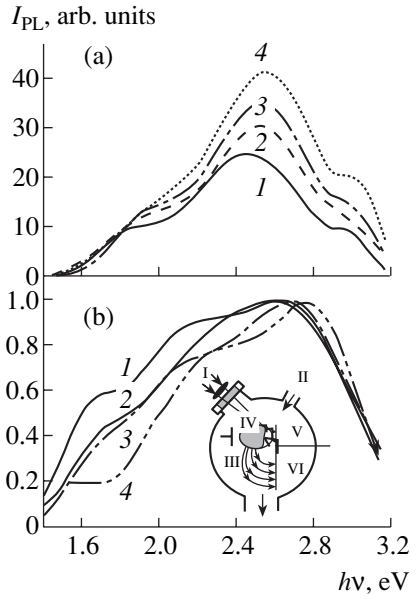

Fig. 1. (*1–4*) Normalized TRPL spectra from four points with different sizes of Si nanocrystals, $d_1 > d_2 > d_3 > d_4$ for (a) undoped and (b) Au-doped *nc*-Si films of the second type at PL relaxation times of (a) < 50 and (b) ≲250 ns. Insert: schematic of the vacuum chamber: I is the laser beam; II, inlet of the inert gas; III and VI, substrates; IV, erosion plume; and V, target.

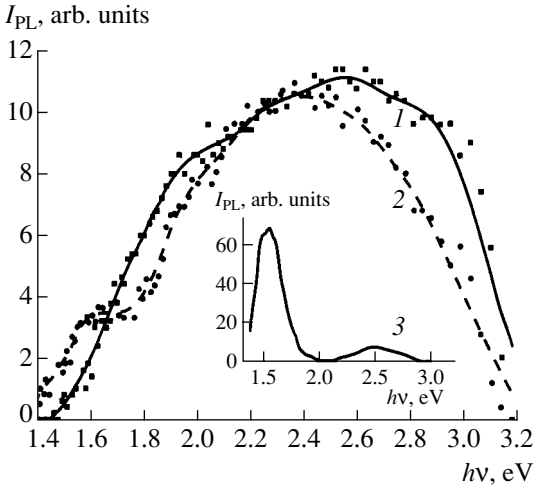

Fig. 2. TRPL spectra of (*1*) undoped and (*2*, *3*) Au-doped *nc*-Si films deposited from the direct flux of the torch particles. PL relaxation time τ: (*1*) < 50 ns, (*2*) ≤ 250 ns, and (*3*) 250 ns < $\tau \le 10$ μs.

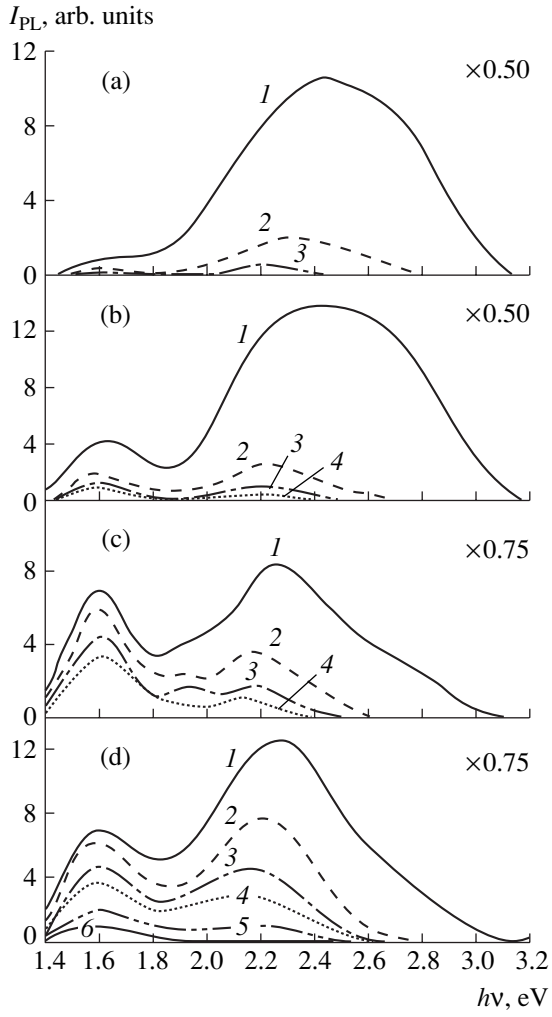

Fig. 3. (a–d) TRPL spectra from four points of Au-doped *nc*-Si films. PL relaxation time: (*1*) 250 ns < τ ≤ 500 ns, (*2*) 500 ns < τ ≤ 750 ns, (*3*) 750 ns < τ ≤ 1 μs, (*4*) 1 μs < τ ≤ 1.25 μs, (*5*) 1.25 μs < τ ≤ 1.5 μs, and (*6*) 1.5 μs < τ ≤ 1.75 μs. (a–d) Correspond to four points (*1–4*) in Fig. 1.

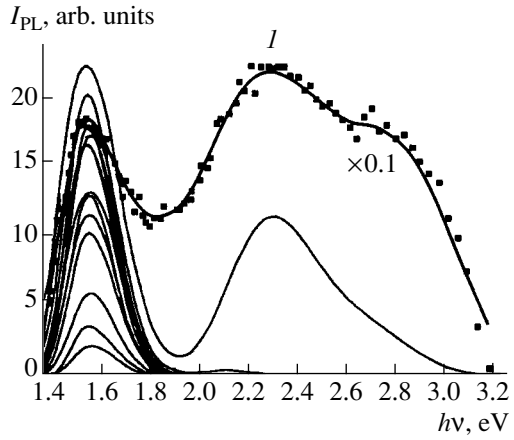

Fig. 4. TRPL spectra integrated over the film area for an Au-doped *nc*-Si film deposited from the reverse flux of particles and additionally oxidized by keeping in air for several months. Spectra recorded with times of the PL relaxation increasing: (*1*) τ ≤ 250 ns; the lowest curve, 10.5 μs < τ ≤ 12 μs.

Such temporal behavior of the spectra can be attributed to the manifestation in radiative recombination of two kinetically coupled subsystems: electron–hole pairs and excitons, with quantum confinement and dielectric amplification effects observed [1–5, 9, 10]. The decreasing of the NC size results in an increase in the oscillator strength and in a decrease in the relaxation time of radiative recombination for nonequilibrium carriers on the quantum-confinement levels of Si nanocrystals. The radiative recombination time reaches several tens of nanoseconds for the blue emission and several to tens of microseconds for the red emission. The longest time of radiative recombination is associated with the recombination of excitons in the triplet state (tens to hundreds of microseconds). Due to dielectric amplification, the exciton binding energy can become as high as 1 eV, with the excitonic emission defined by its singlet and triplet states lying in the low-energy range and its intensity increasing [10, 11]. This allows us to attribute the high-energy (1.9–3.2 eV) band mainly to the electron–hole pair emission and the low-energy band (1.4–1.8 eV) to excitonic emission.

Comparison of spectra of films of the second type, differing by the NC size (Fig. 3), shows that the PL relaxation times are longer in smaller NCs. The PL intensity is lower for larger NCs due to a lower oscillator strength and lower intensity of the light absorption associated with stronger scattering of light on larger NCs. The shorter relaxation times observed for large NCs are due to the sensitivity of our experimental setup. Calculation of the rate of nonradiative recombination for $D^{\times}$-bonds of NCs characterized by quantum confinement [12] yields values decreasing by many orders of magnitude, from 10^{11} to 10^{1} s^{-1}, with the NC size decreasing. The presence of a $D^{\times}$-bond quenches the PL from large NCs, with an emission energy of 1.4–2.2 eV, but for small NCs, with an emission energy above 2.2 eV, this nonradiative capture of carriers is much less effective. Therefore, the passivation of $D^{\times}$-bonds is more efficient for large NCs due to their large surface area. The red shift of the spectrum is related to the stronger PL from larger NCs.

The enhancement of exciton recombination in Au-doped films occurs due to the fact that Au ions and atoms capture not only electrons from $D^{\times}$-bonds, but, in further adsorption, also the valence electrons of weakened Si–Si bonds at the NC surface. By rupturing these bonds, gold contributes to the oxidation of NCs [13]. The catalytic activation by gold of the oxidation process on the surface of Si/SiO_x NCs favors the formation of dioxide SiO_2 envelopes of NCs, instead of SiO_x ($0 < x < 2$). This raises the potential barrier and reduces the dielectric constant of the envelope and the NC size. All of these factors favor the quantum-confinement and dielectric-amplification effects, and, consequently, lead

to an increase in the excitonic component in PL. In this case, the role of Au consists in that it enhances the effect of oxygen, which is observed in oxidized *por*-Si layers characterized by a higher PL intensity and longer relaxation time.

To confirm the predominance of excitonic PL with an increase in the height of the potential barrier in a quantum well, Fig. 4 shows TRPL spectra of a film similar to that represented in Fig. 3, but differing from the latter in that it was kept in air for several months, i.e., was subjected to additional oxidation. The PL spectra in Fig. 4 are characterized by a higher intensity and longer relaxation times of PL. Only a single low-energy (1.6 eV) excitonic band is observed in PL spectra at relaxation times longer than 500 ns $< \tau \leq$ 750 ns. A PL spectrum with a high intensity of its excitonic band is also observed for the Au-doped films deposited from the direct flux of particles of the erosion torch (Fig. 2).

In oxidized *por*-Si with an NC size <1.5 nm, compared with an unoxidized material, spectra are redshifted by ~1 eV, the peak position is independent of the NC size, and the PL relaxation time is longer by an order of magnitude [14, 15]. The results were accounted for by the localization of an exciton on the Si=O bond. Taking into account the catalytic activity of gold in the oxidation process, the observed independence of the 1.6-eV peak position from the NC size, and the correlation of this position with the excitonic recombination, we believe that the partial localization of excitons on Si=O bonds is possible in the case of the small NC size specified.

4. CONCLUSION

The possibility of observing the evolution of PL spectra at relaxation times of up to tens of microseconds in nanocrystalline silicon films deposited by pulsed laser ablation and doped with gold has been demonstrated. At short times, broad spectra in the energy range $h\nu$ = 1.4–3.2 eV are observed. With increasing relaxation time, two spectral bands appear with peaks at 1.6 and 2.1–2.5 eV. The high-energy band dominates at short times, and only the low-energy band peaked at 1.6 eV is seen at the longest relaxation times. The results are discussed in terms of the quantum-confinement and dielectric-amplification effects and in terms of the involvement of kinetically coupled electron–hole (band at 1.8–3.2 eV) and exciton (band at 1.6 eV) subsystems in the recombination process. Gold contributes to the saturation of Si dangling bonds on the surface of Si nanocrystals and to the activation of oxidation processes. A similarity has been revealed between the recombination processes in photoluminescent Si nanocrystals in *por*-Si produced by anodizing and in laser-ablated *nc*-Si films.

REFERENCES

1. M. S. Bresler and I. N. Yassievich, Fiz. Tekh. Poluprovodn. (St. Petersburg) **27**, 873 (1993) [Semiconductors **27**, 475 (1993)].
2. A. G. Cullis, L. T. Canham, and P. D. J. Calcott, J. Appl. Phys. **82**, 909 (1997).
3. D. Kovalev, H. Mekler, G. Polisski, and F. Koch, Phys. Status Solidi B **215**, 871 (1999).
4. Y. Kanemitsu, Phys. Rep. **263**, 1 (1995).
5. O. Bisi, S. Ossicini, and L. Pavesi, Surf. Sci. Rep. **38**, 1 (2000).
6. É. B. Kaganovich, I. M. Kizyak, S. I. Kirillova, *et al.*, Fiz. Tekh. Poluprovodn. (St. Petersburg) **36**, 1105 (2002) [Semiconductors **36**, 1027 (2002)].
7. E. V. Kaganovich, A. A. Kudryavtsev, E. G. Manoilov, *et al.*, Thin Solid Films **349**, 298 (1999).
8. L. Patrone, D. Nelson, V. Safarov, *et al.*, J. Lumin. **80**, 217 (1999).
9. A. V. Sachenko, É. B. Kaganovich, É. G. Manoĭlov, and S. V. Svechnikov, Fiz. Tekh. Poluprovodn. (St. Petersburg) **35**, 1445 (2001) [Semiconductors **35**, 1383 (2001)].
10. P. K. Kashkarov, B. V. Kamenev, E. A. Konstantinova, *et al.*, Ukr. Fiz. Zh. **168** (5), 577 (1998).
11. Yu. Krychenko and A. V. Sachenko, Physica E (Amsterdam) **14**, 299 (2002).
12. M. Lanoo, C. Delerue, and G. Allan, J. Lumin. **57**, 243 (1993).
13. V. E. Primachenko and O. V. Snitko, *Physics of Semiconductor Surfaces Doped with Metals* (Naukova Dumka, Kiev, 1988).
14. M. V. Wolkin, J. Jorne, P. M. Fauchet, *et al.*, Phys. Rev. Lett. **82** (1), 197 (1999).
15. X. L. Wu, S. J. Xiong, D. L. Fan, *et al.*, Phys. Rev. B **62**, R7759 (2000).

Translated by D. Mashovets

Semiconductors, Vol. 37, No. 3, 2003, pp. 340–346. Translated from Fizika i Tekhnika Poluprovodnikov, Vol. 37, No. 3, 2003, pp. 358–364.

AMORPHOUS, VITREOUS, AND POROUS SEMICONDUCTORS

Kinetics of Growth of Surface Amorphous Layers under Irradiation of Silicon with Low-Energy Light Ions

A. I. Titov*, A. Yu. Azarov, and V. S. Belyakov

St. Petersburg State Polytechnical University, ul. Politekhnicheskaya 29, St. Petersburg, 195251 Russia

**e-mail: titov@phtf.stu.neva.ru*

Submitted July 15, 2002; accepted for publication July 22, 2002

Abstract—The damage buildup in Si single crystals irradiated with 10-keV Ne^+ ions was studied by a method based on measurements of anisotropy in inelastic electron scattering. It is shown that disorder buildup occurs as a result of growth of an amorphous layer starting from the boundary between the native oxide and crystalline Si. It is ascertained that the growth rate of the amorphous layer is independent of the current density of ions and that a threshold dose for the defect accumulation exists. The results are explained in terms of a model based on diffusion of generated mobile point defects to the surface with their subsequent segregation; the assumption that there are saturable sinks in the as-grown single crystals is also used. The results of calculations based on this model are in good agreement with experimental data obtained both in this study and reported in available publications. © *2003 MAIK "Nauka/Interperiodica".*

1. INTRODUCTION

In the production of integrated circuits, it is sometimes of interest to use active components with a doped-layer thickness no larger than 20–30 nm. In particular, such components can be obtained using ion implantation with an ion energy no higher than 10 keV. As is well known, bombardment with ions having energies even as low as those mentioned above leads to the buildup of structural defects in the irradiated region; as a result, the *p–n*-junction depth increases owing to the radiation-enhanced diffusion of impurities, which occurs both during irradiation and in the course of postimplantation annealing [1, 2]. In addition, the stable structural defects that remain unannealed can affect the electrical properties of implanted layers. In this context, it is important to gain insight into the special features of defect formation in semiconductors irradiated with low-energy ions. Data on structural changes resulting from bombardment with ions having energies no higher than 10 keV are sparse. However, there is experimental evidence (see, for example, [3–10]) that the damage buildup during irradiation of semiconductors with low-energy light ions proceeds as a gradual widening of the amorphous layer (AL); this process sets in at the boundary between the native-oxide layer and the semiconductor itself.

In order to gain insight into processes that occur during irradiation of materials with low-energy ions, we need structure-investigation methods that would make it possible to analyze layers whose thickness ranges from 0.2 to 20 nm. Traditionally, one of the most widely used methods for structure analysis is Rutherford backscattering (RBS) of ions in combination with channeling; however, the depth resolution of this method (~10 nm) is not sufficiently high. The use of a high-resolution technique (HRBS) makes it possible, in certain cases [9], to improve the depth resolution to 1 nm. The same resolution can be attained using the spectroscopy of scattering of medium-energy (100–500 keV) ions (MEIS) combined with channeling of incident ions and detection of the particles scattered in the blocking direction [10]. It is also noteworthy that the thickness of thin ALs can be measured using spectroscopic ellipsometry [7] and transverse transmission electron microscopy (XTEM) [8]. Additional difficulties encountered in measuring the very small thickness of ALs using the methods of ion backscattering emerge owing to the presence of a native-oxide layer on the surface; the thickness of this layer should be evaluated separately.

In order to quantitatively study the structure quality in thin surface layers of irradiated semiconductor single crystals, we developed (see [3, 11–13] and extensively used a new method for measuring the thickness of thin surface ALs; this method is based on measurements of the magnitude of anisotropy in the inelastic backscattering of electrons with energies ranging from 1 to 100 keV [3–6, 11, 14–16]. This anisotropy manifests itself in a nonmonotonic dependence of the reflection coefficient on the angle of incidence onto the surface [17, 18] and in the emergence of channeling patterns observed in scanning electron microscopy [19]; this anisotropy is a result of diffraction channeling, which can be explained on the basis of the dynamical theory of electron diffraction [20, 21]. The possibility of using this method to characterize the state of the structure in

surface layers of single-crystal samples was demonstrated previously [22, 23]. The basic concepts of using this method for measuring the thickness of ALs on a single-crystal substrate will be briefly outlined in Section 2.

2. EXPERIMENTAL

As mentioned in Section 1, the coefficient of inelastic backscattering of electrons η depends nonmonotonically on the angle of incidence φ on the single-crystal surface. In Fig. 1, we show (in arbitrary units) "rectified" (multiplied by cosφ) angular dependences η(φ) obtained for the initial (unirradiated) surface of a (111)Ge sample (curve *1*) and for the same surface after irradiation with ions (curve *2*), which gave rise to a continuous amorphous surface layer. The energy of the probing electrons was 5 keV. The scale for curve *2* was enlarged by a factor of 5 compared to curve *1*, and the curves were shifted relative to each other in order to make comparison more convenient. It can be seen from Fig. 1 that the presence of an amorphous layer at the surface reduces the modulation of the angular dependence as a whole while leaving the spectrum shape virtually unchanged. It is reasonable to relate the decrease in modulation to the fact that electrons pass the scattering amorphous layer (and, thus, cease to satisfy the coherence conditions) before entering the crystal. This suggests that the magnitudes of peaks can be used to assess the thickness of the AL at the surface of a single-crystal sample.

We now introduce the relative contrast Δ, which is defined as the ratio between the peak height measured when the beam is incident in a low-index direction onto a sample with an AL and the peak height obtained for the as-grown sample (without an AL). Evidently, the value of Δ should be proportional to exp(–*h*/*L*), where *h* is the AL thickness, $L = (\sigma n_a)^{-1}$ is the mean free-path length of primary electrons between two events of scattering by atoms in the AL, σ is the scattering cross section for electrons, and n_a is the concentration of atoms. It has been shown [24] that the contribution to the detected signal is made not only by reflected electrons but also by fast secondary electrons, which are excited in the surface layer with a thickness *l* and can escape from it. Taking this circumstance into account, we can express the dependence Δ(*h*) as

$$\Delta = [A + B\exp(-h/l)]\exp(-h/L), \qquad (1)$$

where *A* and *B* are constants (*A* + *B* = 1). It has been shown that *A* = 0.8 and *B* = 0.2 both for Si [24] and Ge [3]. Evidently, σ (and, consequently, *L*) depends on the energy of primary electrons E_e.[1] Thus, one can determine the AL thickness by measuring the angular dependences η(φ) for various values of E_e and the slope of resulting linear dependences $\ln\Delta = f(L^{-1})$.

[1] It has been shown [3] that good agreement with experimental data is attained if the values of σ reported in [25] are used.

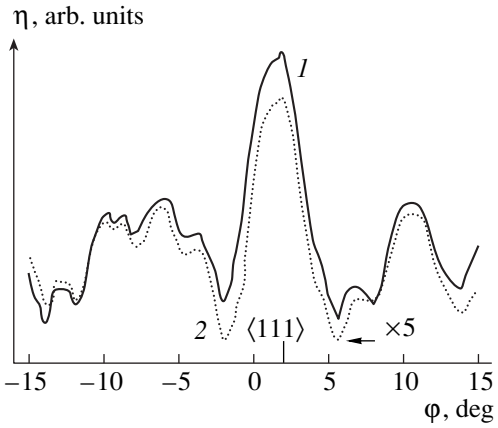

Fig. 1. Angular dependences for the coefficient of inelastic backscattering of 5-keV electrons for the initial Ge sample (curve *1*) and the Ge sample with the surface amorphous layer (curve *2*, the scale is enlarged by a factor of 5).

It is noteworthy that, in the case of only partly disordered (incompletely amorphous) surface layers, formula (1) is invalid and the experimental dependences $\Delta = f(L^{-1})$ cease to be linear. Therefore, the shape of these dependences represents reliable evidence as to which type of surface layer (amorphous or only partly disordered) is encountered experimentally. Additional evidence that the layers under consideration are not amorphous but have only slightly damaged structure can be deduced from nonproportionality in the reduction of special features, which corresponds to diffraction at the low- and high-index planes; this diffraction arises in the case of layers with a slightly damaged structure [26–28].

In concluding our consideration of the basic principles of the method used, we note that the AL thicknesses determined using RBS and the method we employed were in good agreement for the same samples [16, 29]. Another circumstance is also noteworthy. If the native-oxide thickness is not affected by ion irradiation, the presence of this oxide is automatically excluded in measurements of contrast.

Experimentally, we studied *in situ* the special features of the buildup of structural defects in silicon irradiated at room temperature with 10-keV Ne^+ ions with ion-current densities of 0.1 or 1 μA/cm^2. Epitaxial Si:B layers (ρ = 15 Ω cm) on the Si(100) surface were used. In order to suppress channeling, irradiation was performed at an angle of 8° to the normal to the surface. During analysis, the electron energy ranged from 3 to 12 keV.

3. RESULTS

In Fig. 2, we show the dependences $\ln\Delta = f(L^{-1})$ obtained for various doses of irradiation with Ne^+ ions for an ion-current density of 0.1 μA/cm^2. The linearity of these dependences, which was reliably ascertained at

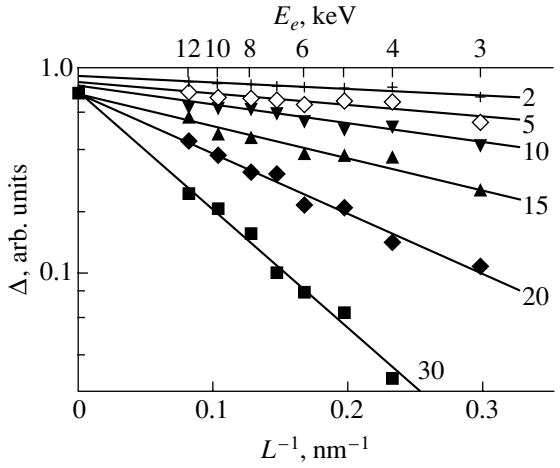

Fig. 2. Dependences of relative contrast in the anisotropy of inelastic electron reflection Δ on the reciprocal free-path length of electrons between the events of scattering by the atoms of an amorphous layer for an Si(100) sample irradiated with 10-keV Ne^+ ions at room temperature. The ion-current density was 0.1 μA/cm^2. The numbers at the curves correspond to the irradiation dose multiplied by 10^{-13} cm^2.

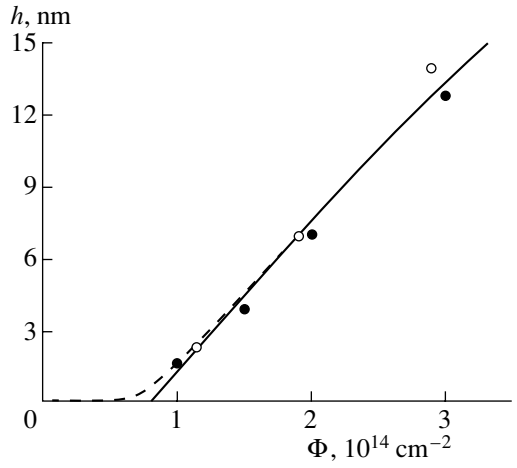

Fig. 3. Dependences of the thickness of the amorphous layer at the surface of an Si(100) sample on the dose of irradiation with 10-keV Ne^+ ions at room temperature. Unfilled and filled circles represent experimental data obtained at the ion-current densities of 1 and 0.1 μA/cm^2, respectively. The solid and dashed lines correspond to the results of calculations performed according to the simple model and to the model with saturable sinks, respectively.

least for the doses $\Phi \geq 10^{14}$ cm^{-2}, and the increase in the slope of the $\ln\Delta$ vs. the L^{-1} curve with the irradiation dose indicate that, in accordance with conclusions made previously [3–10], the buildup of structural defects proceeds in the case under consideration, as well as via a gradual broadening of the AL starting from the surface. In Fig. 3, we show the dependence of the AL thickness on the irradiation dose Φ; this dependence was calculated on the basis of the data presented in Fig. 2. Filled circles represent the data on the growth of an AL obtained for an ion-current density an order of magnitude higher than that referred to in Fig. 2. It can be easily seen from Fig. 3 that, first, the growth of the AL is independent of the ion-current density (within the chosen range of variations in this quantity) and, second, there is a threshold dose for the onset of efficient AL growth. It is worth noting that the existence of a threshold dose for formation and subsequent rapid AL growth were observed previously [7, 9].

Similarly, we have studied the buildup of defects in Ge and GaAs single crystals irradiated with 2- to 10-keV Ne^+ ions. As in the case of the experiments with Si samples, it was also ascertained that disorder buildup occurs via a gradual widening of the AL in contact with the surface. In addition, it was shown that a decrease in the growth rate of the AL occurred at high irradiation doses. This decrease is observed when the inner boundary of the growing AL becomes more deeply located than the position of the peak in the defect-generation profile R_{pd}. As can be seen from Fig. 3, AL growth was monitored only for thickness values no larger than 13 nm in the experiments with silicon. At the same time, the value of R_{pd} is somewhat larger (14 nm, according to calculations using the TRIM 95 application program [30]) when Si is irradiated with 10-keV Ne^+ ions. As a result, the portion of the curve with a lower rate of AL growth (with subsequent leveling off) is not observed in the dependence shown in Fig. 3.

4. DISCUSSION OF RESULTS AND SIMULATION CONCEPTS

The formation of amorphous layers at the interphase boundary between a native SiO_2 layer and crystalline Si during implantation of ions with relatively high energies has been known since the 1970s [31–33] and is still being studied [7, 34–36]. It is conventionally assumed (see, for example, [33, 37]) that formation of such surface ALs occurs as a result of migration of mobile point defects to the surface with subsequent processes of segregation. In these cases (i.e., for ions penetrating to a considerable depth), only a fraction of all point defects is generated near the surface and can be trapped by the SiO_2–Si interphase boundary. The major fraction of generated defects either forms a region of stable disorder in the vicinity of the maximum of elastic energy losses for slowing-down ions or annihilates.

In the case of implantation of low-energy light ions, virtually all point defects are generated near the surface. This means that the majority of these defects can be trapped by the interphase boundary, thus forming an AL, or recombine [3]. Such an AL is formed as a result of the planar growth of an amorphous phase at the SiO_2–Si boundary. It should be noted that, in the case of irradiation with low-energy light ions at elevated temperatures, competition between planar growth and ion-stimulated epitaxial recrystallization of amorphous layers plays a determining role in the formation of a sur-

face AL, as was shown for the case of irradiation of Ge with 5-keV Ar^+ ions [6]. As a result, quasi-stationary amorphous layers are formed under irradiation. Their thickness is governed by the type and energy of ions, ion-current density, and the target temperature.

The aforementioned assumptions concerning the mechanism of AL formation under the effect of irradiation with low-energy light ions at room temperature make it possible to assess quantitatively the dependence of the AL thickness on the irradiation dose. To this end, we assumed that the AL growth at the SiO_2–Si boundary is the result of diffusion of some mobile point defects (vacancies or interstitial atoms) to the surface. It was further assumed that the condition for the quasi-steady state of point defects had been satisfied; i.e., we assumed that the point-defect concentration n varied fairly slowly, so that we could set $dn/dt = 0$ at each point of time t. Evidently, this assumption is valid for the entire irradiation time, except for a very short initial period. The generation function for mobile point defects $g(x)$, where x is the depth, was calculated using the TRIM 95 [30] standard application program and was approximated by a Gaussian function. The effective threshold displacement energy E_d was chosen to equal 13 eV [38]. Taking into consideration that mobile defects recombine at unsaturable sinks with a rate characterized by an average lifitime τ, we can write the equation

$$D(d^2n/dx^2) - n/\tau + gF = 0, \quad (2)$$

where D is the diffusion coefficient of mobile point defects and F is the ion flux. If we assume that all defects that arrived at the interphase boundary are trapped at this boundary, the boundary conditions in this formulation of the problem become evident: $n = 0$ at $x \longrightarrow \infty$ and $x = h$, where $h = h(t)$ is the coordinate of the inner amorphous-layer boundary.

Finally, we assumed that, for a unit crystal volume to be transformed into the amorphous phase, a certain (relative) critical concentration of defects n_c should accumulate in this volume; if this concentration is attained, the structure transforms spontaneously from the crystalline state into the amorphous one [39–41]. On the basis of theoretical and experimental estimates [3, 35, 39–41], the relative critical concentration of defects in Si required for a spontaneous transition from the crystalline to the amorphous state should range from 0.1 to 0.4. In this study, we assumed that $n_c = 0.2$. In this case, the growth rate for the amorphous layer, $dh/d\Phi$, can be written as [42]

$$dh/d\Phi = (n_0 n_c F)^{-1} D(dn/dx)|_{x=h}, \quad (3)$$

where n_0 is the concentration of atoms in the target ($n_0 = 5 \times 10^{22}$ cm^{-3} for Si) and $\Phi = Ft$ is the irradiation dose. The system of Eqs. (2) and (3) can be easily transformed into

$$d^2y/dx^2 - y/L_d^2 + g = 0, \quad (4)$$

$$dh/d\Phi = (n_0 n_c)^{-1}(dy/dx)|_{x=h}, \quad (5)$$

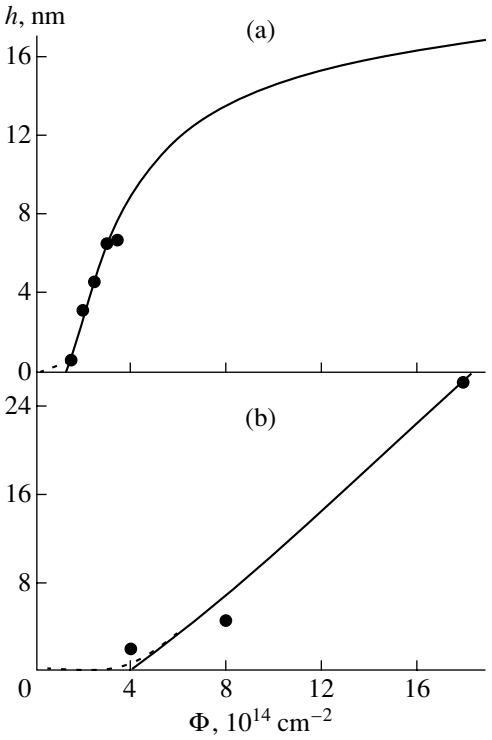

Fig. 4. Dependences of the amorphous-layer thickness on irradiation dose for (a) 5-keV Si^+ ions [9] and (b) 10-keV B^+ ions [7]. The filled circles correspond to the relevant experimental data. The solid and dotted lines represent the results of calculations performed according to the simple model and the model with saturable sinks, respectively.

where $y = Dn/F$ and $L_d = (D\tau)^{1/2}$ is the diffusion length of the point defects under consideration.

By discretely specifying the coordinate of the amorphous-layer boundary and solving Eqs. (4) and (5), we can obtain the dependence of $dh/d\Phi$ on h and, consequently, the dependence $h(\Phi)$. This problem was solved numerically. The adjustable parameter in this case was the diffusion length L_d.

As was mentioned above, it follows from previous experimental data [7, 9] and the results shown in Fig. 3 that a threshold dose exists that is required for formation and subsequent planar growth of an amorphous layer. This threshold dose Φ_{th} is determined from experimental data and is introduced into the model as an additional parameter. In this case, the threshold dose Φ_{th} should be added to the dose that was used for calculating $h(\Phi)$. The results of the model calculations are shown by the solid line in Fig. 3. In the case under consideration, the diffusion length L_d was found to be equal to 20 nm.

Similar calculations were performed in order to describe the results obtained in other studies [7, 9]. In Figs. 4a and 4b, the solid lines represent the results of simulation for the cases of irradiation of Si with 5-keV Si^+ [9] and 10-keV B^+ [7] ions, respectively. In these two cases, the adjustable parameter L_d was found to be

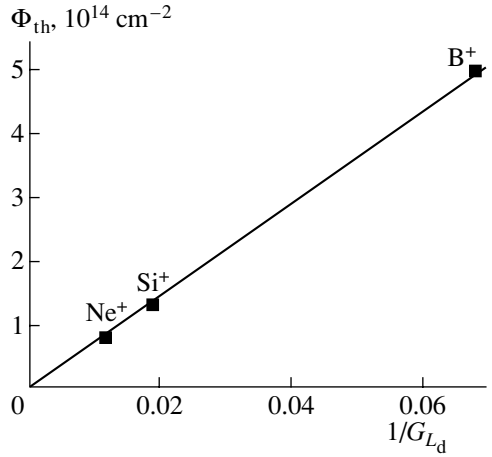

Fig. 5. Dependence of the threshold dose for amorphization on the reciprocal number of point defects generated by various ions over the diffusion length L_d. The data were obtained in this study (for Ne^+), in [9] (for Si^+), and in [7] (for B^+).

equal to 10 and 9.5 nm, respectively. It can be seen that there is good agreement with experimental data, as in the case of irradiation of Si with Ne^+ ions.

The obtained values of L_d = 10–20 nm seem to be quite realistic. In fact, it is well known that, when irradiating Si with light ions with energies of about 50 keV and at a low dose at room temperature, the variances in the distribution of stable defects calculated using the TRIM application program and that obtained experimentally differ from one another by a value close to the obtained quantity L_d (see, for example, [35]). The difference in diffusion lengths used in simulating the results obtained by various research teams should not be surprising because the silicon samples, in these cases, were of different origin; consequently, the spectra of saturable sinks can differ in these samples. Thus, we expected that there would be a difference between the values of τ for the samples irradiated in this study and those irradiated in [7, 9].

Let us now consider the origin for the appearance of the threshold dose Φ_{th}. It follows from experimental data [3, 35] that, in the case of implantation of 40-keV N^+ ions at low doses ($<10^{14}$ cm^{-2}) into Si at room temperature, the mode of effective buildup of defects in the bulk is observed, with disorder in this mode being independent of the ion-current density. This mode has been related [3, 35] to the accumulation of defects in saturable sinks that exist in silicon before irradiation and which have a large capture cross section for point defects. In this case, diffusion of mobile point defects over fairly large distances is possible only after these sinks are saturated. Thus, the dose corresponding to the saturation of these sinks may be treated as the threshold dose Φ_{th}.

It is well known [43] that growth defects are present in initial silicon samples; the concentration of the largest of these defects can be as high as ~10^{11} cm^{-3}, whereas the concentration of smaller defects is unknown and can be much higher. We believe that it is the latter defects which act as the aforementioned saturable sinks. Let us assume that their concentration is equal to N_s and that each of these defects can consecutively trap p mobile point defects on average. If this is true, it is then evident that the expression $\Phi_{th}G_{L_d} = C_pN_sL_d$ should be valid for the threshold dose; here, G_{L_d} is the total average number of mobile defects produced by an ion over a distance from the surface equal to the diffusion length (this number is equal to the generation function integrated between the limits of 0 and L_d) and C is a constant ($C \geq 1$). Thus, the threshold dose is bound to be inversely proportional to the quantity G_{L_d}. In Fig. 5, we show the dependence of experimental values of the threshold dose, measured by us and reported in [7, 9], on $1/G_{L_d}$; the quantity G_{L_d} was determined using the TRIM 95 application program. We used the values of L_d obtained for all cases in this study as the upper limits of integration.

It can be seen from Fig. 5 that the dependence $\Phi_{th}(1/G_{L_d})$ is linear and fits the straight line which issues out of the origin of coordinates reasonably well. This fact is somewhat surprising since, as follows from the preceding, the value of Φ_{th} should also be proportional to the product pN_sL_d, the factors in which are different in the experiments under consideration. In particular, this circumstance follows for L_d from the aforementioned calculations. However, it is possible that the constancy of the product pN_sL_d for all cases represented in Fig. 5 is related to a quite understandable circumstance. The value of L_d is inversely proportional to the concentration of nonsaturable sinks, whereas pN_s is naturally proportional to the concentration of saturable sinks. Both types of sinks are formed during crystal growth; therefore, if their concentrations are proportional to each other, the product under consideration should indeed be expected to be constant.

We can attempt to perform simulation taking into account trapping of mobile defects by saturable sinks. Let us assume that the concentration of complexes formed of a saturable defect (a sink) and i point defects is equal to N_i (i varies from 0 to p) and that the capture of a point defect by any incompletely saturated sink occurs with an identical kinetic constant α. Taking into account all that was stated above, we can transform Eq. (2) into the system of differential equations

$$\begin{gathered} dn/dt = D(d^2n/dx^2) - n/\tau - \alpha nN_s(1 - N_p/N_s) + gF, \\ dN_0/dt = -\alpha nN_s, \\ dN_i/dt = \alpha n(N_{i-1} - N_i), \quad i = 1, \ldots, p-1, \\ dN_p/dt = \alpha nN_{p-1}, \end{gathered} \tag{6}$$

with boundary conditions that are similar to the previous case and with the following initial conditions at $t = 0$: $n = 0$, $N_0 = N_s$, and $N_i = 0$ for $i = 1, \ldots, p$.

The results of numerical calculations for a system of Eqs. (6) and for Eq. (3) showed that the value of the threshold dose is found to be proportional to the product of N_s and p; i.e., this product can be treated as a unified parameter. It was found that the values of Φ_{th} obtained within the model are in good agreement with experimental data if, when solving the system of Eqs. (6) and (3), one uses the expression $pN_s = 0.7\Phi_{th}g_m$, where g_m is the number of mobile defects formed (on average) by an ion at the maximum of the generation function $g(x)$. Thus, we used the following values of pN_s for the cases of implantation of the Ne^+, Si^+, and B^+ ions under consideration: 2.9, 5.9, and 6.5 (expressed in units of 10^{21} cm^{-3}). It is noteworthy that, in these cases, the product pN_sL_d indeed remained constant to within ~5%. The values of the diffusion length were assumed to be the same as in previous calculations (L_d = 20, 10, and 9.5 nm for implantations of Ne^+, Si^+, and B^+ ions, respectively). The values of other parameters were assumed to be equal to $D = 1.7 \times 10^{-9}$ cm^2/s [42] (on the assumption that vacancies are point defects responsible for diffusion) and $\alpha = 5 \times 10^{-17}$ cm^3/s. As can be seen from Figs. 3 and 4, where the results of numerical simulation with the aforementioned parameters are represented by dashed lines, the theoretical curves are in satisfactory agreement with experimental data.

Thus, the model based on the diffusion of mobile point defects to the surface, the formation of a surface amorphous layer, and the recombination of the above defects at saturable sinks adequately describes experimental data on the buildup of defects in silicon irradiated with low-energy light ions at room temperature.

5. CONCLUSION

We studied the buildup of defects during irradiation of Si with 10-keV Ne^+ ions at room temperature; in our studies, we used the method based on the anisotropy of inelastic electron reflection. The results show that damage buildup can be treated as the growth of an amorphous layer at the SiO_2–Si interphase boundary, in accordance with previously published experimental data on irradiation of semiconductors with low-energy particles. We showed that a certain threshold dose should be accumulated for initiation and subsequent planar growth of the amorphous layer; we also showed that the current density of the primary (impinging) ions did not affect the rate of amorphous-layer growth. We suggested a model of the growth of amorphous layers; this model is based on the assumption that mobile point defects diffuse to the surface with subsequent segregation. It is assumed that a delay in amorphous-layer growth (the existence of a threshold dose) is caused by the buildup of defects at saturable sinks, which exist in silicon prior to irradiation. The results of calculations based on the aforementioned model are in good agreement with the experimental data obtained in this study and reported in previous publications by other authors.

REFERENCES

1. E. Chason, S. T. Picraux, J. M. Poate, *et al.*, J. Appl. Phys. **81**, 6513 (1997).
2. N. E. B. Cowern, G. F. A. van der Walle, P. C. Zalm, and D. W. E. Vandenhoudt, Appl. Phys. Lett. **65**, 2981 (1994).
3. A. I. Titov, Doctoral Dissertation (Leningrad, 1989).
4. V. S. Belyakov, S. V. Bryksin, and A. I. Titov, Vysokochist. Veshchestva **3**, 38 (1993).
5. I. A. Abroyan, V. S. Belyakov, and A. I. Titov, Izv. Ross. Akad. Nauk, Ser. Fiz. **58** (10), 59 (1994).
6. V. S. Belyakov and A. I. Titov, Radiat. Eff. **138**, 231 (1996).
7. T. Lohner, E. Kotai, N. Q. Khanh, *et al.*, Nucl. Instrum. Methods Phys. Res. B **85**, 335 (1994).
8. A. Agarwal, T. Haynes, D. J. Eaglesham, *et al.*, Appl. Phys. Lett. **70**, 3332 (1997).
9. K. Kimura, A. Agarwal, H. Toyofuku, *et al.*, Nucl. Instrum. Methods Phys. Res. B **148**, 284 (1999).
10. J. A. van den Berg, S. Zhang, S. Whelan, *et al.*, Nucl. Instrum. Methods Phys. Res. B **183**, 154 (2001).
11. A. I. Titov, in *Proceedings of 1st Conference on Physical Fundamentals of Ion Implantation* (Gor'kiĭ, 1972), p. 143.
12. I. A. Abroyan, V. S. Belyakov, and A. I. Titov, Mikroélektronika **5** (3), 231 (1976).
13. I. A. Abroyan, V. S. Belyakov, and A. I. Titov, Izv. Akad. Nauk SSSR, Ser. Fiz. **40**, 1678 (1976).
14. I. A. Abroyan, O. B. Babanina, S. L. Zaslavskiĭ, and A. I. Titov, Fiz. Tverd. Tela (Leningrad) **15**, 2215 (1973) [Sov. Phys. Solid State **15**, 1477 (1973)].
15. I. A. Abroyan, O. A. Podsvirov, A. I. Sidorov, and A. I. Titov, Pis'ma Zh. Tekh. Fiz. **5**, 1287 (1979) [Sov. Tech. Phys. Lett. **5**, 540 (1979)].
16. O. A. Podsvirov, A. I. Titov, and V. V. Makarov, Poverkhnost **11**, 87 (1982).
17. A. B. Laponsky and N. R. Whetten, Phys. Rev. Lett. **3**, 510 (1959).
18. A. J. Dekker and R. W. Soshea, Phys. Rev. **121**, 1362 (1961).
19. *Practical Scanning Electron Microscopy: Electron and Ion Microprobe Analysis*, Ed. by J. I. Goldstein and H. Yakowitz (Plenum, New York, 1975; Mir, Moscow, 1978).
20. R. Heidenreich, *Fundamentals of Transmission Electron Microscopy* (Interscience, New York, 1964; Mir, Moscow, 1966).
21. *Electron Microscopy of Thin Crystals*, Ed. by P. B. Hirsch, A. Howie, R. B. Nicholson, D. W. Pashley, and M. J. Whelan (Plenum, New York, 1965; Mir, Moscow, 1968).
22. I. A. Abroyan and A. I. Titov, Fiz. Tverd. Tela (Leningrad) **10**, 3432 (1968) [Sov. Phys. Solid State **10**, 2716 (1968)].

23. S. M. Davidson and G. R. Booker, in *Proceedings of 1st International Conference on Ion Implantation* (Gordon and Breach, New York, 1971), p. 51.
24. O. A. Podsvirov and Yu. A. Kuznetsov, Fiz. Tverd. Tela (Leningrad) **22**, 1676 (1980) [Sov. Phys. Solid State **22**, 978 (1980)].
25. M. E. Riley, C. J. MacCallum, and F. Biggs, At. Data Nucl. Data Tables **15**, 443 (1975).
26. V. V. Makarov, Doctoral Dissertation (Leningr. State Tech. Univ., Leningrad, 1990).
27. I. A. Abroyan, O. A. Podsvirov, and A. I. Titov, Pis'ma Zh. Tekh. Fiz. **6** (1), 14 (1980) [Sov. Tech. Phys. Lett. **6**, 5 (1980)].
28. A. I. Abroyan, A. V. Kotov, O. A. Podsvirov, and A. I. Titov, Optoélektron. Poluprovodn. Tekh., No. 10, 51 (1986).
29. V. S. Belyakov, V. V. Emtsev, J. S. Colligon, *et al.*, Surf. Invest. **14**, 627 (1998).
30. J. P. Biersack and L. G. Haggmark, Nucl. Instrum. Methods **174**, 257 (1980).
31. A. I. Gerasimov, E. I. Zorin, P. V. Pavlov, and D. I. Tetel'baum, Phys. Status Solidi A **12**, 679 (1972).
32. V. N. Gashtol'd, N. N. Gerasimenko, A. V. Dvurechenskiĭ, and L. S. Smirnov, Fiz. Tekh. Poluprovodn. (Leningrad) **9**, 554 (1975) [Sov. Phys. Semicond. **9**, 364 (1975)].
33. I. A. Abroyan, A. I. Titov, and A. V. Khlebalkin, Fiz. Tekh. Poluprovodn. (Leningrad) **11**, 1204 (1977) [Sov. Phys. Semicond. **11**, 712 (1977)].
34. R. D. Goldberg, J. S. Williams, and R. G. Elliman, Mater. Res. Soc. Symp. Proc. **316**, 259 (1994).
35. A. I. Titov and G. Carter, Nucl. Instrum. Methods Phys. Res. B **119**, 491 (1996).
36. T. Lohner, M. Fried, N. Q. Khanh, *et al.*, Nucl. Instrum. Methods Phys. Res. B **147**, 90 (1999).
37. W. Fukarek *et al.*, Nucl. Instrum. Methods Phys. Res. B **127/128**, 879 (1997).
38. J. J. Loferski and P. Rappaport, Phys. Rev. **111**, 432 (1958).
39. M. L. Swanson, J. R. Parsons, and C. W. Hoelke, Radiat. Eff. **9**, 249 (1971).
40. E. L. Vook, *Radiation Damage and Defects in Semiconductors* (Inst. of Physics, London, 1972).
41. L. A. Chistel, J. F. Gibbons, and T. W. Sigmon, J. Appl. Phys. **52**, 7143 (1981).
42. A. I. Titov and S. O. Kucheyev, Nucl. Instrum. Methods Phys. Res. B **168**, 365 (2000).
43. K. V. Ravi, *Imperfections and Impurities in Semiconducting Silicon* (Wiley, New York, 1981; Mir, Moscow, 1984).

Translated by A. Spitsyn

Semiconductors, Vol. 37, No. 3, 2003, pp. 347–353. Translated from Fizika i Tekhnika Poluprovodnikov, Vol. 37, No. 3, 2003, pp. 365–371.

AMORPHOUS, VITREOUS, AND POROUS SEMICONDUCTORS

Structure and Optical Properties of C_{60} Films on Polymer Substrates

Yu. F. Biryulin, V. N. Zgonnik***, E. Yu. Melenevskaya***, S. N. Mikov*, S. S. Moliver*, S. E. Orlov*, A. V. Novoselova***, V. D. Petrikov**, V. V. Rozanov****, D. A. Sykmanov**, and M. A. Yagovkina****

** Ul'yanovsk State University, Ul'yanovsk, 432700 Russia*

*** Ioffe Physicotechnical Institute, Russian Academy of Sciences, Politekhnicheskaya ul. 26, St. Petersburg, 194021 Russia*

e-mail: biryulina@mail.ioffe.ru

**** Institute of Macromolecular Compounds, Russian Academy of Sciences, Bol'shoi proezd 31, St. Petersburg, 199004 Russia*

***** Institute of Analytical Instrument Making, Russian Academy of Sciences, Rizhskiĭ pr. 26, St. Petersburg, 198103 Russia*

Submitted July 24, 2002; accepted for publication September 6, 2002

Abstract—The results of investigations of the structure and optical properties of films of fullerene C_{60} are reported. The films were obtained by vacuum thermal evaporation on substrates from heat-resistant polymers (polyacrylonitrile and cyclized polyacrylonitrile in composition with polyimide). The structure of C_{60} films was determined by X-ray diffractometry. In all diffraction patterns of fullerene films, their structure manifests itself through reflections from the (111), (220), and (311) planes. Cubic C_{60} films were obtained by fullerene deposition at substrate temperatures as high as 200°C. Atomic force microscopy of the film surface revealed the existence of a laminated structure. The infrared (IR) transmission spectra are indicative of the presence and constancy of the position of characteristic bands of C_{60} (527, 576, 1183, and 1428 cm^{-1}) for all fullerene films. The investigation of photoluminescence of fullerene films revealed bands whose energy position both exceeded typical values for molecular C_{60} or fell below these values. This circumstance is caused by the interaction between the electron π systems of C_{60} and the polymer substrate at the heterointerface, as well as by the photopolymerization reaction of fullerene under the effect of high-energy laser radiation and by the emergence of trap centers in the films. © *2003 MAIK "Nauka/Interperiodica".*

1. INTRODUCTION

In recent years, ever increasing interest of researchers in various fields is being drawn to polymers. This stage in the development of science and technology has been named the "polymer electronic revolution" [1]. Numerous recent publications have shown that polymers are also very useful for investigating a new allotropic form of carbon, specifically fullerenes. Due to their specific structure, fullerenes exhibit high chemical and biological activity. The introduction of fullerenes into the composition of polymers, covalent- or complex-bonded, extends the possibility of investigating them and applying them in the form of solutions or solid composition materials (films, fibers) for various purposes. Fullerenes can substantially affect the properties of polymers, namely, their strength, thermal stability, conductivity, and tendency to form associations. Understanding the mechanism of interaction between fullerene and polymer macromolecules is the basis for controlling the properties of fullerene–polymer compositions, especially in such systems as nanoheterostructures on substrates of a different nature [2].

The aim of this study was to obtain and investigate the structure and optical properties of fullerene on substrates from thermostable polymers, namely, polyacrylonitrile (PAN) and the composition of cyclized PAN with polyimide (CPAN-PI). This study is aimed at investigating the chemical interaction of fullerenes with a polymer substrate, which differs from the van der Waals interaction for typical crystalline and amorphous solid-state substrates, and at analyzing the structure of such films.

2. EXPERIMENTAL

The PAN films, which were synthesized in an anionic system [3], and the composite based on chemically cyclized PAN (CPAN) and polyamide acid (4,4'-oxydiphenylenpyromethylamide acid) were used as thermostable polymer substrates. Composite films of the composition 20 : 80 were heat treated at 400°C. Under these conditions, CPAN acquires a completely cyclized structure, whereas polyamide acid transforms to PI during dehydration.

1063-7826/03/3703-0347$24.00 © 2003 MAIK "Nauka/Interperiodica"

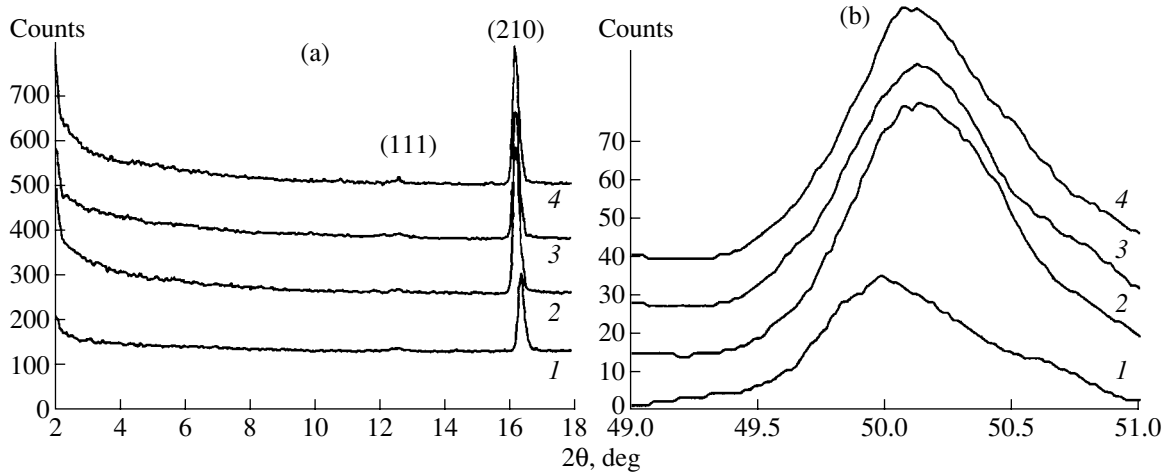

Fig. 1. X-ray diffraction patterns of the C_{60} films on the Si(111) substrate. (a) The (111) and (210) diffraction peaks of C_{60} and (b) the (630) diffraction peaks of C_{60}. Curves are numbered according to the numbers of growth experiments (see table).

PAN films, 20 and 300 μm thick, were transparent, colorless, and thermostable to 250°C. The composition CPAN-PI films, 25 μm thick, were dark-colored. However, they possessed a considerably higher strength, pliability, and thermal stability.

The fullerene films on the mentioned substrates were obtained by vacuum thermal evaporation of mircocrystalline C_{60} powder with a purity of 99.95 %. The evaporation temperature was 450°C, and the condensation temperature (the substrate temperature) was varied from room temperature to 300°C in accordance with the data listed in the table. Polished single-crystal Si(111) KDB (*p*-Si:B) wafers were used as reference substrates.

The thickness of the obtained C_{60} films, which was measured using an MII-11 interference microscope, varied from 0.05 to 1 μm depending on the substrate type and experimental conditions. The adhesion of the C_{60} films to the CPAN-PI substrates permitted retaining the pliability of the heterostructures during all experiments, including several immersions into liquid nitrogen.

Experimental conditions of deposition of the C_{60} films on various substrates

No. of experiment	Substrate temperature, °C	Substrates	Layer thickness, μm
1	20	PAN, CPAN-PI, Si	0.4 (on Si)
2	200	PAN, CPAN-PI, Si	0.35 (on Si)
3	200*	PAN, CPAN-PI, Si	0.5 (on Si), 0.8 (on PAN)
4	300	CPAN-PI, Si	$\lesssim$0.06 (on Si)

* The substrates were preliminarily heated in vacuum at 200°C for 2 h.

The C_{60} films were investigated by X-ray diffractometry using a Geigerflex-D/max-RC powder diffractometer (Rigaku, Japan). The experimental conditions were as follows: Co$K\alpha_1$ radiation (wavelength λ = 1.789 Å, monochromatic); step mode; the step of recording was 0.02°; and the current and accelerating voltage of the X-ray tube were 40 mA and 50 kV, respectively.

The surface of the obtained films was investigated using an NT-MDT atomic force microscope (Russia). The scanning step was 6 nm.

The infrared transmission spectra of the C_{60}/PAN heterostructures were measured using a Specord-M80 spectrophotometer in the wavenumber range of 500–1500 cm^{-1}. The integration time was 3 s.

The photoluminescence (PL) of the samples was investigated at room temperature. We used a DFS-52 spectrophotometer with the radiation detection in the photon counting mode using an FEU-79 as the photodetector. Correction for the spectral sensitivity of the photomultiplier was introduced. The excitation source was an LCS-DTL-3216 YAG:Nd solid-state laser with the wavelength λ = 532 nm pumped by semiconductor lasers. The beam power could be varied from 1 to 200 mW, which corresponded to the range of power densities of 35–7000 W/cm^2, upon focusing on a spot with a diameter of 0.06 mm.

3. RESULTS OF INVESTIGATION OF C_{60} FILMS BY X-RAY DIFFRACTOMETRY

The diffractometry of fullerene films on various substrates revealed an obvious dependence of the type of the film crystal structure on the substrate structure. Thus, the films on Si(111) were epitaxial layers, which grew according to the orientation (*h*, *h*/2, 0) for C_{60} with a face-centered cubic (fcc) lattice (Figs. 1a, 1b). The reflections from the (210), (420), and (630) planes of

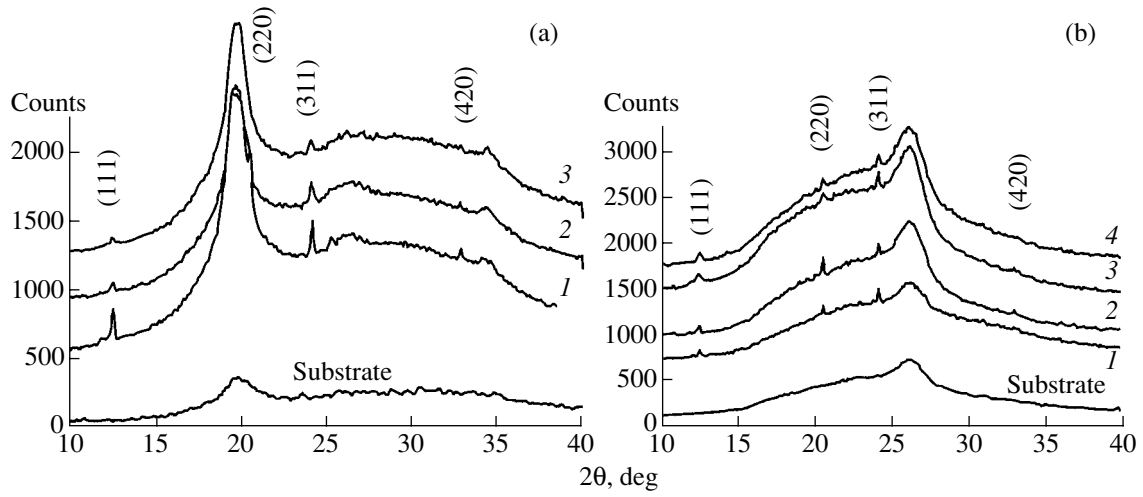

Fig. 2. X-ray diffraction patterns of the C_{60} films on the (a) PAN and (b) CPAN-PI substrates. Curves are numbered according to the numbers of growth experiments (see table).

the fcc lattice of C_{60} manifest themselves in the X-ray diffraction patterns. The (420) reflection with a double Bragg angle $2\theta = 32.9°$ is closest to the position of the intense diffraction peak for Si(111) ($2\theta = 33.15°$). For this reason, this reflection is not shown in Fig. 1. Along with these reflections, a weak (111) reflection manifests itself (Fig. 1a), which is indicative of the presence of a minor impurity of the polycrystalline constituent in the fullerene film.

For the Si-based heterostructures, the coherent scattering regions parallel to the (210) plane in the C_{60} films were 110–120 nm in size; along the normal direction, these regions were 30–40 nm in size (for the first experiment, these were somewhat less, specifically, 25–30 nm in size). The parameters obtained for the C_{60} lattice are as follows: experiment 1: (14.02 ± 0.01) Å; experiment 2: (14.14 ± 0.01) Å; experiment 3: (14.14 ± 0.01) Å; and experiment 4: (14.15 ± 0.01) Å.

The fullerene films on polymer substrates without a crystalline structure (broadened halo) (Figs. 2a, 2b) represented polycrystalline layers. All reflections for C_{60} with an fcc lattice, namely, the (111), (220), (311), and (420) reflections, manifest themselves in the X-ray diffraction patterns in the angle range 2θ from 10° to 40°. The unit-cell parameters for the series of films on the PAN and CPAN-PI substrates remain unchanged over the entire range of deposition temperatures and are equal to (14.17 ± 0.03) and (14.15 ± 0.01) Å, respectively. For all experiments at a substrate temperature above room temperature, the diffraction peaks of fullerenes are broadened, which is indicative of decreasing dimensions of the coherent scattering region or degradation of the crystalline structure (Figs. 2a, 2b). This fact correlates with the surface relief of the film in the two-dimensional image, which was obtained using the atomic force microscope (Fig. 3a). Note that the dimensions of the coherent scattering region, which were obtained by X-ray diffractometry, coincide with characteristic dimensions of the fragments at the film surface (stacked planes), which are clearly seen in Fig. 3a, by an order of magnitude.

The shape of the halo for the CPAN-PI substrates remains virtually unchanged over the entire series of experiments (Fig. 4b), whereas the shape of the halo for the PAN substrates varies (Fig. 4a). This fact can be attributed to the cyclization reactions, which proceed in anionic polyacrylonitrile under the effects of temperature and vacuum. For this material, narrower (compared with the starting material) peaks emerge in the angle region $2\theta = 20°$, 27°, and 34°. These variations are not associated with the deposition of C_{60} films since they manifest themselves in polymer films which were subjected to the entire technological treatment, but without deposition of fullerenes.

For both series of C_{60}/polymer heterostructures in the temperature range under investigation (20–300°C), an apparent decrease in the intensity of the diffraction peaks of C_{60} is noted as the substrate temperature increases (Figs. 2a, 2b). The use of substrates with an intense intrinsic absorption in the region of peaks and in the halo region, to some extent, can be the reason for the decreasing intensity of certain peaks which are characteristic of C_{60}. However, the retention of these peaks at elevated temperatures is indicative of the absence of chemical transformations in the heterostructures.

For the PAN substrates, a certain structural ordering is observed under these conditions. The degree of this ordering increases with increasing temperature. For the CPAN-PI composite substrates, the halo has another shape and structure; however, it depends only slightly on temperature.

In conclusion, we may state that variation in the substrate temperature (20–300°C) during the deposition of C_{60} had no substantial effect on the film structure if sin-

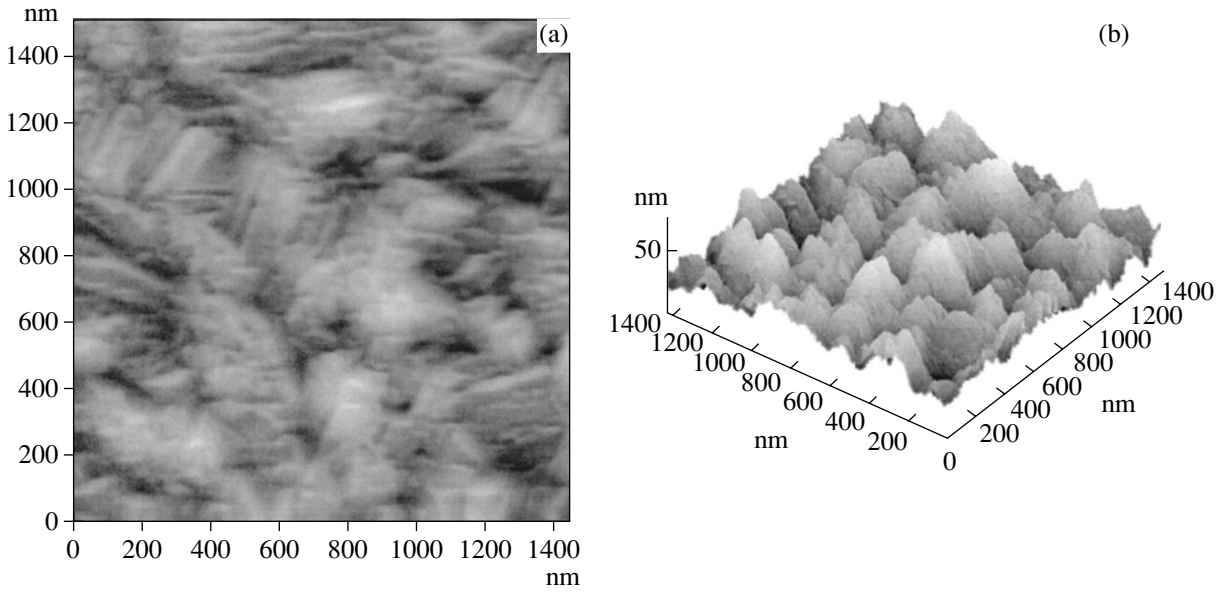

Fig. 3. (a) Two-dimensional and (b) three-dimensional images of the surface of the C_{60} films on PAN (experiment 3); the images were obtained using atomic force microscopy. The scanning area is 1400×1400 nm^2. The scanning step is 6 nm. Images were obtained in air.

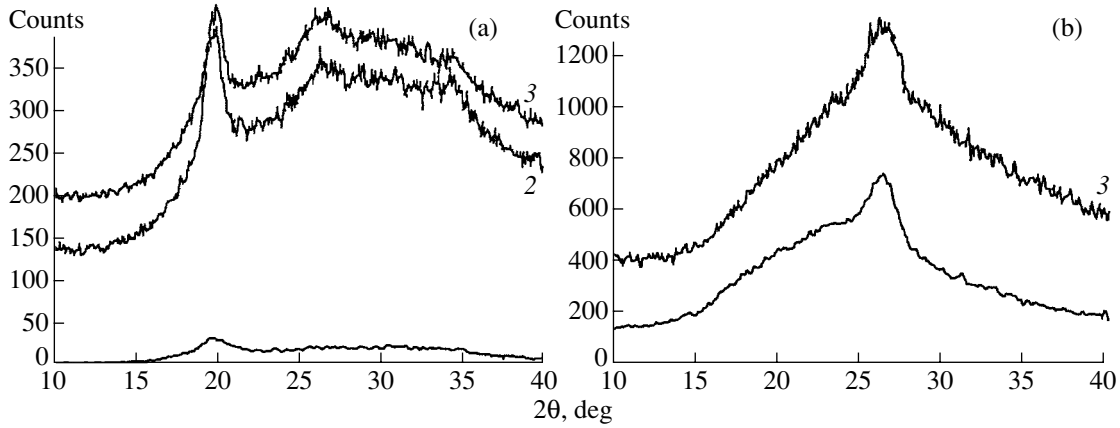

Fig. 4. X-ray diffraction patterns of the (a) PAN and (b) CPAN-PI substrates before (bottom curves) and after the treatment cycle. Curves are numbered according to the numbers of growth experiments (see table).

gle-crystal Si(111) was used as the substrate. For the films on PAN and CPAN-PI, such variation in temperature led to noticeable degradation of the structure. This degradation manifested itself in a decreasing intensity and broadening of the peaks of the (111), (220), (311), and (420) reflections in Fig. 2.

4. OPTICAL TRANSMISSION SPECTRA OF C_{60} FILMS

The optical transmission spectra of the C_{60} films were measured in the wavenumber range of 500–1500 cm^{-1} (Fig. 5). In the spectra for all four experiments with PAN substrates, four characteristic bands of C_{60} are clearly observed, namely, 527, 576, 1183, and 1428 cm^{-1}. Their positions and intensities were almost the same for various samples, which was indicative of the absence of covalent interactions in the films both between C_{60} molecules, which are inherent to polymerized crystals and fullerene films [4], and between the fullerene molecules and substrate macromolecules. In the region of 1050–1400 cm^{-1}, variations in the absorption bands of the PAN substrates were observed as the temperature effect during the fullerene deposition emerged and increased (Fig. 4b). Such variations in the IR transmission spectra for the heat-treated PAN can be caused by an increasing mobility of segments and their compaction, since the anionic PAN is a stereoblock polymer. It is possible that it is this mechanism which is responsible for the emergence of a halo in the X-ray diffraction patterns.

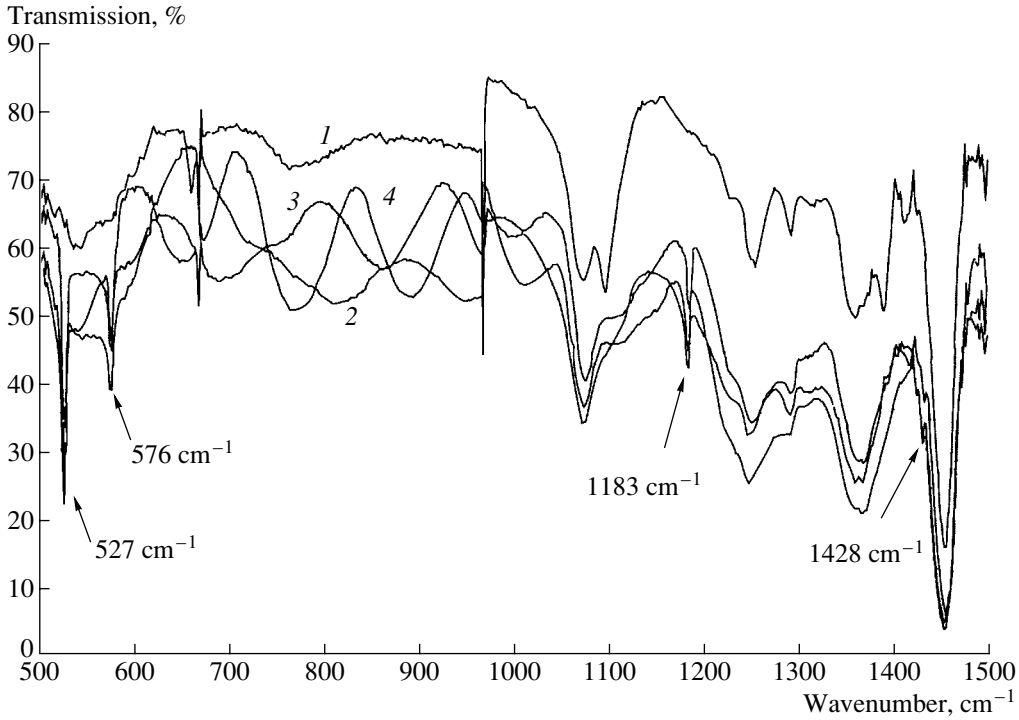

Fig. 5. Infrared transmission spectra of the C_{60}/PAN heterostructures at 300 K. Curves are numbered according to the numbers of growth experiments (see table).

5. PHOTOLUMINESCENCE SPECTRA OF C_{60} FILMS

The measurements of the PL spectra revealed that the peak at 1.69 eV, which corresponds to the van der Waals polycrystalline fullerene film, is dominant in the spectra of the C_{60}/Si films [5]. With an increasing excitation level, the peak gradually shifts to 1.67–1.665 eV, which corresponds to the photopolymerized states of fullerene [6] and the spectra of the C_{60} polymer crystals [7]. Furthermore, shoulders are observed for energies of 1.80 and 1.89 eV (Fig. 6).

For the C_{60} films on the PAN substrates, the PL spectra of the PAN substrate and C_{60}/PAN heterostructure from the substrate side were recorded initially. These spectra are shown in Fig. 7 (spectra *a* and *b*, respectively). It can be seen that the emission from the PAN film lies in the wavelength region of 630–650 nm (the peak of 1.93 eV in spectrum *a*). Upon excitation from the substrate side, emission from the C_{60} film from the heterointerface side is also superimposed on the PAN spectrum. Such emission is characteristic of shoulders for the photon energies of 1.88 and 1.77 eV (spectrum *b*). Consequently, the presence of a C_{60} film gives rise to trap levels and/or defect levels at the heterointerface, which manifest themselves in the PL spectra as these shoulders. The intrinsic emission of C_{60}, which corresponds to a HOMO–LUMO transition, is absorbed by PAN. The PL spectra of the C_{60} films for the same samples illuminated from the fullerene film side are also shown in Fig. 7 (spectra *c* and *d*). The C_{60}/PAN heterostructure formed at room temperature is characterized by a spectrum with an absolute maximum at 1.68 eV and shoulders at 1.93 and 1.86 eV (spectrum *c*). Spectrum *d* corresponds to the PL spectrum of the C_{60}/PAN structure formed at 200°C with preliminary heating. Two peaks are observed in this case, namely, at 1.67 and 1.93 eV; the band at 1.88 eV is superimposed on the latter peak, and the transition at 1.78 eV is very weakly

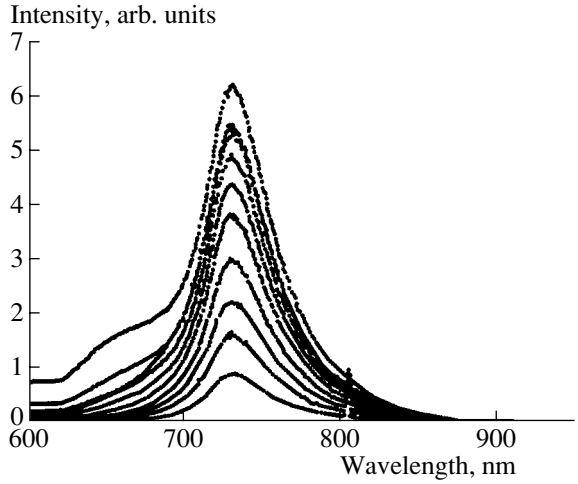

Fig. 6. Photoluminescence spectra of the fullerene film on Si (experiment 2) at 300 K. An increase in the excitation level from 70 to 700 W/cm^2 corresponds to the curves from bottom to top.

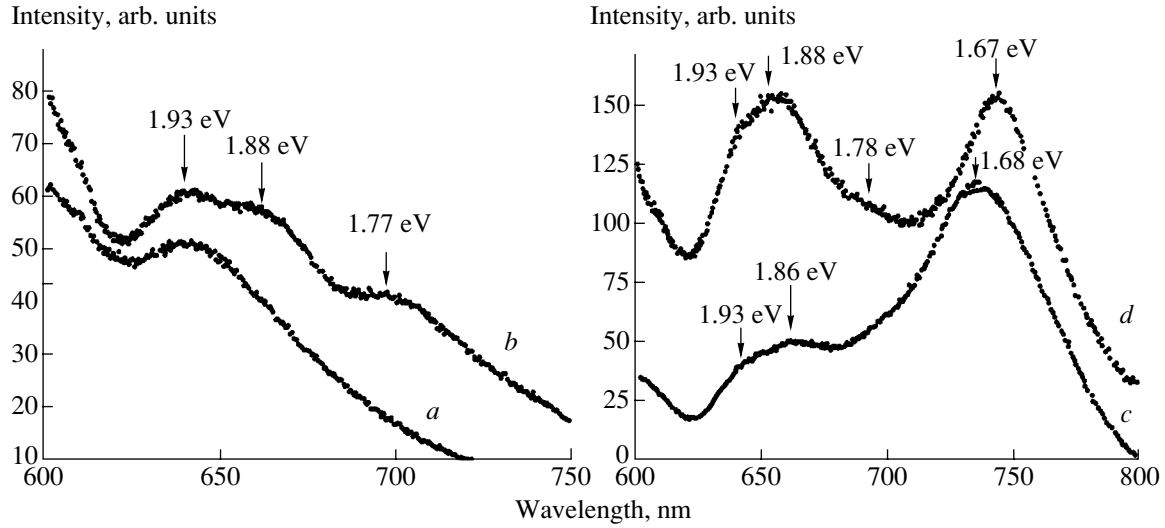

Fig. 7. Photoluminescence spectra of (a) the PAN substrate and the C_{60} films on PAN grown at (c) 20°C and (b, d) 200°C. (b) Excitation and measurement from the substrate side and (c, d) excitation and measurement from the film side. The measurement temperature is 300 K.

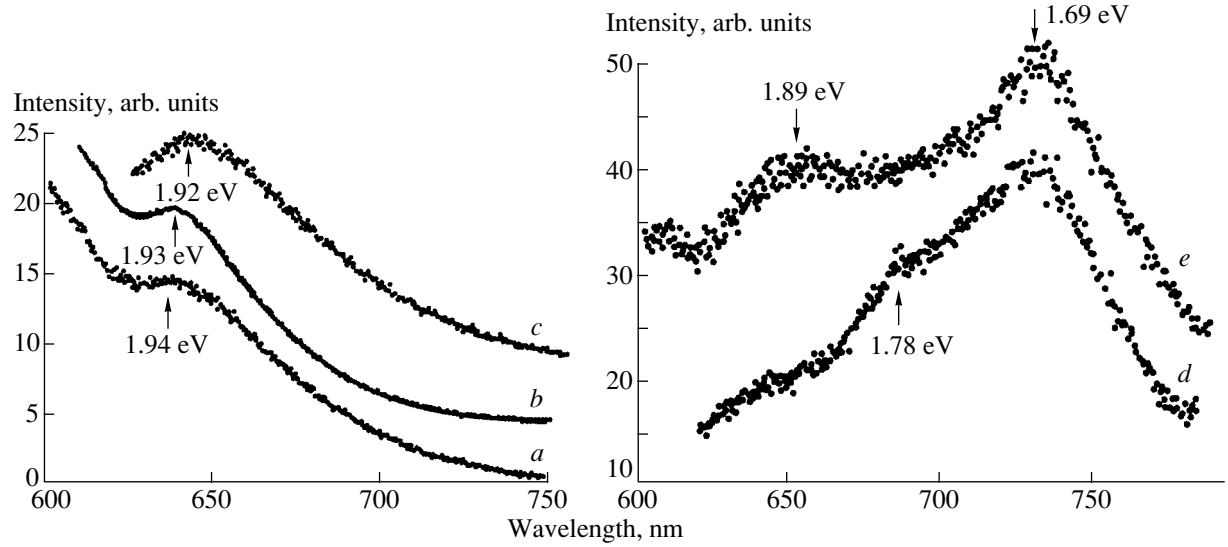

Fig. 8. Photoluminescence spectra of the CPAN-PI substrates after the treatment in vacuum at (a) 20, (b) 200, and (c) 300°C, and the spectra of C_{60} films on CPAN-PI deposited at (d) 20 and (e) 200°C. The measurement temperature is 300 K.

pronounced. The first peak corresponds to the emission of the C_{60} film, and the second peak corresponds to the emission of the PAN substrate. In this case, the intensity of the band at 1.93 eV increases due to PAN cyclization resulting from preliminary heating of the substrate. A weak line at 1.78 eV can most likely be attributed to the fullerene layer at the heterointerface. This line is shifted by energy from the chemical interaction between C_{60} and PAN at the level of π bonds. In our opinion, the band at 1.86–1.88 eV is related to defects in the fullerene film.

The CPAN-PI substrates are characterized by the PL spectra shown in Fig. 8. As the substrate temperature increases, the peak in the CPAN-PI spectrum shifts somewhat from 1.94 eV (experiment 1, room temperature, Fig. 8, spectrum *a*) to 1.93 eV (experiment 2, 200°C, Fig. 8, spectrum *b*) and 1.92 eV (experiment 4, 300°C, Fig. 8, spectrum *c*). Consequently, the reconstruction of the structure, which was mentioned above, also proceeds in this thermostable polymer. However, this process manifests itself only slightly in the X-ray diffraction patterns.

The PL spectra of the C_{60} films on the CPAN-PI substrates are shown in Fig. 8 (spectra *d* and *e*). The PL spectrum of the C_{60}/CPAN-PI heterostructure formed at room temperature is characterized by a peak at 1.69 eV

(the C_{60} film itself) and a shoulder at 1.78 eV (the contribution of fullerene at the heterointerface). An increase in the substrate temperature to 200°C leads to the emergence of a band at 1.89 eV. In our opinion, this observation indicates that the fullerene layer becomes more imperfect. This is also in agreement with the results of X-ray diffractometry.

6. CONCLUSION

The investigations carried out revealed that C_{60} films on PAN and CPAN-PI substrates are crystalline, can photopolymerize, and have good adhesion. The basis of this adhesion is a C_{60} transition layer at the heterointerface. This layer is associated with the polymer substrate and apparently constitutes the molecular layer of the C_{60}/polymer complex, with a characteristic PL band at 1.78 eV. In the complex mentioned, fullerene interacts with the polymer via π electrons. This leads to the formation of a stronger bond than the van der Waals bond, which is characteristic of physical adsorption. It is this circumstance that causes the good adhesion of the C_{60} films to polymer substrates.

The results obtained can serve as the starting point for the development of C_{60}/polymer heterostructures and more complex compositions based on them.

ACKNOWLEDGMENTS

We thank V. I. Kon'kov for carrying out four experiments on the deposition of C_{60} on polymer substrates.

This study was supported by the state research program "Controlled Synthesis of Fullerenes and Other Atomic Clusters" and by the Presidium of the Russian Academy of Sciences program "Low-Dimensional Quantum Structures" (project: "Investigation of the Interaction of Fullerenes with Various Substrates and the Electronic Properties of Such Heterosystems").

REFERENCES

1. G. Marsh, Mater. Today **3/4**, 4 (2000/2001).
2. Y. Wada, M. Tsukada, M. Fujihira, *et al.*, Jpn. J. Appl. Phys. **39** (7A), 3835 (2000).
3. B. L. Erussallimsky and A. V. Novoselova, Faserforsch. Textiltech. **26**, 293 (1975).
4. A. M. Rao, P. C. Eklund, J.-L. Hodeau, *et al.*, Phys. Rev. B **55**, 4766 (1997).
5. Y. Wang, J. M. Holden, A. M. Rao, *et al.*, Phys. Rev. B **51**, 4547 (1995).
6. V. Capozzi, G. Celetano, G. Perna, *et al.*, J. Lumin. **86**, 129 (2000).
7. U. D. Venkateswaran, D. Sanzi, A. M. Rao, *et al.*, Phys. Rev. B **57**, R3193 (1998).

Translated by N. Korovin

Semiconductors, Vol. 37, No. 3, 2003, pp. 354–359. Translated from Fizika i Tekhnika Poluprovodnikov, Vol. 37, No. 3, 2003, pp. 372–377.

PHYSICS OF SEMICONDUCTOR DEVICES

Tunnel Emission of Electrons in Photo-Field Detectors and in an Auger Transistor in Very Strong Electric Fields

V. D. Kalganov*, N. V. Mileshkina*, and E. V. Ostroumova^**

** Institute of Physics, St. Petersburg State University, St. Petersburg, 198904 Russia*

*** Ioffe Physicotechnical Institute, Russian Academy of Sciences, St. Petersburg, 194021 Russia*

^ e-mail: trirog@mail.wplus.net

Submitted July 8, 2002; accepted for publication July 22, 2002

Abstract—The effect of a strong electric field [$(5–7) \times 10^7$ V cm^{-1}] on the electron emission from a semiconductor to vacuum in photo-field detectors and in MIS structures with a tunnel-transparent insulator layer (Al–SiO_2–*n*-Si Auger transistor) has been studied. It is shown for the first time that the existence of deep self-consistent quantum wells on the semiconductor surface in a strong electric field provides a possibility of controlling the energy of fast electrons responsible for the impact ionization near the base of the Auger transistor and changes the photosensitivity of narrow-gap photo-field cathodes in the IR spectral range due to the formation of a transistor structure at the semiconductor–vacuum interface. It is also demonstrated that, both in photo-field detectors and in tunnel Al–SiO_2–*n*-Si transistor structures, only the electron tunnel current should be taken into account and the hole current, disregarded. The reason for this is that only the electron current exists in vacuum, and the tunneling of holes in Al–SiO_2–*n*-Si from the semiconductor into the metal is unlikely because of the large hole effective mass in the valence band of SiO_2. *© 2003 MAIK "Nauka/Interperiodica".*

1. INTRODUCTION

The tunnel emission of electrons in a strong electric field in needle-type semiconductor photo-field detectors and in MIS structures with a tunnel-transparent insulator layer in an Al–SiO_2–*n*-Si Auger transistor presents a unique opportunity for the experimental and theoretical study of current transport in semiconductors at electric fields up to $(5–7) \times 10^7$ V cm^{-1} [1, 2]. We present first evidence for the existence of deep self-consistent quantum wells (QW) for holes on an *n*-Si surface, which opens the way to control the energy of fast electrons responsible for the impact ionization near the base of the Auger transistor. Quantum phenomena on the semiconductor surface are taken into account for the first time in constructing a model of field emission of electrons from a semiconductor tip into free space. It is shown that, in both cases, the carrier density in self-consistent QWs controls the tunnel current of electrons from the valence band of a semiconductor in the case of tips and from the metal to the conduction band of a semiconductor for the Auger transistor. The tunneling (collector) current in the Auger transistor is controlled by the current of the base, which is a self-consistent QW for holes in these transistors (Fig. 1). For semiconductor (GaAs, InSb, *p*-Ge) tips, the emission current is controlled by the intensity of tip illumination (Fig. 2). Moreover, it has been found that the formation of self-consistent QWs on the semiconductor surface changes the photosensitivity of narrow-gap field-emission photocathodes in the IR spectral range due to the formation of a transistor structure in the tips at the semiconductor–vacuum interface.

Semiconductor photo-field emitters, as well as a wide-gap metal–insulator emitter in the Auger transistor, are emitters of fast electrons. The theoretical possibility of using semiconductor photo-field emitters as effective detectors of radiation was demonstrated as early as in the 1970s, when it was established that the spectral characteristic of the field-emission current lies in the range of fundamental absorption of a semiconductor [3]. However, the commercial application of this experimental result was hindered mainly due to technological problems in the fabrication of field-emitters from semiconductor crystals and to the uncertainty of their photo-field emission characteristics.

It is known that photocathodes are the best detectors of radiation. However, until now, even the best of these have been inapplicable in the IR spectral range of greatest interest for a number of industries and for ecological monitoring of the atmosphere, in which the absorption bands of a variety of widespread toxic gases lie. The necessity for studying semiconductor field emitters was determined by fundamental problems related to the understanding of electron tunneling through a potential barrier between a solid and vacuum and by practical interest in designing efficient long-wavelength photodetectors, since the spectral range of photosensitivity of a photo-field detector is shifted to longer wavelengths compared with that of a standard photocathode, with the shift equal to the electron affinity of a semiconductor.

In spite of multiple experimental investigations of the photo-field emission characteristics of semiconductors [4,5], the quantum efficiency has not yet been measured correctly. There exists a widely accepted opinion

[6] that the quantum efficiency of these cathodes may exceed 100% due to a possible increase in the photoelectron density in the space-charge region of a semiconductor. In the present study, the quantum efficiency of single-crystal GaAs needle-type photo-field cathodes has been determined experimentally in different modes of cathode operation and the position of the maximum photosensitivity region for the field-emission current from the semiconductor has been defined.

At the same time, the study of MIS tunneling structures, involving analysis of a wide variety of essential effects, such as tunneling emission of hot electrons from metal to semiconductor and the heating of electrons in the field of a self-consistent QW on the surface, has made it possible to create an Auger transistor based on an Al–SiO_2–*n*-Si heterojunction, which is presently the fastest bipolar semiconductor transistor [7–9]. The combined study of semiconductor tip systems (InSb, *p*-Ge, GaAs) and Al–SiO_2–*n*-Si structures with a tunnel-thin oxide layer is of special interest because, in both cases, in studying the electron emission, account should be taken only of the electron current through vacuum (tips) and the tunnel-thin oxide (the Auger transistor), and the hole current can be ignored. This is due to the fact that, to be sure, only electron current exists in vacuum and the tunneling current in Al–SiO_2–*n*-Si structures can always be considered purely electronic, because hole tunneling through an SiO_2 layer is unlikely due to the large effective hole mass in the SiO_2 valence band ($m_h > 5m_0$) [1, 10], and this current can be disregarded.

2. EXPERIMENTAL

Needle-type field emitters were fabricated from semi-insulating ⟨001⟩ GaAs single-crystals with a resistivity of ~10^6 Ω cm. The half-finished emitters were etched in CP-4; in some cases, the etching rate was modified with special additives.

The devices were evacuated and degassed by a standard procedure with heating to 500°C. After mounting the single-crystal GaAs field cathode, the devices were pumped at lower temperatures, depending on the specific aims of study.

The spatial position and the profile of the maximum photosensitivity region of the emission current from the tip, as well as the quantum efficiency *Y*, were determined by laser probing of the field cathode. The semiconductor was illuminated with a He–Ne laser (the emission wavelength λ = 0.63 μm) through a slit and an optical system that allowed illumination of any region on the emitter with a real optical image of the slit, used here as a light probe, with the light beam incident normal to the axis of the semiconductor tip.

The coordinates of the light probe on the tip were determined using a reference grid on a flat screen located at a distance of the real optical image of the emitter, with an optical magnification of 100. The use of a laser beam allowed us to form a narrow optical probe for the proper determination of the number of incident photons in calculating the quantum efficiency and spatial localization of the maximum photosensitivity region.

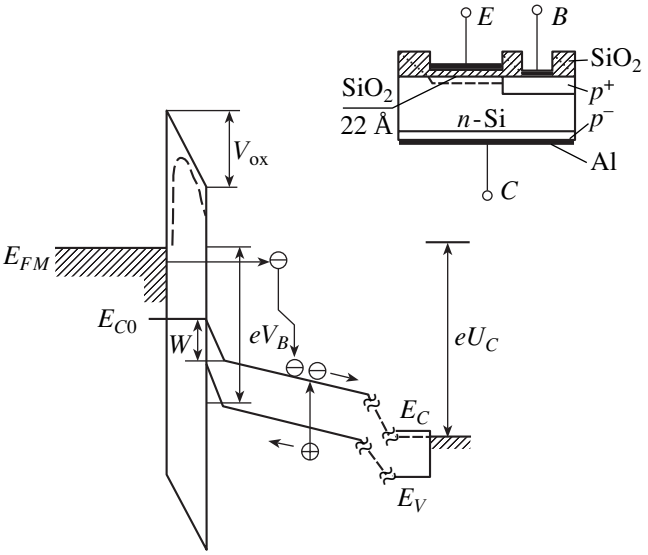

Fig. 1. The energy diagram of the Al–SiO_2–*n*-Si Auger transistor with a tunnel-thin oxide layer. A reverse bias is applied across the structure. E_{FM} is the Fermi level in metal; E_{C0}, the edge of the Si conduction band at the interface; V_{ox} (eV) the voltage drop across the oxide; *W*, the QW depth; U_B and U_C, the base and collector voltages; E_C and E_V, the conduction and valence band edges. Inset: a schematic representation of the Auger transistor: *E* is the emitter; *B*, the base; and *C*, the collector.

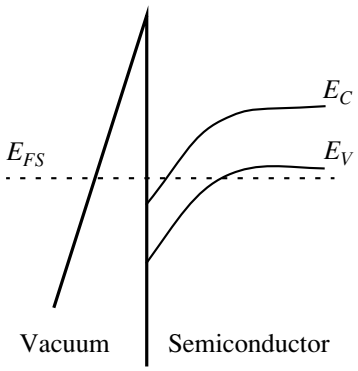

Fig. 2. The energy diagram of a *p*-type semiconductor photodetector. The photo-field emission of electrons occurs directly from the semiconductor to vacuum. E_{FS} is the Fermi level in the semiconductor.

The Al–SiO_2–*n*-Si structure of the Auger transistor was fabricated using standard Si technology; the tunnel-transparent oxide was grown in dry oxygen at a rather low oxidation temperature (600–700°C). The oxide thickness was 20 Å as determined by ellipsometry. The current voltage (*I–V*) characteristics were recorded in the common-emitter configuration.

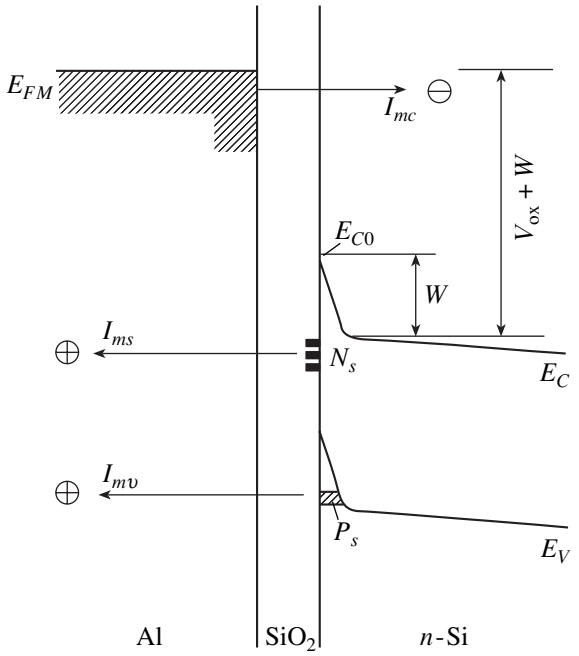

Fig. 3. The tunnel currents in the Auger transistor. I_{mc} is the tunnel current of electrons from the emitter; I_{ms} and I_{mv}, the leakage currents of holes; P_s, the hole density in the well; N_s, the density of surface states.

3. RESULTS AND DISCUSSION

3.1. Tunnel Currents in the Al–SiO_2–*n*-Si *Auger Transistor*

An electric field greater than 3×10^7 V cm^{-1} can be applied to the semiconductor surface in Al–SiO_2–*n*-Si structures with a tunnel-thin oxide layer (the Auger transistor). In this situation, the tunnel emission of electrons from metal to semiconductor and vice versa can be observed. In the Auger transistor, it is possible to obtain emission of hot electrons injected into Si with an energy of 2 eV and higher, which exceeds the impact-ionization threshold in Si, i.e., the threshold for the generation of electron–hole pairs. The increase in the gain of the Auger transistor is related precisely to these new electron–hole pairs. Additional heating of electrons in the field of a self-consistent QW at the surface constitutes more than 30% relative to the energy of tunneling electrons and enables impact ionization when there is a rather low voltage drop across the oxide. Impact ionization underlies the operation of an Auger transistor, and this is the fastest known physical process in transistors, with a characteristic time no greater than 10^{-13} s.

Strong electric fields at the semiconductor surface induce self-consistent QWs, whose depth increases in parallel with a rise in the strength of an electric field. This is the base of the Auger transistor (Fig. 1). For a self-consistent QW in a field greater than 10^7 V cm^{-1}, the typical depth is 0.5–0.7 eV for a well thickness of 10–15 Å. Such a small base width allows ballistic transport of electrons. The density of electrons or holes in self-consistent QWs exceeds 10^{13} cm^{-2}.

Up to now, the use of an Al–SiO_2–*n*-Si heterostructure with a tunnel-thin oxide layer [7, 8] for fabricating an Auger transistor has been the only application of Kroemer's idea of a transistor with a wide-gap heteroemitter [11], in spite of multiple theoretical attempts at heterocouple matching. The current amplification in the Auger transistor is due to the impact ionization by hot electrons injected from the wide-gap emitter to the narrow-gap base [11]. In the Al–SiO_2–*n*-Si transistor structure, the wide-gap semiconductor emitter is replaced with the metal–SiO_2 heterojunction (Fig. 1) and the oxide must be tunnel-transparent for electrons (several nanometers) [7, 8]. In this case, the kinetic energy of electrons tunneling from metal to semiconductor is so high that the generation of electron–hole pairs in Si via impact ionization (the Auger generation) becomes possible. In bipolar transistors, current amplification is due to the diffusion or drift of carriers through the base of a transistor. In the Auger transistor, the regions of generation and drift of carriers are virtually totally separated in space. Impact ionization occurs near the base, and the drift, in the region of the base–collector junction. The rate of electron–hole pair generation is determined by the bias applied to the transistor base [9, 10]. A self-consistent QW, having a depth of about 0.7 eV, controls the energy of fast electrons involved in impact ionization [12]. Additional heating of injected electrons in the electric field of the transistor base and subsequent cooling occur along a free path of 10^{-6} cm. At the same time, the drift region, i.e., the width of the space-charge region at the base–collector junction, is usually no less than 10^{-5} cm.

The generation of electron–hole pairs under impact ionization results in current amplification in the Auger transistor, because three carriers appear instead of a single injected electron. Additional currents, i.e., electron and hole Auger currents, arise. The electron Auger current flows into the collector, thus increasing the collector current, whereas the hole Auger current flows from the generation region (the base–collector junction) into the transistor base, and the current in the base circuit (the hole current), from the base into the emitter (Fig. 3). The electron and hole tunneling currents across the tunnel barrier are commonly described in a quasi-classical approximation. In this approximation, the tunneling current can be represented as

$$I = \frac{eN}{\tau}\exp[-(2/\hbar)\int p\,dx], \qquad (1)$$

where the integral $(2/\hbar)\int p\,dx$, determining tunneling probability, is taken over the classically inaccessible region; N is the 2D density of electrons that can be involved in tunneling; and τ is the characteristic time of collisions of electrons localized in a QW with the QW walls. All the tunneling currents in the Auger transistor

can be represented in a form similar, e.g., to the current of electrons tunneling from metal to semiconductor across an oxide layer [4]:

$$I_{mc} = \frac{eV}{16\pi^2\hbar d^2} \times \exp\left\{-\frac{4\sqrt{2m^*}d}{3\hbar V_{ox}}[V^{3/2} - (V - V_{ox})^{3/2}]\right\}, \quad (2)$$

where $V = \varphi_m$ (eV) is the work function for electrons passing from metal to the SiO_2 conduction band, $m^* = 0.29m_0$ is the effective mass of the tunneling electrons in SiO_2, d is the oxide layer thickness, and $V_{ox} = E_{FM} - E_{C0}$ is the voltage drop across the oxide. The details of this calculation were published elsewhere [9, 10, 13].

The holes attracted to the silicon surface by the electric field play only an insignificant role in balancing the transistor currents, but they do control the much stronger tunneling current of electrons from metal to semiconductor. Moreover, the transistor base voltage determines the kinetic energy of tunnel electrons injected into the semiconductor. This is the key issue determining the possibility of applying a metal–insulator heterojunction in an Auger transistor.

3.2. Emission Currents in Photo-Field Detectors

Figure 4 shows typical distributions of the photoresponse of a photo-field emission current for a light probe moving from the needle base to its tip (over the distance l) at different anode voltages corresponding to different portions of the *I–V* characteristics of the emission current, shown in Fig. 5. As follows from Fig. 4, the photoresponse is strongly dependent on the electric field strength. At low fields corresponding to the beginning of portion II in the *I–V* characteristic (Fig. 5), the region of maximum photosensitivity is situated at the needle tip near the emitting surface of the cathode. When the electric field strength increases, the region of maximum photosensitivity shifts deeper into the semiconductor toward the needle base. With a further rise in the field intensity, which corresponds to a transition from portion II to III in the *I–V* characteristic, the region of maximum photosensitivity returns to the emitter tip.

A physical model taking into account the penetration of the external electric field into the semiconductor bulk allows a consistent description of the observed effects. At the beginning of portion II in the *I–V* characteristic, when field penetration into the semiconductor is negligible, the region of maximum photosensitivity is located near the emitting surface (Fig. 4, curve *1*) and it shifts deeper as the field rises (Fig. 4, curve *2*). In portion II of the *I–V* characteristic, variation of the emission current with the anode voltage increasing is insignificant; i.e., the electron density in the semiconductor changes only slightly. In portion III, with further

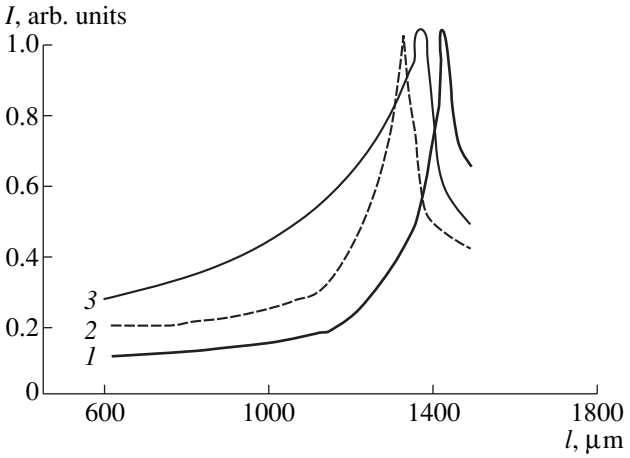

Fig. 4. The distributions of the maximum photosensitivity of the field-emission current from GaAs tips along the tip for different anode voltages U at 77 K. U: (*1*) 2.5, (*2*) 6, and (*3*) 7 kV. The curves are normalized to their peak values.

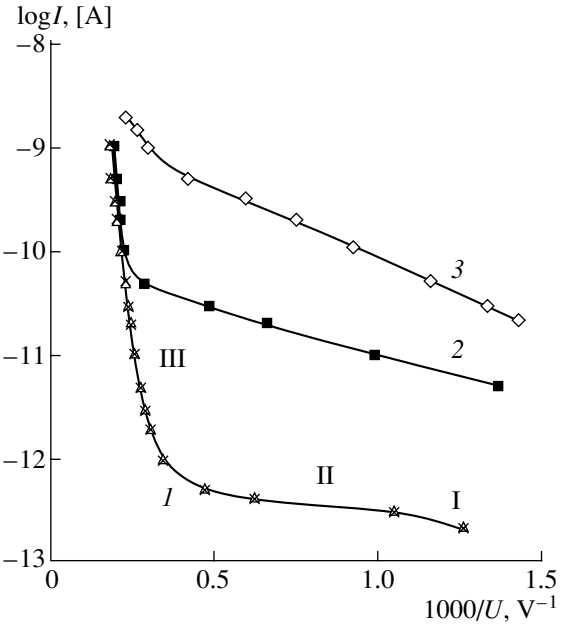

Fig. 5. *I–V* characteristics of the total emission current from a photo-field cathode at 77 K. (*1*) Dark current, (*2*) current under illumination with a probe, and (*3*) current under full illumination.

increase of the electric field, the mechanisms for electron generation in the bulk are switched on (impact ionization, inter-band tunneling, etc.).

As is known, the depth of field penetration depends on the electron density in the bulk and at the surface of a semiconductor. A sharp increase in current is observed in portion III of the *I–V* characteristic; the electron density in the bulk of the semiconductor increases significantly, which leads to a decrease in the field penetration depth due to screening. This causes a

reverse shift of the maximum photosensitivity region to the emitter tip (Fig. 4, curve *3*).

The quantum efficiency of a photocathode was measured under the conditions of maximum photosensitivity of the field emission current in GaAs, with due regard for the power losses for reflection and absorption in the system of lenses and in the device (a photodiode was used). The method for quantum efficiency determination was described in detail in [14]. The experimental data indicate that the quantum efficiencies $Y = 0.8$–4.0 for different portions of the *I–V* characteristic, depending on the electric field strength.

Thus, the possibility of designing a photocathode with a quantum efficiency above 100% on the basis of a GaAs field-emitter has been proved experimentally and verified for a set of emitters fabricated with a high reproducibility of their configuration.

4. CONCLUSION

In two kinds of experiments with electron emission from semiconductor tips to vacuum and the electron injection from metal to semiconductor in Al–SiO_2–*n*-Si structures, the tunnel current of electrons from a self-consistent QW was found to be less than the tunnel current of electrons from the valence band in the case of photo-field detectors or the tunnel current from metal to the conduction band of Si (the emitter current) in Al–SiO_2–*n*-Si structures.

However, the current density in self-consistent QWs controls the magnitude of the electron tunneling current in both cases: either that from the valence band of a semiconductor for tips (Fig. 2) or the electron tunneling current from metal to the Si valence band in the Auger transistor (Figs. 1, 3) [1]. The electron tunneling current in the Auger transistor is controlled by the voltage applied to the base, which is formed in this case as a self-consistent QW for holes at the surface of *n*-Si [8]. In the case of photo-field detectors, the tunneling emission current is controlled by the illumination intensity, which also gives rise to a transistor structure at the semiconductor–vacuum interface due to the formation of a self-consistent QW for electrons (Fig. 2) [1, 15].

When a strong electric field is applied to the semiconductor surface, a balance is set between the nonequilibrium electrons and holes in the semiconductor bulk, on the one hand, and electrons or holes localized in the self-consistent QW at the surface, on the other. The density of carriers that accumulated at the surfaces may be as high as $(2–4) \times 10^{13}$ cm^{-2}. Equally high densities are also observed in the study of emission currents in photo-field detectors. The analogy between the tunnel currents in the Auger transistor and currents from the semiconductor tips is due to the fact that, in both cases, these are the currents of electron tunneling. The hole tunneling current in the Al–SiO_2–*n*-Si Auger transistor nearly always flows via the conduction band of the oxide and, consequently, across a much higher potential barrier (Fig. 1). The hole tunneling current via the oxide valence band is very small due to the high effective mass of holes in SiO_2 ($m_h > 5m_0$) [9, 10, 13].

Another general problem is that, in such a strong electric field (up to 7×10^7 V cm^{-1}), the energies of the valence and conduction band levels are close. Therefore, the tunneling current in a semiconductor can be treated in terms of the Zener breakdown. Currently, this problem is of most interest in investigations of emission currents from *p*-type semiconductor tips to vacuum. In a relatively weak field, the semiconductor tip behaves as a dielectric tip when there are no electrons to tunnel into vacuum. A strong electric field mixes the states of the conduction and valence bands, and the current carried by electrons in vacuum or in a narrow semiconductor layer in the tip is carried only by holes in the semiconductor bulk [1].

The essence of the problem is as follows. Electrons in the valence band of a semiconductor do not carry current, because the valence band is completely filled. In principle, all the electrons of the valence band can participate in the current transport at the semiconductor–vacuum interface or MIS heterojunction, but, in this case, it is necessary to apply a strong electric field, which is realized by the attraction of electrons (in the case of tips) or holes (in the Auger transistor) to the surface. These electrons and holes themselves do not produce a high tunneling current, but they direct a high density of electrons into the vacuum or insulator in the form of a tunneling current. In terms of the bulk density, the density of electrons and holes attracted to the interface is about 10^{20}–10^{21} cm^{-3}, whereas the density of electrons in the valence band is 10^{22}–10^{23} cm^{-3} [1, 13].

The tunnel currents of holes from the base to metal in the Auger transistor are less than the electron tunneling currents from metal to the collector. Similarly, the electron current to vacuum from the conduction band of *p*-type semiconductor tips is less than the electron current from the valence band. Otherwise, the problem under study would not exist. It is this fact that enabled the design of the Auger transistor based on an Al–SiO_2–*n*-Si heterojunction with a tunnel-thin oxide layer and accounted for the extremely high density of the emission current from the semiconductor tips.

ACKNOWLEDGMENTS

We would like to emphasize that this study was initiated by A.A. Rogachev and underline his leadership in the formulation of the problem and construction of the physical model of tunneling in the systems under study.

This study was supported by the Russian Foundation for Basic Research (project no. 00-02-17042), the federal program "Integration," the scientific division of NATO in the framework of the "Science for Peace" program, and by the Ministry of Industry and Science of the Russian Federation program "Surface Atomic Structures."

REFERENCES

1. A. A. Rogachev, V. D. Kalganov, N. V. Mileshkina, and E. V. Ostroumova, Microelectron. J. **31**, 905 (2000).
2. T. Deck, V. D. Kalganov, N. V. Mileshkina, *et al.*, Phys. Low-Dimens. Semicond. Struct., Nos. 11/12, 147 (2000).
3. D. R. Schreder and R. N. Thomas, IEEE Trans. Electron. Devices **21**, 785 (1974).
4. *Nonincandescent Cathodes*, Ed. by M. I. Elinson (Sovetskoe Radio, Moscow, 1974).
5. T. Deck, V. D. Kalganov, N. V. Mileshkina, and A. Moscardini, Phys. Low-Dimens. Semicond. Struct., Nos. 5/6, 9 (2001).
6. R. Fischer and H. Neumann, Fortschr. Phys. **14**, 603 (1966); *Autoelectron Emission of Semiconductors* (Nauka, Moscow, 1971), Chap. 4.
7. I. V. Grekhov, E. V. Ostroumova, A. A. Rogachev, and A. F. Shulekin, Pis'ma Zh. Tekh. Fiz. **17** (7), 44 (1991) [Sov. Tech. Phys. Lett. **17**, 476 (1991)].
8. E. V. Ostroumova and A. A. Rogachev, Fiz. Tekh. Poluprovodn. (St. Petersburg) **28**, 1411 (1994) [Semiconductors **28**, 793 (1994)].
9. E. V. Ostroumova and A. A. Rogachev, Microelectron. J. **29**, 701 (1998).
10. E. V. Ostroumova and A. A. Rogachev, in *Fundamental Aspects of Ultrathin Dielectrics on* Si-*Based Devices: Towards an Atomic-Scale Understanding* (Kluwer Academic, Dordrecht, 1998); NATO ASI Ser., Ser. 3 **47**, 383 (1998).
11. A. G. Milns and J. J. Feucht, *Heterojunctions and Metal–Semiconductor Junctions* (Academic, New York, 1972; Mir, Moscow, 1975).
12. E. V. Ostroumova and A. A. Rogachev, Fiz. Tekh. Poluprovodn. (St. Petersburg) **33**, 1126 (1999) [Semiconductors **33**, 1027 (1999)].
13. E. V. Ostroumova and A. A. Rogachev, Appl. Surf. Sci. **166**, 480 (2000).
14. S. N. Goncharov, V. D. Kalganov, N. V. Mileshkina, *et al.*, Phys. Low-Dimens. Semicond. Struct., Nos. 9/10, 143 (2001).
15. V. D. Kalganov, N. V. Mileshkina, and E. V. Ostroumova, in *Proceedings of 10th International Symposium on Nanostructures: Physics and Technology* (St. Petersburg, 2002), p. 357.

Translated by D. Mashovets

Semiconductors, Vol. 37, No. 3, 2003, pp. 360–366. Translated from Fizika i Tekhnika Poluprovodnikov, Vol. 37, No. 3, 2003, pp. 378–384.

PHYSICS OF SEMICONDUCTOR DEVICES

Charge Transport in Superlattices with Low-Strength Barriers and the Problem of a Terahertz Bloch Oscillator

A. A. Andronov*, I. M. Nefedov, and A. V. Sosnin

Institute for the Physics of Microstructures, Russian Academy of Sciences, Nizhni Novgorod, 603950 Russia

**e-mail: andron@ipm.sci–nnov.ru*

Submitted July 25, 2002; accepted for publication September 2, 2002

Abstract—Charge-transport properties of superlattices with low-strength barriers and the possibility of designing a Bloch oscillator based on these superlattices are discussed. A terahertz Bloch oscillator based on *n*-GaAs–GaAlAs structures with low-strength barriers is suggested. Because of interminiband tunneling, the current is an increasing function of electric-field strength, so that domains cannot be formed. At the same time, tunneling and Bloch oscillations give rise to dynamic negative electrical conductivity in the terahertz region. Monte Carlo simulations show that dynamic negative conductivity exists in the frequency range of 1–7 THz for superlattices with moderate charge-carrier mobility at 77 K. A Bloch oscillator should include a superlattice with 350–700 periods of 150-Å, with this superlattice being sandwiched between contact regions, which are in fact strip-line sections (the oscillator cavity). Presumably, such an oscillator can operate at 77 K in the continuous-wave mode. © *2003 MAIK "Nauka/Interperiodica".*

1. INTRODUCTION

The idea of a Bloch oscillator can be traced back to the papers concerned with bulk semiconductors and published by Bloch (1928) [1], Zener (1934) [2], Kroemer (1954) (see [3]), and Yakovlev (1961) [4] and then to the papers concerned with artificial semiconductor systems (superlattices) published by Keldysh (1962) [5] and then by Esaki and Tsu (1970) [6]. This idea consists in the following (see, for example, [7]). If a fairly strong electric field E is applied along the axis of a superlattice (SL) with a period d (i.e., the field direction is transverse to the SL layers), an electron moves within a single energy band from one boundary of the Brillouin zone to the other virtually without scattering, then undergoes Bragg scattering (Fig. 1), and the motion process recurs. Thus, the electron exerts oscillations at the Bloch frequency

$$\omega_B = eEd/\hbar,$$

where e is the elementary charge and $\hbar$ is Planck's constant. Setting $E = 3$ kV/cm and $d = 150$ Å, we obtain the frequency $f_B = \omega_B/2\pi = 1$ THz. These are the Bloch oscillations. The frequency f_B can be continuously tuned by an applied electric field, which provides the basis for the development of a universal source of radiation (an oscillator) in the terahertz region.

Of course, the presence of oscillations does not yet ensure that they can be used to generate radiation. An oscillator should be able to generate coherent radiation at a selected frequency. In order to realize this possibility, there should be negative conductivity in the vicinity of this frequency.

Negative conductivity represents a traditional subject of studies related to charge transport in semiconductor SLs in the presence of strong electric fields (see, for example, [7, 8]). In the majority of publications in this field, charge-carrier transport in SLs with wide forbidden minibands has been studied. In this case, the electron transport in strong electric fields and in the presence of Bloch oscillations actually occurs within a single allowed miniband. The current j then decreases with increasing electric-field strength E in strong fields (Fig. 2a), since the current vanishes if we have ideal (uninterrupted by scattering) Bloch oscillations. In the

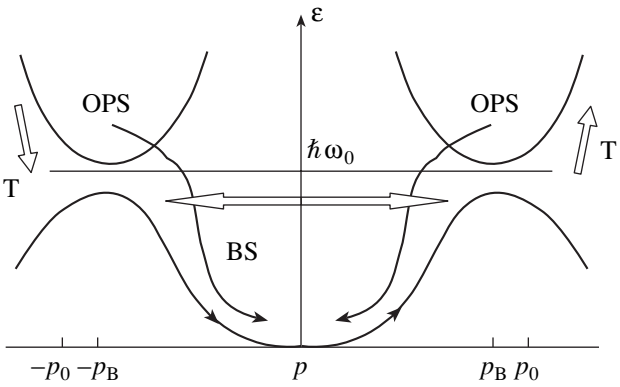

Fig. 1. Schematic representation of main transport processes in the Brillouin zone in the considered superlattices with narrow forbidden bands. Arrows indicate the carrier motion in an electric field (the Bloch oscillations), the Bragg scattering (BS), and tunneling (T). OPS stands for scattering by optical phonons. Here, $p_B = \hbar\pi/d$ and $p_0 = 2m^*/\hbar\omega_0$, where $\hbar\omega_0$ is the optical-phonon energy.

1063-7826/03/3703-0360$24.00 © 2003 MAIK "Nauka/Interperiodica"

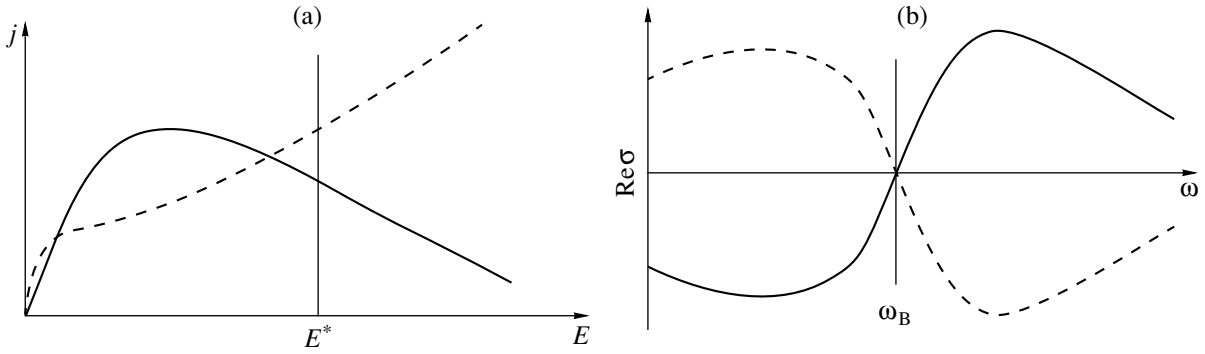

Fig. 2. (a) Current–voltage characteristics and (b) the frequency dependences of differential electrical conductivity for an electric-field strength E^* indicated in panel (a) in the case of a superlattice with narrow allowed minibands (solid lines) and with narrow forbidden minibands (dashed lines); ω_B is the Bloch frequency.

simplest situation, the descending portion in the current–voltage characteristic $j(E)$ is observed if $\omega_B\tau > 1$, where τ is the relaxation time. In essence, this circumstance was noted in the aforementioned publications by Kroemer, Yakovlev, Keldysh, and Esaki and Tsu. A negative differential conductivity (NDC) is observed in the descending portion of the current–voltage (I–V) characteristic; the NDC occurs in the frequency range from $\omega = 0$ to $\omega \approx \omega_B$ [9] (Fig. 2b).

A Bloch oscillator can be visualized in the following way (see the inset in Fig. 3). An SL with a thickness l is grown on a high-conductivity substrate (n^+); this SL is then overgrown with a second high-conductivity layer n^+. A strip with a length of $L = \lambda/2$ (or $n\lambda/2$, where λ is the wavelength at the Bloch frequency in the strip and n is an integer) is then etched off from this structure. Such an n^+–SL–n^+ strip line with a voltage V applied to it (as illustrated in Fig. 3) represents a Bloch oscillator, in which an open segment with a length amounting to an integer number of half-wavelengths represents a resonance electrodynamic system.

The SL thickness l (the number of SL periods N) should be chosen from the requirement that damping of the strip mode in the n^+ layers be lower than amplification of the mode due to the NDC in an SL. The NDC in an SL is low; its magnitude is on the order of that for static conductivity (cf. [9, 10] and the results reported below). Therefore, in order to excite the strip mode, an SR should consist of a large number of periods (500 or more). Unfortunately, in an SL with narrow allowed minibands (in which case electron transport occurs within a single miniband), there necessarily exists an NDC at low frequencies along with the NDC in the vicinity of the Bloch frequency; this low-frequency NDC is caused by the presence of the descending portion in the I–V characteristic (Fig. 2). In sufficiently thick SLs, the existence of static NDC brings about the formation of domains (i.e., a nonuniform distribution of the electric field comes into existence). This effect hinders the existence and study of Bloch oscillations and destroys the NDC in strong electric fields at frequencies on the order of ω_B. Due to this circumstance, a terahertz Bloch oscillator based on an SL with narrow allowed minibands has not been developed (and, most likely, will never be developed for the aforementioned reasons). Notably, "thick" SLs are SLs with a large number of periods, which is necessary, as was mentioned above, for the realization of a Bloch oscillator. As far as we know, there has been only a single report on the development of a microwave oscillator (with a fre-

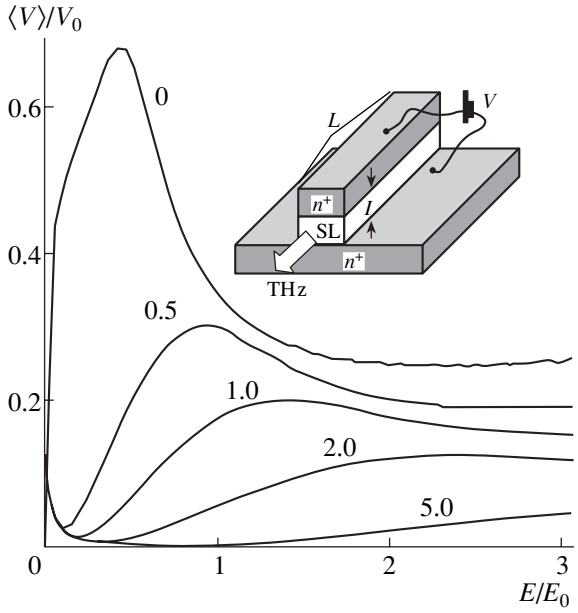

Fig. 3. The current–voltage characteristics (the current is represented by the drift velocity V) of the superlattice in relation to the barrier strengths at a high electron mobility ($\mu = 10^5$ cm^2 V^{-1} s^{-1}); here, V_0 is the electron velocity at the energy equal to that of an optical phonon. Numbers at the curves correspond to the values of the ratio E_t/E_0 at $T = 77$ K. In the inset, we show the schematic representation of a terahertz Bloch oscillator composed of a superlattice (SL) sandwiched between two n^+-type contact layers; this SL represents a segment of a strip line and acts as the oscillator cavity.

quency f of about 150 GHz) based on an SL [11]; this oscillator operated owing to moving strong-field domains in the structure, much the same as in similar Gunn diodes.

The presence of NDC at low frequencies is related to the presence of the descending portion in the I–V characteristic. This descending portion can be eliminated if we consider charge transport in many minibands. To this end, we need a superlattice with narrow forbidden minibands, in which case the role of interminiband transition (tunneling) in an electric field (the Zener breakdown) is important (see Fig. 1). We may assume that the Bloch oscillations and (dynamic) NDC at $\omega \approx \omega_B$ are retained in this situation as well (see Fig. 2b). In this context, we should mention a recent theoretical study [12] in which the relaxation-time approximation in the equation for the density matrix applied to two tunneling-coupled minibands was used to consider a number of cases where the dynamic NDC (DNDC) originates at frequencies close to that of Bloch oscillations and their harmonics. At the same time, Andronov and Nefedov [10] previously discussed the possibility of obtaining DNDC in an SL with narrow forbidden minibands as a result of interminiband tunneling and rapid return of electrons to the lower allowed miniband, accompanied with the emission of optical phonons. In this case, the mechanism of DNDC origination is related to the bunching of electrons in the Brillouin zone of the SL; this bunching is caused by a strong (exponential) dependence of the probability of interminiband tunneling on the electric-field strength. If there are both constant and variable electric fields, the probability of tunneling (and, consequently, the electron lifetime in the lower miniband) depends on the phase of the variable field. This circumstance gives rise to the preferential bunching of electrons in a specific region of the Brillouin zone, depending on the ratio between the field frequency and the Bloch frequency, and also to NDC at frequencies exceeding the Bloch frequency. This inference was corroborated by the data obtained by Andronov and Nefedov [10]; however, numerical results demonstrating the feasibility of realizing such a DNDC in actual structures were not reported [10].

It is also worth noting that numerical simulations of the electrons' dynamics (disregarding the scattering processes) in an SL where Bloch oscillations and interminiband tunneling exist simultaneously have been performed by Bouchard and Luban [13]. Recently, interminiband tunneling in an SL has been studied experimentally [14].

In this paper (based to a great extent on Sosnin's dissertation [15]), we return to a consideration of the above problem and report the results of simulating the charge transport in an SL that has narrow forbidden minibands and is based on the GaAlAs compound. Simulation showed that DNDC can exist in the system under investigation if there is a certain relation between temperature and the SL parameters in the absence of static NDC. In particular, theoretical analysis of a decrease in the electron mobility shows that the NDC is retained at $T = 77$ K under conditions of very moderate mobility (10000 $cm^2 V^{-1} s^{-1}$ at $T = 77$ K).

This circumstance makes it possible to treat these results as being extremely important in the context of developing a universal tuned semiconductor source of terahertz radiation.

In what follows, we consider the model used, the results of simulation, and the possible structure and parameters of the oscillators under consideration.

First of all, we note that the DNDC under consideration in an SL with narrow forbidden minibands is merely an example of DNDCs originating owing to bunching of electrons in the momentum space. The idea of such NDCs was suggested almost 30 years ago and was (then) based on the transit-time resonance in the momentum space under the effect of a strong electric field in conditions of carrier scattering by optical phonons in a semiconductor with strong interaction of charge carriers with optical phonons [16–18]. Stimulated radiation related to the above DNDC in the millimeter-wavelength region was observed not long ago in InP [19]; recently, a similar DNDC in the terahertz region was detected in simulating a GaN SL [20]. Bunching of electrons in the charge transport in an SL with narrow forbidden minibands (with this bunching related to a strong exponential dependence of the interminiband Zener tunneling on the electric-field strength) is much more pronounced than bunching caused by interaction with optical phonons. Therefore, the aforementioned results related to the DNDC in the case of the transit-time resonance and scattering by optical phonons can be treated as direct evidence for the presence of DNDC in an SL with narrow forbidden bands.

Notably, Kroemer has recently drawn attention to the fact that DNDC can exist in a strong variable electric field as a result of bunching of electrons in the momentum space during charge transport in an SL with narrow allowed minibands [21].

2. THE MODEL

In simulation, we used a two-valley n-GaAs model which accounts for electron motion in the Γ and X valleys. It is assumed that, in bulk n-GaAs, there is a weak periodic potential caused by introducing a 10-Å-thick layer of the $Ga_{1-x}Al_xAs$ ternary compound ($x = 0.05$–0.2) in order to form an SL with narrow forbidden bands. The SL period was chosen (150 Å) so that the optical-phonon energy corresponded to the middle of the first forbidden miniband (see Fig. 1). Thus, an electron in the second miniband rapidly emits an optical phonon and is brought into the first miniband. The chosen value of the period corresponds to the boundary of the Brillouin zone $k_B = 0.8p_0/\hbar$, where p_0 is the electron momentum at an electron energy which is equal to the

optical-phonon energy $\hbar\omega_0$ in the bulk of GaAs. The calculated values (in meV) of the positions of the bottoms of the first (ε_0) and second (ε_2) subbands, the top of the first subband (ε_1), and the band gap (ε_g) for various values of the barrier width (a) or various atomic fractions of aluminum (x) for a fixed period d = 150 Å are listed in the table. The values of the ratio between a characteristic tunneling field and a characteristic field of scattering E_t by optical phonons E_0 (see below) are also given in the table. In simulation, we took into account the scattering of charge carriers by acoustical, polar optical, and intervalley phonons (the parameters of scattering processes and valleys were taken from [22]); interminiband tunneling; and the Bragg scattering at the SL potential. It is assumed that, in a parabolic electron band in GaAs, the SL potential gives rise to Bragg scattering with a probability of $P_B = 1 - P_t$, where P_t is the probability of tunneling through the forbidden miniband; the latter probability was assumed to be equal [23] to

$$P_t = \exp(E_t/E), \quad (1)$$

where $E_t = \pi^2\varepsilon_g^2/4\varepsilon_B ed$ is the characteristic tunneling energy and ε_B is the unperturbed electron energy at the Brillouin zone boundary ($\varepsilon_B \approx \hbar\omega_0$, where $\hbar\omega_0$ is the optical-phonon energy) (see Fig. 1). The influence of variations in the energy spectrum of the system, which are caused by the SL potential, on the probability of carrier scattering by phonons was disregarded. The interminiband tunneling was treated as one of the scattering processes: an electron moving in an electric field and reaching the Brillouin zone boundary can execute interminiband tunneling with a probability P_t or can be subjected to the Bragg scattering and transferred to the other boundary of the Brillouin zone with a probability $P_B = 1 - P_t$. Taking into account that an actual scattering event accompanied with the emission of an optical phonon almost inevitably follows tunneling (see the schematic representation of the main transport processes under consideration in Fig. 1), the above assumption seems to be reasonable. We calculated the *I–V* characteristic and differential conductivity in relation to frequency. A decrease in the charge-carrier mobility in the system (due to impurity scattering) was simulated by increasing the deformation potential of scattering by acoustical phonons. In the DNDC effects under discussion, the upper electron valleys in GaAs are, in fact, unimportant. Therefore, the use of the simplified two-valley model in the calculations under consideration is just an illustration and cannot represent realistically the influence of upper valleys on the static carrier transport properties of a material when there is an SL potential.

3. RESULTS OF SIMULATION

In Fig. 3, we show the results of simulating the SL *I–V* characteristic in relation to the SL potential

Characteristic parameters of GaAs–$Ga_{1-x}Al_xAs$ superlattices with a period d = 150 Å

a	x	ε_0	ε_1	ε_2	ε_g	E_t/E_0
10	0.05	2.3	25	33	8	0.75
10	0.1	4.4	24	34	10	1.17
10	0.15	6.1	24	38	14	2.65
10	0.17	6.0	24	39	15	3.04
10	0.2	7.8	24	42	16	4.7
12	0.1	5.2	24	35	11	1.42
15	0.1	6.3	24	38	14	2.65
18	0.1	7.3	24	40	16	2.99

Note: a is the barrier width, x is the Al atomic fraction, ε_0 is the energy corresponding to the bottom of the first subband, ε_1 is the energy corresponding to the top of the first subband, and ε_2 is the energy corresponding to the bottom of the second subband; the ratios between the characteristic tunneling field E_t and the characteristic field of scattering by optical phonons E_0 are also listed.

"strength" expressed in terms of a characteristic tunneling field E_t. It is noteworthy that, for the aforementioned SL based on a structure consisting of GaAs(140 Å) and $Ga_{1-x}Al_xAs$(10 Å) layers, the variation in the value of x in the barrier from 0.05 to 0.2 changes the value of E_t within the range of (0.7–0.5)E_0 (see table). The values of both the applied field E and the tunneling field E_t are divided by a characteristic field of scattering by optical phonons E_0 ($E_0 \approx 6$ kV/cm in GaAs). In the absence of an SL potential ($E_t = 0$), we observe a descending portion in the *I–V* characteristic; this portion sets in at a field strength of $E \approx E_0/2$ and is caused by the intervalley charge transport. The shape of the *I–V* characteristic differs somewhat from that reported in [22], which is caused by the fact that a simple two-valley Γ–*X* model is used in the simulation. As the strength of the SL potential increases (as E_t increases), a descending portion appears in the *I–V* characteristic in the region of weak electric fields; this portion is typical of the *I–V* characteristics of SLs with a narrow allowed miniband and is related to localization of electrons within the lower miniband in weak fields. As the field strength increases, the descending portion gives way to an increase in the current owing to the onset of interminiband tunneling, so that the *I–V* characteristic in a strong field is almost the same as that at $E_t = 0$. The field corresponding to the transformation of the descending portion in the *I–V* characteristic into the ascending one increases with increasing E_t.

In Fig. 4, we show the results of simulating the frequency dependence of differential electrical conductivity for a fixed applied electric field E and three values of the tunneling field strength E_t. It can be seen that, at a large value of E_t (in which case, according to Fig. 3, there is a descending portion in the *I–V* characteristic), the differential conductivity is negative at frequencies lower than the Bloch frequency (as in Fig. 2). As E_t

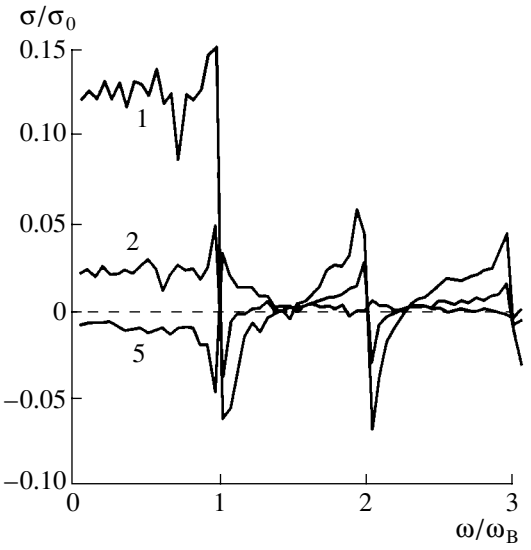

Fig. 4. The frequency dependences of differential electrical conductivity for several values of the barrier strength E_t/E_0 indicated by numbers at each curve. $E/E_0 = 0.5$, $T = 77$ K, and $\mu = 10^5$ cm^2 V^{-1} s^{-1}.

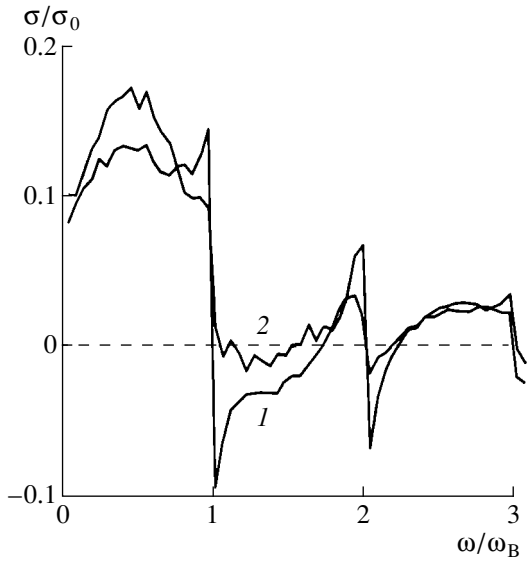

Fig. 5. The frequency dependences of differential conductivity for a superlattice with electron mobility μ = (*1*) 10^5 and (*2*) 10^4 cm^2 V^{-1} s^{-1}. $f_B = \omega_B/2\pi = 2.1$ THz, $E/E_0 = 1.0$, and $E_t/E_0 = 2.0$.

decreases, a DNDC region with positive differential conductivity appears at low frequencies. Other calculations (we are not going to dwell on these here) show that, as the field strength E increases, the optimal (with respect to the DNDC magnitude) value of E_t is approximately equal to $2E$; notably, the DNDC magnitude even increases somewhat with increasing E (and the Bloch frequency). The limiting value of the frequency $\omega \approx \omega_B$ up to which DNDC is expected to be retained is determined from the following condition for the absence of direct interminiband transitions (the latter, as a result of their high intensity, suppress the DNDC):

$$\hbar\omega < \varepsilon_g.$$

Assuming that $\omega = \omega_B$ and $E_t \approx 2E$ and using expression (1) for the relation between ε_g and E_t, we find that the limiting value of the DNDC frequency is equal to

$$\omega_{max} \approx 8\omega_0/\pi^2.$$

This formula yields a limiting value of the DNDC frequency roughly equal to 7 THz in the structures under consideration.

It is worth noting that calculations involving an increased value of the constant of deformation scattering by acoustical phonons and, consequently, involving a lower electron mobility (which simulates the effect of impurity scattering) show (see Fig. 5) that DNDC is retained for a mobility as high as about 10^4 cm^2 V^{-1} s^{-1}. This value corresponds to an electron concentration greater than 10^{16} cm^{-3} at $T = 77$ K.

In addition to the aforementioned simulations, we also calculated the *I–V* characteristic and differential electrical conductivity in the context of a one-dimensional (1D) model; we assumed that an electron reaching the second miniband emits an optical phonon instantaneously (see also [10]). The magnitudes of DNDC derived based on this model are close to those obtained by simulation using the Monte Carlo method in the case of a fairly high Bloch frequency.

Finally, we note that, in the context of a 1D model, the origination of electron bunching in the momentum space can be easily simulated if we simultaneously have variable (weak) and constant fields in the presence of interminiband tunneling. Thus, we considered the following problem. Let us assume that a momentum-uniform electron distribution is formed in the 1D Brillouin zone at an initial point in time. Electrons move within the Brillouin zone without scattering under the effect of constant and weak variable fields. The latter field was approximated by a step function. At the Brillouin zone boundary, electrons tunnel into the second miniband and are either no longer considered or undergo Bragg scattering and continue to move within the zone. The probability of tunneling depends on the field strength, as in the case of the probability given by formula (1). Electrons leave the zone, so that their number decreases. However, electron bunches are formed simultaneously in the Brillouin zone in several periods; these bunches are especially pronounced at $\omega = \omega_B$. If $\omega \neq \omega_B$, the electrical conductivity provided by electrons which remain in the zone depends on the relation between the frequencies ω and ω_B; the conductivity is

positive if $\omega < \omega_B$ and negative if $\omega > \omega_B$ (as in the aforementioned results of simulation).

4. THE STRUCTURE AND PARAMETERS OF A BLOCH OSCILLATOR

As mentioned in Section 1, a Bloch oscillator should constitute a diode that consists of an SL layer sandwiched between two contact n^+-type layers, which also form the strip line for the terahertz radiation caused by DNDC (see the inset in Fig. 3). In order to estimate the thickness of the layer with an SL, we should compare the losses in the strip line with the gain caused by DNDC. To this end, we use the calculated magnitude of NDC (Fig. 5), i.e., $|\sigma| = (0.05–0.1)\sigma_0$. Here, $\sigma_0 = e^2N/m\nu_0$ is the characteristic static electrical conductivity of GaAs in a strong field and $\nu_0 \approx 4 \times 10^{12}$ s^{-1} is the characteristic scattering frequency. Taking into account that the NDC is retained at $T = 77$ K even at moderately low mobility, we choose the electron concentration $N = 10^{16}$ cm^{-3}. As a result, we obtain an amplification coefficient on the order of 50–100 cm^{-1}. For the value of losses in the strip line, we took the value [24] measured at the wavelength $\lambda = 75$ μm; i.e., we assumed that the losses for the strip line with spacing between the strips of 10 μm were equal to about 50 cm^{-1}. At high frequencies ($\omega \gg \nu$, where ν is the scattering frequency in the contact regions), the losses in the strip line are independent of frequency. From these estimates, we find that the SL thickness should be equal to 5–10 μm (350–700 periods). Apparently, the number of periods can be reduced if one uses more heavily doped (or metallic) contact regions. Presumably, such an oscillator can operate in the continuous-wave mode at a temperature of 77 K.

5. CONCLUSION

We considered transport properties of superlattices (SLs) with a weak periodic potential and narrow forbidden minibands in the situation where the bottom of the second miniband is separated from the bottom of the first miniband by an energy exceeding that of an optical phonon; under these conditions, electrons appearing in the upper minibands return rapidly to the first miniband with the emission of optical phonons. We performed numerical simulation of the *I–V* characteristic and differential electrical conductivity of such SLs based on the GaAs–GaAlAs structure; we used certain assumptions that simplified the analysis. Specifically, we assumed that the energy spectrum of electrons in such SLs is the same as in bulk GaAs (i.e., this spectrum is parabolic). Furthermore, we took the SL potential into account by introducing additional transport processes; these processes depend on the electric-field strength and include (i) a transition (tunneling) in an electric field through thin forbidden minibands and (ii) Bragg scattering within the allowed minibands. The aforementioned processes were treated as conventional scattering mechanisms, which is justified since the process of tunneling to the second miniband is followed (with very high probability) by scattering by optical phonons. It is shown that, even in an SL with moderate carrier mobility, one can realize the situation where only dynamic negative differential conductivity (DNDC) (in the terahertz-frequency region) exists in the system at a temperature of 77 K and there is no descending portion in the *I–V* characteristic. This circumstance opens the way to developing a terahertz Bloch oscillator.

Undoubtedly, further studies will refine the obtained results. However, the general pattern and the magnitudes of the DNDC should remain virtually intact, since the basic process responsible for DNDC is quite evident; this process consists in the bunching of electrons in the Brillouin zone in the presence of both constant and weak variable fields and is caused by a strong dependence of the probability of interminiband tunneling on the magnitude of the total electric field. This circumstance gives rise to discrimination of electrons with respect to phases of the variable field and, in the absence of Bloch oscillations, to bunching of electrons in the Brillouin zone with the resulting formation of DNDC.

The main drawback of the DNDC under consideration is its small magnitude. This is related to the fact that a Bloch oscillator is a "laser without population inversion," since an energy quantum corresponding to the Bloch frequency separates the Wannier–Stark levels; the latter are filled equally in a uniform electric field (see discussion of this issue in [10]). The small magnitude of DNDC requires that fairly thick (5–10 μm) SLs be used in the design of a Bloch oscillator. This is necessary in order to overcome the absorption in the oscillator cavity; the latter is represented by a strip line sandwiched between contact regions. Nevertheless, this thickness is no larger than the total thickness (in excess of 10 μm) of a recently developed terahertz cascade laser which operates at temperatures as high as 50 K [25]. Thus, we may assume that the Bloch oscillator suggested could be quite competitive with the aforementioned cascade laser, especially as the SL required for Bloch oscillator operation is much simpler than that for a cascade-laser structure; in addition, the oscillator under consideration is expected to operate at $T \approx 80$–100 K.

Finally, we note that diodes of the type shown in Fig. 3 but with thinner SLs (with a thickness of about 1 μm) might be used for the detection of luminescence (noncoherent spontaneous emission) at the Bloch frequency, which has not been done so far. As far as we know, only emission generated by electron bunches at the Bloch frequency has been observed; these bunches were formed by short laser pulses [26].

ACKNOWLEDGMENTS

We thank V.Ya. Aleshkin for his helpful participation in discussions and for assistance and encourage-

ment. Thanks are also due to D.D. Zinchenko for participating in investigations.

This study was supported by grants from the programs “Physics of Microwaves” and “Leading Scientific Schools.”

REFERENCES

1. F. Bloch, Z. Phys. **52**, 555 (1928).
2. C. Zener, Proc. R. Soc. London, Ser. A **145**, 523 (1934).
3. C. Hilsum, Solid-State Electron. **21**, 5 (1978).
4. L. V. Keldysh, Fiz. Tverd. Tela (Leningrad) **4**, 2265 (1962) [Sov. Phys. Solid State **4**, 1658 (1962)].
5. L. Esaki and R. Tsu, IBM J. Res. Dev. **14**, 61 (1970).
6. V. A. Yakovlev, Fiz. Tverd. Tela (Leningrad) **3**, 1983 (1961) [Sov. Phys. Solid State **3**, 1442 (1962)].
7. E. E. Mendez and G. Bastard, Phys. Today **46** (6), 34 (1993).
8. A. Ya. Shik, Fiz. Tekh. Poluprovodn. (Leningrad) **8**, 1841 (1974) [Sov. Phys. Semicond. **8**, 1195 (1975)].
9. S. A. Ktitorov, G. S. Simin, and V. Ya. Sandalovskiĭ, Fiz. Tverd. Tela (Leningrad) **13**, 2230 (1971) [Sov. Phys. Solid State **13**, 1872 (1971)].
10. A. Andronov and I. Nefedov, in *Hot Carries in Semiconductors* (Plenum, New York, 1996), p. 153.
11. E. Schomburg, R. Scheuerer, S. Brandl, *et al.*, Electron. Lett. **35**, 12 (1999).
12. L. K. Orlov and Yu. A. Romanov, Izv. Vyssh. Uchebn. Zaved., Radiofiz. **32**, 282 (1989).
13. A. M. Bouchard and M. Luban, Phys. Rev. B **52**, 5105 (1995).
14. B. Rosam, D. Meinhold, F. Loser, *et al.*, Phys. Rev. Lett. **86**, 1307 (2001).
15. A. Sosnin, Master’s Dissertation (Nizhni Novgorod State Univ., Nizhni Novgorod, 2001).
16. V. L. Bonch-Bruevich and El-Sharnubi, Vestn. Mosk. Univ., Ser. 3: Fiz., Astron. **13**, 616 (1972).
17. A. A. Andronov and V. A. Kozlov, Pis’ma Zh. Éksp. Teor. Fiz. **17**, 124 (1973) [JETP Lett. **17**, 87 (1973)].
18. E. Starikov and P. Shiktorov, Litov. Fiz. Sb. **32**, 471 (1992).
19. L. E. Vorob’ev, S. N. Danilov, V. N. Tulupenko, and D. A. Firsov, Pis’ma Zh. Éksp. Teor. Fiz. **73**, 253 (2001) [JETP Lett. **73**, 219 (2001)].
20. E. Starikov, P. Shiktorov, *et al.*, IEEE Trans. Electron Devices **48**, 438 (2001).
21. H. Kroemer, cond-mat/0009311.
22. M. Shur, GaAs *Devices and Circuits* (Plenum, New York, 1987; Mir, Moscow, 1991).
23. J. M. Ziman, *Principles of the Theory of Solids*, 2nd ed. (Cambridge Univ. Press, London, 1972; Mir, Moscow, 1974).
24. M. Rochat, M. Beck, J. Faist, and U. Oesterle, Appl. Phys. Lett. **78**, 1967 (2001).
25. R. Kohler, A. Tredicucci, F. Beltram, *et al.*, Nature **417**, 156 (2002).
26. C. Waschke, H. G. Roskos, R. Schwedler, *et al.*, Phys. Rev. Lett. **70**, 3319 (1993).

Translated by A. Spitsyn